Manipulation of a Large Magneto-Optical Trap:application to Four-Wave Mixing

Giovanni Luca Gattobigio

▶ **To cite this version:**

Giovanni Luca Gattobigio. Manipulation of a Large Magneto-Optical Trap:application to Four-Wave Mixing. Atomic Physics [physics.atom-ph]. Università degli studi di Ferrara; Université Nice Sophia Antipolis, 2008. English. NNT : . tel-00312718

HAL Id: tel-00312718

https://theses.hal.science/tel-00312718

Submitted on 25 Aug 2008

HAL is a multi-disciplinary open access archive for the deposit and dissemination of scientific research documents, whether they are published or not. The documents may come from teaching and research institutions in France or abroad, or from public or private research centers.

L'archive ouverte pluridisciplinaire **HAL**, est destinée au dépôt et à la diffusion de documents scientifiques de niveau recherche, publiés ou non, émanant des établissements d'enseignement et de recherche français ou étrangers, des laboratoires publics ou privés.

Università degli Studi di Ferrara

DOTTORATO DI RICERCA IN

FISICA

CICLO

XIX°

COORDINATORE Prof. Filippo Frontera

Manipulation of a Large Magneto-Optical Trap: application to Four-Wave Mixing

Settore Scientifico Disciplinare FIS/01

Dottorando
Dott. Giovanni Luca Gattobigio

Tutore
Prof. Roberto Calabrese

Tutore Esterno
Prof. Robin Kaiser

Anni 2004-2008

Contents

"....Ma tu dagli atomi freddi, cosa ti aspetti ?"

Fabiola, Roma 2008

Introduction

Multiple Scattering and wave localization

The propagation of waves, for example light waves, in a disordered media is an active research area nowadays. The original scientific motivation came from an astrophysical question about the properties of light radiated by interstellar atmospheres [1]. After that, in general, wave propagation was studied in many fields of physics such as, for example, acoustics, solid states (electrons in metal), geophysics (seismic waves in earth-crust), and so on.

Generally, in a slab of thickness L, characterized by a mean free path ℓ, we define the opacity (optical thickness) as $b = L/\ell$. In multiple scattering regimes ($b \gg 1$) wave propagation is governed by the diffusion equation [2]. However, in the case of light, as well as in the case of electrons, the quantum nature of the wave has to be considered. In fact, in random media, interference can modify wave propagation (by reducing the diffusion coefficient), and even lead to it vanishing completely, where the diffusion is suppressed [3]. In this latter case, the wave function is localized in the media, and the phenomena is known as Anderson's localization.

A macroscopic criteria, in order to observe such localization, is expressed by the Ioffe-Regel criteria [4]:

$$\ell \sim \lambda \tag{1}$$

which gives a relation between the wavelength (λ) and the mean-free path (ℓ).

Particularly, such criteria requires a scattering medium with high spatial densities n, and a high scattering cross-section σ ($\ell \propto 1/\sigma\, n$).

Photons traveling through strongly scattering media are an ideal model system with which to study localization. This is because the photons are not charged and do not interact with each other. In the optical domain, the experimental realization of such a dense sample is very difficult but many ideas have been put forward and experiments carried out to try to achieve this intriguing regime. In particular, we point to the experiment carried out in 1997 [5], where the authors claim to have observed Anderson's localization by using semiconductor powder in 3D geometry. But the results were contested by proposing an alternative interpretation which includes the absorption of the sample [6]. However, a more recent experiment shows that close to the localized threshold, a modification of the diffusion coefficient was observed by performing time-resolved photon transport [7] [8].

Multiple Scattering and Cold Atoms

The effects of interference in wave transport can also be seen even in the diluted regime ($\ell \gg \lambda$), called the weak localization regime, with the observation of coherent light transport properties such as coherent back scattering (CBS), observable even with cold atoms [9].

Nowadays, with more developed laser cooling techniques [10], we are able to trap atoms, starting from a "hot" vapour, in a Magneto-Optical Trap (MOT), realizing an atomic sample which is controllable across a wide range of parameters.

The choice to use cold atoms to study multiple scattering, particularly for the observation of Anderson's localization, is motived by the complete absence of absorption and by the possibility of controlling the scattering properties of the sample including, for example, the atomic cross-section.

In the case of cold atoms, with for example ^{85}Rb, the Ioffe-Regel criteria impose a spatial density of about $10^{13} - 10^{14}\, atms/cm^3$ in order to observe localization effects. This means that one has to increase the atomic density by three or four orders of magnitude compared to that obtainable in a standard MOT.

However, it is well known in the cold atom research community that multiple scattering has been a major limitation on the possibility of obtaining large phase space density, and particularly high spatial density, in cold atomic traps. In fact, Bose-Einstein condensation in diluted atomic vapors was only achieved after switching off all laser fields and using evaporation techniques [11] [12]. Moreover, when the number of trapped atoms is increased the light scattered by these atoms will modify the phenomena of light induced forces. In this regime two competing effects have to be considered: an opacity effect, which leads to a compression of the trap, and a repulsive radiation pressure, which tends to increase the size of the atomic cloud. The model proposed by [13] predicts a constant density n when more and more atoms are added into the MOT. This means that if we want to increase the density, we need to "control" the interaction induced by the scattered light within the MOT.

Multiple Scattering and Gain

As we already mentioned, light can also be trapped in a disordered system due to multiple scattering. In an active medium (with gain) the propagating light wave will travel along a long random route before it leaves the medium, and will be amplified at every scattering event. As we already observed, interference effects can survive random multiple scattering (e.g. CBS or weak localization) and such an interference effect is still observable if we introduce gain into the medium. Moreover, it is possible to observe that long, deeply penetrating light paths become much more important with the introduction of gain. This means that if we think of Anderson's localization of light as closed loops made by the light in an extremely strong scattering media, the introduction of gain can amplify such a "localized state". Further, we can be confident that the presence of gain can allow us to observe the pre-localized state. This justifies our interest in having an active sample, with gain, to study new effects in the multiple scattering even though the localization threshold is not reached. In order to do this we decided to use a pump-probe scheme with our large cloud of cold atoms to pump energy into the atomic medium, and found a very

large gain [14]. The investigation of unexplored regimes of cold atomic clouds, namely the limit of very large numbers of atoms in the presence of quasi-resonant light, could also be helpful in reaching the dense regime needed for the investigation of light localization. This latter aspect is the main subject of this thesis.

Outline of the thesis

We will present the experimental set-up in Chapter 1. In Chapter 2 we will present a detailed experimental investigation of size and density scaling laws for large magneto-optical traps with up to 10^{10} atoms and identify a new mechanism which can limit the density of the atoms in such a system. In Chapter 3 we will present the strategies used to compress our atomic sample by up to two orders of magnitude with respect to a standard MOT. This study was finalized to design new compression techniques to achieve high spatial densities, in order to study localization effects of light in a dense cloud of cold atoms.

However, before doing that, the pump-probe scheme provides us with the possibility of investigating the Degenerate Four-Wave Mixing (DFWM) signal in a sample of cold atoms. In Chapter 4, after a brief introduction of its theoretical aspect, we will present the observation of a new effect, the red-blue asymmetry of the DFWM signal for high intensities of the pump beams. This asymmetry can be explained as the spatial bunching of the atoms in the nodes or antinodes of the strong standing wave of the pump beams.

Chapter 1

Experimental Setup

In the following section, we will describe the *Rb* set-up used for the experiments performed during this thesis.

The set-up has already been described in [9]. However, several items have been changed. Therefore we will give more details of the present laser set-up, including the laser cooling system, as well as the repumper laser, with a description of the MOT configuration. In this part, we will also show all calibration curves used during all the experimental measurements performed.

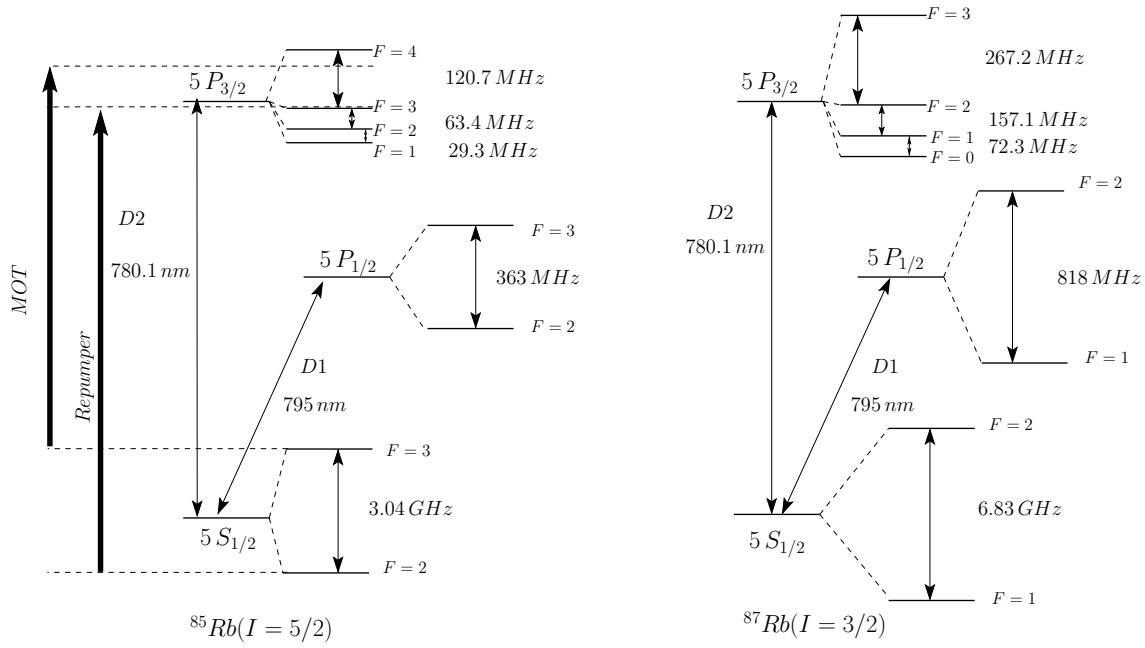

Figure 1.1: *Atomic levels of energy* ^{85}Rb, ^{87}Rb. *The transitions used for trapping and repumper atoms of* ^{85}Rb *are reported.*

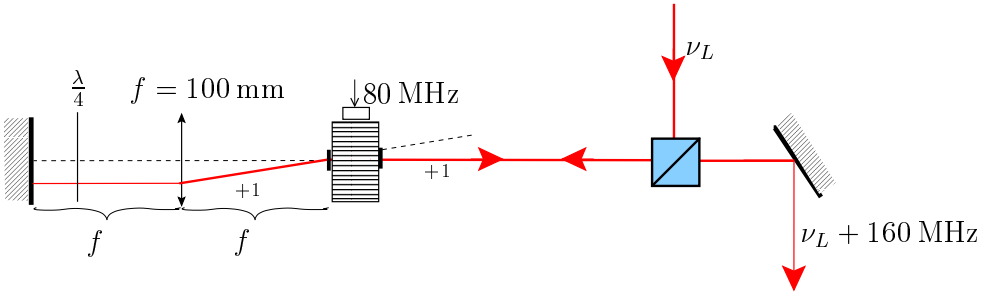

Figure 1.2: *The diagram shows the typical double-pass arrangement for the acousto-optical modulator (AOM). In such a configuration we shift the laser frequency by changing the frequency of the RF field applied to the AOM without any displacement of the output laser beam.*

1.1 The Laser System

The complex laser set-up, shown in Table (1.1) and described in the following sections, was necessary to allow flexible time and frequency control of all lasers and to obtain the relatively high power obtained for all beams. The high power is needed because of the large beam waists used to trap a lot of atoms.

One additional advantage of this set-up is that intensity fluctuations are reduced by the injection technique we use (the Master-Slave technique). In fact, the good spectral quality of the Distributed Bragg Reflector (DBR) laser diodes, our Master frequency-stabilized laser, is transferred into a more powerful laser diode (Slave), which follows the frequency imposed by the Master. The typical Master-Slave arrangement is presented in Fig. (1.1), and the frequency injection is checked by using a home-made *confocal* Fabry-Perot (FP) Fig. (1.1). Frequency is controlled by double passing through an acousto-optical modulator (AOM) as shown in Fig. (1.2).

After this brief presentation of the ideas behind the laser control we will present the laser arrangement for both repumper and cooling lasers in greater detail.

1.1.1 Cooling laser

Cooling and trapping is performed on the D2 line of the Rubidium ($5S_{1/2} \rightarrow 5P_{3/2}$) at wavelength $\lambda = 780nm$. To be precise we use the hyperfine cycling transition $F = 3 \rightarrow F' = 4$. The laser light for this transition is obtained by a DBR diode (Yokogawa YL78XN), with a nominal power of about $5mW$ and a line width of $2\,MHz$. The laser is frequency-stabilized on the cross-over transition of the saturated absorption, as we can see in the Fig. (1.3). Then, it is frequency-shifted via a double pass acousto-optical modulator (AOM1) roughly $80\,MHz$ on the blue side of the resonant transition $F = 3 \rightarrow F' = 4$. As we need more power for the trapping beams, we inject a slave diode (SDL5401-G1) which provides us with more than $20mW$. The injection is made by the geometric alignment of a laser beam through the optical isolator of the slave. The operating range of such an injection, monitored by a Fabry-Perot Fig. (1.1), depends on the slave temperature and current. Even with the controlled temperature and stabilized current source we are using,

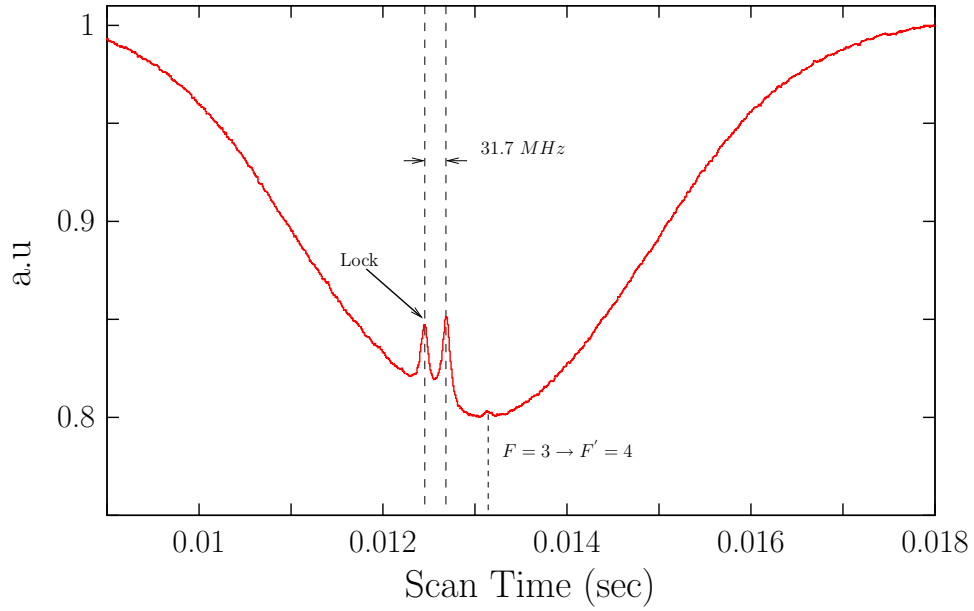

Figure 1.3: *Signal of Saturated absorption used to obtain the derivative signal for laser stabilization. We lock the MOT master-laser in the cross-over (CO_{24}) between the $F^{'} = 2$ and $F^{'} = 4$ transition, indicated by the arrow. This transition is about $\sim 90\,MHz$ below the cycling $F = 3 \rightarrow F^{'} = 4$ atomic transition. To calibrate the time scale, we used the difference between the two cross-over ($CO_{34}$and CO_{24}), that we know are $31.7\,MHz$ distant from each other, as reported in the figure.*

an injection might hold for only half an hour in the worst case, but might run all day without readjustment under more stable conditions (e.g. less room temperature fluctuations). The output of this slave is then passed through a tapered amplifier (SDL-8630-E) Fig. (1.1). A second acousto-optical modulator (AOM2) Fig. (1.1), used in a single pass configuration, is used to bring the frequency of the laser close to the resonant transition $F = 3 \rightarrow F^{'} = 4$ of ^{85}Rb and is also used as a switch (with a reduction of 10^{-4} in the first diffraction order). A spatial filter (diameter of $100\,\mu m$) Fig. (1.1), allows us to clean up the transverse mode of the laser and we routinely obtain $180\,mW$ power after using the spatial filter. Using polarizing cubes the laser is then split into 3 pairs of counter propagating beams crossing into a $10\,cm$ sized cubic vacuum chamber.

The 6 beams (not retro-reflected) have each been expanded by a telescope to a waist of $w = 2.4\,cm$ before entering the vacuum chamber. We thus have intensities of about $1\,mW/cm^2$ for each of the six beams.

The optimization of the number of trapped atoms had lead us to misalign the counter propagating beams in some experiments. However, by very carefully adjusting the center of the counter propagating beams we finally obtained an optimal trap with as many as 10^{10} atoms trapped.

As we use a time sequence where the second acousto-optical(AOM2) modulator is periodically switched off (for the detection procedure), the polarization of the laser after this acousto-optical modulator can change depending on the applied time sequence.

Therefore, the intensities of the 6 MOT beams have to be balanced very carefully. During the period when we switch off the cooling and trapping beams (and the magnetic field gradient as well), all the light passes without diffraction through AOM2 (Fig. (1.1)), and is directed to a third acousto-optical modulator (AOM3) where we use the first diffraction order as a probe beam. The single pass AOMs (AOM2 and AOM3) are used as switches, and the frequency of the cooling and trapping beam as well as of the probe beam (during the corresponding time period) is controlled via a double pass on the acousto-optical modulator (AOM1). The frequency can be calibrated by looking at the displacement of the transmission signal of the Fabry-Perot (Fig. (1.1)) as a function of the voltage applied to the AOM1. Typically we found a calibration coefficient of $2.1\,\Gamma/Volt$.

1.1.2 Repumper

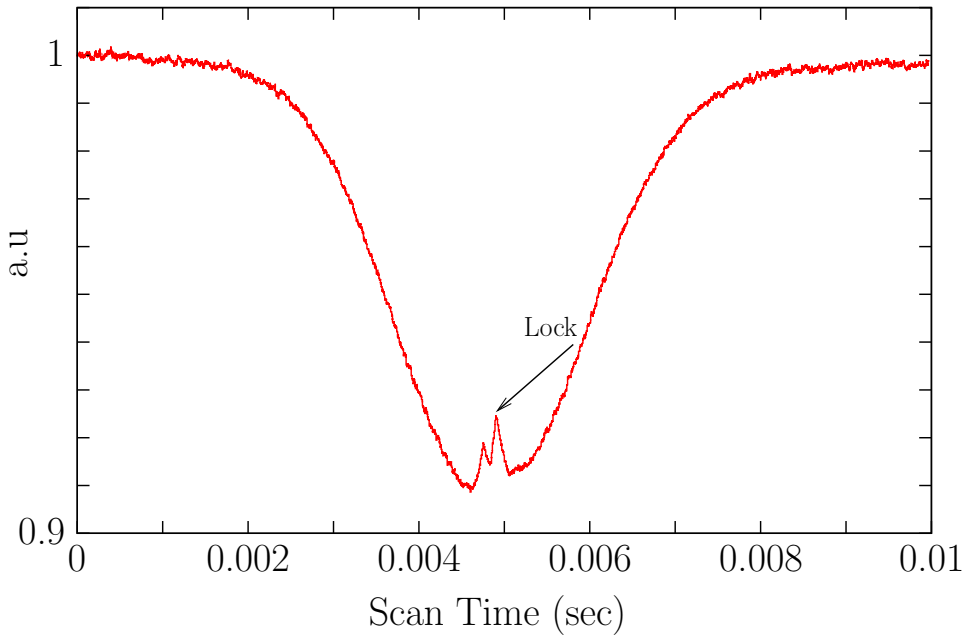

Figure 1.4: *The diagram shows the saturated-absorption signal for the repumper transition. The repumper-laser is stabilized in a cross-over transition. Then we finely adjust its frequency by looking at the maximum number of atoms trapped as we will see later on in Fig. (1.5).*

As we perform the atomic cooling by using the $F = 3 \rightarrow F^{'} = 4$ slightly red-detuned by $\sim 3\Gamma$, as we already saw in the Sec. (1.1.1), we also have a probability different from zero, to excite the $F = 3 \rightarrow F^{'} = 3$, which is an open transition. This latter transition is responsible for the hyperfine ground changing state via a spontaneous Raman-Transition. This transition happens for every 10^3 photons exchanged between the atom and the cooling laser. Thus we need a repumper laser tuned, for example, to $F = 2 \rightarrow F^{'} = 3^{\prime}$ to 'repump' the atoms back into the $F = 3$ hyperfine ground state to be ready to be cooled and trapped again.

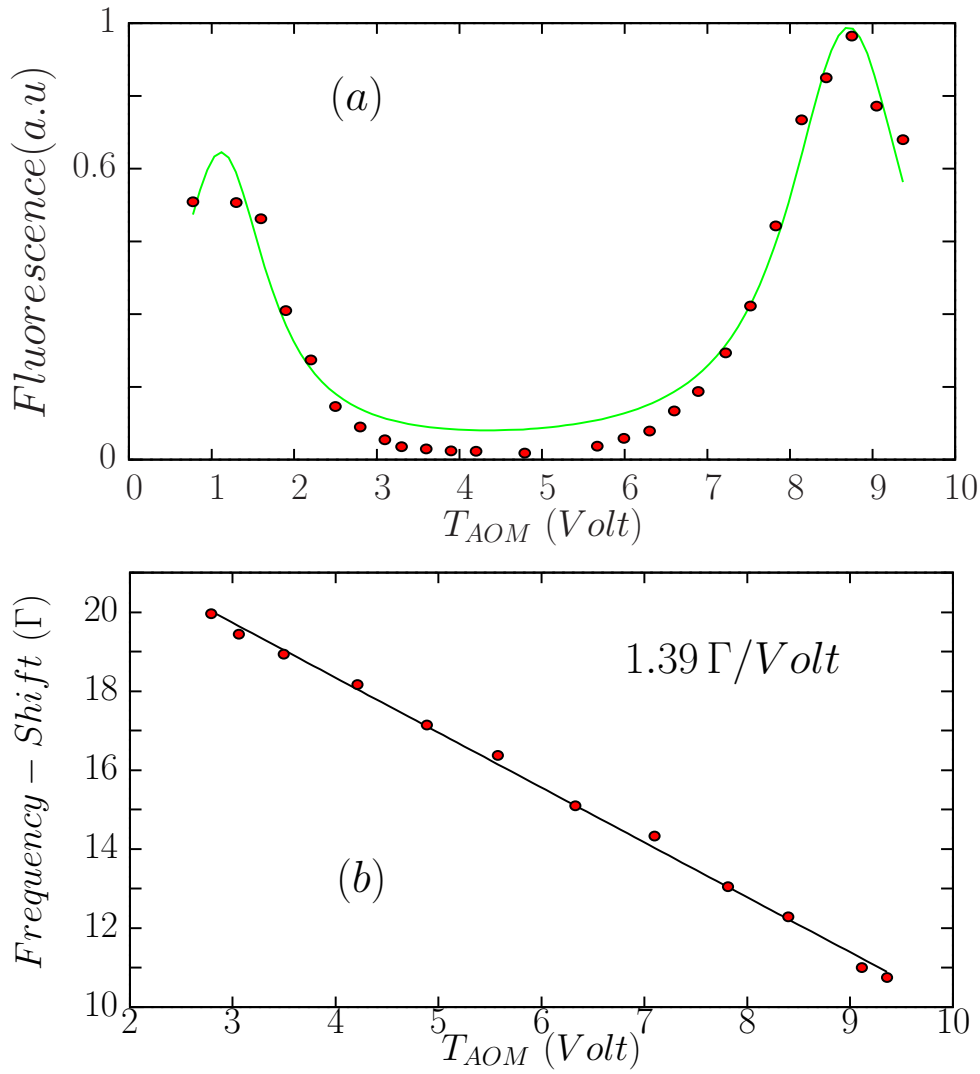

Figure 1.5: *The diagram shows the calibration of the repumper laser. The frequency shift of the double-passing as a function of tension control, Fig. (b), is monitored by looking at the Fabry-Perot transmission and we found a calibration coefficient of* $1.39\,\Gamma/Volt$*. The tension necessary to be at resonance is found by looking at the atomic fluorescence obtained during a 'Dark-Phase' of* $2\,ms$ *with a large probe detuning of about* $\delta_{probe} \sim -6\,\Gamma$*, Fig. (a). By looking at Fig. (a), we observe that the optimum repumper transition* ($F = 2 \rightarrow F^{'} = 3$) *corresponds to a control tension in the AOM of about* $8.71\,Volt$*. A less favourable transition is also found for a control tension of* $1.12\,Volt$*, which corresponds to* $F = 2 \rightarrow F^{'} = 2$ *atomic transition that is about* $\sim 60\,MHz$ *away from the* $F = 2 \rightarrow F^{'} = 3$*.*

In the past we used several different lasers as repumpers. The present configuration uses a master-slave configuration with a DBR master (Yokogawa YL78XNW/S) and a SDL slave (SDL-5401-G1). The master laser is locked to a cross-over transition and shifted, Fig. (1.4) by a double pass AOM (AOM4), before injecting the slave laser. The output beam of the slave laser is passed through an AOM (AOM5) in single pass configuration allowing the possibility of switching the repumper laser on and off at will. We

also inserted a half-wave plate and a polarizing cube (intensity control Fig. (1.1)), which allowed us to change the intensity of the repumping laser, one of the techniques employed to change the number of atoms in the MOT. The size of the repumping beam was also increased by a telescope before entering the vacuum chamber and was limited by the size of the lenses used to $\phi = 10\,cm$, providing a maximum intensity for the repumping beam of $I_{rep} = 0.5\,mW/cm^2$. We also placed a diaphragm at the conjugate position of the MOT, allowing us to reduce the capture volume of the MOT without affecting the MOT dynamics directly. We used a retro-reflection scheme for the repumper along one axis at about 20 degree from the axis defined by the magnetic field coils.

1.1.3 Probe

The probe beam was obtained by using the first diffraction order of the acousto-optical modulator AOM3 Fig. (1.1). As we periodically switched off the cooling and trapping beams by the AOM2 Fig. (1.1), during the period when the MOT was off, all the light passed through AOM2 without diffraction. Then, this light was sent into the AOM3. The time duration of the probe could be set by controlling the duration of TTL applied to AOM3, while its detuning was imposed by the double-passing AOM1 Fig. (1.1), which could be changed independently of the MOT's detuning, ranging between -4Γ and $+4\Gamma$.

1.2 The MOT

After we had realized laser stabilization for both the cooling and the repumper laser, as described in the Sec. (1.1), and after the separation into three branches as shown in Fig. (1.1), we again separated each branch into two others, to obtain the three counter propagating pairs, for the $\sigma^- - \sigma^+$ configuration required for the Magneto-Optical Trap (MOT), as shown Fig. (1.6).

The MOT was loaded from a room temperature vapor of Rubidium ^{85}Rb atoms in a cubic quartz cell sized $10\,cm$ [15]. A system of vacuum valves connects the cell to an ionic pump ($25\,l/sec$) that allows a vacuum of $10^{-8}\,mbar$ inside the cell, and a $reservoir$ of Rb.

The magnetic field gradient is obtained by two coils in configuration $anti-Helmholtz$. We typically obtained a magnetic field gradient of about $10\,Gauss/cm$ with a current of $2\,A$ with a relative tension of $6Volt$. We were also able to switch off such a magnetic field in about $50\mu sec$.

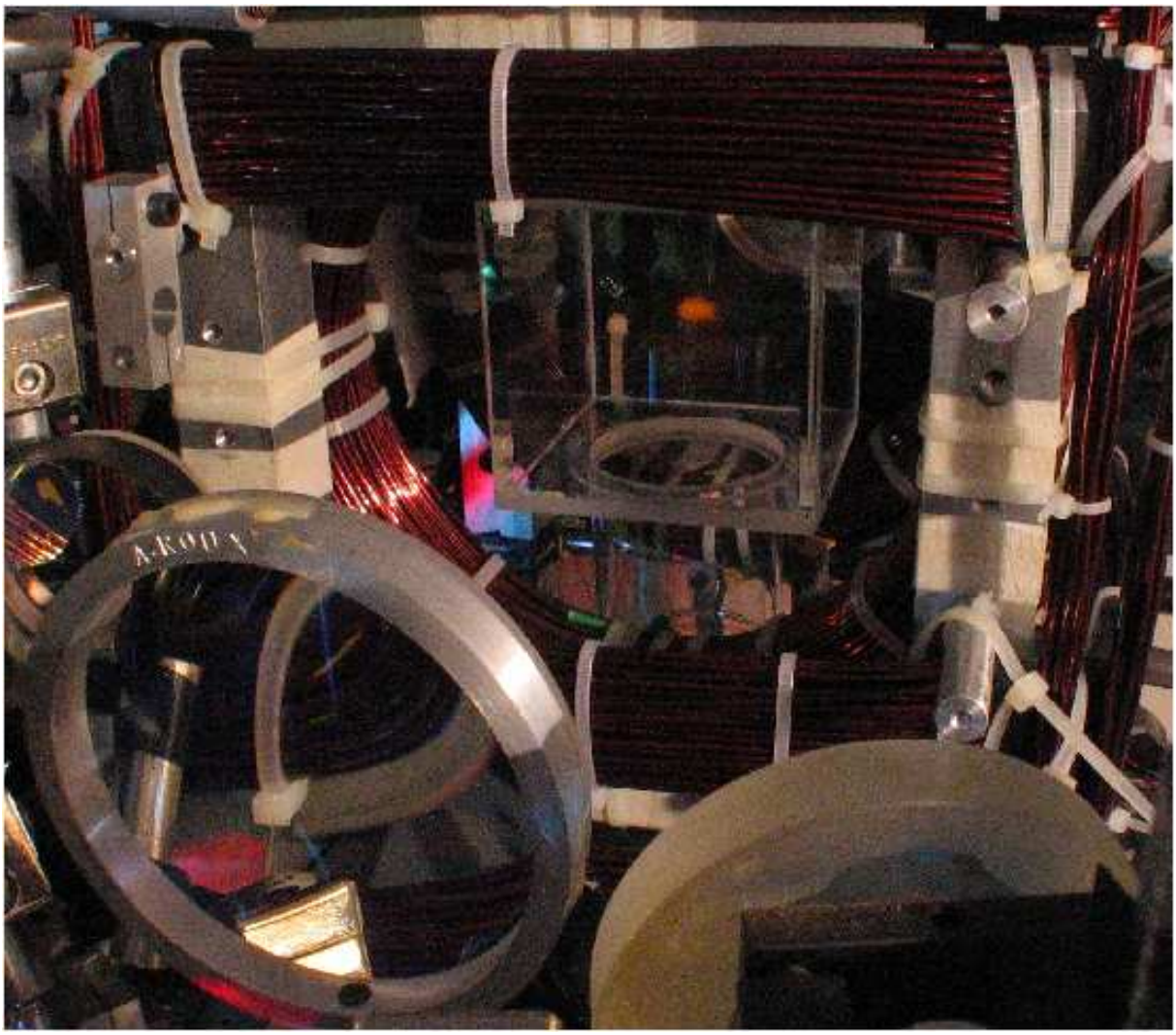

Figure 1.6: *Photo of the Rb MOT (red spot) realized in the center of the vacuum cell .*

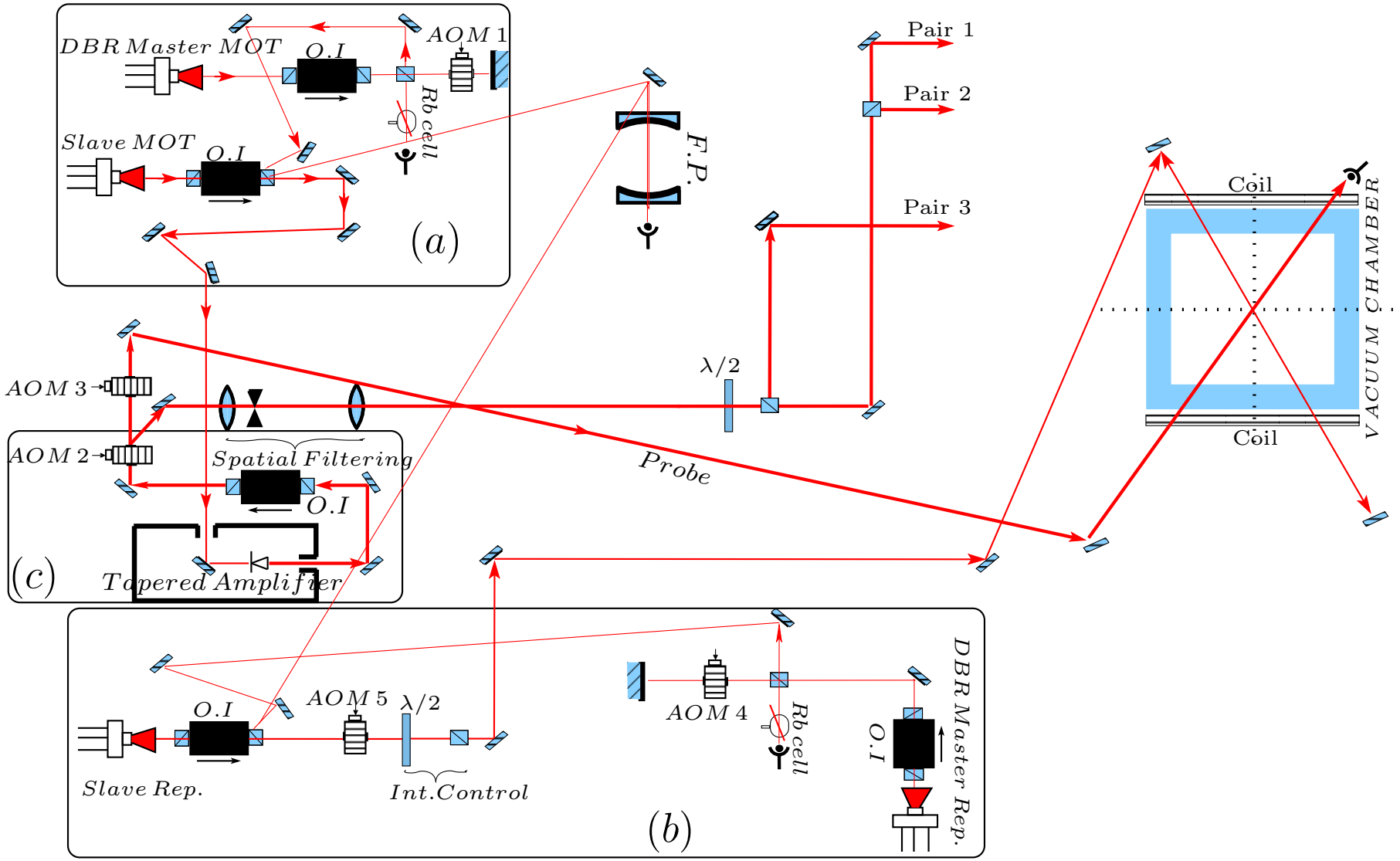

Table 1.1: *In the figure we show the set-up arrangement used for cooling and trapping the atoms. Basically, the set-up is formed by three main blocks. The block (a), shows the master-slave configuration used for the frequency stabilization of the laser MOT, we used the block (c) as a power-amplifier that gave us sufficient power to produce six independent beams for trapping. First of all, the outgoing beam is split into three beams (pair 1, pair 2, pair 3) and then each beam is split again into two more beams. Finally, the block (b) shows the master-slave configuration for the repumper laser. More details for each block are given in the text.*

Chapter 2

Size Experiments

The first realization of a Magneto-Optical-Trap (MOT), where atoms are cooled and trapped by using quasi resonant-light, was achieved at the end of the '90s. We will briefly review the physical process at the origin of such mechanisms. Several references on the basic processes and physical mechanisms which govern atomic motion in laser-light were studied [16],[17]. Here we will report only the main results and useful relations used during this thesis. Starting from the simplest atomic model (a two-level atom) at rest, we will review the light-induced forces, giving the expression for the radiation pressure and dipole force. Then we will quickly pass through the description of the well-known Doppler Cooling and end up with the role played by the structure of multi-level atoms.

2.1 Atom-light Interaction

In atom light interaction the laser field is assumed to be monochromatic with frequency ω_L, and can be described as a classical field dependent on time, after a unitary transformation [18]:

$$\vec{E_L}(\vec{r},t) = \frac{E_L^0(\vec{r})}{2}(\vec{\epsilon_L}(\vec{r})e^{-i\omega_L t - i\phi(\vec{r})} + c.c) \ , \tag{2.1}$$

where E_L^0, $\vec{\epsilon_L}$ and $\phi(\vec{r})$ are respectively the amplitude, polarization and phase of the laser field in the $\vec{r}$ position.

The atom-laser interaction is given in the dipole approximation, and is characterized by Rabi frequency Ω, which is proportional to the scalar product of dipole moment matrix ($< e|\vec{d}|g >$) and laser field $\vec{E_L}(\vec{r},t)$. The atom-vacuum field interaction is responsible for the spontaneous emission of photons by excited atoms which is characterized by the natural width Γ.

In the case where separation between internal and external degrees of freedom is possible, we can adiabatically eliminate the fast internal variables and derive reduced equations of motion for external variables. The evolution of the internal degrees of freedom is described by the Optical-Bloch-Equation (OBE). In a stationary regime, using the Rotating-Wave-Approximation (RWA), which neglects the anti-resonant terms of the interaction terms, and by solving the OBE, we can arrive at an expression of the force acting on one atom at rest [16]. The total force can be resumed in the following way [16] : an atom in a monochromatic light field with a frequency tuned close to an atomic resonance ω_0, experiences strong forces and large acceleration which can be used for slowing

down the atomic velocity. The force has two contributions: the conservative dipole force arising from the energy shift of atomic states in a light field, and the dissipative radiation pressure arising from momentum transfer and scattered photons.

In the following sections, we will review both forces, and give their expressions and characteristics.

The radiation pressure

The expression of radiation pressure, for an atom at the position $\vec{r}$ and with a $\vec{v} = 0$ is given by [16] :

$$\vec{F_{pr}} = \frac{\hbar\,\Gamma}{2}\,\vec{\nabla}\phi(\vec{r})\frac{s(\vec{r})}{1+s(\vec{r})}\ , \tag{2.2}$$

where $\phi(\vec{r})$ is the phase of electric field, $\delta = \omega_L - \omega_0$ the laser detuning, $s(\vec{r}) = \dfrac{\Omega^2(\vec{r})/2}{\delta^2+\Gamma^2/4}$ is the saturation parameter and $\Omega(\vec{r})$ the Rabi frequency where the atom is located.

In the simplest case, a plane running wave, the phase is $\phi(\vec{r}) = -\vec{k_L}\cdot\vec{r}$, and Ω is uniform and thus s. Then the Eq. (2.2) reads:

$$\vec{F_{pr}} = \frac{\hbar\,\vec{k}_L\Gamma}{2}\,\frac{s}{1+s}, \qquad s = \frac{I/I_s}{(1+4\frac{\delta^2}{\Gamma^2})} \tag{2.3}$$

where we observed that Ω^2 is proportional to the intensity laser I and we usually express I in units of saturation intensity I_s. Also, it is useful to define the saturation parameters for $\delta = 0$ as $s_0 = I/I_s = 2\,\Omega^2/\Gamma^2$.

We observed that the force expressed by the Eq. (2.3), is proportional to photon scattering rate $\Gamma\cdot\sigma_{ee}$, where $\sigma_{ee} = \frac{1}{2}\cdot\frac{s}{1+s}$ is the excited state population.

Finally, we concluded that the radiation force is simply related to the momentum transfer $\hbar\,\vec{k}_L$ for each absorbed photon of the plane wave.

The dipole force

The second term of the total atomic force is given by:

$$\vec{F}_{dip}(\vec{r}) = -\frac{\hbar\,\delta}{2}\frac{\vec{\nabla}\,s}{1+s}\ . \tag{2.4}$$

This force is equal to zero for a plane wave because of $\Omega(\vec{r}) = const$. It is related to the intensity gradient and can be deduced from a potential in stationary regime [18]:

$$U_{dip} = \frac{\hbar\delta}{2}log(1+s)\ . \tag{2.5}$$

In the limit of small saturation parameters ($s \ll 1$), and large detuning $|\delta| \gg \Gamma, \Omega$, Eq. (2.5) reads:

$$U_{dip} = \frac{\hbar\Omega^2}{4\delta}. \tag{2.6}$$

And for example, when $\delta < 0$ the potential U_{dip} has a minimum where the intensity is maximal. This peculiarity can be used to trap atoms using Gaussian beams, with few microns in waist, where we have the highest intensity, for a red-detuned laser.

2.1.1 The Magneto Optical Trap (MOT)

We will give a basic description of MOT by first introducing the Doppler-Cooling model, used to slow down the atomic velocities, and indeed, we are neglecting dipole forces that give rise to the well-known Sisyphus Effects [16]. Then we will explain how we obtained the spatial confinement required for trapping the atoms.

Doppler Cooling

Doppler cooling was suggested in 1975 by Hänsch and Schawlow [19]. It is based on the fact that the frequency laser is shifted for a moving atom by $-\vec{k}\cdot\vec{v}$. This fact should be taken into account by replacing, in the Eq. (2.3), the detuning $\delta' \rightarrow \delta - \vec{k}_L\cdot\vec{v}$. In a 1D situation, we considered two counter propagating plane waves in Oz directions, and one atom with a velocity v_z. In the low saturation limit ($s \ll 1$), the total force experienced by the atom can be written:

$$F_z(v_z) \;=\; \hbar\, k_L \frac{\Gamma}{2}\Big(\frac{I/I_{sat}}{1+4\cdot\frac{(\delta-k_L v_z)^2}{\Gamma^2}} \;-\; \frac{I/I_{sat}}{1+4\cdot\frac{(\delta+k_L v_z)^2}{\Gamma^2}}\Big)\;. \tag{2.7}$$

We can further simplify the expression (2.7) by taking the limit for small velocities $k_L v_z \ll \Gamma$, and writing it as a friction function:

$$F_z(v_z) \;\cong\; -\gamma\, v_z\;, \qquad\qquad \gamma \;=\; -\hbar\, k_L^2\, s\, \frac{2\,\delta\,\Gamma}{\delta^2 \;+\; \frac{\Gamma^2}{4}}\;. \tag{2.8}$$

The generalization in the third dimension is straightforward in the case $s \ll 1$, where the forces add independently to the three standing waves. But the result in Eq. (2.8), and its generalization, is completely wrong in the case of large intensity.

Because of the important friction coefficient γ (for $\delta < 0$), this type of cooling has been called "Optical Molasses". If one changes the frequency of the laser to positive ($\delta > 0$) one will get a heating process (i.e. increasing of the atomic velocities).

In this approximation, the Doppler model leads to a zero velocity for all atoms. This is because we are neglecting the fluctuations of the forces due to spontaneously emitted photons, which have random directions, and photon absorption processes, which depend on the recoil velocity ($\hbar k_L/M$). These two effects both contribute to the diffusion coefficient in momentum space D_p, responsible for the atomic heating.

The final temperature achievable in the optical molasses is a balance between the heating and cooling mechanisms, and is related to D_p and γ via the following expression [16]:

$$k_B\, T \;=\; \frac{D_p}{M\gamma}\;, \tag{2.9}$$

where M is the atomic mass and k_B the Boltzmann constant.

In the 3D generalization, we can show that [16] :

$$k_B\,T \;=\; \frac{\hbar\,\Gamma}{4}\left(\frac{2|\delta|}{\Gamma} \;+\; \frac{\Gamma}{2\,|\delta|}\right)\,. \tag{2.10}$$

The Eq. (2.10) has a lower limit in temperature. If we choose a $\delta \;=\; -\frac{\Gamma}{2}$ the limit temperature of the Doppler cooling T_D can be written as:

$$k_B\,T_D \;=\; \frac{\hbar\,\Gamma}{2}\,. \tag{2.11}$$

In the case of ^{85}Rb the Doppler cooling limits give rise to $T_D \;=\; 140\,\mu K$, with corresponding mean velocity distribution $\bar{v}_D \;=\; 0.1\,m/sec$.

This Doppler force can be useful for decelerating atoms but does not provide spatial confinement and the atoms may quit the laser beams and be lost. The solution to this problem is to generate a spatial restoring force, directed towards the trap center, by using the Zeeman shift of the atomic frequency. Such an effect is achieved by applying an external magnetic field gradient.

Spatial Confinement

The idea was proposed by J.Dalibard and then realized by S.Chu and is based on multi-level atoms. In general, in the context of laser cooling, the term "multi-level atoms" is used to indicate the atoms with the degenerate Zeeman structure for both ground and excited states. Let's considerer the case of an atomic transition ($J \;=\; 0 \;\rightarrow\; J \;=\; 1$) with the three times degenerate excited state. Then, the energy shift due to an external magnetic field B is given by $g_J\,m_J\,\mu_B\,B$, where $\mu_B \;=\; e\hbar/2m_e$ is the Bohr magneton , m_J is the projection of angular momentum along the direction of the magnetic field, and g_J is the Landé-factor.

In the case of a standing wave with appropriate polarizations (σ^+/σ^-) and applying the magnetic field gradient, with zero crossing in the trap center, we broke the symmetry along the laser cooling beams. Thus, the atoms can distinguish between laser beam directions. If the magnetic field can be written as $B \;=\; (\nabla B)z$, introducing magnetic field gradient (∇B), in the direction of the standing wave as described above, we modified the force acting on the atom adding the Zeeman effect. In fact, (in the case $J = 0 \rightarrow J = 1$ transition with $m_J \;=\; \pm 1, 0$) the atomic detuning modifies in the following way:

$$\begin{cases} \delta' \;\rightarrow\; \delta \;\pm\; \dfrac{g_J\mu_B\,(\nabla B)\,z}{\hbar} & ,m_J = \pm 1 \\ \\ \delta' \;\rightarrow\; \delta & ,m_J = 0 \end{cases} \tag{2.12}$$

We note that the Zeeman shift plays a role in the Doppler effect on the optical molasses. Thus, the expression of the total force is exactly analogous with Doppler cooling if we make the substitution $k_L v_z \leftrightarrow \dfrac{\mu(\nabla B)z}{\hbar}$, with $\mu \;=\; g_J\mu_B$.

Due to the magnetic field gradient, we can introduce spatial dependence into the expression of the force given by Eq. (2.7). With a limit of $s \;\ll\; 1$ and considering a linear approximation of around $v_z \;\cong\; 0$ and $z \;\cong\; 0$, the force looks like that of a damped harmonic oscillator:

$$F_z(v_z, z) \;=\; -\,\gamma\, v_z \;-\; \kappa_0\, z, \qquad \kappa_0 \;=\; -\,2\, s\; k_L\, \mu\, b' \frac{\delta\,\Gamma}{\delta^2 + \frac{\Gamma^2}{4}} \tag{2.13}$$

that leads to a restoring force for a red detuning ($\delta < 0$).

With such a description and in a low density limit, the mean extension of the MOT can be deduced from its temperature by using the equipartition theorem in the following way:

$$\frac{1}{2} M\, v_z^2 \;=\; \frac{1}{2}\, k_B\, T_D \;=\; \frac{1}{2}\, \kappa\, \langle z^2 \rangle \;. \tag{2.14}$$

From the Eq. (2.14) in the Doppler limit with optimum detuning $\delta = -\dfrac{\Gamma}{2}$ we found that:

$$\begin{aligned} \langle z^2 \rangle \;&=\; \frac{\hbar\,\Gamma}{\kappa} \\ &=\; \frac{\hbar\,\Gamma}{4\, k_L\, s\, \mu\, b'} \;, \end{aligned} \tag{2.15}$$

and for the typical parameters of our MOT ^{85}Rb, $T_D \;=\; 140\,\mu K$, $b' \;=\; 10\,G/cm$ and $s \;=\; 0.5$ we defined as standard deviation for the size $\sigma_z = \sqrt{\langle z^2 \rangle} \cong 15 \mu m$.

In this condition the MOT's size is independent of the number of atoms and is only limited by the temperature. Thus, in principle, if the temperature goes to zero, the density can diverge. This means that we can set the density value as we prefer. Particularly, in the case of ^{85}Rb MOT, it is possible to obtain a temperature lower than T_D, just by using the Sisyphus cooling [20] to increase the density. This is because we are neglecting the collective effects in the MOT.

The first manifestation of such effects in the MOT is the increase in its size when more and more atoms are added. This is responsible for the transition between the temperature-limited regime (TL), where the size is independent of numbers of atoms, and the multiple-scattering regime (MS), where the atom-atom interactions are important, and they start interacting with each other due to the scattering of the photons within the atomic cloud. In the MS regime, the one-atom model is no longer valid. If we want a reliable description for density behavior in a MOT we need to include such effects in a possible model.

In the next sections, we'll take an overview of the following effects: absorption and re-radiation within an atomic cloud. We will also see how they can be combined together.

2.1.2 Re-radiation and Absorption: The Wieman model

When the number of trapped atoms is increased, the light scattered by atoms starts to modify the light-induced forces. Two competing effects have to be taken into account: the shadow effect [21], arising from the attenuation of the trapping beam, which compresses the cloud; and the repulsive radiation pressure effect [22], which increases the size of the cloud. The size of the atomic cloud is determined by the relative importance of these effects. A standard MOT works in the MS scattering regime, where the re-scattering

process is more important than the attenuation. Consequently the size increases with the numbers of atoms while the spatial density stays constant. In such a regime, the density is limited to $n \cong 10^{10} - 10^{11} cm^{-3}$.

Finally, to resume we can say that: the force acting on a trapped atom is made up of three contributing forces. The first is the trapping force produced by laser beams and the Zeeman shifts of the atomic energy. The second is the attenuation force, called the shadow effect, due to atomic density. The last, the multiple scattering force, arises from the atoms reradiating the absorbed photons which are subsequently scattered a second time by other atoms. The physical origin of the two latter forces will be discussed in the following paragraphs.

Shadow Effect

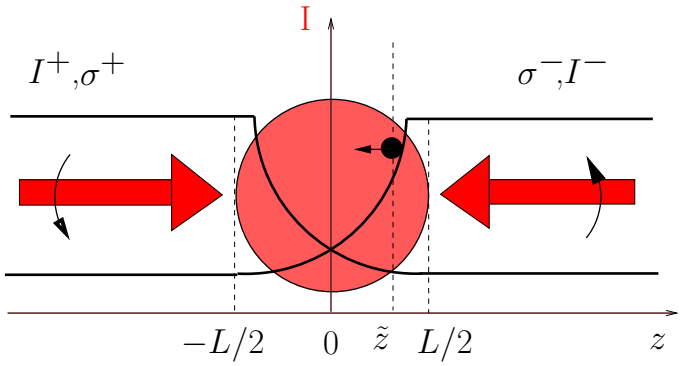

Figure 2.1: *Shadow effects: The trapping beams are absorbed when travelling through the cloud and this effect gives rise to a compressive force i.e directed towards the center of the MOT.*

The intensity loss due to the scattering of light from a laser beam when it travels through a sample of resonant atoms with atomic frequency ω_0, and density $n(z)$, in the limit $s \ll 1$ is given by:

$$\frac{dI}{dz} = -\hbar\,\omega_0\,\frac{\Gamma}{2}\,s\,n(z) \tag{2.16}$$

where for $\delta = 0$ the Eq. (2.16) can be written as:

$$\begin{aligned} \frac{dI}{dz} &= -\hbar\,\omega_0\,n(z)\,\frac{\Gamma}{2}\,\frac{I}{I_{sat}} \\ &= -\sigma_0\,n(z)\,I \end{aligned} \tag{2.17}$$

where we define the atomic resonant cross-section as $\sigma_0 = \frac{3\lambda^2}{2\,\pi}$.

The general solution of the differential Eq. (2.17), for an incoming beam with $\delta \neq 0$, can be expressed by:

$$I(z) = I_\infty\, e^{-\sigma_L \int_{-\infty}^{z} n(z)\,dz}\,, \qquad \sigma_L = \frac{\sigma_0}{1 + 4(\frac{\delta}{\Gamma})^2} \tag{2.18}$$

In the case of constant density $n(z) = const = n_0$ for a slab with a thickness of L ($0 \leq z \leq L$), with boundary condition $I(z = 0) = I_\infty$, we can write:

$$T(\delta) = I(z = L)/I_\infty \; = \; e^{-b(\delta)} \tag{2.19}$$

where $T(\delta)$ is the transmission coefficient measured at the end of the sample. We define the atomic optical thickness as the following quantity:

$$b(\delta) \; = \; -\ln(T(\delta)) \; , \qquad b = \int_{-\infty}^{+\infty} \sigma_L \, n(z) \, dz \; . \tag{2.20}$$

If the σ_L does not have spatial dependence, and for constant density in the slab, we have $b(\delta) \; = \; n_0 \sigma_L(\delta) \, L$. The optical thickness can also be expressed as $b = L/\ell$, where $\ell = 1/\sigma_L n_0$ is the mean free path in the diffusing medium. In some sense, b measures the number of diffusions made by the laser light before escaping from the medium.

Let us consider the 1D-model illustrated in Fig. (2.1), two plane waves respectively of intensity I^+ (I^-) for the laser coming from the left (right) with respect to the atomic cloud. Their intensities are attenuated by the optically thick atomic cloud. Such attenuation leads to a local imbalance between the two counter propagating beams that produces the so called attenuation force (shadow effects). The two unattenuated beams are assumed to have the same incoming intensity I_∞. The strength of the force associated with the local intensity imbalance is found in the following way for $\delta \; = \; 0$, and for atoms at rest:

$$\begin{aligned} F_{shw}(z) \quad &= \quad \frac{\hbar k_L \, \Gamma}{2 \, I_{sat}} \; (I^+(z) \; - \; I^-(z)) \\ &= \quad \frac{\hbar k_L \, \Gamma \, I_\infty}{2 \, I_{sat}} \; (e^{-\int_{-\infty}^{z} \sigma_0 \, n(z) dz} \; - \; e^{-\int_{z}^{+\infty} \sigma_0 \, n(z) dz}) \end{aligned} \tag{2.21}$$

If we derivate the Eq. (2.21) with respect to z and then we make the limit of small optical thickness $b = \int_{-\infty}^{+\infty} \sigma_L \, n(x, y, z) \, dz \; \ll 1$ we obtain:

$$\partial_z F_{shw}(z) \; = -2 \cdot \frac{\hbar k_L \Gamma I_\infty n(x, y, z) \sigma_L}{2 \, I_{sat}} \; (1 \; - \; \frac{b_z}{2}) \tag{2.22}$$

The generalization of the force in three dimensions is straightforward. By using the same arguments, we find $\partial_y F_{shw}(y)$, $\partial_x F_{shw}(x)$, and the total force is given by the following relation:

$$\vec{\nabla} \cdot \vec{F}_{shw} \; = \; -2 \frac{\hbar k_L \Gamma I_\infty \sigma_L}{2 \, I_{sat}} \, n(x, y, z) \, (3 \; - \; \frac{b_x \; + \; b_y + \; b_z}{2}) \; . \tag{2.23}$$

Assuming spherical density distribution for the atomic cloud and small optical thickness ($b_x \; = \; b_y \; = \; b_z \; \ll \; 1$) the Eq. (2.23) can be rewritten as:

$$\begin{aligned} \vec{\nabla} \cdot \vec{F}_{shw}(r) \quad &= \quad -6 \frac{\hbar k_L \Gamma I_\infty \sigma_L}{2 \, I_{sat}} \, n(r) \\ &= \quad -6 \frac{\sigma_L^2}{c} \, I_\infty \, n(r) \, , \qquad k_L \; = \; \omega_L / c \end{aligned} \tag{2.24}$$

The negative sign of the divergence indicates that this attenuation force yields to a compression of the atomic cloud.

Correction of the Spring Constant

As already mentioned in [13], when many atoms are added in the trap, the attenuation of the trap beams can give rise to a slight reduction of the spring constant of the MOT. In the following we will try to characterize this effect, and in order to simplify the discussion, we will consider a 1D-model for a two-level atom.

As shown in Fig. (2.1), for small optical thickness ($b = \frac{L}{\ell} \ll 1$), the force experienced by one atom at rest, including the shadow effect, can be written:

$$F_{tot}(z) \;=\; \frac{\hbar\, k_L\, \Gamma\, I}{2 \cdot I_{sat}} \{ \frac{1 - (z + L/2)/\ell}{1 + 4 \cdot \frac{(\delta - \mu z)^2}{\Gamma^2}} \;-\; \frac{1 + (z - L/2)/\ell}{1 + 4 \cdot \frac{(\delta - \mu z)^2}{\Gamma^2}} \} \tag{2.25}$$

where we simplified the notation using $\mu = \frac{\mu_B(\nabla B)}{\hbar}$. As usual, we linearized the force around $z \cong 0$ by taking the limit $\mu \cdot z \ll \delta$, and arriving at the expression for the force:

$$F_{tot}(z) \;\cong\; -\kappa \cdot z \;,$$

$$\kappa \;=\; \kappa_0 \{ 1 \;-\; b/2 \;-\; \frac{n\, \sigma_0}{8\, \delta\, \mu/\Gamma^2} \} \tag{2.26}$$

where κ_0 is the spring constant for the "one-atom" MOT, given by Eq. (2.13).

The correction to the spring constant, the $\frac{b}{2}$ factor, can be neglected if

$$b/2 \;\ll\; \frac{n\, \sigma_0}{8\, |\delta|\, \mu/\Gamma^2} \;. \tag{2.27}$$

Eq. (2.27) with $b \;=\; n\, \sigma_L\, L$ leads to a condition for the magnetic-field gradient (∇B):

$$b^{'} \;\ll\; \frac{[1 + 4(\delta/\Gamma)^2]\, \Gamma^2\, \hbar}{(4\, |\delta|\, \mu_B)\, L} \tag{2.28}$$

For our typical parameters of MOT, i.e $L \;=\; 10^{-3}\, m$, and $\delta \;=\; -\,2\Gamma$ this condition is completely verified.
At the end this correction to the spring constant has to be taken into account only when we deal with magnetic field gradients of the order of $10^2\, G/cm$.

Multiple scattering

In a laser field of intensity I, an atom absorbs and subsequently re-radiates energy at a rate of $P_{diff} \;= \sigma_L \cdot I$. Thus, the intensity of light radiated by one atom at the position of a second atom located a distance d away is:

$$I_{diff} \;=\; \frac{I \sigma_L}{4\pi d^2} \;. \tag{2.29}$$

The multiple scattering force for two atoms is $\frac{I_{diff}}{c} \langle \sigma_R \rangle$, where we indicate with $\langle \sigma_R \rangle$ the average absorption cross section for re-scattered photons. In general, the frequency of

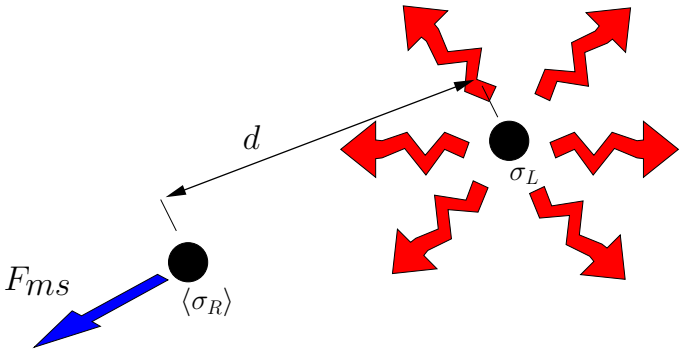

Figure 2.2: *Multiple-Scattering Force: when a photon is 'scattered' by an atom it can be reabsorbed by another atom with a different cross-section $\langle\sigma_R\rangle$. These processes give rise to a repulsive force between the atoms within the atomic cloud.*

the reradiated light is different from the incident light because of frequency redistribution. In the high intensity limit, $\langle\sigma_R\rangle$ is different from the absorption cross section σ_L because the fluorescence spectrum for an atom is formed by three components called Mollow's Triplet [23]. The complete expression for $\langle\sigma_R\rangle$, in the high intensity limit, can be found in the appendix A. Here we will give just an approximate expression in the limit of $|\delta| \gg \Omega \gg \Gamma$ for the difference between the two cross sections, and we get :

$$\langle\sigma_R\rangle - \sigma_L \cong \sigma_0 \frac{\Omega^2}{8 \cdot \delta^2} \tag{2.30}$$

Using Eq. (2.29) the multiple scattering force for two atoms at a distance from each other of d, can be written as:

$$\mathcal{F}_{ms} = \frac{\langle\sigma_R\rangle\ \sigma_L\, I}{4\,\pi\, c\, d^2}. \tag{2.31}$$

To generalize to an arbitrary distribution of atoms, we consider that an incident photon is unlikely to be absorbed and emitted more than twice by atoms in the MOT (double scattering approximation). In such an approximation we can write the following expression for F_{ms}:

$$\vec{F}_{ms}(r) = \frac{\langle\sigma_R\rangle\ \sigma_L}{4\,\pi\, c} \int I(r')n(r') \frac{r - r'}{|r - r'|^3} d^3r' \ . \tag{2.32}$$

Like in electrostatic, we can use Gauss's law to obtain a differential equation for $F_{ms}(r)$, with the assumption that absorption of the beams in the MOT is small.

Let us consider a surface S, with an element of surface area $d\vec{S}$ which contains the atomic density distribution $n(r)$. We define r as the point connecting the center of atomic distribution and one point on the surface. Then, $F_{ms}(r)$ at that point r, can be rewritten as:

$$\oint_S \vec{F}_{ms}(r) \cdot d\vec{S} = \frac{I\ \langle\sigma_R\rangle\ \sigma_L}{c} \int_V n(r) d^3r\,, \tag{2.33}$$

where V is the volume enclosed by S.
Then, by using the divergence theorem, we obtain:

$$\int_V (\vec{\nabla} \cdot \vec{F}_{ms}(r) \; - \; \frac{I}{c} \; \langle \sigma_R \rangle \; \sigma_L \, n(r) d^3 r) \, dV \; = \; 0 \; . \tag{2.34}$$

and because Eq. (2.34) is independent of the particular choice of Volume (V), we arrive at the differential form of Eq. (2.33):

$$\vec{\nabla} \cdot \vec{F}_{ms}(r) \; = \; \frac{I}{c} \; \langle \sigma_R \rangle \; \sigma_L \, n(r) \tag{2.35}$$

The form of the divergence of F_{ms} is similar to that found for F_{shw} but, in this case, with the opposite sign. This means that the F_{ms} force expands the atomic cloud. We can note that the multiple scattering is a Coulomb-like force: proportional to r inside the atomic cloud, and decreases like $1/r^2$ outside.

Steady state regime in the small optical thickness regime ($b \ll 1$).

The three forces (and their divergences) discussed above, neglecting the correction to the spring constant, will now be combined to form the total force acting on the atoms in the MOT.

$$\vec{\nabla} \cdot \vec{F}_{tot}(r) \; = \; \vec{\nabla} \cdot (\vec{F}_{ms} \; + \; \vec{F}_{shw} \; + \; \vec{F}_{trap}) = 0 \tag{2.36}$$

From that relation we can have an analytical expression for the upper limit of the density achievable in a MOT.

If we get the total intensity as $I \; = \; 6 I_\infty$, (because we have six independent beams), we end up with an equation like this:

$$6 \frac{I_\infty}{c} \; (\sigma_L)^2 \, n_{cw} (\langle \sigma_R \rangle \; / \sigma_L \; - \; 1) \; - \; 3 \kappa_0 \; = \; 0 \tag{2.37}$$

In Eq. (2.37) the spring constant κ_0 can be deduced from a trapping model Eq. (2.13), that can be supposed to be described by a Doppler model that takes account of degenerate atomic structure.
In Eq. (2.37), where the density (n_{cw}) is constant, the only unknown parameter is $\eta \; = \; \langle \sigma_R \rangle \, / \sigma_L$, which depends on the properties of reradiated light that can have spectral distribution different from that of the laser light.
In the situation where $\langle \sigma_R \rangle \neq \sigma_L$, the density can be written:

$$n_{cw} \; = \; \frac{\kappa \; c}{2 \, I_\infty \, \sigma_L (\langle \sigma_R \rangle - \sigma_L)} \tag{2.38}$$

that can be rewritten as :

$$n_{cw} \; = \; \frac{\kappa_0}{G_3} \; , \qquad G_3 = 2 \, \frac{I_\infty}{c} \, (\eta \; - \; 1) \tag{2.39}$$

where we introduced an effective interaction term G_3 between the trapped atoms, as a function of the η parameter.

This is called the Wieman model [13]. The model gives us an upper limit for the atomic density that does not depend on the number of atoms but only on the trapping

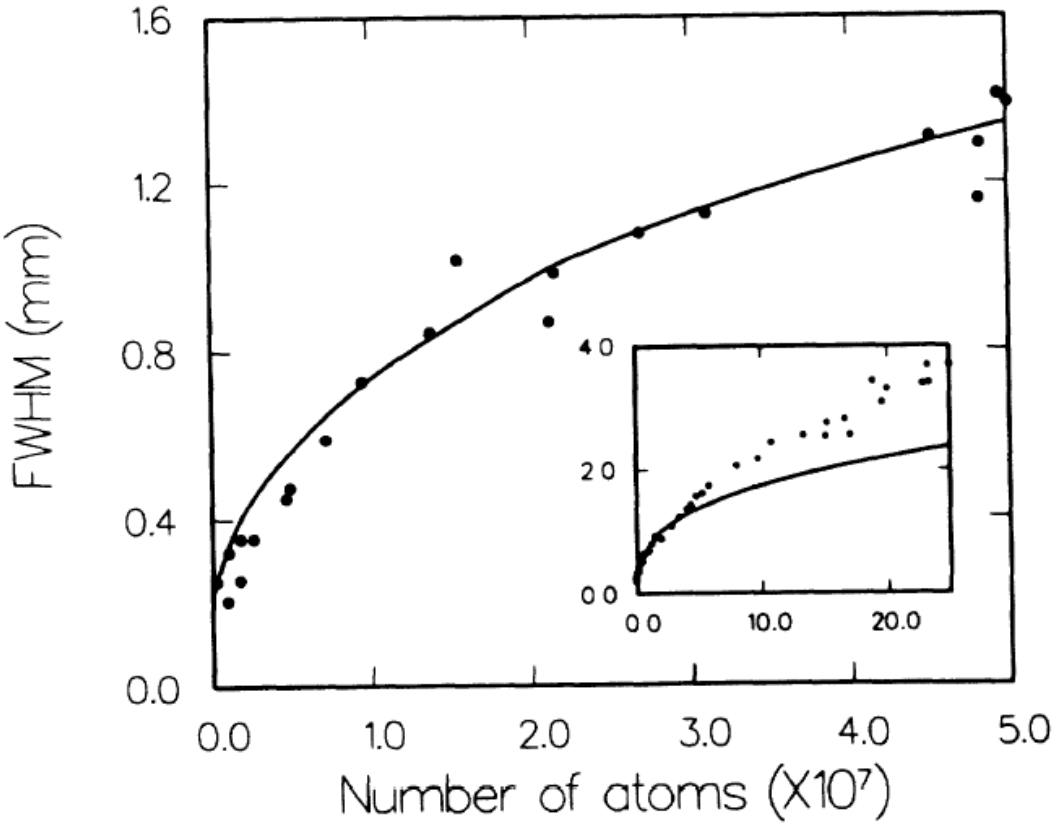

Figure 2.3: *Figure showing the size vs. number of atoms taken from the reference [13]. The inset shows a discrepancy of experimental observation (dot points) with respect to the model* $N_{at}^{1/3}$*, proposed [13], when the number of atoms became of the order of* $5\,10^7$*.*

parameters. That is equivalent to saying that the cloud's volume increases linearly with the number of atoms (N_{at}) trapped in the MOT.

The Wieman model is well validated in the regime of $N_{at} < 5 \cdot 10^7$. However, deviation from that model has been observed experimentally in the limit of large atomic clouds (10^8) Fig. (2.3).

The experimental results presented in Fig. (2.3) seem to indicate the existence of a new regime, where the scaling law for the size(L) is $L \propto N_{at}^{1/2}$. One possible explanation has been proposed in reference [13]. The new regime occurs when the growing of the atomic cloud is made a constant optical thickness b. In such a situation, the MOT adapts itself to have a constant optical thickness.

With our set-up, we were able to observe the same behavior when the number of atoms rises above 10^9. The measured evolution of the atomic size L is reported in FIG. (2.4). Even though the two experiments are showing the same qualitative behavior, they cannot be compared directly to each other. As we will describe more precisely in the experimental set up sections, the experiments were made with different protocols.
Data shown in FIG. 2.3, are gathered by looking at the total fluorescence and the size defined as the FWHM of the fluorescence recorded with a CCD. Also, during the probe phase, the magnetic field gradient is always kept on. This can lead to a more involved

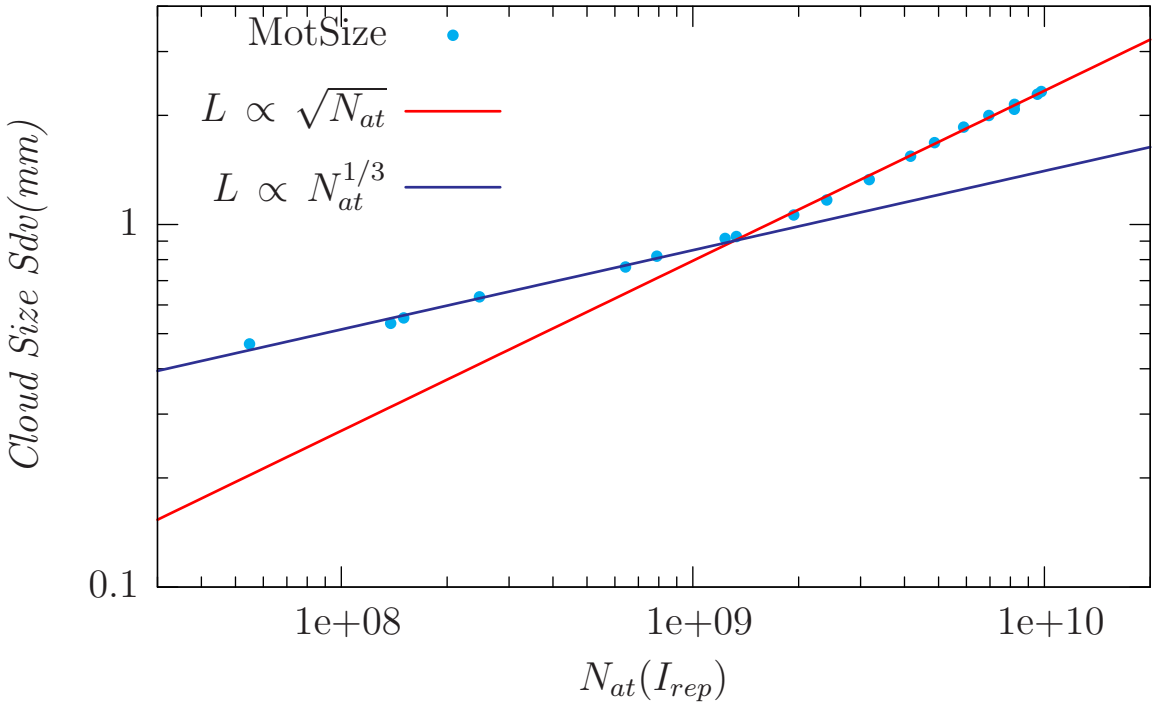

Figure 2.4: *Experimental data for the size as function of N_{at} is given. Indeed, an evident new regime for the size is observed with our set-up. This might be in agreement with the observation made in [13].*

theoretical discussion, including the spatial dependence on the absorption cross section (Zeeman shift). That is why, in order to simplify things, we decided to do more "clean" experiments where, during the probe phase, only the probe is present.

The confirmation of $N_{at}^{1/2}$ regime in our MOT can be one possible limitation on achievement of high atomic density. In fact, if we suppose that the new regime appears when the optical thickness of the MOT is constant,($b = n\sigma_L L = const$) the consequence would be a decrease in density. Therefore, its highest value is not reached at maximum N_{at}.

A complete understanding of $N_{at}^{1/2}$ regime, and its behavior as a function of the control's parameters, may help us towards the best, or at least, a correct starting point for the following compression stage if we want to compress the atomic cloud.
In the following subsection we will list possible effects which can contribute to density limitation.

Taking into account the correct spring constant

As we already saw we can include the corrections of spring constant as mentioned in Sec.(2.1.2) in the complete model. We can show that, for one atom at rest, in 1-D configuration, after the force presented in Eq. (2.25) Sec.(2.1.2), including the multiple-scattering terms (MS-term) (in approximation of double-scattering) and with the same

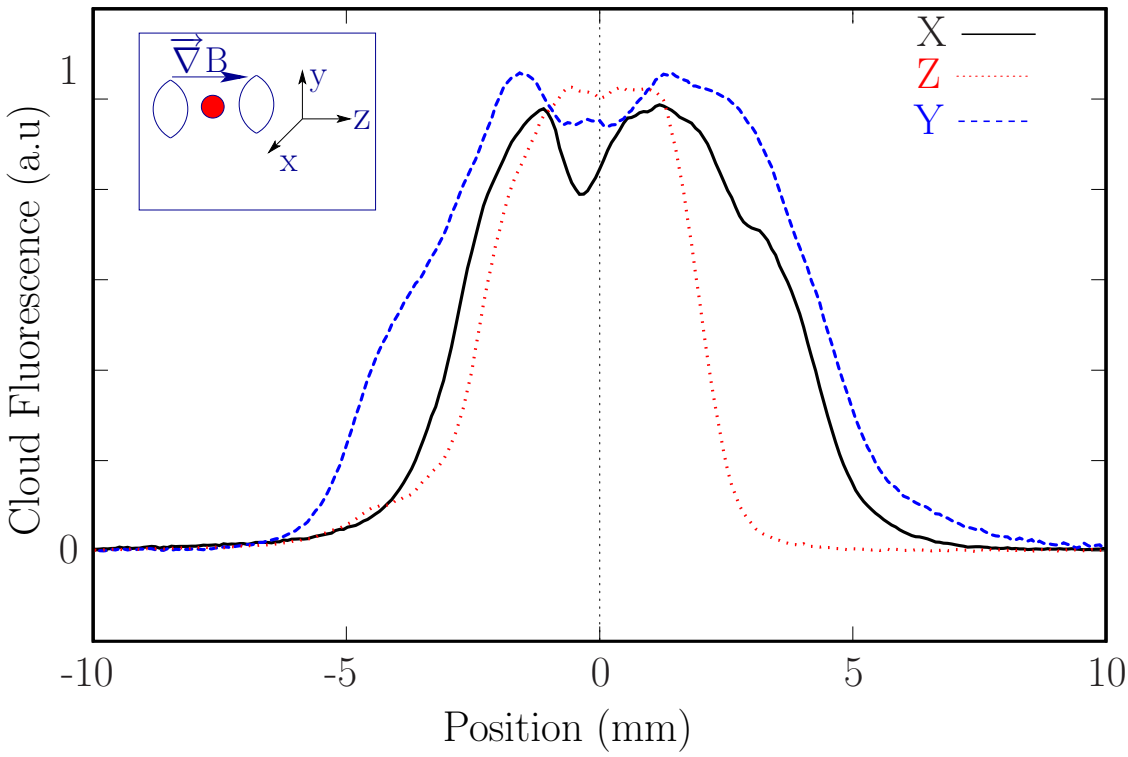

Figure 2.5: *Typical MOT profiles are shown for the three spatial directions. The profiles are obtained for standard MOT parameters with a total number of trapped atoms of about* 10^{10}.

notation, the multiple scattering force reads:

$$F_{ms}(z) \;=\; \eta\,\frac{b\,\cdot\,z}{(L/2)\;\{1+4\cdot(\delta/\Gamma)^2\}} \tag{2.40}$$

where, again, $\eta = \langle\sigma_R\rangle/\sigma_L$ and $b = n\,\sigma(\delta)\,L$ is optical-thickness. If we include such a term for the linearized-force around the trap's center and for $b \ll 1$, we end up with the following expression:

$$F_{tot}(z) = -\kappa_0\{1 - b/2 + (\eta-1)\frac{(\Gamma^2+4\delta^2)}{8\delta\mu L}\,b\cdot z\}\;. \tag{2.41}$$

When we look for the steady-state, we find that the following condition has to be fulfilled:

$$1 - b/2 + (\eta-1)\frac{(\Gamma^2+4\delta^2)}{8\delta\mu L}\cdot b \;=\; 0 \tag{2.42}$$

But still, the model takes into account the correction to the spring constant which gives rise to a constant density:

$$n_0 \;=\; \frac{8\,|\delta|\mu}{\sigma_0\,\Gamma^2(\eta\;-\;1)}\;, \tag{2.43}$$

that corresponds exactly to the CW-model.

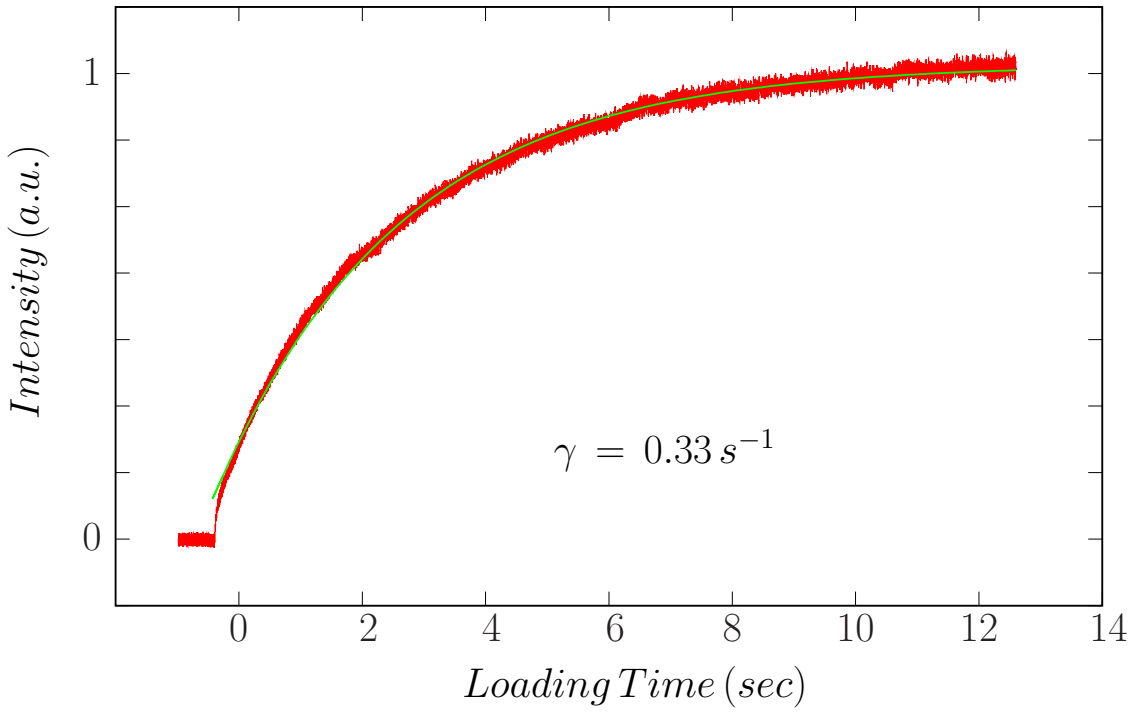

Figure 2.6: *Figure shows the typical loading time of the MOT with standard parameters. The line fits the recorded fluorescence via Eq. (2.45). From the fit we extract a* $\sim 3\,sec$ *life-time.*

Cold Collisions limiting atomic density

In our set-up, the trap is loaded continuously from the background room-temperature atomic vapor, with a loading rate L (atoms/sec). The evolution of the total number of atoms trapped can be written as [24]:

$$\frac{dN}{dt} = L - \gamma \cdot N - \beta \cdot \int n^2(r,t) d^3r \ , \tag{2.44}$$

where $n(r,t)$ is the atomic density, and where we have taken into account two types of loss process: collisions with room-temperature background atoms which occur at rate γ (proportional to both $Rb(P_{Rb})$ and residual vacuum-pressure P_{vac}), and the collisions between trapped atoms (cold collisions). They can impact each other and have enough kinetic energy to allow them to escape from the trap.

The loss rate of the trapped atoms increases quadratically with the atom density n and is characterized by a trap loss β term. In fact, β accounts for two-body losses, i.e two atoms are lost in the trap for each collision. In the limit of low spatial density, where we can neglect the cold collision, the general solution of Eq. (2.44), with the condition $N(t=0) = 0$ is given by:

$$N(t) = N_\infty (1 - e^{-\gamma t}) \tag{2.45}$$

and the stationary solution $N_\infty = \dfrac{L}{\gamma}$. If $P_{vac} \ll P_{Rb}$ the N_∞ is independent of the pressure, ($L \propto P_{Rb}$ and $\gamma \propto P_{Rb} + R_{vax}$). However, the life-time $\tau = 1/\gamma$, which is also the time

taken to fill the trap, does depend on pressure. The general expressions for the two coefficients L and γ can be computed by using kinetic theory for a room-temperature gas [25]. We assumed the loss-rate due to collisions between trapped atoms and room-temperature atomic background to be $\gamma = \rho_0 \cdot \sigma_{rb-rb} \cdot v_{rms}$ where $\sigma_{rb-rb} \sim 10^{-13}\, cm^2$, and ρ_0 is the density of background gas, and $v_{rms} \sim 236\, m/s$ is the root-mean-square of the Maxwell Boltzmann velocity distribution.

The measured $\gamma = 0.3\, s^{-1}$ corresponds to an indicative pressure of $P_{Rb} = 0.9 \cdot 10^{-9}\, mbar$, in the science cell. This value is in complete agreement with another kind of measurement: the transmission of a resonant atomic beam through the cell. If we define T_{cell} as the transmission on the cell's MOT over a distance L_{cell}, and T_{ref} as the transmission in a reference cell of length L_{ref}, we can deduce the following relation between the two relative pressures:

$$\frac{P_{cell}}{P_{ref}} = \frac{\ln(T_{cell})}{\ln(T_{ref})} \cdot \frac{L_{ref}}{L_{cell}} \ . \tag{2.46}$$

By computing the Eq. (2.46) with $L_{ref} = 35\, mm$, $T_{ref} = 22\,\%$, for the reference cell, $L_{cell} = 463\, mm$ $T_{cell} = 2.2\%$ for the science cell, using the results of ref ()for $P_{ref} = 3.8{\cdot}10^{-7}\, mbar$, we end up with a 'hot' pressure for Rb of about $P_{cell} = P_{Rb} = 0.7\, 10^{-9}\, mbar$.

Suppose now that we cannot neglect cold collisions. Thus, we need to solve the complete Eq. (2.44) supposing a constant density n_0. Hence, the evolution of total number of atoms in the MOT is found to be :

$$N(t) = N_\infty(1 - e^{-(\gamma+\beta\, n_0)\, t}) \ . \tag{2.47}$$

The only unknown parameter is then the cold collision coefficient β.

There are several ways to measure such a term. For example the easiest could be done either by monitoring the time evolution of the number of trapped atoms [26] or by illuminating the atomic cloud with the light from a "catalysis" laser to increase the collisions rate without affecting the operation trap [27].

In the case of Rb-atom, we can find in reference [28], for our parameters and the same isotope (^{85}Rb), the measured $\beta = 2 \cdot 10^{-12} cm^3 \cdot s^{-1}$. In order to be limited by cold collision, we need to fulfill the condition $\gamma \sim \beta\, n_0$. In our case, we measured a maximum density's value of $n_0 \sim 10^{10} cm^{-3}$ and $\gamma = 0.3\, s^{-1}$, thus we are in the regime $\beta \cdot n_0 \ll \gamma$.

We can conclude that, in order to be limited by cold collisions, we need to reach a density of about $n_0 \sim 10^{12}\, cm^{-3}$.

Alignment of the Trapping Beams.

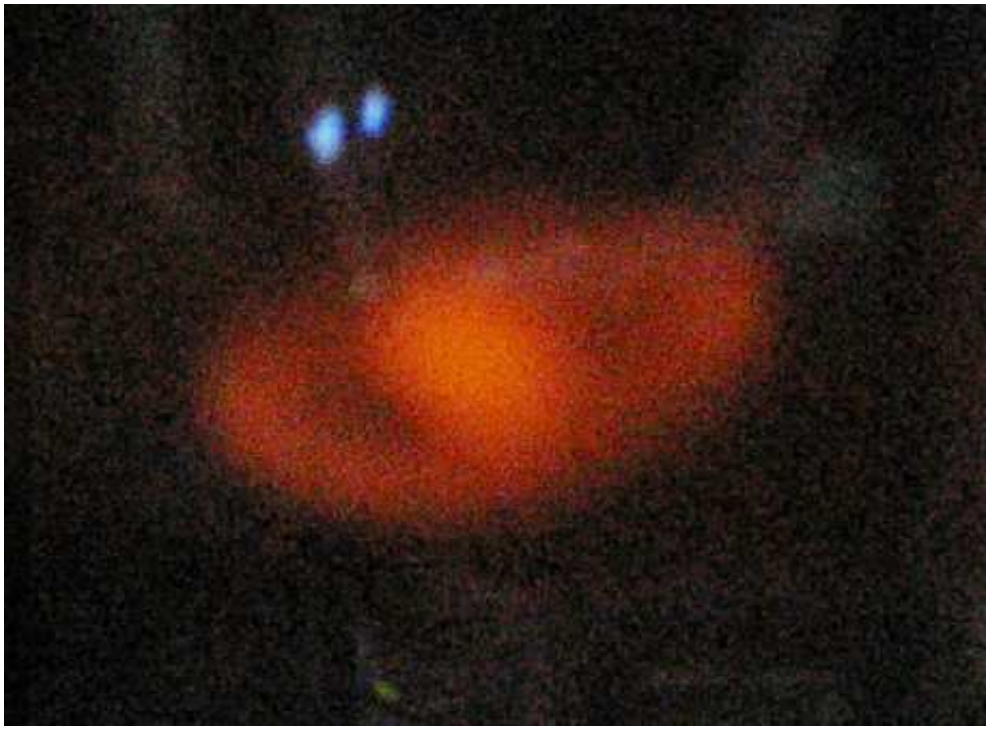

Figure 2.7: *Spatial atomic distribution is shown in the case of misalignment of the trapping beams. Even with few atoms in the trap, clumps of rotating atoms around a nucleus can be produced, giving rise to a Saturn-like image. Approximate size of the atomic cloud is about* $1\,cm$.

It is well known [22], that a misalignment of trapping beams can yield to an atomic clump rotating around a central core. This effect can be easily seen, and can be another possible limitation of the density. In fact, in such as situation, one more term $a_{cent}\,r$ (centripetal-like acceleration) has to be added. This force, directed out of the atomic cloud and responsible for the stable orbit-generation, can be added to the total force experienced by the trapped atom in the following way:

$$F(r) \;=\; -\kappa_0\, r \;+\; G_3\, n\, r \;+\; a_{cent}\, r \;. \tag{2.48}$$

Eq. (2.48), in the equilibrium situation, gives a maximum density

$$n_0 \;=\; \frac{\kappa \;-\; a_{cent}}{G_3} \;<\; n_{CW} \tag{2.49}$$

where n_{cw} is the density in the CW-model without accounting for this effect.

On the whole, as shown by Eq. (2.49), the misalignment of trapping beams could decrease the atomic density and that is why particular attention has to be taken in order to avoid such an effect.

During all the experiments presented in this thesis, the trapping beams were well aligned.

2.1.3 The Wieman-Pritchard Model

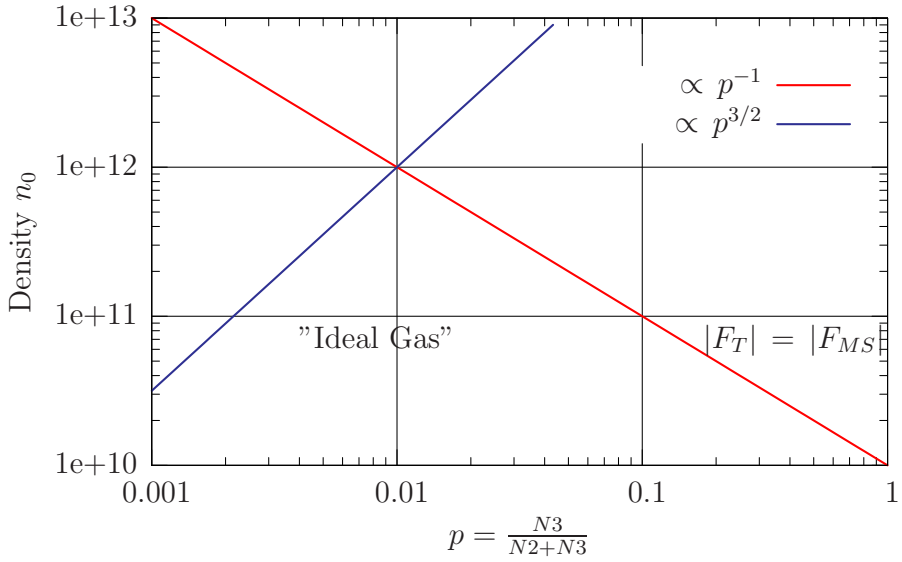

Figure 2.8: *Theoretical prediction given by the Wieman-Pritchard model. For $p \sim 0.01$, we observe a transition between the TL-regime and MS-regime for which the highest density is obtained.*

So far we have learned that the main limitation to obtaining high atomic density in the cloud is due to multiple scattering. This is one evident limitation to obtaining degenerate gases like Bose-Einstein Condensate (BEC) in standard MOT.

Over the years, many efforts have been made in order to circumvent such a limitation. The most important attempt to overcome this problem was proposed in reference [29] where for the first time a new type of MOT was proposed and obtained. It consists of a confinement of atoms predominantly in a "dark" hyperfine level (for ^{85}Rb $F = 2$) that does not interact with the trapping light. This leads to much higher densities because repulsive forces between atoms, due to multiple scattering, are reduced. As reported in the original paper: "..in such a trap, more than 10^{10} atoms have been confined to densities approaching 10^{12} atoms/cm^{-3}" for the Sodium atom.

In reference [29], a generalization of the Wieman-model was presented including a "dark" and "bright" hyperfine ground state. We will call such a generalization the Wieman-Pritchard model. In this new model a new parameter $p = \frac{N_3}{N_3+N_2}$ is introduced where p gives the probability that an atom is in the bright hyperfine state. Thus, both trapping and multiple scattering forces modify in the following way:

$$\begin{aligned} F_T(r) &= -\kappa\, p\, r\ , \\ F_{ms}(r) &= G_3\, n\, p^2\, r \end{aligned} \tag{2.50}$$

In the steady-state regime, we have $|F_T| = |F_{ms}|$, and this gives the following expression for the density:

$$n = \frac{n_0}{p} \quad , \qquad n_0 = \frac{\kappa}{G_3}. \tag{2.51}$$

We note that for $p = 1$, we recover the Wieman model. If we are able to set a $p \sim 0.01$, the density can be enlarged by two orders of magnitude.

Technically speaking, we can get such a low "p" by realizing a spatial "dark-spot" in the center of the repumper laser. Indeed, an atom trapped in the center of MOT doesn't see the repumper photons and spends most of its time in the Dark $F = 2$ hyperfine state. It can only be repumped in the bright state and cooled again when it goes out of the dark-zone. However, looking at the Eq. (2.50), as p is decreased, a second limit for the density appears. In fact, we arrive in the Temperature-Limited regime where because $\kappa_0 \propto p$ the density adheres to $n \propto p^{3/2}$. This means that there is an optimum value of p which optimizes the density as shown in FIG (2.8)

Our interest in the behavior of the Magneto-Optical Trap in general lost its fascination after the realization of the first Bose-Einstein Condensate (BEC) with the evaporating-cooling technique, and because of the difficulty of dealing with multiple scattering, which is especially problematic in MOTs with a very large number of atoms.

In the following sections, we will present an experimental study of a MOT with the possibility of trapping up to 10^{10} atoms. A complete investigation of this special MOT, and an understanding of the main limitations of the density's value, could be a step towards answering the following question: "Why can't we set as high density in the MOT as we want?".

In all the following experiments, we varied the total number of atoms (N_{at}) to investigate a region that spanned from the multiple-scattering regime to the new regime where we observed a $\sqrt{N_{at}}$ scaling law for the size.

The most important results of this study are published in the paper titled: "Scaling laws for large magneto-optical traps.", here attached.

In Sec. (2.2) we will comment on some parts of the paper by giving more details, particularly focusing on atomic and spatial calibration discussed in Sec. (2.2.1).
Then, in Sec. (2.2.2) we will present the 'preliminary test' part, which covers the description of all experiments performed before doing a systematic study of the MOT, to be sure that the results obtained are independent of the way we probed the atomic cloud. This section also includes a description of image analysis treatment and the different ways used to change the numbers of atoms in the MOT.
The Sec. (2.3) concludes the experimental part, where the size experiments are shown and qualitative differences are pointed out when the total number on the MOT is changed in different ways.
Finally, in Sec. (2.3.2), one particular case of the generalized Wieman-Pritchard model introduced in the attached paper is presented.

2.2 Experimental set-up and detection techniques

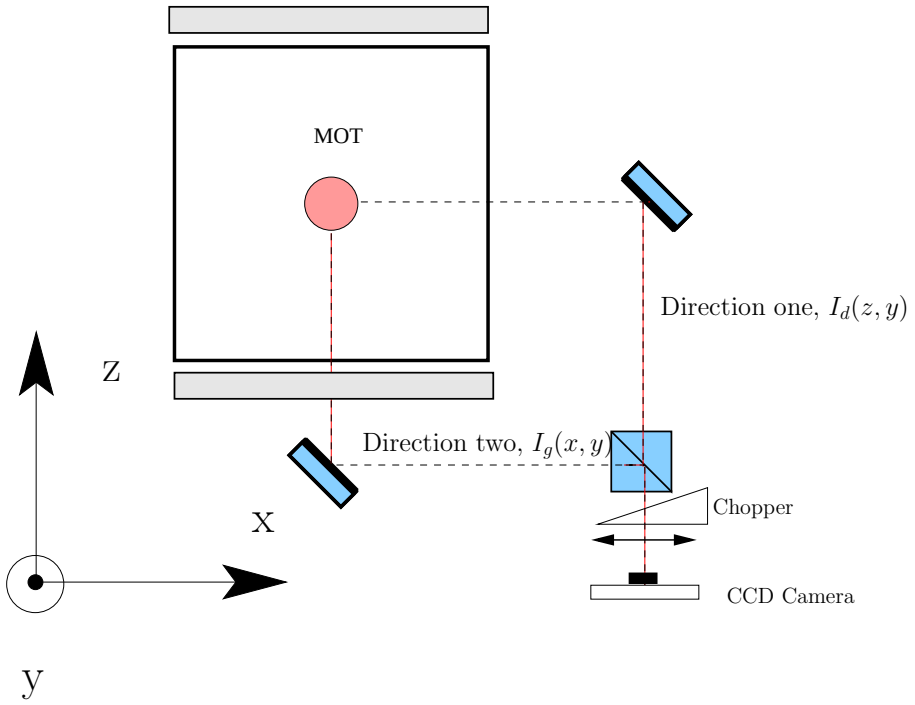

Figure 2.9: *Detection system used to take an image of the MOT. In this configuration we are able to have access to 3-D density profiles. The two orthogonal images are recorded into a CCD by using a polarized cube. We define I_g as the image coming from the left-side of the cube, while I_d is for that coming straight as shown in the illustration.*

In the following sections, we will report the detection scheme used to probe the cloud. We will detail the calibration both for atom and CCD camera. We will also give the preliminary tests carried out to ensure that the size of the cloud does not depend on the laser parameters used to probe the cloud.

In order to perform the size measurements we recorded the cloud fluorescence in a CCD camera.

In order to obtain a 3-D reconstruction of the density distribution we use two 2-D images from orthogonal directions. We collect both by polarizing a cube into the CCD camera using the set-up shown in Fig. (2.9).
Referring to Fig. (2.9), we will refer to the image taken in "direction one" as I_d, while "direction two" will be referred to as I_g.
From the two images we can retrieve spatial information as well as the 2-D fluorescence integrated in one direction. I_g measures the size in the Ox and Oy directions, while I_d measures the size in the Oy and Oz with respect to the laboratory frame.

The two images are taken in the simple-scattering regime. Such a regime is achieved with a time sequence. We alternate a "MOT phase" with the duration of $30ms$ where the trapping beams, repumper and magnetic field are switched off, and the dark-phase of $5ms$ within which the trapping beams are switched on and far-red detuned (-7Γ).

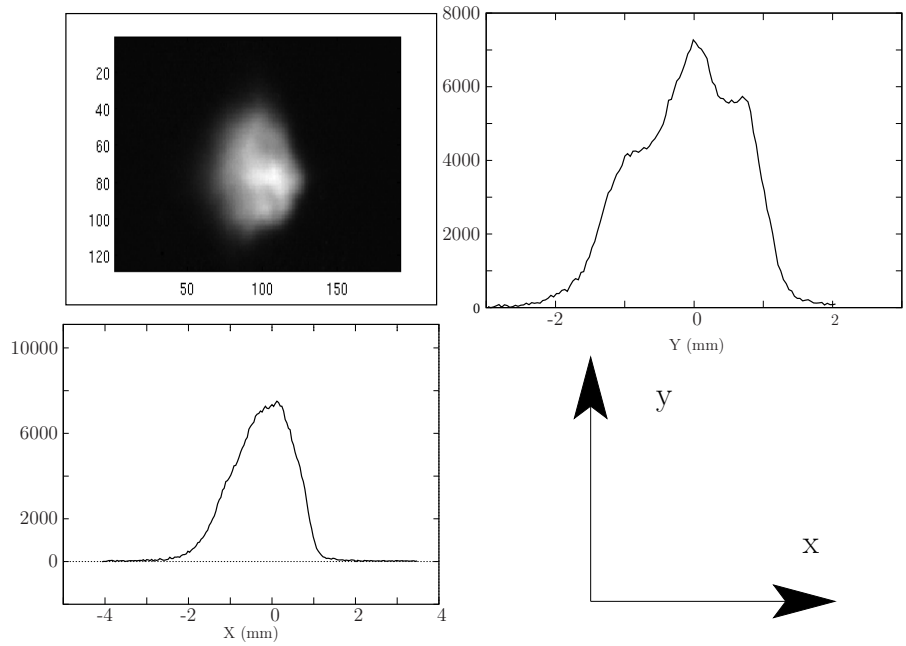

Figure 2.10: *Typical MOT fluorescence signal recoded in $I_g(x, y)$. In the upper-right position a cut of the Y-direction is plotted, while in the lower-left there is a cut of the X-direction.*

We will see later (in the 'preliminary test' section) that with this detuning, the MOT size isn't going to be modified by the scattering light of the probe. The dark phase is also sufficiently short so that all the atoms remain in the capture zone and are efficiently recaptured when the MOT is switched back on.
With the duty cycle described above, the only problem we have is that the CCD camera cannot be triggered. The minimum exposition time t_{exp} is $20\,ms$ due to the opening of the mechanical shutter. To overcome such a problem, the CCD remains in the acquisition mode for all of the exposition time and is protected from the bright light scattered during the MOT phase by a shutter as shown in Fig (2.9).

The trapping laser is turned on and off with an acusto-optical modulator. The same TTL signal, generated by computer, drives the modulator and serves as a reference for the controller of the shutter. Then its phase is adjusted so that we don't detect the scattering light during the MOT phase. In this way, we are able to perform acquisition during up to several tens of seconds, or even more, depending on the signal to noise ratio that we're interesting in. However, one typical exposition time is of about $15\,s$. Further, a background image ('dark' for us), taken without cold atoms and with the same exposition times, is obtained by turning off the repumper when the trapper laser is on. The dark image is necessary to subtract stray light from the cold atoms.
The typical images, with relative MOT profiles along the three spatial directions (Ox, Oy, Oz) are shown in FIG. (2.10) for the $I_g(x, y)$ image and FIG. (2.11) for $I_d(z, y)$.

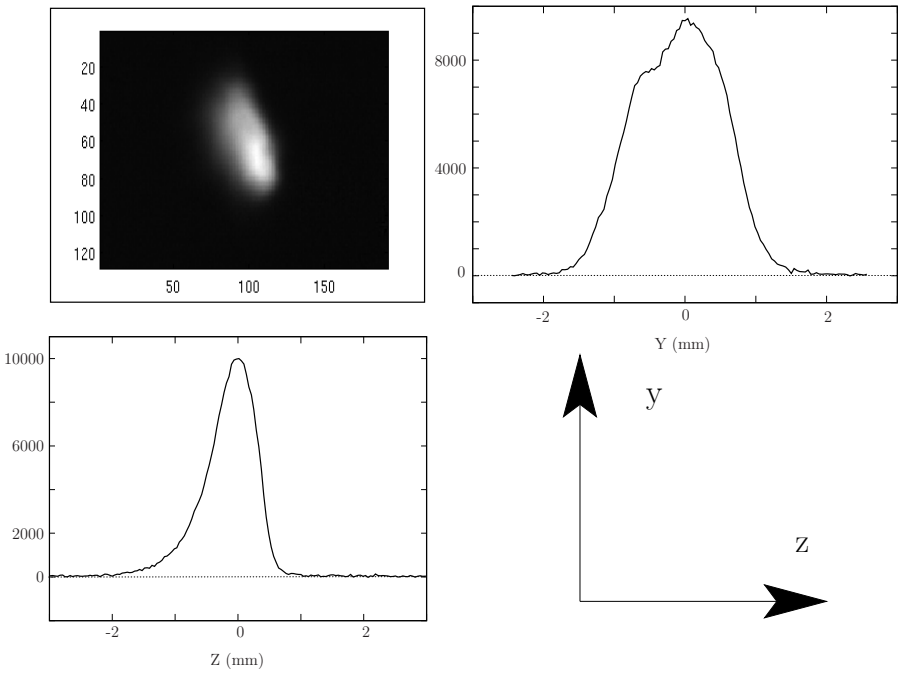

Figure 2.11: *Typical MOT fluorescence signal recoded in $I_d(x, y)$. In the upper-right position a cut of the oy direction is plotted , while in the lower-left there is a cut of the oz direction.*

2.2.1 Calibration

In this section we detail the calibration procedure used both for the atoms and the CCD camera.

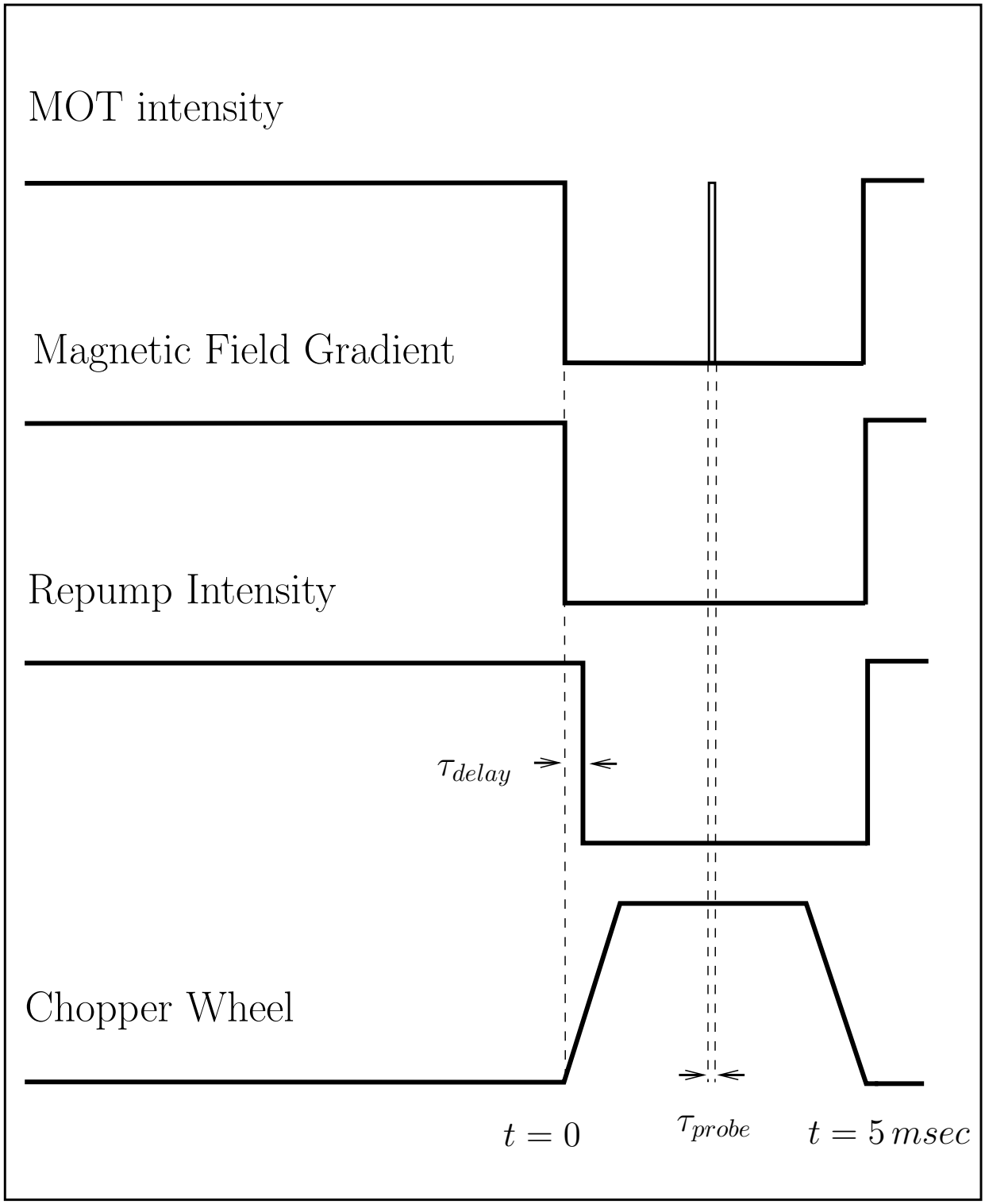

Figure 2.12: *The typical time sequence used for the size experiments is shown. We alternate a* $30\,msec$ *MOT-phase to a* $2\,msec$ *for the 'dark'. We collect the signal only for a time* τ_{probe}*, and we average over many cycles.*

Spatial Calibration

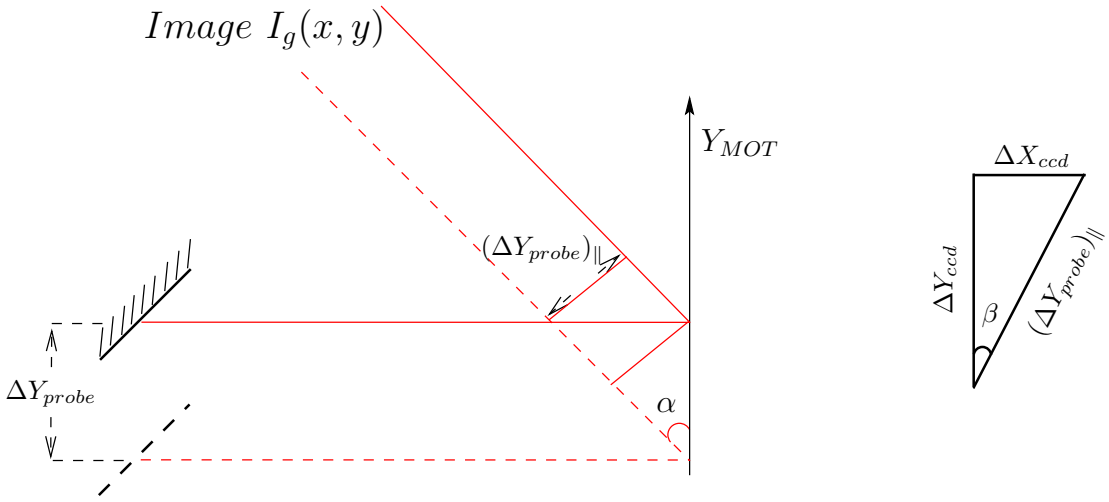

Figure 2.13: *An illustration of the technique used for the spatial-calibration of the CCD. We related the horizontal fluorescence of an on-resonance laser beam imaged directly into the CCD and recorded its horizontal displacement using a graduate translation-stage as described in the text. In the illustration on the left-side the angle β between the CCD and probe axis is defined .*

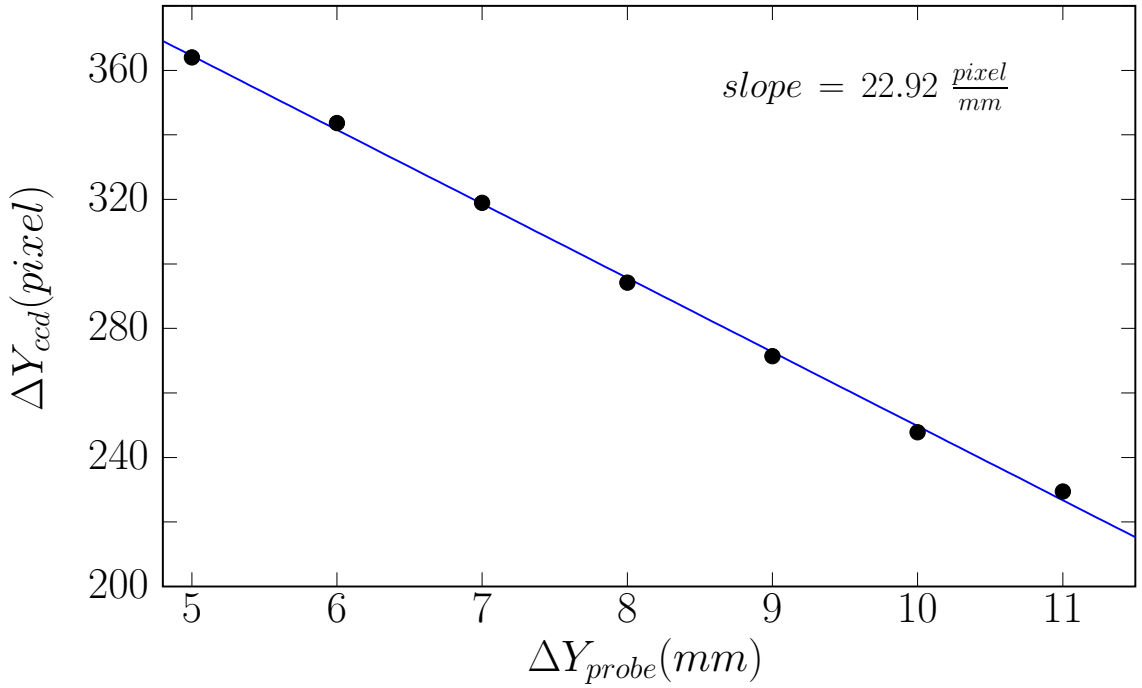

Figure 2.14: *Linear fit used to determine the $\eta(mm/pixel)$ factor for spatial calibration. Experimental points were obtained in the way described in the text, and using the method illustrated by Fig. (2.13).*

The camera used for the following experiments is a cooled CCD (APOGEE AP1) with a checked linearity curve, and square pixels ($9\mu m \cdot 9\mu m$). The magnification $\zeta\,(mm/pixels)$ of our detections system was found by using the experimental set-up shown in Fig. (2.13). We used a probe tuned at resonance with the atomic hot vapor inside the vacuum cell, and we moved it parallel to the probe direction where the MOT is formed by using a translation stage. Thus, knowing the real vertical displacement in mm and recording the position of the fluorescence of the hot atoms in $pixel$ in one direction of the CCD camera (for example $I_g(x, y)$ Fig. (2.13)), we can precisely deduce ζ. In order to do that, we account for the relative angles as defined in Fig. (2.13): the first made between the probe and the angle of view α; the second one β, made with respect to the CCD.
By looking at the Fig. (2.13), we can easily be convinced that the magnification ζ can be written in the following way:

$$\begin{aligned} \zeta\,(mm/pixels) &= \frac{\Delta Y_{\perp}}{\Delta Y_{ccd}} \\ &= \frac{\Delta Y_{probe} \cdot \cos(\alpha) \cdot \cos(\beta)}{\Delta Y_{ccd}} \end{aligned} \tag{2.52}$$

where β is defined as $\tan(\beta) = \frac{\Delta X_{ccd}}{\Delta Y_{ccd}}$, the angle between the CCD and the probe axis. We also estimated that $\tan(\alpha) = \frac{6\,cm}{16.5\,cm}$ and thus $\alpha = 0.35\,rad$.

From the measure shown in Fig. (2.15), we extracted $\dfrac{\Delta Y_{ccd}}{\Delta Y_{probe}} = 22.92\,pixel/mm$; also for a horizontal displacement of $\Delta X_{ccd} = 30.96\,pixels$ when a vertical is moved by $\Delta Y_{probe} = 5\,mm$, we calculated $\beta = 0.263\,rad$ and finally using Eq. (2.52), we found a calibration value of:

$$\zeta\,(mm/pixels) = 39.5\ \mu m/pixel \tag{2.53}$$

Atomic Calibration

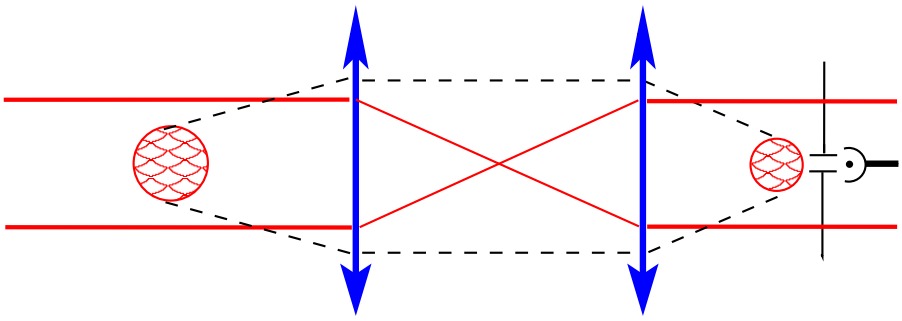

Figure 2.15: *Experimental Set-up used to measure the Coherent Transmission. We image the MOT center with two lenses into a photodiode, and select the central part of it by diaphragm. This arrangement, replacing the photodiode with a CCD camera, can be used for the absorption image technique.*

After the spatial calibration, the next important stage is to calibrate the fluorescence signal of the CCD camera. In the low intensity limit $s \ll 1$, we can write the scattering rate as $\Gamma/2 \cdot s$. In such a regime, the fluorescence recorded into the CCD with the I_g (I_d) image, integrated in the directions Oz (Ox), is proportional to the number of atoms, and the signal obtained can be written, for the I_g image, as:

$$I_g(x,y) = \beta \frac{\sigma_o}{1+4(\frac{\delta}{\Gamma})^2} \int n(x,y,z)\, dz \tag{2.54}$$

as well as for I_d:

$$I_d(z,y) = \beta' \frac{\sigma_o}{1+4(\frac{\delta}{\Gamma})^2} \int n(x,y,z)\, dx \ . \tag{2.55}$$

Indeed, β and β' depend on the solid angle of the detection system as well as on the intensity of the laser beams and on the duration of the probe illumination.

In principle, as the total number of atoms in MOT does not depend on which directions we look at, we conclude that $\frac{\beta}{\beta'}(N_{at}) = const = 1$. This could be checked in the experimental images and for both directions, as a control that everything works as one would expect.

We calibrate the fluorescence by measuring the optical thickness across the z direction of the atomic cloud at the center ($x = 0, y = 0$), by looking at the coherent transmission curve of the probe laser as a function of laser detuning δ (Fig. (2.16)).

Generally, a large optical thickness b_0 is responsible for the flat transmission around the resonance $\delta = 0$, and is too small to be measured. The non zero transmission is due to the finite linewidth of our probe laser estimated to be $2\,MHz$ and assumed to be Lorentzian. In order to take this into account we convolute the monochromatic coherent transmission with the probe laser spectrum $\mathcal{L}(\delta\nu)$:

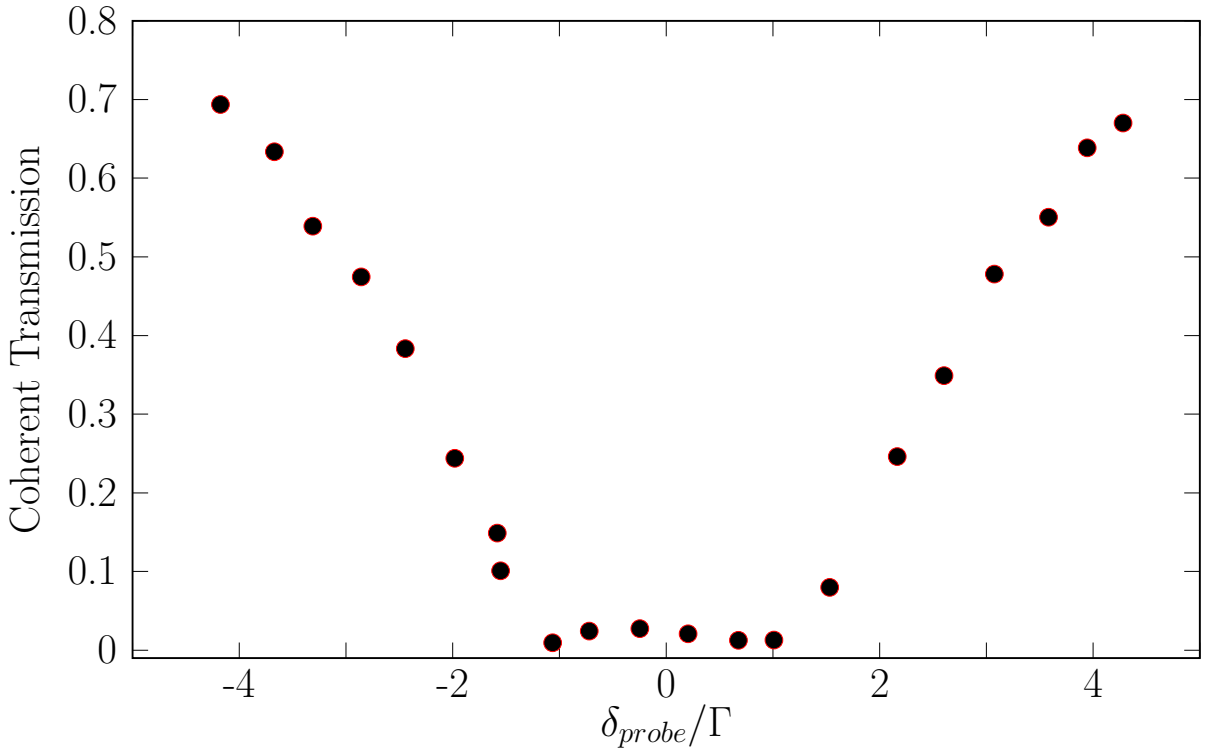

Figure 2.16: *Experimental curve showing the absorption (coherent transmission) of the probe beams with its frequency scanned across the atomic resonance (^{85}Rb,$F = 3 \rightarrow F' = 4$). From its width, defined as $FWHM$ (given in γ units), we extracted the on-resonance optical thickness (b_0) as described in the text. In this particular case we found $FWHM = 6\Gamma$ that corresponds to $b_0 = 30$.*

$$T(\delta) = \int_{-\infty}^{+\infty} \mathcal{L}(\delta\nu)\, e^{\frac{b_0}{1+4(\frac{\delta+\delta\nu}{\Gamma})^2}} d(\delta\nu)\ . \tag{2.56}$$

By computing the FWHM in units of Γ, from Eq. (2.56) for different b_0, we end up with the curve shown in Fig. (2.17) that we use to characterize our atomic sample.

If we assume a monochromatic spectrum for the probe laser, we can easily give an analytical expression for mapping the FWHM (in Γ units) of the coherent transmission with the on-resonance optical thickness (b_0) expressed by:

$$\Delta\nu_{FWHM} = \Gamma\sqrt{\frac{b_0}{\ln(2)} - 1} \tag{2.57}$$

The graph in Fig. (2.17) shows that if the spectral properties of the probe laser are not taken into account, the calibration of the number of atoms can be wrong. We can overestimate the total number of atoms in the MOT and consequently the atomic density. Also, from the figure Fig. (2.17), we computed the FWHM of coherent transmission $T_c(\delta)$ by numerically integrating Eq. (2.56), and the results can be fitted by the following function:

$$\Delta\nu_{FWHM}(b_0) = \Gamma \cdot A(\sqrt{(G \cdot b_0 - 1)}) \tag{2.58}$$

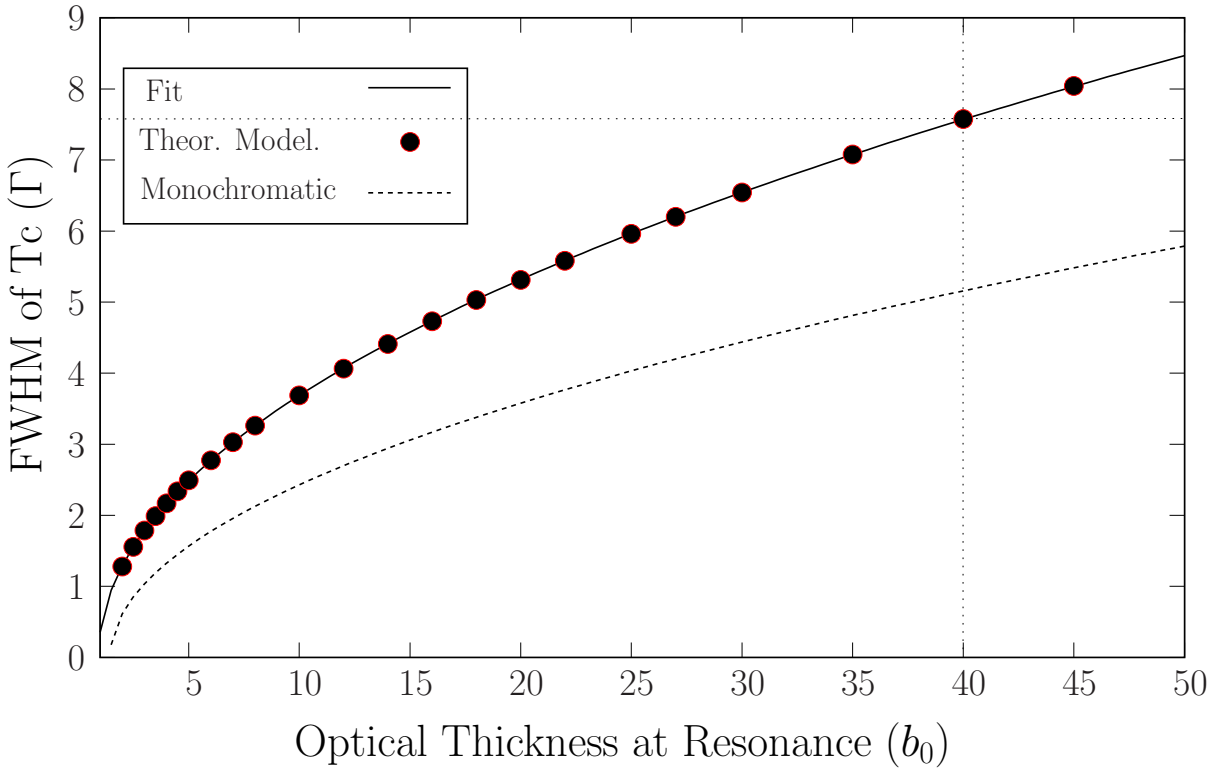

Figure 2.17: *Theoretical model for FWHM of Coherent Transmission. The circle dots represent a theoretical model for coherent transmission convoluted with a Lorentzian spectrum of* $2\,MHz$*; the dashed line is the transmission without taking into account the spectral properties of the laser probe (monochromatic case), while the solid line is a fit with the function given in Eq. (2.58). Finally, the dotted line represents normal work conditions (standard parameters) for our MOT (*$b_0 = 30$*).*

with two free fitting parameters $A = 1.10$ and $G = 1.21$.

In order to improve the experimental determination of b_0, each value of the transmitted intensity taken in presence of cold atoms is divided by the incident intensity without the cold atoms. With this protocol, the coherent transmission curve shown in Fig. (2.16) is obtained. From its FWHM, we extract the on-resonance optical thickness b_0 (typically found to be $b_0 = 30$ in our MOT) which is independent of density profile as integrated along one direction:

$$b(\delta) = \sigma_L(\delta) \int_{-\infty}^{+\infty} n(0,0,z)\, dz \ . \tag{2.59}$$

By comparing, for example, the center values for the image $I_g(0,0)$ Eq. (2.54) and the Eq. (2.59) we are now able to calibrate our detection system.

Supposing a Gaussian density distribution for the atomic cloud, characterized by the standard deviations $\sigma_x\,, \sigma_y\,, \sigma_z$, the total number of atoms in the cloud is found to be:

$$N_{at} = (2\pi)^{3/2}\, n_0 \sigma_x\, \sigma_y\, \sigma_z \ , \tag{2.60}$$

and equivalently using Eq. (2.59) for a Gaussian distribution:

$$N_{at} = \frac{(2\pi)\, b_0\, \sigma_x\, \sigma_y}{\sigma_0} \ . \tag{2.61}$$

We can further deduce the center density at the MOT's center via a direct measurement of b_0 still using Eq. (2.59):

$$n_0 = \frac{b_0}{\sqrt{(2\pi)} \cdot \sigma_0 \cdot \sigma_z} \tag{2.62}$$

In conclusion, the calibration of N_{at} can be done with only the images I_g while the density needs the I_d image, as we have to look at the Oz direction.

This apparently complicated protocol of measurement allows us to extract all the quantities we are interested in from three experimental measurements, b_0, I_g,I_d.

During all calibrations, we assume that the atoms are equally distributed among all the Zeeman sublevels of the ground state. This is accounted for by considering a g factor equal to:

$$g \ = \ \frac{1}{3}\, \frac{2F' + 1}{2F + 1} \tag{2.63}$$

This reduces the total cross section $g \cdot \dfrac{3\lambda^2}{2\pi}$. For the transition $F = 3 \rightarrow F' = 4$ on the ^{85}Rb, we have $g = 3/7$.

2.2.2 Preliminary test

In this part, we will detail all experiments done before the beginning of the systematic scan of the MOT parameters. Such tests are useful in order to control all possible physical effects that can be involved in the size measurements. Particularly, we want to be sure that what we are measuring does not depend on the laser parameters we use to probe the atomic cloud.

From the curves shown in Fig. (2.18), we see that the apparent MOT size does not depend on the probe detuning when its value is set to be $\delta_{probe} = -6\Gamma$. For that detuning value we also investigated the size for different values of probe duration for both large and small MOT (Fig. (2.19)).

From the experiment observation Fig. (2.20) we conclude that size didn't change during different probe durations for either the large or the small MOT. However, we observed dramatical drops in the total number of atoms due to optical pumping towards lower hyperfine ground state ($F = 2$) Fig. (2.19). This is because of the absence of a repumping laser during the probe phase. This means that if we don't want a loss of signal, the duration of illumination, done with the six trapping beams red-detuned, has to be as small as possible.

During all the experiments, we chose such a duration to be of the order $\tau_{probe} = 10\mu s$.

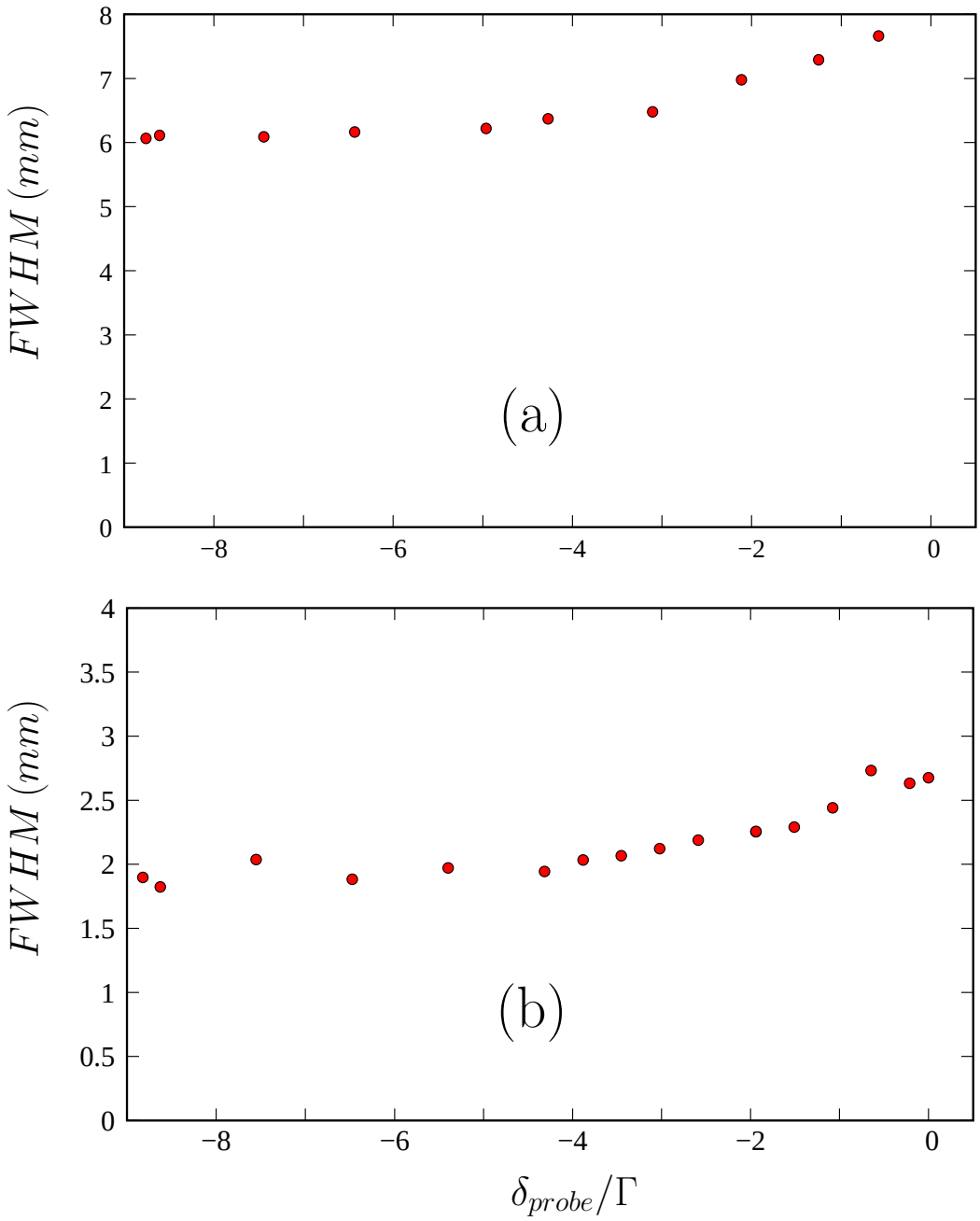

Figure 2.18: *Cloud size as a function of probe detuning. Keeping the number of atoms in the trap constant, we varied the probe detuning of six trapping beams. From the experimental observations, we deduced that a* $\delta_{probe} = -6\,\Gamma$ *doesn't modify the MOT's size and is independent of it. We checked this in the two extreme cases that could be realized with our set-up: a 'large' MOT, shown in Fig. (a) with* 10^{10} *atoms, and a relatively 'small' MOT, Fig. (b) with* 10^8*. These are the extremes of the ranges we looked at.*

Atomic control

We are able to control, and measure, the total number of atoms in the MOT in different ways illustrated below. As before, we can control the delay (τ_{delay}) between the TTL's

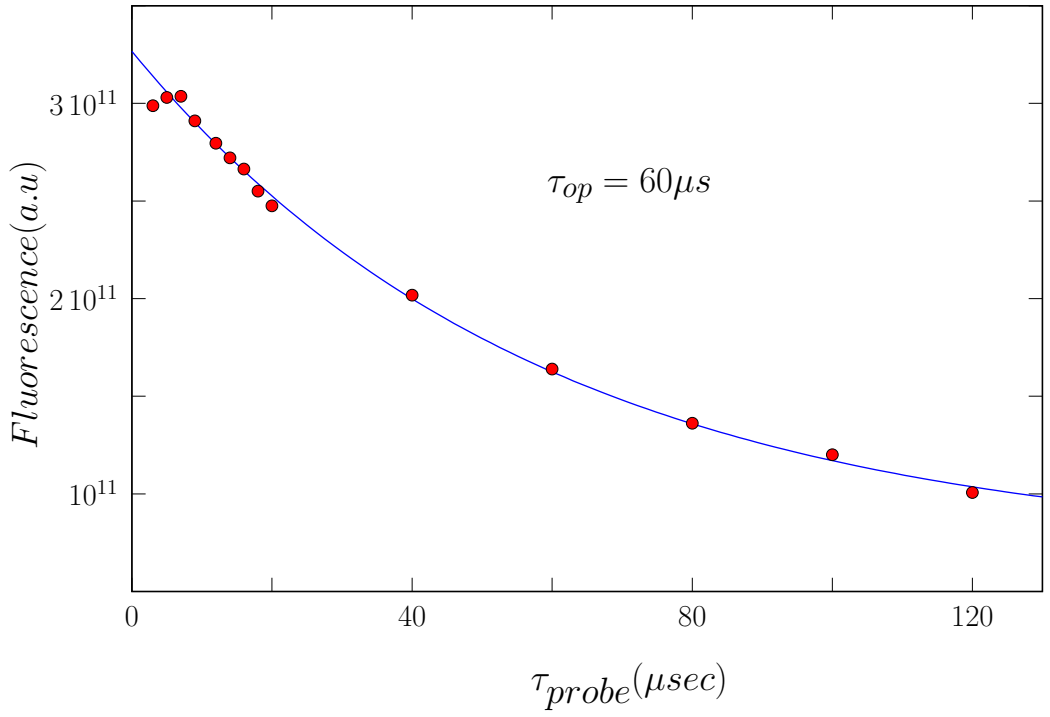

Figure 2.19: *Optical Pumping due to probe interactions with an MOT optical thickness at resonance of* $b_0 = 30$ *and* $\delta_{probe} = -6\Gamma$ *for the probing-beams. The result shows that we need to choose smaller probe durations in order to avoid optical pumping the* $F = 2$ *hyperfine ground state.*

signals of the repumper and trapping beams Fig. (2.22). Indeed, when we switch off the trapping beams intensities as before and then the repumper ($\tau_{delay} > 0$), the light recorded in the CCD (for example in image I_1) is proportional to the total number of atoms N_{at} ($N_{F=3} + N_{F=2}$). On the other hand, when the repumper and trapping beams are switched off at the same time ($\tau_{delay} = 0$)), the total fluorescence (image I_2) is proportional to $N_{at} = N_{F=3}$. Thus the difference between the two images ($I_1 - I_2$) gives us information about the total number of atoms present in the $F = 2 (N_{at} = N_2)$ state. Finally, in the case in which $\tau_{delay} < 0$ we have a loss of atoms due to optical pumping.

In the standard condition where the MOT works, we have a defined repartition between the atomic population in the different hyperfine ground states ($F = 3\,, F = 2$). Using the delay method illustrated above we are able to measure such a repartition and monitor it as a function of control parameters.

The delay-method could also be employed to change the total number of atoms in the MOT without affecting any MOT parameters, once we have calibrated the 'delay' curve as we did in Fig. (2.21).

A second method is provided by putting a $\lambda/2$ wave plate and a polarized cube system in the path of the repumper laser. We can thus change its total intensity before it enters the vacuum chamber. However, by altering the repumper intensity we also change the hyperfine ground-state repartition.

The last technique implemented in our set-up was to reduce the capture volume of our

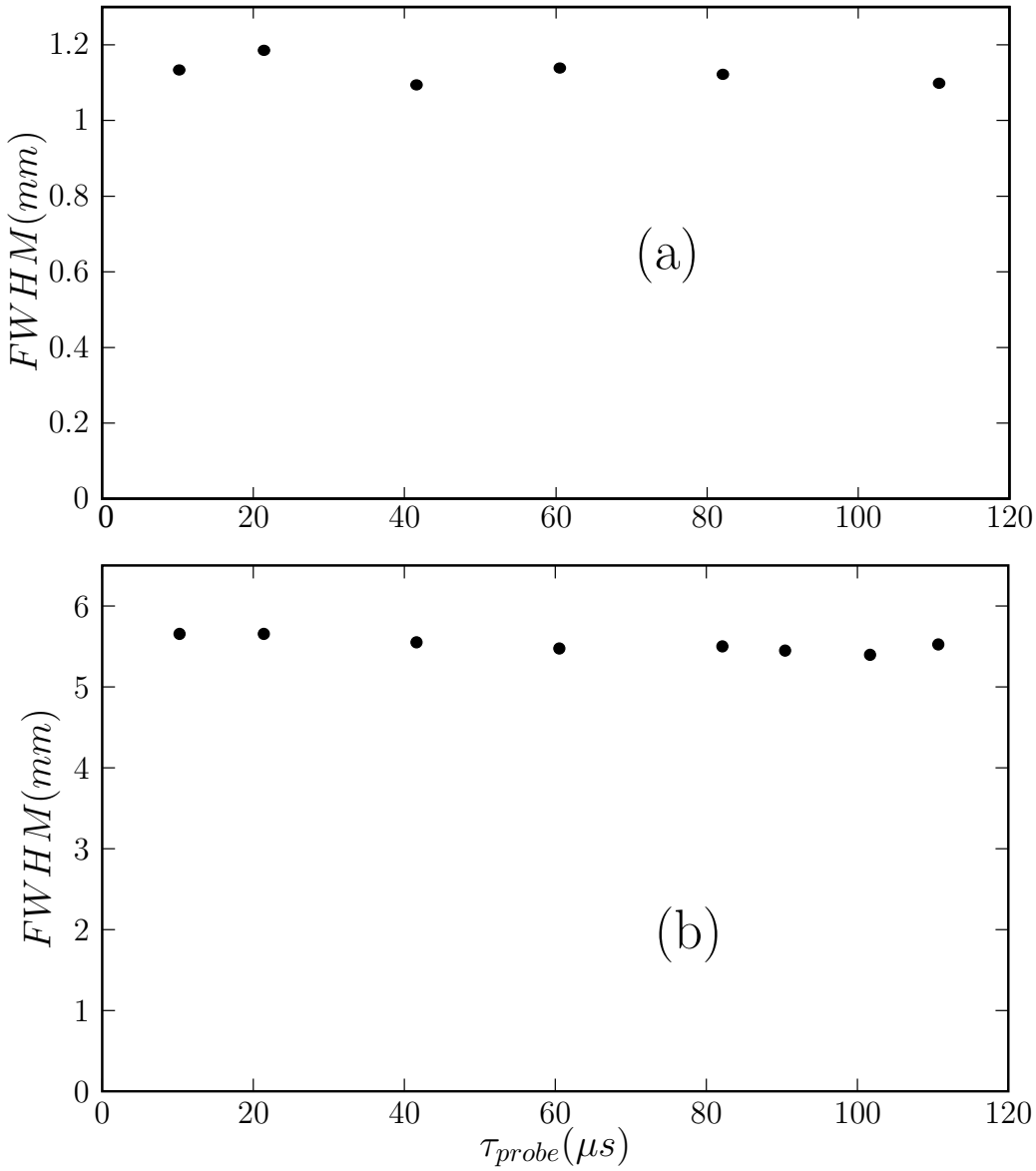

Figure 2.20: *Size as a function of probe duration τ_{probe} for our two extremes: 'large' MOT (b) and 'small' MOT (a). In conclusion the probe used doesn't depend on the τ_{probe}; the only dramatic consequence is the optical hyperfine pumping (Fig. (2.19)).*

trap by limiting the repumper size (ϕ). The total number of atoms trapped in the MOT varies in accordance with $N_{at} \propto \phi^4$ [25]. This is realized by imaging a diaphragm, with a controllable aperture, in the center of the MOT chamber using the telescope system of the repumper laser.

In this way, changing the size of the diaphragm results in a variation of the total number of atoms in the MOT without affecting the external control parameters at the cloud location. We have also verified that the intensity at the center of the repumper laser, at the level of the vacuum cell, is constant, as shown in Fig. (2.24).

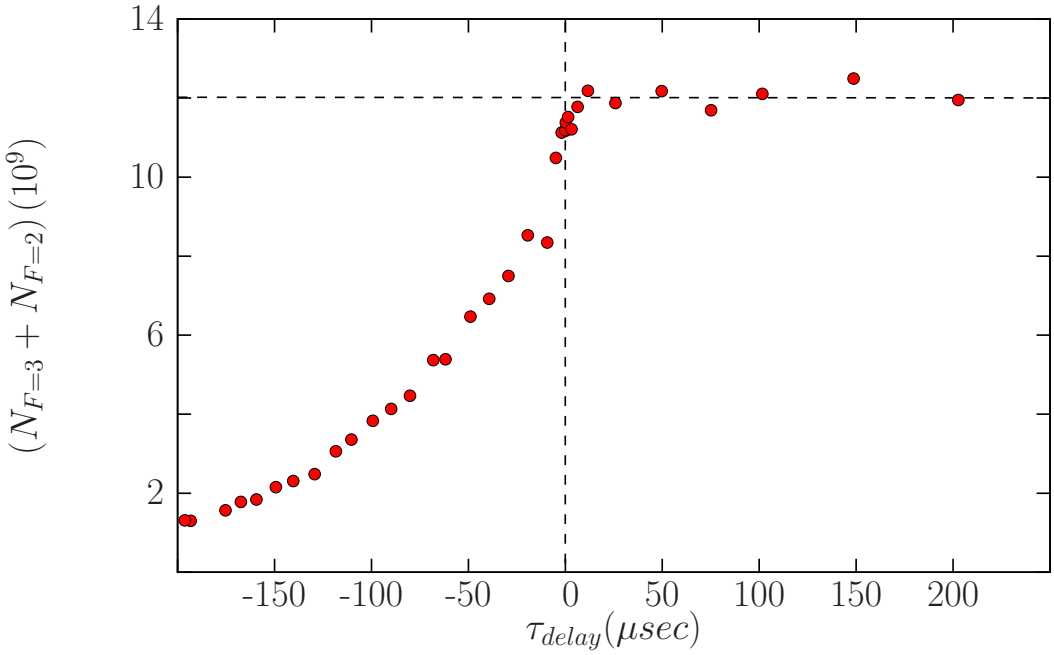

Figure 2.21: *Number of atoms in the 'bright' state as a function of turn-off delay τ_{delay} of the repumper with respect to MOT beams. When $\tau_{delay} > 0$ all atoms are 'repumped' in the bright $F = 3$ state.*

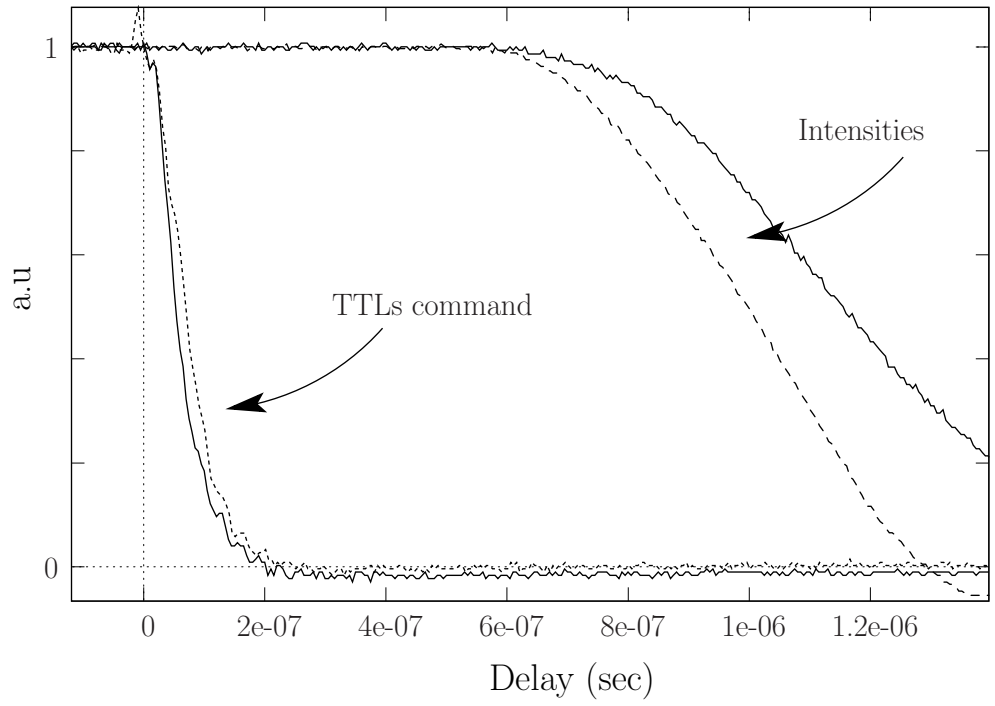

Figure 2.22: *Calibration of the delays for the TTL's signals: the MOT and repumper intensity. We can conclude that the two signals have the same delay.*

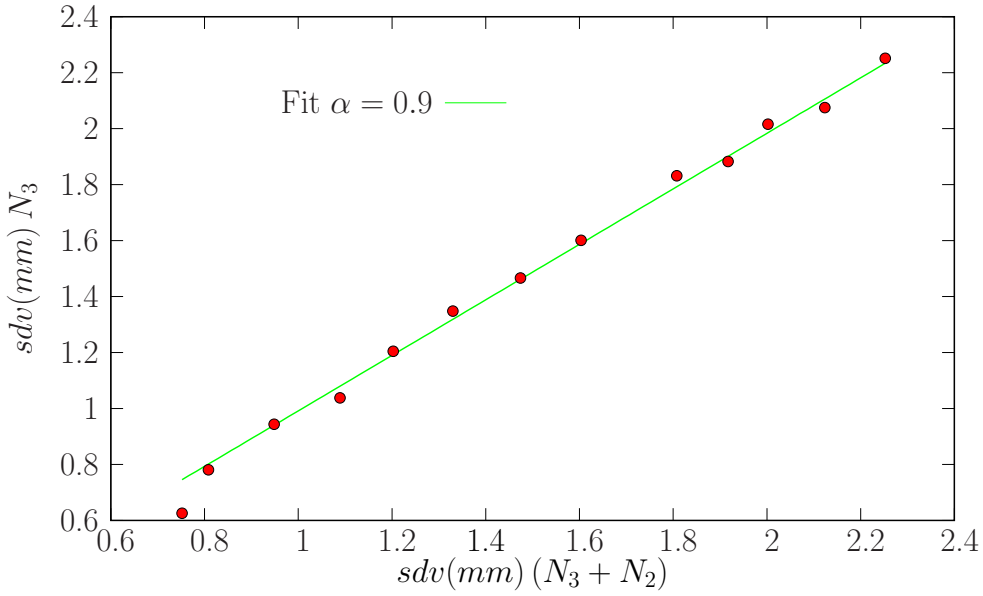

Figure 2.23: *Standard deviation (sdv) of the size of the images when they are taken with either N_3 or $N_3 + N_2$ atoms. In both cases, the final sdv is independent of such a choice.*

Image analysis

From the images we obtained we are able to extract plenty of information. First of all, the total fluorescence (the integral made over all pixels' values) is proportional to the total number of atoms. Then, as we have already seen, from the central value of image $I_g(0,0) \propto b_0$, we can monitor the optical thickness as a function of N_{at}.

The only delicate point is the determination of the size of the atomic cloud. In the case of a small MOT (with only 10^7), the profile of the fluorescence can be well fitted by Gaussian function Fig. (2.25)-(a). While in the case of $N_{at} = 10^{10}$ Fig. (2.25)-(c), such a profile is dramatically different from a Gaussian.

This is why we decided to realize a computer routine to evaluate a standard deviation, in pixels, extracted from the intensity distribution recorded in the images; this quantity is well defined and independent of any assumption of density distribution.

The standard protocol used to analyze the date is resumed as follows:

- Each image is subtracted from a correspondent 'dark (background)', taken in the same experimental conditions and exposition time (t_{exp}), without the cold atoms to eliminate the stray light [30].

- After the subtraction, we defined a region-of-interest (ROI) centered around the atomic cloud. This is used to resize the scientific image in order obtain a better signal to noise ratio, and to be less sensitive to background pixel fluctuation. Then, for both directions of the CCD, $x_{ccd} = x$ and $y_{ccd} = y$, we use the standard deviation

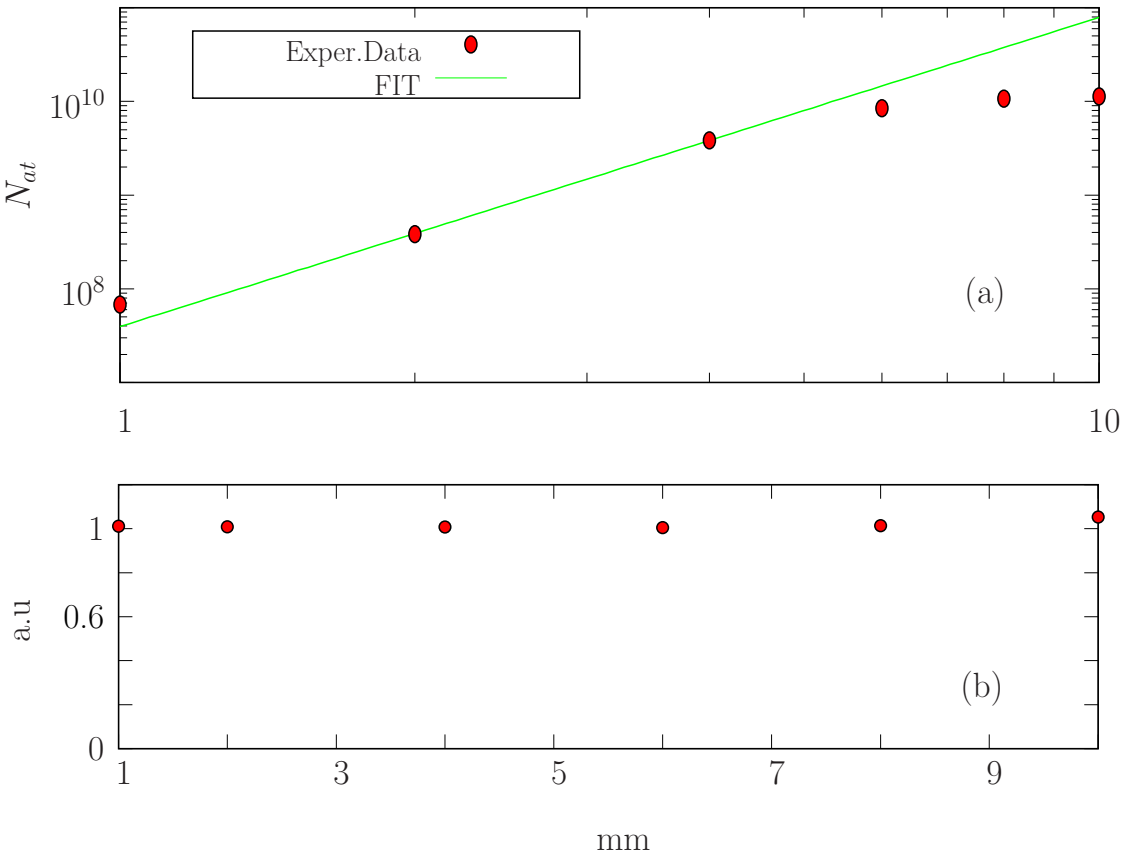

Figure 2.24: *The graphs show the experimental evidence that when we change the number of atoms via diaphragm (a) the repumper intensity, at the center, remains constant, Fig. (b).*

as a definition of size, defined by the following quantity:

$$\sigma_\xi = \sqrt{\frac{\sum_{ij}(\xi_i - \xi_c)^2 \cdot (I_O)_{ij}}{\sum_{ij}(I_O)_{ij}}} \ , \qquad \xi = x, y, z \tag{2.64}$$

with the 'center of mass' ξ_c, defined as

$$\xi_c = \frac{\sum_{ij} \xi_i \cdot (I_O)_{ij}}{\sum_{ij}(I_g)_{ij}} \ , \qquad \xi = x, y, z \tag{2.65}$$

where in Eqs. (2.64) (2.65) instead of I_O the appropriate image has to be used: I_d for $\xi = y, z$ and I_g for $\xi = x, y$. In this way, the scaling-law for the *sdv* as a function of N_{at} is obtained without any assumption for the atomic density distribution.

- However, during all measurements, for the sake of simplicity, we compute the central density value (n_0) assuming a Gaussian density profile.

2.3 Qualitative Observations

In this section, we will give a resume of all qualitative observations that we have made during the investigation of the new regime. A systematic study of the MOT is made

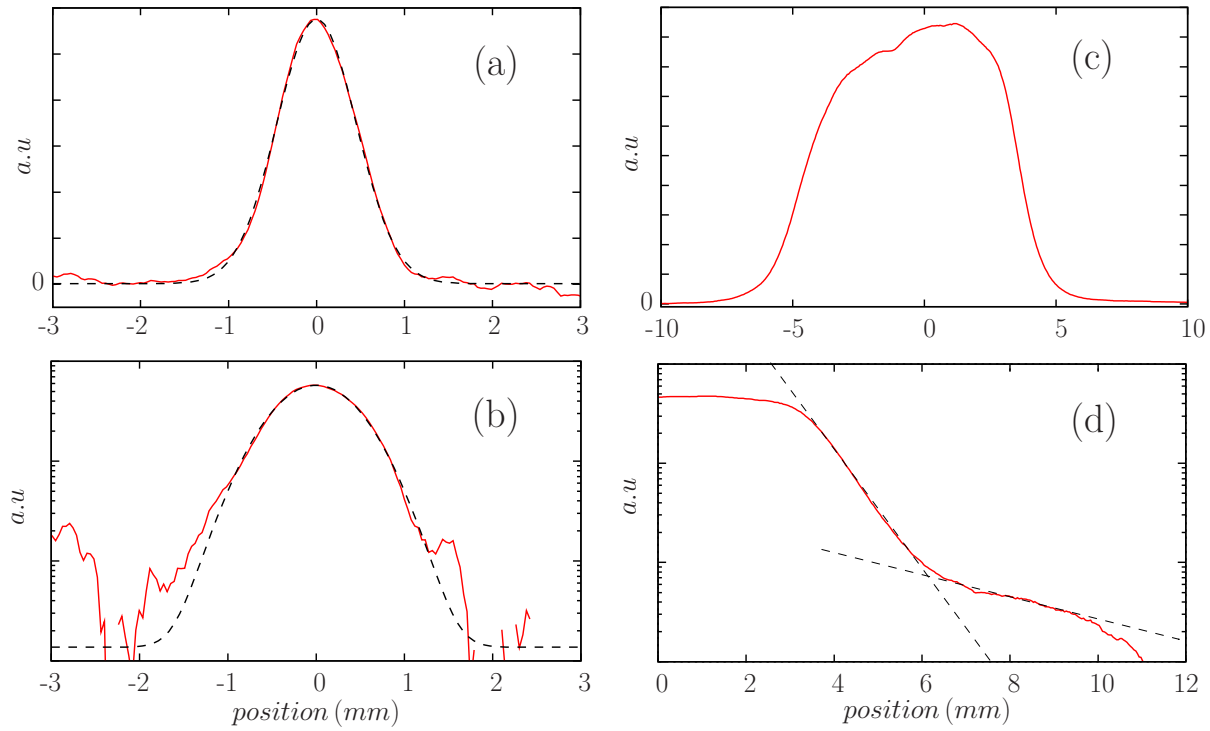

Figure 2.25: *Experimental data showing the density profile. The MOT with a moderate number of atoms (10^7), profile (a), is well fitted by a Gaussian (dotted-line). In (b) we plot the same data as (a) but in log-linear scale. For a maximum number of atoms in the trap ($\sim 10^{10}$) the Gaussian approximation is no longer valid (c). We found a more 'squared' density profile and, in a log-linear plot (d), we can see two different regimes. The dotted-line in (d) is used to illustrate two such regimes.*

by altering the standard parameters defined as $I_{MOT} = 7\,mW/cm^2$, $\delta_{MOT} = -2.5\,\Gamma$ and $\vec{\nabla}B = 10\,G/cm$. The results are presented in the following sub-sections.

2.3.1 Size Scaling Law: L(N_{at})

In this particular sub-section we show the main experimental results we obtained from the size experiments.
As in the first investigation, we varied the MOT parameters around the standard one. In this way we want to be able to characterize the cross-over between the two regimes; multiple-scattering and constant optical thickness. This kind of study has also been used to optimize the MOT with our set-up. We further present two different ways to change the number of atoms in the MOT in two separated sections, surprisingly giving different results: atom number controlled by the intensity of the repumper and atom number controlled by its size.

Repumper Intensity controlled atom number: N(I_{rep})

In this paragraph, we will present the studies for the MOT when we change the total number of atoms by altering the repumper intensity.
For each choice of set of parameters we took about 25 images with the relative dark image and an average exposition time of 60 *sec* for both directions: I_g and I_d.

Once we had performed the MOT optimization we carried out a series of 8 experiments over the two full days that the set-up was kept running in order to maintain the same experimental conditions and to allow us to compare the different series with each other. Throughout the discussion we will present only the results for one size defined as:

$$L = 1/3(\sigma_x + (\frac{\sigma_{y_{Id}} + \sigma_{y_{Ig}}}{2}) + \sigma_z) \tag{2.66}$$

where the size in the Y direction is already defined as an average of the Y-size coming from I_g and I_d images. The Eq. (2.66) is justified because the 3 dimensions follow approximately the same scaling law, as we can see from Fig. (2.26).

The results of the 8 experiments are reported in a separate section, in which they are followed by the relative table giving a resume of the main information we can extract from the analyzed images.

- Varying the MOT intensity, where the intensity of trapping beams are changed: I_{max}, $I_{max}/2$, $I_{max}/10$ and the Tab. (2.1);
- Varying the MOT detuning: $\delta = -2\Gamma \ -2.5\Gamma \ -3\Gamma$ shown in Tab. (2.2);
- Varying the Magnetic field gradient: 4.8, 10, 16 G/cm shown in the Tab. (2.3).

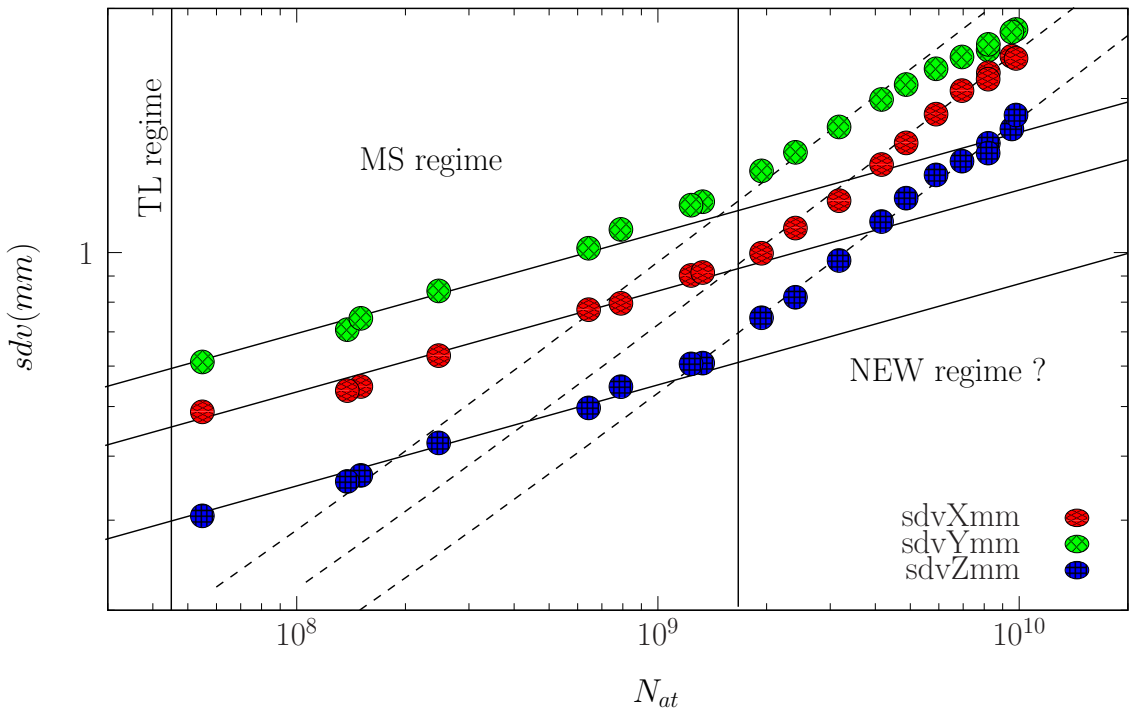

Figure 2.26: *Graph shows the scaling laws for the three spatial directions obtained from one experimental run. The scaling laws are the same for all directions which is why we chose to only monitor an average L, defined by Eq. (2.66). The regimes discussed in the text are also represented on the graph: temperature-limited (TL), multiple-scattering (MS) and maybe a new one: constant optical thickness .*

Varying MOT Intensity ("I_{MOT}")

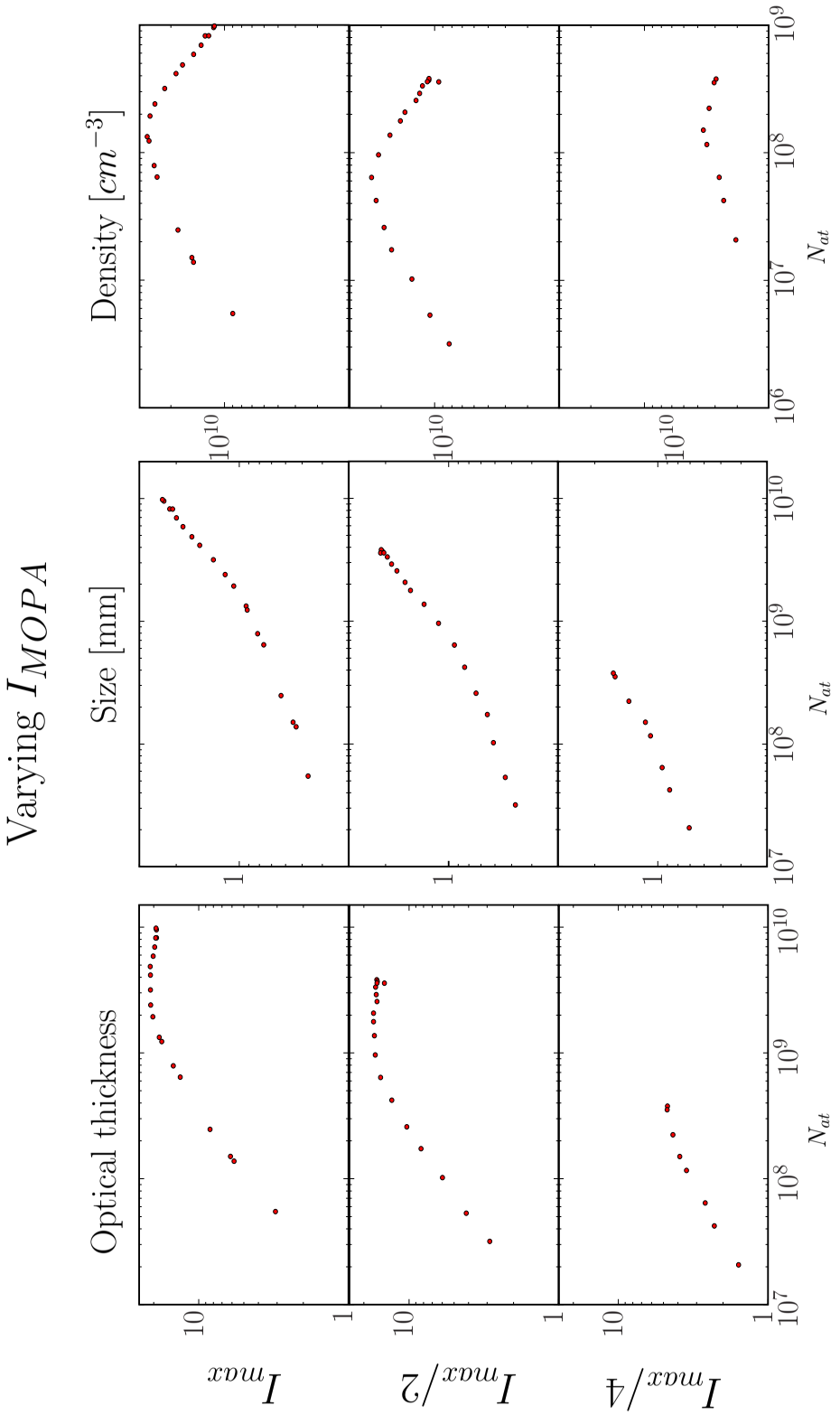

Name of Experiment	$I_{MOPA}(\frac{mW}{cm^2})$	δ_{MOT}	$\vec{\nabla}B\,(G/cm)$	b_0^{max}	N_{cr}^{avg}	$L_{cr}^{avg}(mm)$	N_{at}^{max}	$L_{max}(mm)$	$n_0^{max}\,(cm^{-3})$	$\alpha_{cr}^{1/3}$	$\alpha_{cr}^{1/2}$
Manip1	7	$-2.5\,\Gamma$	10	21	$1.6\cdot 10^9$	0.96	$9.8\cdot 10^9$	2.32	$2.7\cdot 10^{10}$	0.22	0.49
Manip2	3.5	$-2.5\,\Gamma$	10	17	$0.6\cdot 10^9$	0.86	$3.8\cdot 10^9$	2.10	$2.3\cdot 10^{10}$	0.21	0.45
Manip3	1.75	$-2.5\,\Gamma$	10	5	$0.16\cdot 10^9$	1.15	$0.38\cdot 10^9$	1.63	$0.46\cdot 10^{10}$	0.23	0.41

Table 2.1: *The table shows all parameters concerning the experiments for different MOT intensities*

Varying MOT detuning ("δ_{MOT}")

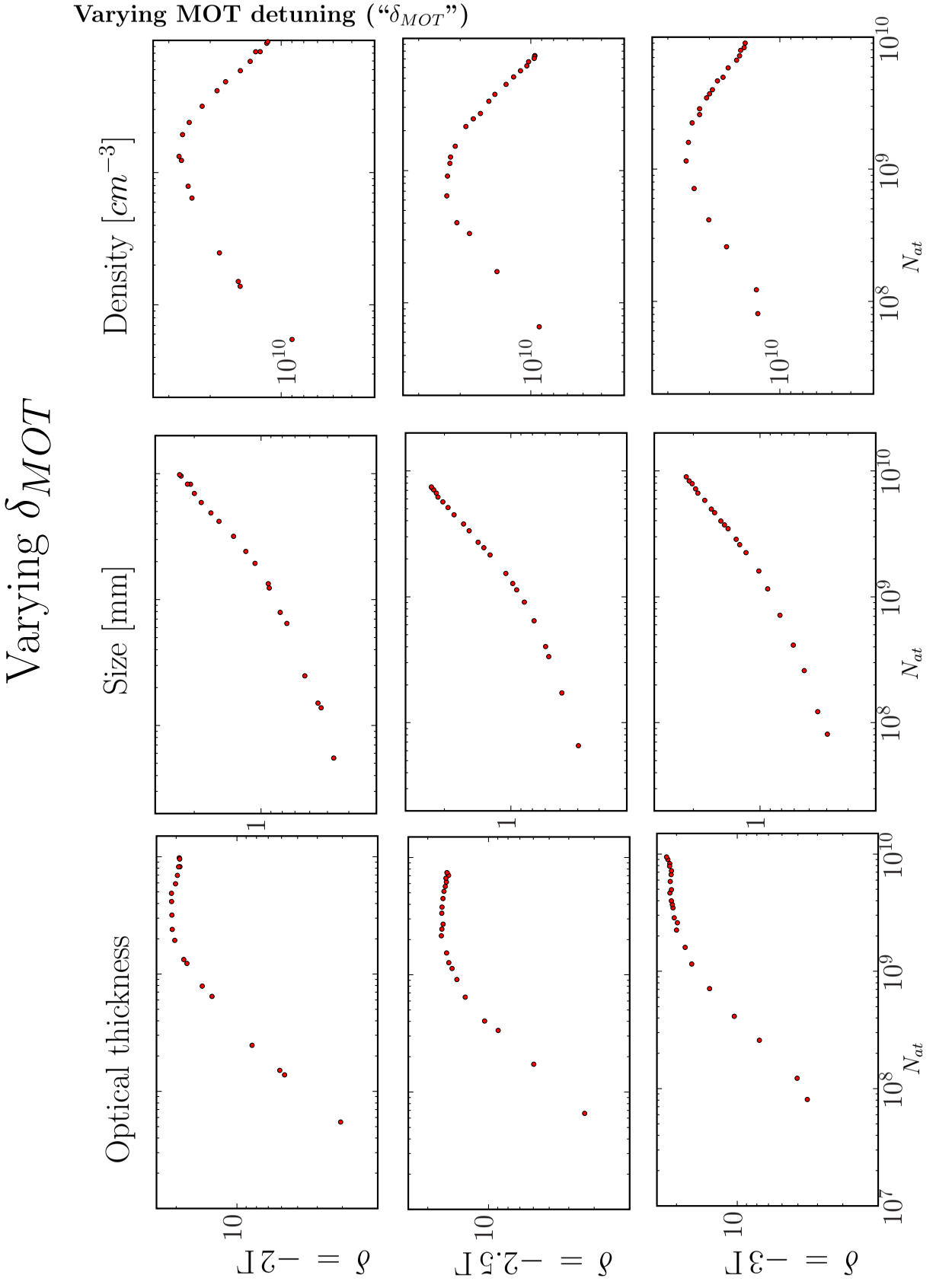

Name of Experiment	$I_{MOPA}(\frac{mW}{cm^2})$	δ_{MOT}	$\vec{\nabla}B\,(G/cm)$	b_0^{max}	N_{cr}^{avg}	$L_{cr}^{avg}(mm)$	N_{at}^{max}	$L_{max}(mm)$	$n_0^{max}\,(cm^{-3})$	$\alpha_{cr}^{1/3}$	$\alpha_{cr}^{1/2}$
Manip1	7	$-2.5\,\Gamma$	10	21	$1.6\cdot 10^9$	0.96	$9.8\cdot 10^9$	2.32	$2.7\cdot 10^{10}$	0.22	0.49
Manip4	7	$-2\,\Gamma$	10	17.0	$1.0\cdot 10^9$	0.87	$7.4\cdot 10^9$	2.30	$2.3\cdot 10^{10}$	0.21	0.48
Manip6	7	$-3\,\Gamma$	10	21.4	$1.60\cdot 10^9$	1.01	$9.0\cdot 10^9$	2.16	$2.5\cdot 10^{10}$	0.24	0.45

Table 2.2: *In this table we put together all parameters concerning the experiments for different detuning of MOT beams.*

Varying Magnetic Field Gradient ("$\vec{\nabla}B$")

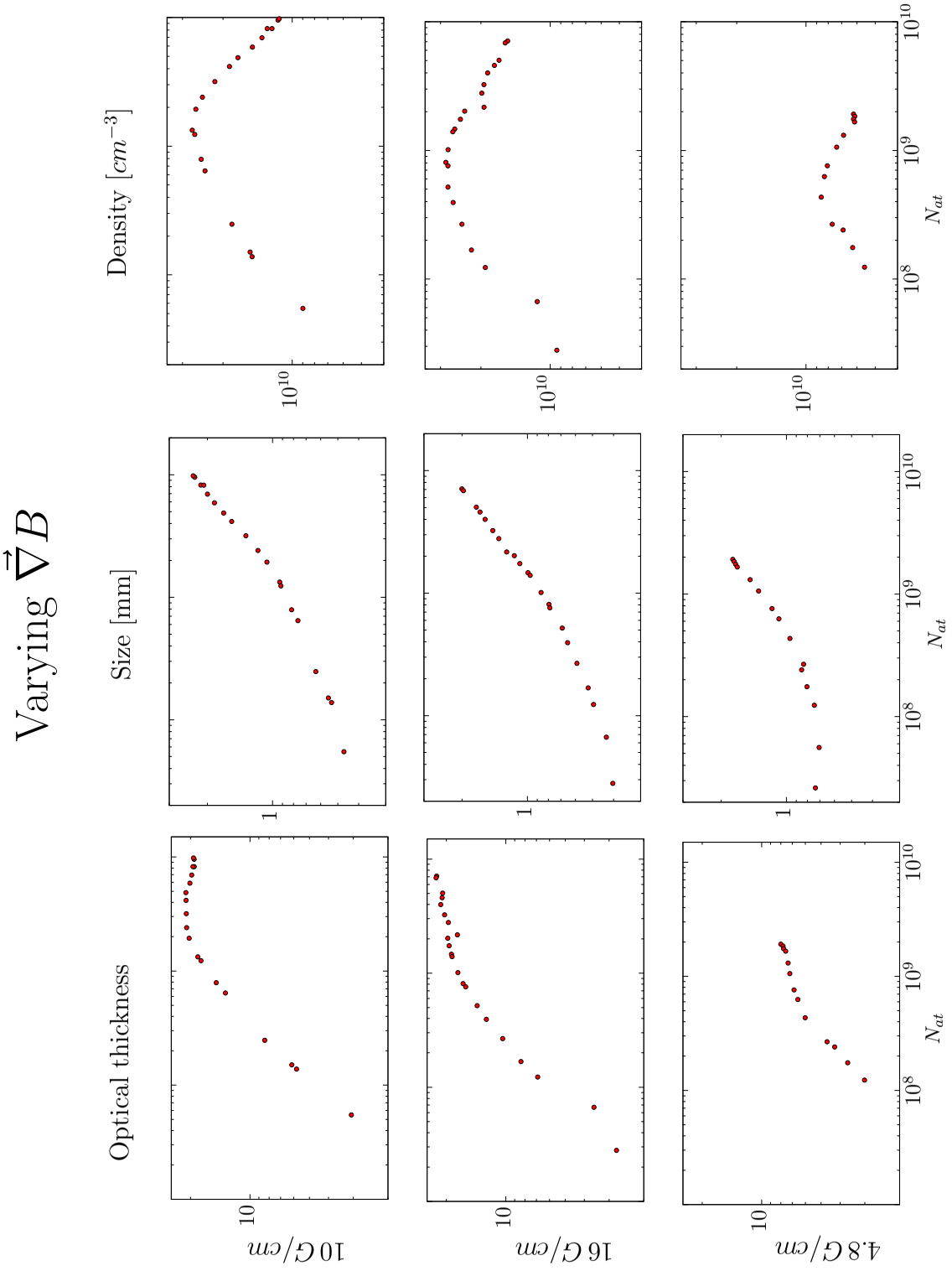

Name of Experiment	$I_{MOPA}(\frac{mW}{cm^2})$	δ_{MOT}	$\vec{\nabla}B\,(G/cm)$	b_0^{max}	N_{cr}^{avg}	$L_{cr}^{avg}(mm)$	N_{at}^{max}	$L_{max}(mm)$	$n_0^{max}\,(cm^{-3})$	$\alpha_{cr}^{1/3}$	$\alpha_{cr}^{1/2}$
Manip8	7	$-2.5\,\Gamma$	5	8	$0.47\cdot 10^8$	0.96	$1.92\cdot 10^9$	1.77	$0.86\cdot 10^{10}$	0.20	0.43
Manip1	7	$-2.5\,\Gamma$	10	21	$1.6\cdot 10^9$	0.96	$9.8\cdot 10^9$	2.32	$2.7\cdot 10^{10}$	0.22	0.49
Manip7	7	$-2.5\,\Gamma$	16	22.5	$0.9\cdot 10^9$	0.81	$7.1\cdot 10^9$	2.0	$2.8\cdot 10^{10}$	0.25	0.44

Table 2.3: *In this table we put together all parameters concerning the experiments for different values of Magnetic field gradient.*

Conclusions on repumper controlled Atom numbers.

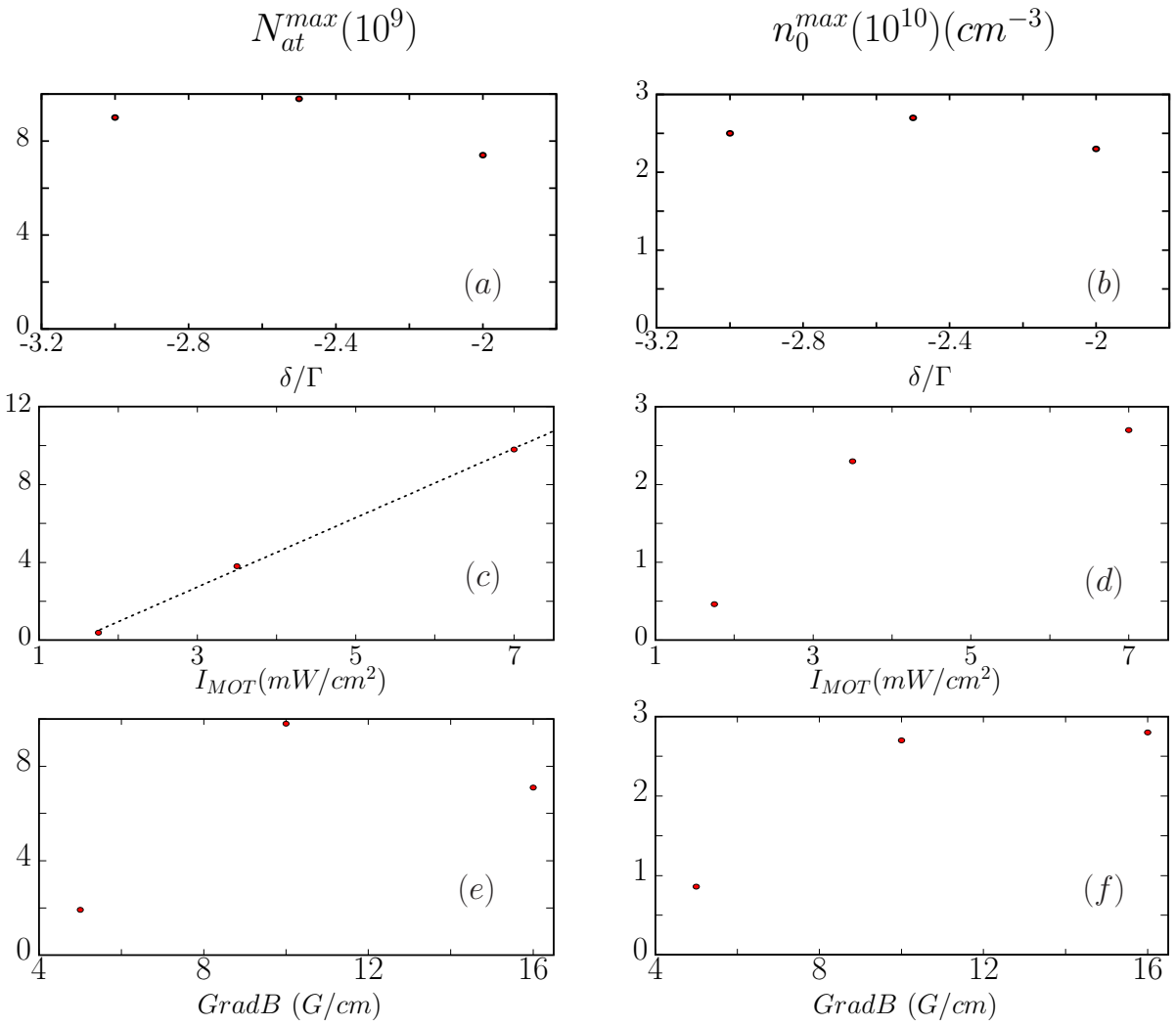

Figure 2.27: *In the graph we give a resume of the main results obtained from the study: in particular we look at N_{at}^{max}, (a)-(c)-(e), and n_0^{max} (b)-(d)-(f), obtainable in our MOT. The standard parameters are defined as: $I_{MOT} = 7\,mW/cm^2$, $\nabla\vec{B} = 10\,G/cm$,$\delta_{MOT} = -2.5\,\Gamma$. From the experiments we found confirmation that for these values the atomic density is optimized while the total number of atoms is not. In fact, as we can see from (c), with the highest power we have, we are still in the linear regime.*

From the data reported in table (2.1),(2.2) and (2.3) we can conclude that the threshold (for example in numbers of atoms N_{at}^{cr}) of the new regime does not depend on the MOT parameters. The only notable thing is the evolution of the maximum number of atoms captured in the MOT, and the consequent decreasing of the optical thickness. In fact it is evident that by changing the MOT parameters we only affect the capture volume of our trap. To avoid this kind of problem, we could perform the same experiment by keeping the capture volume fixed during the loading time (typically 2 sec), and only changing the MOT parameters at the end of the sequence before probing the cloud. Such

a time sequence was not possible in our set-up at that time for the following reasons: slow acquisition image shutter synchronization, and realization of the time sequence up to several seconds.

Therefore, we used this study to optimize the MOT as shown in the Fig. (2.27). In this graph we give a resume of the results obtained from the experiments described in the above sections. As usual, we moved from a starting point defined as: $I_{MOT} = 7\, mW/cm^2$, $\vec{\nabla B} = 10\, G/cm$, $\delta_{MOT} = -2.5\, \Gamma$ and then we altered the standard conditions by changing only one parameter and leaving the other parameters fixed. The maximum number of atoms (N_{at}^{max}), the maximum density (n_0^{max}) obtained as a function (vertical direction) of the total intensity, detuning and magnetic field gradient are reported.

From the experimental observation, Fig. (2.27)-(c), we claim that the N_{at}^{max} in our trap is limited only by the total intensity of the laser beams provided by the MOPA. The maximum output power from the amplifier is about 300 mWatt but we end up with only 150 mWatt due to spatial mode cleaning.
Never the less, we are not interested in trapping as many atoms as possible but we want to optimize the achievable density value in the MOT. As we can see in the right column in Fig. (2.27)-(b),(d),(f), for the standard parameters (where the MOT usually works) we get the highest density. This means that if we want to increase the atomic density by introducing a compression phase by for example suddenly changing either the magnetic field gradient or the MOT detuning, it won't work.

Repumper Size controlled number of atoms: N(ϕ)

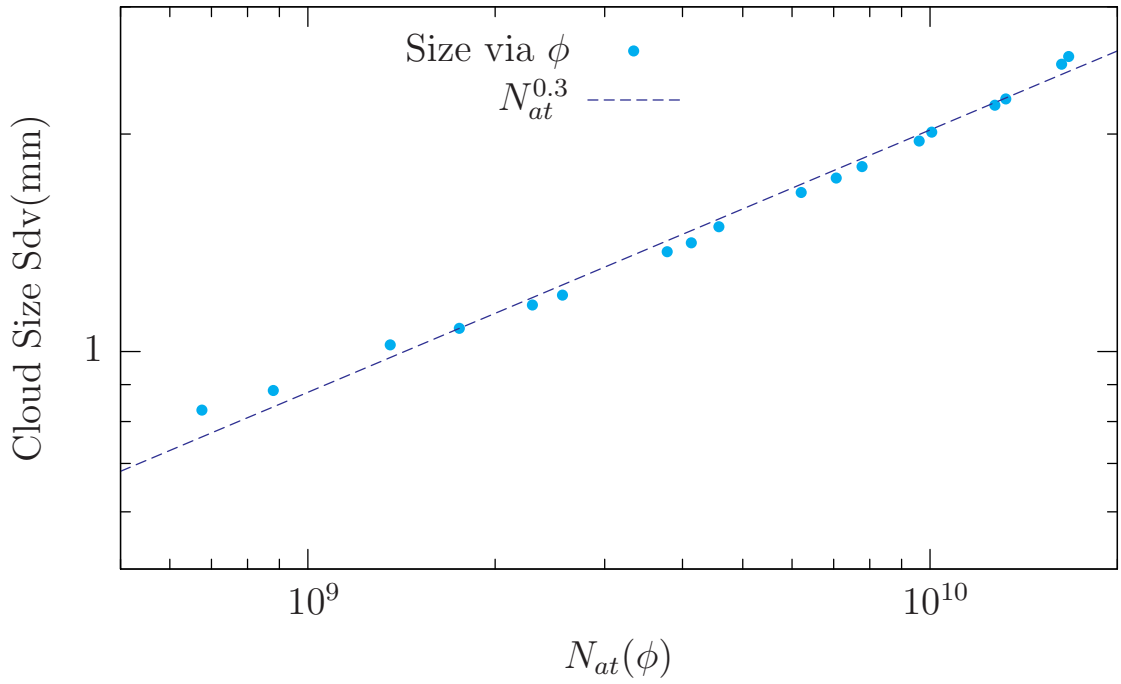

Figure 2.28: *In the Figure we show the evolution of the total number of atoms by changing the size of the repumper. We can clearly see that we follow the 1/3 scaling law over the whole atomic range. The experiments were carried out with the standard parameters for the MOT ($I_{MOT} = 7\,mW/cm^2$, $\vec{\nabla B} = 10\,G/cm$,$\delta_{MOT} = -2.5\,\Gamma$).*

As we couldn't come up with a convincing model for the description of the "New Regime" and also because of the observation that the threshold does not depend on the MOT parameters, we decided to change the number of atoms in a different way. We controlled the size of the repumper laser as described in 'Atomic Control' sec.(2.2.2). In this way all local parameters at the level of the trapped atoms were kept fixed. However, this alternative method does not exclude the possibility that the average intensity of the trapping and repumping laser can affect the populations in the different hyperfine ground states (dark (N_2) and bright (N_3) states) for different numbers of atoms trapped. In fact, a modification of the optical thickness in the atomic cloud may change the attenuation of the incoming beams and thus the atoms in the bright state. Hence, in the new experiments, the $d = N_2/N_3$ quantity was measured. From this we can easily extract the p-parameters ($p = 1/1 + d$) introduced in the Ketterle model.

With the new protocol scheme, the "1/2" regimes disappeared as we can clearly see from the result shown in Fig. (2.28). In such a situation, where the total intensity of the repumper remains constant, the role played by the repumper laser was investigated, both in detuning and intensity.

The results of this alternative protocol are reported in the following sections, where the evolution of the size, optical thickness and the p are shown as functions of the total number of atoms ($N_{at} = N_2 + N_3$).

All the results are reported in two different sections as before, organized in the following manner:

- Varying "δ_{rep}", where the detuning of the repumper is changed: $\delta_{rep} = \pm\Gamma$ and $\delta_{rep} = \pm 2\Gamma$ are investigated;
- Varying Repumper Intensity, where the repumper intensity is spanned in the range $I_{rep}/2$, $I_{rep}/4$ and $I_{rep}/10$.

Varying repumper detuning ("δ_{rep}")

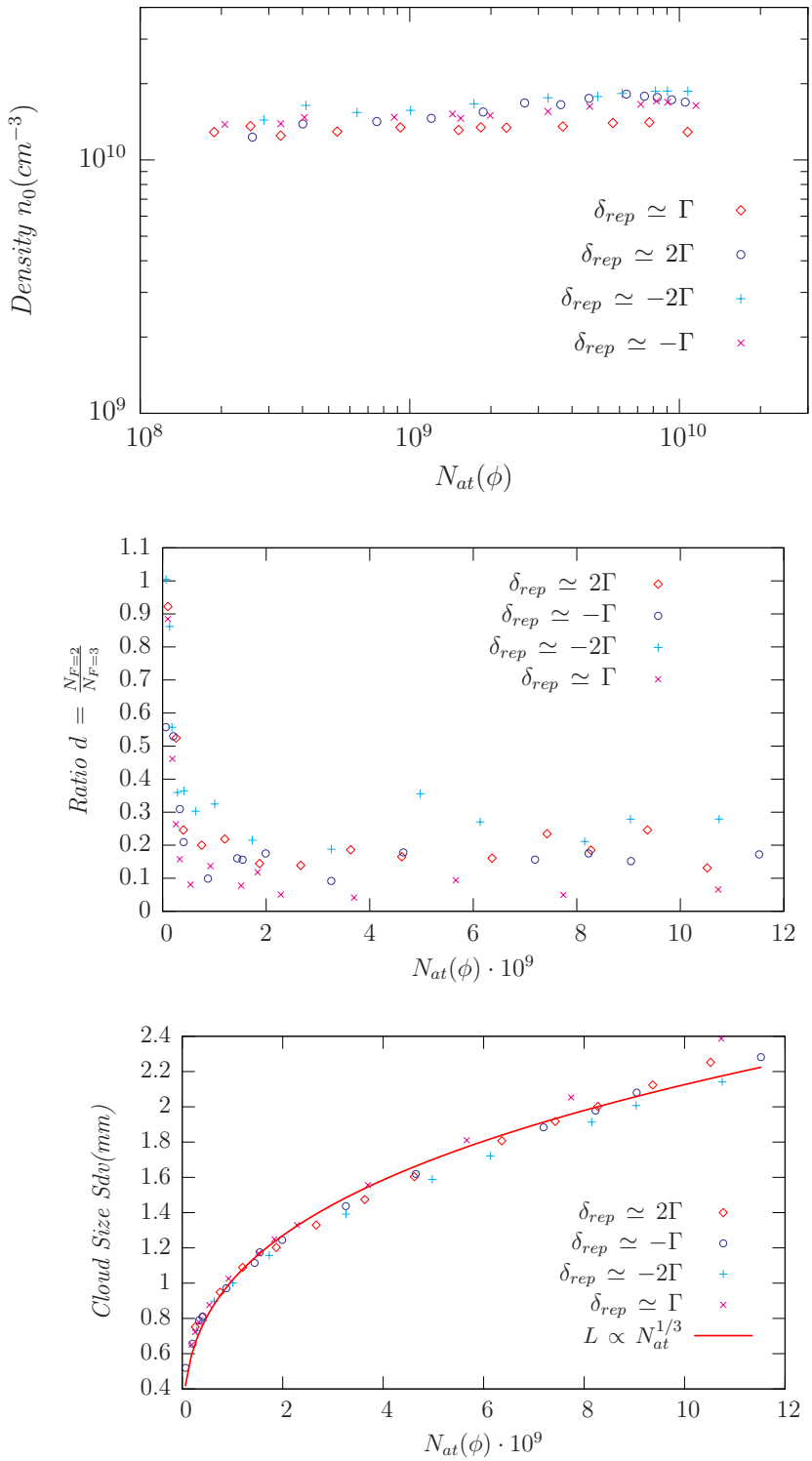

Figure 2.29: *We respectively show the density, ratio $d = N_2/N_3$ and the size of the cloud for different values of the repumper intensity as a function of different detuning (δ_{rep}). We can conclude that the density and the other relevant quantities are, more or less, independent of the detuning.*

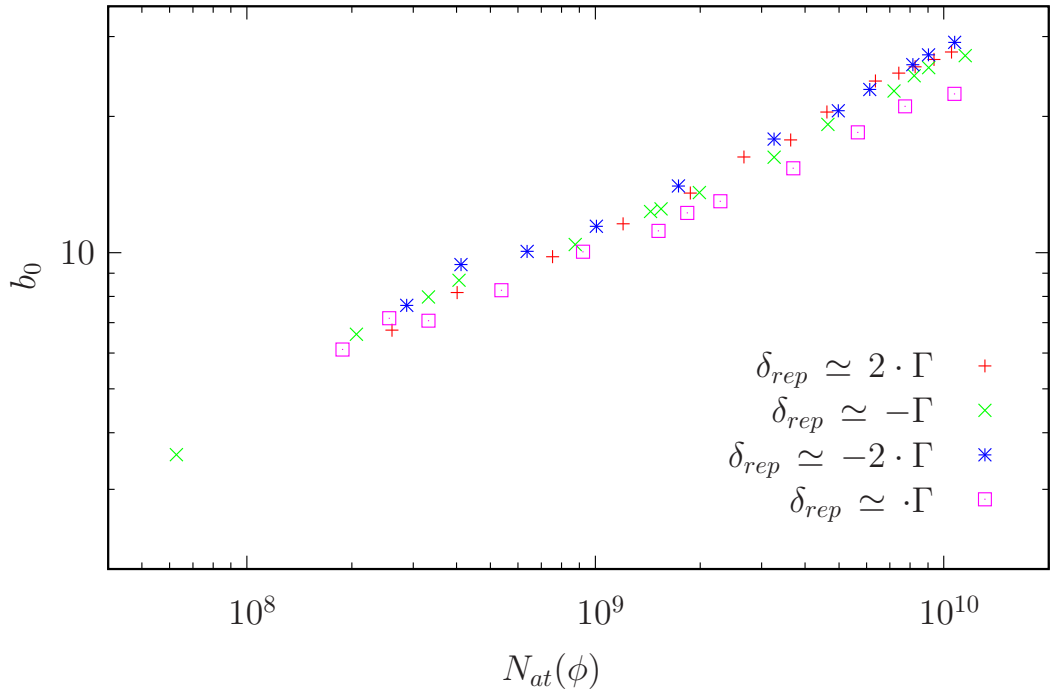

Figure 2.30: *The optical thickness is not affected by the choice of the repumper detuning, and its value is almost independent of the choice of the detuning.*

Varying Repumper Intensity ("I_{rep}")

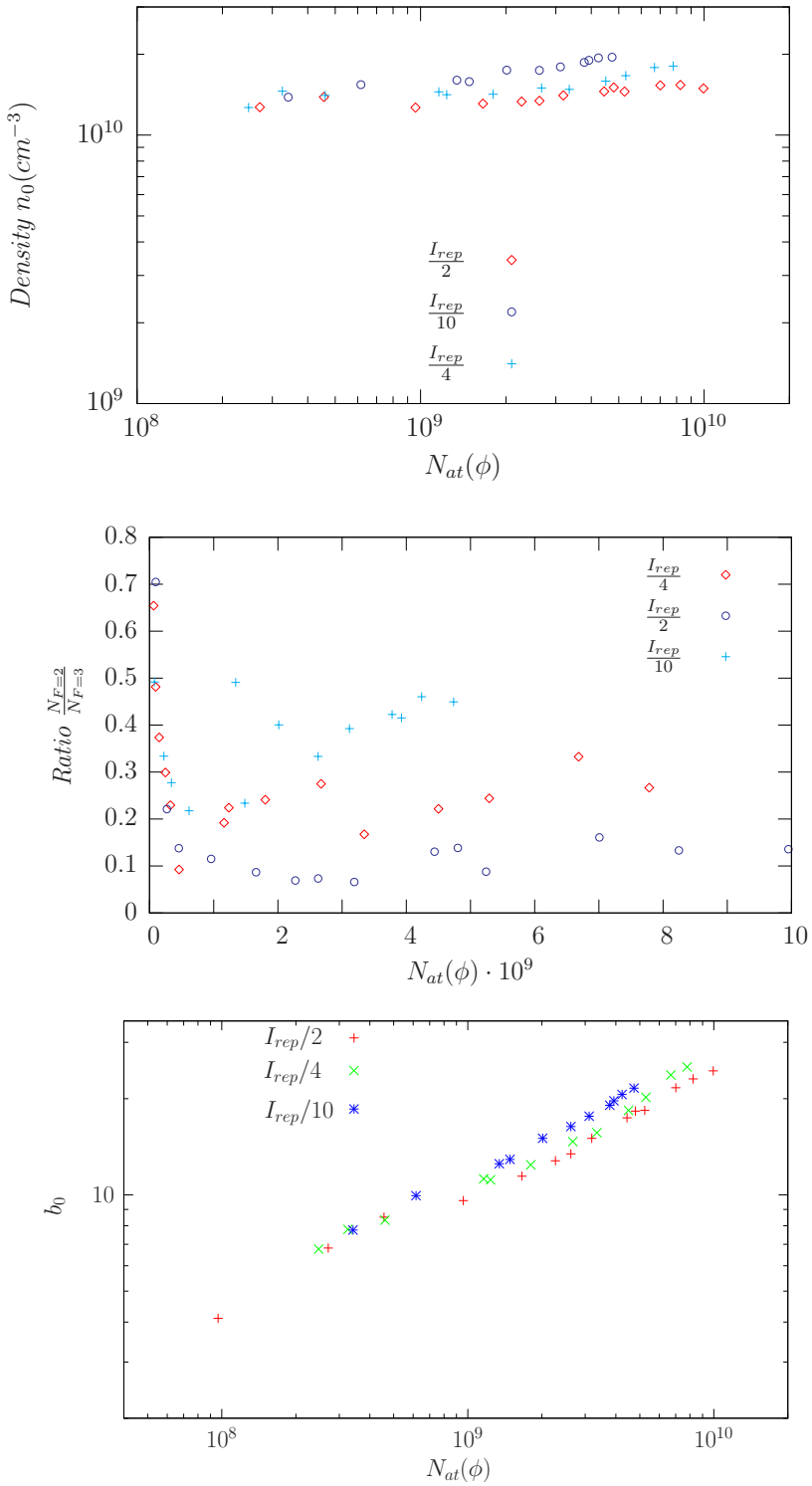

Figure 2.31: *We report the density, the ratio $d = N_2/N_3$ and the optical thickness for different values of repumper intensity.*

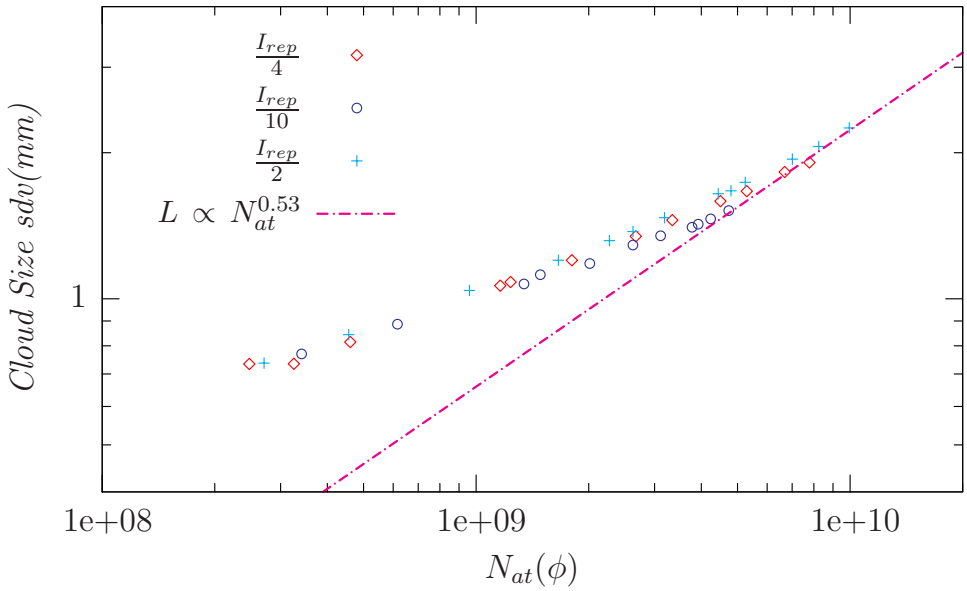

Figure 2.32: *In the graph we show size behavior for different repumper intensity in the range $I_{rep}/2$, $I_{rep}/4$, $I_{rep}/10$. For the three parameters we always saw the Wieman regime. Therefore, the maximum size follows the $\sqrt{N_{at}}$ law, as one would expect for the intensity controlled numbers of atoms. Such a regime is shown in the figure by the dotted-line.*

Conclusions

Fig. (2.31),(2.30) shows that when the detuning is changed within the range $\pm 2\Gamma, \pm \Gamma$, the density is almost independent of the number of atoms, in accordance with the Wieman-Pritchard model. Indeed, we recovered the "1/3" regime over the whole atomic range. We reached the same conclusion for the optical thickness, while the N_2/N_3 ratio is not as one may expect, even though the repumper intensity does not change. In fact, we couldn't understand the sharp increase of the N_2/N_3 ratio (or an equivalent decrease in p) when atoms approached $1 \cdot 10^9$. From a pure Wieman-model, we would expect a density augmentation as p is lowered. But if we look at the density, Fig. (2.31) remains constant.

The density slightly increases as we reduce the repumper intensity. This observation is consistent with those made in the intensity controlled atom number experiments. In fact the p-value is modified due to the changing of repumping cycle efficiency. Indeed, the largest atomic size (L_{max}) moves into the "1/2" regime when we lower the repumper intensity. In Fig. (2.32) the point-dotted line shows the fit of the three L_{max} obtained from three different intensities. The exponent of the power-law is found to be $\alpha_{1/2} = 0.53$ again. We found the same results obtained in the 'intensity controlled atom number' experiments. The only parameter changing when the repumper intensity is changed is the repartition of atomic population, measured by d Fig. (2.31). Plotting the central density as a function of p for the three repumper intensities, Fig. (2.33), we found $1/p$ power-law in accordance with the Wieman-Pritchard model. This means in our MOT we can talk about "Self-Adjusting Dark MOT" (SADM) created by the repumper laser as its intensity is lowered .

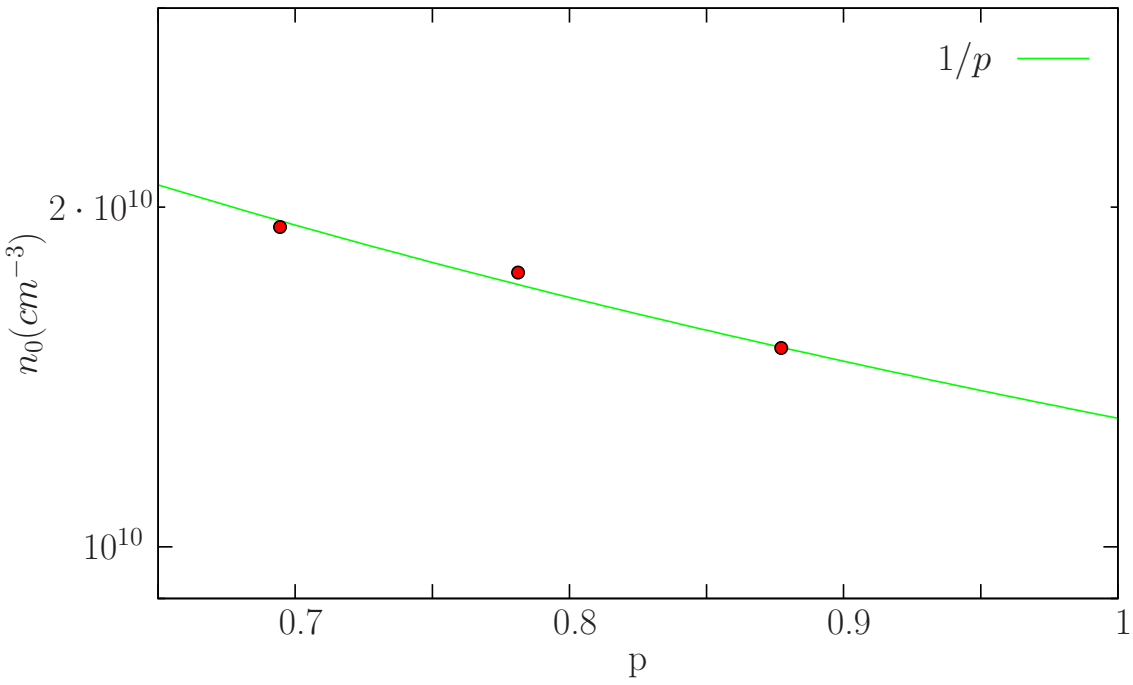

Figure 2.33: *Density as a function of p-parameter. The solid line is a power-law with an exponent of* 1.05*. This is in agreement with the WK-model and can be interpreted as a Self-Adjusted Dark MOT (SADM).*

We can conclude that changing the numbers of atoms in the MOT via the repumper intensity or by controlling its size is not equivalent. In the case of intensity controlled numbers of atoms, we found two regimes: one where the atomic size follows $N_{at}^{1/3}$ above threshold, and the new regime where the size grows in accordance with $N_{at}^{1/2}$. But this is no longer valid in the case of repumper size controlled numbers of atoms. In this latter case, we observed the 1/3 law over the whole atomic range, and we also observed an optical thickness of the rempumper laser as shown in the Fig. (2.34) that yields to a SADM effect.
In the Wieman model, the density limitation is due to the reabsorption of the trapping photons. It therefore seems reasonable to conclude that the repumper photons, also scattered within the clouds, can be reabsorbed and lead to an additional limitation on the total density obtainable in the MOT. This kind of phenomena has to be taken into account as one possible explanation of density decreasing observed in the situation of intensity controlled numbers of atoms. In fact, by decreasing the repumper intensity, we decrease the p-value by adding more and more atoms in the dark state ($F = 2$) arriving in the regime where the repumper starts to be optically-thick (b_{rep}) and can no longer be neglected. In contrast, when the repumper transition is satured the hole completely vanishes, as shown in Fig. (2.34), due to the reduction of the repumper optical thickness.

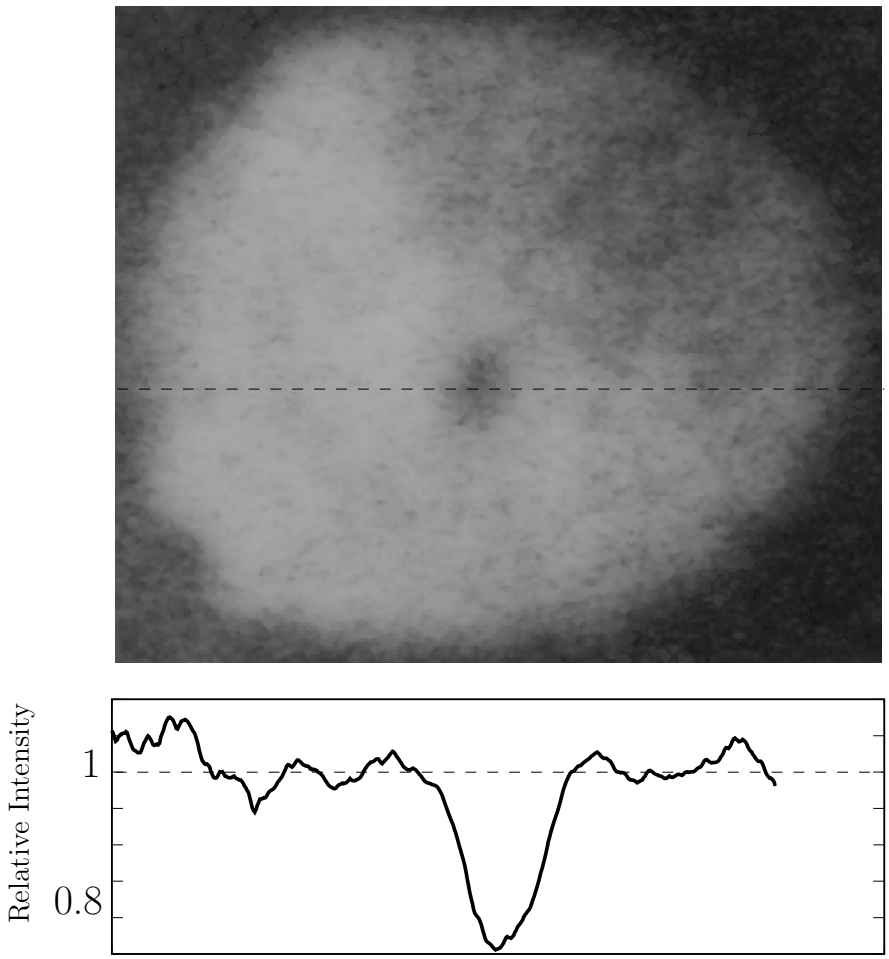

Figure 2.34: *In the Figure we show the transmission of the repumper laser. We can observe a black spot in the middle of the picture. A horizontal plot line passing through the center, showing the relative intensity attenuation on the repumper laser of the atoms in dark-state, is shown above.*

Further investigation is needed, by monitoring the b_{rep} as a function of the number of atoms in the traps, in order to understand the role of repumper induced interaction. In general, the interactions of the repumper in MOT studies are neglected when the description is given.

In the paper attached in sec.(2.4), we will propose one possible generalization of the Wieman-Pritchard model taking into account the additional effective repulsion of the rescattering repumper photons. We do this by adding to the model a new term, G_2, as one more additional repulsion term. In the sec.(2.3.2) we will treat the extreme case where the G_2 is dependent on the repumper laser intensity (I_{rep}), showing the density can drop even for high values of p in contrast with a pure Wieman-Pritchard model, where the density decreases only when the TL-regime is achieved.

2.3.2 Beyond the Wieman-Pritchard model.

In order to introduce the new G_2 parameters, the Wieman-Pritchard model can be modified in the following way:

$$\begin{aligned} F_{WK}^{tr} &= -p \cdot \kappa \cdot r \\ F_{WK}^{MS} &= +n\, G_3\, p^2\, r + n\, G_2\, (1-p)^2\, r \end{aligned} \tag{2.67}$$

where we are neglecting the $p \cdot (1-p)$ interaction.

In the steady-state regime, when the repulsion term completely compensates for the trapping term, the system in the Eq. (2.67) can be easily solved and gives rise to an expression for the upper limit of the density given by the following equation:

$$n_{wk} = \frac{\kappa}{p + \frac{G_2}{G_3} \cdot \frac{(1-p)^2}{p}} \tag{2.68}$$

In the limit of small repumper interaction ($G_2 \ll G_3$) the Eq. (2.68) corresponded to the WK-model.

As soon as G_2 can no longer be neglected with respect to the G_3 term, and approximating $G_2(I_{rep}) = const$, the density decreases as more atoms spend more time in the 'Dark' state.

In the graph shown in Fig. (2.35), we plot the densities given by the model of Eq. (2.68) as a function of p and for different values of the ratio $G_2/G_3 = \alpha$.
Depending on α, we may have a sudden decrease of density even though $p \sim 0.9$, in contrast with the Wieman-Pritchard model.

From the Eq. (2.68) we can also extract the predicted maximum density, which is obtained for a value p_{th}

$$p_{th} = \frac{1}{\sqrt{1 + \frac{G_2}{G_3}}} \,. \tag{2.69}$$

In the repumper intensity controlled atom number, the dependence of p as a function of I_{rep} can be deduced from a simple rate equation:

$$p = p_\infty \frac{I_{rep}}{I_0 + I_{rep}} \tag{2.70}$$

where p_∞ is the p value for the power of an infinity repumper. This result, taking into account the velocity capture of the trap, described in appendix B of the paper, leads to the following dependence for the $N_{at}(I_{rep})$:

$$N = N_{max} \left(\frac{I_{rep}}{I_0 + I_{rep}}\right)^2 \tag{2.71}$$

where N_{max} is the maximum number of atoms trapped.

We equate Eqs. (2.70) (2.71), and we find that $p \propto \sqrt{N/N_{max}}$, which can be used to define a $N_{cr} = N_{max}\,(1 + \frac{G_2}{G_3})$: the critical value on N_{at} at which we have a cross-over

between the MS-regime and the new one. In this way we can obtain an expression for the interaction term $\alpha = G_3/G_2$ given by:

$$\frac{G_3}{G_2} = \frac{N_{max}}{N_{th}} - 1 \ , \tag{2.72}$$

and for standard parameters in our experiment we find $\frac{G_3}{G_2} \sim 0.1$.

From the above consideration one can also understand that as the intensity of the repumper is reduced, the optical thickness of the repumper at resonance $b_{rep}(0)$ increases. Indeed, even in the regime where the optical thickness $b(\delta)$ for the trapping and cooling beams is constant, one has:

$$\frac{b_{rep}(0)}{b(\delta)} = \frac{1-p}{p}(1 + 4(\delta/\Gamma)^2) \ . \tag{2.73}$$

and as we measured a $b(\delta_{MOT}) \sim 1$ and even for 2% of the total population in the 'dark' state, using the Eq. (2.73), the repumper optical-thickness is of the order of 1. This means that the 'repumper induced interaction' has to be taken into account and cannot be neglected .

In the model shown above we have made a rough approximation for the G_2 term. In reality G_2 depends on the repumper intensity ($G_2 = I_{rep}G_2^0$) modifying the interaction parameters of Eq. (2.68) as $\alpha = \frac{I_{rep}G_2^0}{G_3}$.
The expression of α can be very complicated depending on the repumper parameters as well as the MOT and it is difficult to arrive at a general a priori expression .

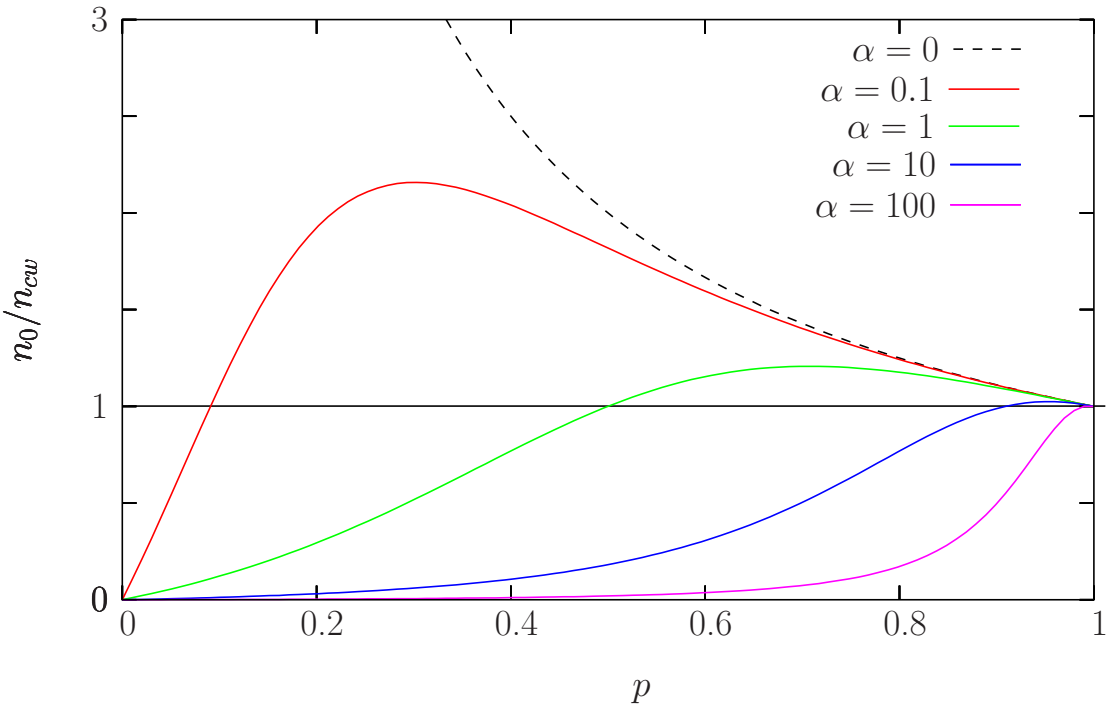

Figure 2.35: *MOT center density n_0, normalized to the density in the Wieman limit n_{cw} as a function of bright state fractions p for different values of $\frac{G_2}{G_3}$-coefficient(α). When α=0 (neglecting repumper induced reaction), we obtain the behavior of the density as predicted by Wieman-Pritchard model.*

2.4 Scaling laws for large magneto-optical traps

EPJ manuscript No.
(will be inserted by the editor)

Scaling laws for large magneto-optical traps

G.L. Gattobigio[1,2], G. Labeyrie[1], T. Pohl[1,3], and R. Kaiser[1]

[1] Institut Non Linéaire de Nice, CNRS and Université de Nice Sophia-Antipolis, 1361 route des Lucioles, 06560 Valbonne, France.

[2] Dipartimento di Fisica dell'Università di Ferrara and INFN-Sezione di Ferrara, 44100 Ferrara, Italy.

[3] ITAMP, 60 Garden Street, Cambridge, MA 02138, USA

Received: date / Revised version: date

Abstract. Multiple scattering of light is known as the main limitation of the maximum atomic density achievable in magneto-optical traps. We present a detailed experimental investigation of the size and density scaling laws for large magneto-optical traps with up to $N = 10^{10}$ atoms. A simple model gives a qualitative account of most of our experimental results. However, several yet unexplained observations lead us to propose a new additional mechanism, based on the repulsion of repumper photons, which limit the atomic density of atoms when the optical thickness for the repumper light becomes important.

PACS. 32.80.Pj – 39.25.+k – 42.50.Vk

1 Introduction

Since the first realization of laser cooling and trapping of dilute atomic vapors, one important goal has always been the realization of a degenerate atomic gas, such as the Bose-Einstein condensate (BEC). Beyond the realization of BEC, large densities of cold atoms are also important for a variety of fundamental studies such as cold collisions and cold molecule formation, cold Rydberg atom experiments, photon localization, local field corrections for the index of refraction and coupled dipole-dipole experiments with cold atoms, with its potential impact for quantum computing.

Achieving high spatial density has, hence, been as important as designing subtle cooling mechanisms [1,2]. Very soon, it has been realized that for a large numbers of atoms rescattering of the trapping light results in an effective repulsion force between the atoms [3,4]. The spatial densities achievable in standard magneto-optical traps (MOTs) has thus been limited to about $n \approx 10^{10} - 10^{11}\mathrm{cm}^{-3}$ and

Send offprint requests to: Robin.Kaiser@inln.cnrs.fr

increasing the number of atoms N in such a MOT results in a MOT size (L) scaling as $L \propto N^{1/3}$, which corresponds to a constant density $n \sim N/L^3$. These density-limiting effects have been studied by many groups [4–11] and several attempts have been made to circumvent this limitation, notably the so-called dark spontaneous force trap (dark SPOT)[12]. A number of systematic studies have investigated the limits of such a dark SPOT, where the fraction p of atoms in the 'bright' hyperfine level (coupled to the cooling and trapping lasers) is an important parameter [12,13]. Different mechanisms have been put forward to explain the observed limitation of the density $n(p)$, such as finite temperature effects, multiple scattering forces and cold collisions. For very large MOTs, the confining force might also become nonlinear (anharmonicity of the trap), which in extreme regimes is at the origin of self-sustained oscillations of the MOT [14].

In our setup we realize a large number of atoms $N \approx 10^{10}$, beyond the typical range used in most previous studies. In this paper we present a systematic study of the sizes and densities in such a large MOT and observe different scaling laws depending on the atom number N and the method used to change that number. In section 2, we describe in detail our experimental setup and detection techniques. In sections 3 and 4 we compare and analyze the experimental data obtained using two different techniques to vary the number of trapped atoms N : either by varying the *diameter* of the repumper laser (section 3) or its *intensity* (section 4). We finally discuss in section 5 results which cannot be explained by the standard models

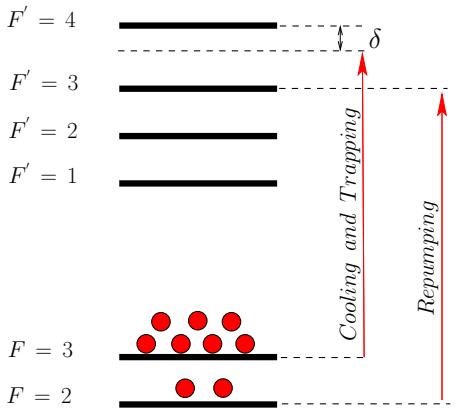

Fig. 1. Relevant atomic hyperfine level of ^{85}Rb. The cooling and trapping laser is detuned by δ from the $F = 3 \rightarrow F' = 4$ transition. The repumper laser is tuned on resonance to the $F = 2 \rightarrow F' = 3$ transition.

used for describing the scaling laws of a MOT and propose to include a new repulsion force, based on the rescattered repumper photons to describe the MOT behavior in new regimes.

2 Experimental setup and detection techniques

We prepare our atomic sample by loading a magneto-optical trap from a dilute vapor of Rubidium atoms. The experimental setup used for the present studies has already been described in [15], and we thus only briefly recall some features of our experimental setup, including calibration techniques.

A magnetic field gradient of typically $10G/cm$ is generated using a pair of coils along the Oz axis. We use a master/slave configuration with subsequent amplification in a tapered amplifier for the MOT beam close to

the $F = 3 \rightarrow F' = 4$ transition of the D2 line of ^{85}Rb (Fig. 1). We routinely obtain 180mW power after spatial filtering, split into 6 beams with a waist of $w = 2.4cm$, directed in pair wise counter propagation into a 10cm sized cubic vacuum chamber. The repumper laser, close to the $F = 2 \rightarrow F' = 3$ transition of the D2 line of ^{85}Rb, is a master/slave configuration as well and is used in a retroreflection geometry along one direction only. The repumper beam diameter is expanded to $\Phi \approx 5cm$ using a telescope. A diaphragm placed at the conjugate position of the MOT allows to vary the repumper diameter, thus modifying the effective capture volume of the MOT without directly affecting its dynamics. Indeed there is no change of external MOT parameters (incident intensities, detunings, magnetic field gradient) when the atom number is changed using the repumper size. Alternatively, we can vary the intensity of the repumper laser (at fixed size), which also allows to change the number of trapped atoms. However, in this case, we expect the overall dynamics of the MOT to be affected. We thus have two methods to change the number of trapped atoms and as we will see, these methods lead to different MOT scaling laws.

The time sequence implemented in this study is a sequence of a MOT period of 30ms followed by a 'dark' period of 5ms. During the dark period, we switch off all beams and the magnetic field, leaving the atoms in free fall expansion for $2ms$ before applying one or more probe beams. The 'dark' period is sufficiently short, such that we do not need to load new atoms to fill up the MOT. This is an important point, allowing a fast duty cycle and efficient data taking. As a probe we use either a single (weak) beam or the 6 beams of the cooling and trapping laser, with an adapted detuning. The single probe beam is used to measure the optical thickness $b(\delta)$ of the cloud, which depends on the detuning δ between the laser frequency ω_L and the atomic resonance frequency ω_{at}. In a different measurement, we use the 6 trap beams to illuminate the whole cloud and take images of the density distribution. A cooled CCD is used to record these fluorescence images. As we are interested in the sizes along all three dimensions of the MOT, we have directed two orthogonal images (labeled I_d and I_g) of the cloud onto the same CCD. From these images we can retrieve spatially-resolved information as well as the total fluorescence. A chopper, closed during the MOT period and opened during the dark period, prevents the strong fluorescence of the MOT from reaching the CCD. In this way, only the fluorescence induced by the off-resonance beams (typically at $\delta = -6\Gamma$) is recorded on the CCD. The use of such a large detuning to illuminate the cloud ensures that multiple scattering, which can modify the intensity distribution in the images, is negligible. Indeed, even the largest on-resonance optical thickness ($b_{res} \approx 40$) obtained in our experiments is reduced to a very small value at the imaging detuning :

$$b(\delta = -6\Gamma) = \frac{b_{res}}{1 + 4(\delta/\Gamma)^2} < 0.3, \qquad (1)$$

where $\Gamma = 2\pi\, 6MHz$ is the inverse lifetime of the excited state. We have verified (see 8.1) that the size extracted via this procedure is independent of the detuning for $|\delta/\Gamma| > 5$. Hence, the CCD images provide us with fluorescence

integrated along one line of sight, e.g. Oz :

$$I(x,y) = \eta \frac{\sigma_{res}}{1+4\delta^2/\Gamma^2} \int n(x,y,z)\, dz, \qquad (2)$$

where η takes into account the detection efficiency of our imaging system, the intensity of the laser beams and the duration of the illumination. The expression of the on-resonance scattering cross-section σ_{res} will be given later.

In order to determine the total number of atoms, we measure the optical thickness of our atomic cloud along Oz by scanning a probe beam across the resonance and looking at the transmission $T(\delta)$ of this probe. This measurement is again done with the MOT switched off. For large enough optical thicknesses $b_{res} \gg 1$, the full width at half-maximum Δ of the transmission curve $T(\delta)$ is connected to b_{res} by:

$$b_{res} \approx ln(2)[1 + (\Delta/\Gamma)^2]. \qquad (3)$$

This technique allows to measure in a reliable fashion large optical thicknesses, which is not possible by measuring directly $T(\delta = 0)$ due to finite signal-to-noise ratio and probe laser spectral width. The measured b_{res} is proportional to the atomic density n integrated along the line of sight:

$$b_{res} = \sigma_{res} \int n(x=0, y=0, z)\, dz. \qquad (4)$$

By comparing the value at the center of the image (2) and (4), we calibrate the detection efficiency of our imaging system. The total number of atoms N, assuming a Gaussian density profile (with rms sizes $\sigma_x\,, \sigma_y\,, \sigma_z$ along each dimension) is:

$$N = (2\pi)^{3/2} \sigma_x\, \sigma_y\, \sigma_z\, n_0 \qquad (5)$$

where n_0 is the peak atomic density. This can also be written:

$$N = \frac{(2\pi)\sigma_x\, \sigma_y\, b_{res}}{\sigma_{res}}. \qquad (6)$$

Thus, combining the data from fluorescence imaging (σ_x, σ_y, see eq. 2) and the optical thickness measurement (b_{res}) we obtain the number of atoms N. This however requires the knowledge of the scattering cross-section:

$$\sigma_{res} = g \frac{3\lambda^2}{2\pi} \qquad (7)$$

where g is the effective coupling strength taking into account the Zeeman structure of the ground state [16]. We assume that the atoms are equally distributed among all the Zeeman sublevels of the ground state, which yields for our $F = 3 \rightarrow F' = 4$ transition $g = \dfrac{2F'+1}{3(2F+1)} = 3/7$. Using the second fluorescence image to obtain σ_z, we then have access to the maximum atomic density:

$$n_0 = \frac{b_{res}}{\sqrt{2\pi}\sigma_{res}\sigma_z}. \qquad (8)$$

As discussed before, we extract from the two orthogonal images the rms sizes $\sigma_x, \sigma_y, \sigma_z$ of the atomic cloud along the 3 spatial dimensions We have verified that the size along each direction obeys the same scaling laws. Thus, in the following, we will simplify the discussion by considering only an averaged size L , defined as:

$$L = \frac{1}{3}(\sigma_x + \sigma_y + \sigma_z). \qquad (9)$$

It is also possible to monitor the fluorescence by collecting the scattered light on a photodetector. This yields a strong signal during the long (30ms) MOT sequence,

with a complicated relation between scattered light and total number of atoms. However, during the short probe time, used to analyze our cold atomic sample when the MOT is switched off, a large detuning of the laser beams eliminates multiple scattering so that the fluorescence is then directly proportional to the atom number. The repumper laser can be switched off at the same time as the main MOT lasers or with a small positive or negative delay (see Appendix 8.2), which influences the hyperfine populations during probing. As we will see below, this allows us to discriminate between the total number of atoms (sum of both hyperfine populations) and the number of atoms in the bright hyperfine level. When not otherwise mentioned, we switched off the repumper after the MOT laser and thus measured the total number of atoms during the short probe pulse.

After this detailed description of our experimental setup and protocol, we will now describe first qualitative observations followed by detailed studies of our MOT.

3 Repumper Size controlled atom number: $N(\Phi)$

3.1 Wieman model and non linear effects

In the past, one of our major objectives has been to optimize the optical thickness of our cloud. Hence, it seems reasonable to trap as many atoms as possible. It is also known, since the pioneering work of [3], that when more than 10^5 atoms are trapped the MOT size becomes determined by an interplay between the confining forces of the MOT beams and repulsive forces induced by multiple scattering of light. In the limit of moderate optical thickness (at the frequency used for trapping and cooling), the model put forward in [3] predicts a uniform density n in this regime. Denoting N the total number of atoms and L (eq. 9) the size of the MOT, the uniform density regime implies that the trap size L scales as:

$$L(N) \propto N^{1/3}. \tag{10}$$

In the following we will call this the 'Wieman model'.

The density limitation predicted by the Wieman model [3] can be understood in simple terms as a competition between a confining force $F_{\rm tr}$ and an effective repulsion force $F_{\rm ms}$ due to multiple scattering. These forces can be generally written as:

$$F_{\rm tr} = -\kappa r \tag{11}$$

$$F_{\rm ms} = G_3 n(r)\, r\ , \tag{12}$$

where κ is the spring constant of the trap and G_3 accounts for the competition between the shadow effect [17] and the repulsion due to the reabsorption of the MOT photons. A stationary density $n(r)$, requires a vanishing total force at any distance r, which yields a constant density of

$$n(r) = n_{\rm W} = \frac{\kappa}{G_3}\ , \tag{13}$$

and leads to the $L(N) \propto N^{1/3}$ scaling law found in [3].

The model proposed in [3] was verified up to a certain number of trapped atoms $N \approx 5 \times 10^7$, above which a deviation was reported by the authors. They invoked higher order multiple scattering and trap nonlinearities as possible candidates to explain this behavior. Our goal has thus

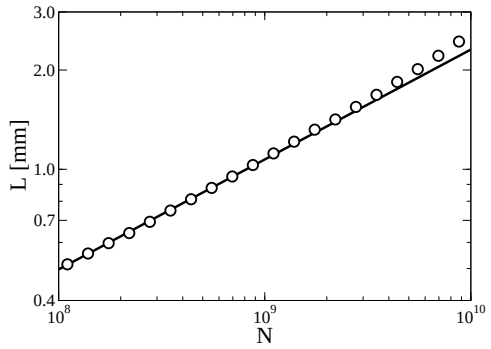

Fig. 2. Calculated MOT size vs atom number (circles) compared to the $N \sim L^{1/3}$ power-law (solid line). The MOT parameters are those of table 1.

been to check the prediction of the Wieman model in the limit of very large number of atoms $N > 10^8$.

In order to work out the influence of magnetic field gradients and nonlinearities in the MOT forces we have developed a numerical treatment including such effects [18, 19]. In spirit, our model is similar to the Wieman model, i.e. we seek a self-consistent solution of the force balance equation

$$\mathbf{F}_{\rm tr}(\rho, \mathbf{r}) + \mathbf{F}_{\rm ms}(\rho, \mathbf{r}) = 0 \qquad (14)$$

for the atomic density ρ, where $\mathbf{F}_{\rm tr}$ and $\mathbf{F}_{\rm ms}$ denote, respectively, the external trapping force and the interaction-induced force. As in the Wieman model, we perform a three dimensional calculation but simplify the considerations by assuming a spherically symmetric intensity pattern and restrict ourselves to Doppler cooling and trapping mechanisms.

Due to attenuation of light inside the atomic cloud the intensities vary with position, such that the trapping force $\mathbf{F}_{\rm tr}$ carries an implicit dependence on the density profile $\rho(r)$.

The Wieman model assumes a homogeneous (spatially independent), i.e. Coulomb-like, interaction between the atoms. As mentioned above, this model predicts a constant density profile, with radius $L \propto N^{1/3}$. To obtain this simple solution, additional simplifications, such as a linear expansion of the external trapping force and a linear laser attenuation, are necessary. While these assumptions are well justified for small MOT sizes, they become questionable for large MOTs, as produced in our experiments. In general, the laser intensities and the absorption/reabsorption cross sections depend on position and on the entire density profile due to the inhomogeneous Zeeman shift and the attenuation of laser light, respectively. We expect both of these effects as well as nonlinearities of the MOT potential to become increasingly important for large atom clouds.

Due to the nonlinear and non local character of the full set of equations, finding direct numerical solution for the atomic density is very demanding. Instead we use an efficient test-particle method, which yields fast convergence to the physically relevant density profile and avoids difficulties with unstable solutions. As discussed in [18], this method also permits studies of the dynamical MOT behavior as described by the corresponding time-dependent kinetic equation for the atomic cloud.

While our numerical results for the size scaling apparently coincide with the prediction of the more simple Wieman model (see Fig. 2), the obtained density profiles, shown in Fig. 3, reveal dramatic differences. In contrast to the Wieman model, which predicts a constant density pro-

MOT Parameters	
Detuning	$\delta_{MOT} = -2.5\Gamma$
Intensity per beam	$I_{MOT} \approx 1.2 mW/cm^2$
Beam waist	$w_{MOT} \approx 2.4 cm$
Repumper Parameters	
Detuning	$\delta_{rep} = 0$
Intensity per beam	$I_{rep} \approx 0.5 mW/cm^2$
Beam diameter (FWHM)	$L_{rep} \approx 5 cm$
Magnetic Field Gradient	
$\nabla B = 10 G/cm$	

Table 1. Standard parameters as used in this paper for the MOT, Repumper and Magnetic field gradient.

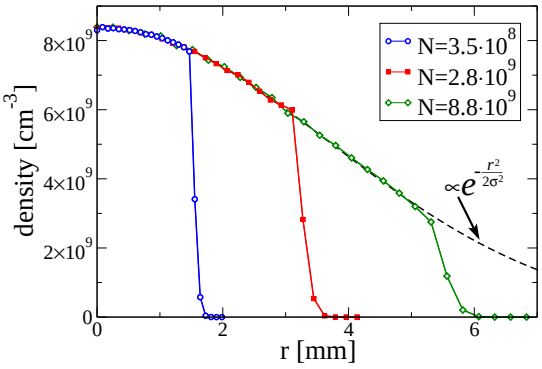

Fig. 3. Calculated density profiles (color online) for three different atom numbers as indicated in the figure. The dashed line shows that the densities follow truncated Gaussian distribution, with σ = 3.5mm. The MOT parameters are those of table 1.

file, our simulations yield a series of truncated Gaussian densities with changing atom number. While the width of the Gaussian density remains constant the cut-off radius increases with increasing atom number which results in the observed size scaling.

Fig. 2 and Fig. 3 exemplify the results of our calculations for the parameters of table 1. As shown in Fig. 2 the calculated atom number dependence of the MOT size reveals the observed power-law $N \sim L^{1/3}$, in accord with the Wieman model prediction (see eq.(13)). At large N we find slight deviations from the power-law behavior, heralding the onset of self-sustained oscillations at $N \sim 10^{10}$, above which the stationary solution disappears due to the onset of a dynamical instability [14,18,19]. A precise comparison with the experimental profiles is somehow difficult. Indeed, one needs to take into account the three dimensional character of the experiment and thus e.g. use an Abel protocol [20] to extract a more reliable radial density profile. The experimental profile often have sharper edges then a pure Gaussian but more systematic data analysis would be required in order to compare the experiment to the results shown in Fig. 3. Despite these finer details the Wieman model apparently yields a surprisingly good description of the size scaling even at large atom numbers.

3.2 Experimental results on $N(\Phi_{rep})$

3.2.1 Atom Number vs Repumper size : $N(\Phi_{rep})$

The number of trapped atoms loaded from background vapor is known to dramatically increase with size (Φ) of the MOT beams [6]. Indeed, the capture velocity (v_{capt}) of the MOT and the capture volume (V_{trap}) influence the number N of atoms as:

$$N \propto v_{capt}^4 V_{trap}^{2/3} . \quad (15)$$

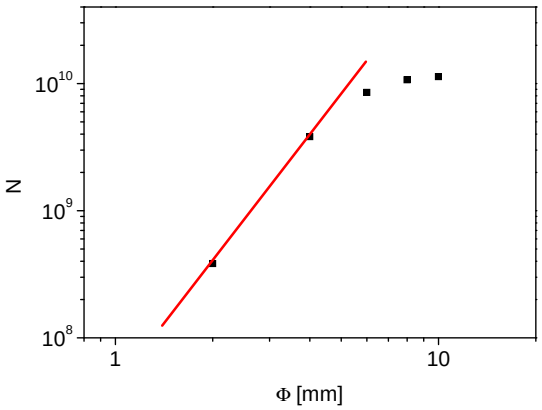

Fig. 4. Number of trapped atoms as a function of diameter of the repumper laser. The solid line (red online) give a power law fit $N \propto \Phi^{\nu}$ with an exponent $\nu = 3.3$

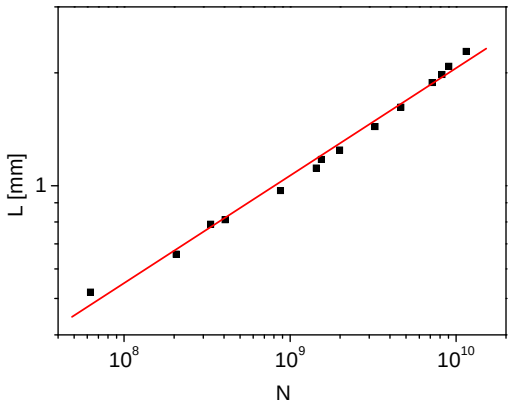

Fig. 5. MOT size vs number of trapped atoms. The atom number is changed using the diameter of the repumper laser. The solid line (red online) shows that a single power law (exponent 0.29) fits the entire range of data.

The capture volume (V_{trap}) and the capture velocity (v_{capt}) depend on the size of the trapping and cooling lasers as well as on the size of the repumper laser. Changing the size Φ of any laser beam (cooling or repumper) is thus a very efficient way to control the number of atoms. In particular one has $v_{capt} \propto \sqrt{\Phi}$ and $V_{trap} \propto \Phi^3$ which, using the eq.(15), yields $N \propto \Phi^4$.

We thus choose to control the number of atoms by changing the size of the repumping laser. As mentioned above, this allows to change the number of atoms in the MOT while leaving the parameters of the incident lasers beams, at the location of the MOT, unaffected. Fig. 4 shows how the number of trapped atoms changes as we increase the size of the repumping laser beam (at standard MOT parameters). A slope of $N \propto \Phi^{3.3}$ is indicated in the solid line, close to the result obtained in [8].

3.2.2 MOT scaling law with $N(\Phi_{rep})$

Having validated our method to change the atom number via the size of the repumper laser, we used this procedure to study the scaling law of the MOT size. Obviously, a systematic scan of all MOT parameters is far too complex, as there are too many parameters which have an impact on e.g. the MOT size and density. Thus we choose to define a 'standard' set of parameters and investigate the MOT as we change one of the parameters, keeping the others fixed at the standard values as given in the table 1. As shown in Fig. 5, we do observe a single scaling law up to $N = 10^{10}$. A power law fit yields an exponent of $\alpha = 0.3$ scaling law close to $L(N) \propto N^{1/3}$. This is in agreement with the standard Wieman model, but in contrast to the results observed previously in [4], where a strong deviation from $L(N) \propto N^{1/3}$ has been reported for an atom number larger than $N \approx 5 \times 10^7$. As we will show in the

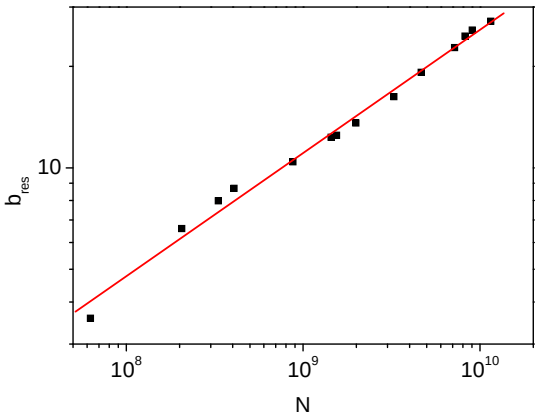

Fig. 6. Optical thickness of the MOT vs number of trapped atoms. The atoms number is changed using the diameter of the repumper laser. The solid line (red online) shows a power law fit with an exponent of 0.37 .

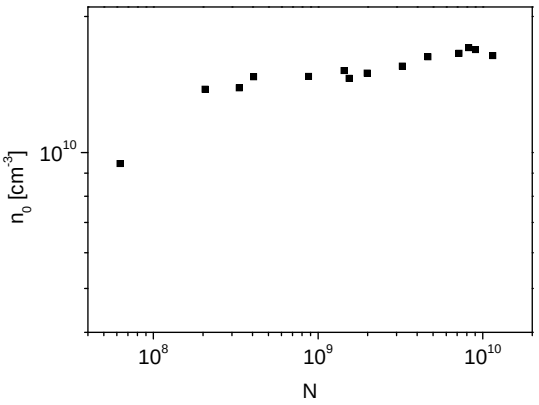

Fig. 7. MOT peak density n_0 vs number of trapped atoms. The atoms number is changed using the diameter of the repumper laser.

next section, this discrepancy has motivated us to perform further experimental studies with different protocols. But before turning to these different investigations, we want to point out that it is also possible to exploit the same experimental data to illustrate more efficiently the scaling law of the MOT. We obtain not only the size of the cloud, but also the resonant optical thickness b_{res} of the MOT (Fig. 6) and the behavior of the central density n_0 (Fig. 7) versus the number of atoms N. As described in section 2, the optical thickness b_{res} is extracted by using the signal at the center of the fluorescence image, which is proportional to the integral of the atom along the line of sight, rescaled to the resonance $\delta = 0$. The peak density (n_0) extracted from the same data, assuming a Gaussian density profile, clearly indicates that we have a constant density of atoms up to $N = 10^{10}$.

The first conclusion of this study is that the Wieman model seems to apply even in our regime of a large MOT (containing up to 10^{10} atoms) which contradicts the earlier observation of [4]. We stress however that our conclusion is reached on the basis of the careful experimental procedure detailed in section 2, which differs from that used in previous studies.

4 Repumper intensity controlled atom number: $N(I_{rep})$

Intrigued by the discrepancy mentioned above between the scaling we have obtained in the previous section and that observed by [4], we have investigated the role of the protocol used to modify the number of trapped atoms. Indeed, the number of atoms in a MOT depends on many control parameters as indicated in table 1. In order to extend our studies of the MOT scaling laws, we have chosen another protocol to vary the number of trapped atoms in

the experiment. The most convenient alternative method in our setup has been to modify the intensity of the repumping laser ($I_{\rm rep}$). In practice we change the power of the repumper laser, but as we keep the beam size constant in this run, this amounts to changing the repumper intensity. We note that in contrast to the previous method, using this protocol we also modify an external control parameter at the location of the MOT. As we will see, this will have an important impact on the scaling law of the MOT.

4.1 Experimental results on $N(I_{rep})$

4.1.1 Atom Number vs Repumper intensity : $N(I_{\rm rep})$

Let us first discuss how the atom number is affected as we change the intensity of the repumper laser. Fig. 8 illustrates how the number of atoms increases with the intensity of the repumper. A previous model [5] predicts the number of atoms growing as $N \propto v_{capt}^4$, where v_{capt} is the capture velocity of the trap. The precise value of the capture velocity depends on the parameters of the trapping and repumper lasers as well as on the magnetic field gradient. Within a simplified picture one can estimate the capture velocity from the laser-deceleration a and stopping distance of an atom, which needs to be smaller than the size of the laser beams L_{laser}, according to

$$v_{\rm capt} \approx \sqrt{2apL_{laser}} \, . \tag{16}$$

Here we added a factor p as the trapping force is only effective for atoms in the bright state ($F = 3$) and the effective deceleration is roughly proportional to the bright-state population p. To determine its dependence on the repumper intensity $I_{\rm rep}$ we use simple rate equations and obtain

$$p = p_\infty \frac{I_{\rm rep}}{I_p + I_{\rm rep}} \, , \tag{17}$$

where p_∞ denotes the bright state population in the high intensity limit. Eq.(17) yields an approximate description for the population of trapped atoms, since both MOT and repumper laser parameters varies in space due absorption inside the high density atom cloud. Combining Eqs. (15)-(17) the number of trapped atoms is thus expected to scale as :

$$N = N_\infty \left(\frac{I_{\rm rep}}{I_N + I_{\rm rep}} \right)^2 \, , \tag{18}$$

where N_∞ denotes the maximally trapped number of atoms. Even though this model seems very convincing, one should allow in principle that the parameters I_p and I_N could be different, as the hyperfine populations inside the MOT are not necessarily the same as in the loading region for the trap.

With these considerations the atom number dependence of the repumper intensity and the bright state population directly follows from eqs.(17) and (18)

$$I_{\rm rep} = I_{\rm N} \frac{N^{1/2}}{N_\infty^{1/2} - N^{1/2}} \, , \tag{19}$$

$$p = p_\infty \frac{N^{1/2}}{\beta N_\infty^{1/2} + (1-\beta) N^{1/2}} \, , \tag{20}$$

where $\beta = I_p / I_N$. As demonstrated in Fig.8, the derived atom number dependence on $I_{\rm rep}$ yields a good description of our experiment, with $N_\infty = 8.9\,10^9$ and $I_N = 0.05{\rm mW/cm}^2$. Note that the precise value for these fitting parameters depends on various experimental conditions,

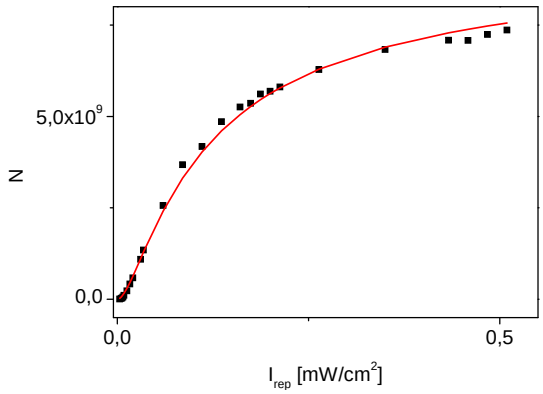

Fig. 8. Experimental result for atom number as a function of repumper intensity. All other parameters correspond to the standard parameters, as defined in the text.

(such as power of the trapping and cooling laser) and can be different for the various experiments performed to extract the data shown in this paper. The loading efficiency, and consequently the number of trapped atoms, is determined by the population dynamics in a large volume around the trap, were we expect a good description by the above model. However, the measured bright state population p mainly contains contributions from atoms confined in the MOT region, where level populations can be strongly altered by absorption of MOT and repumper lasers and by spontaneous Raman photons.

4.1.2 MOT Scaling law with $N(I_{rep})$

Having understood the dependence of the atom number on the repumper intensity, we can now study the scaling law of the MOT size $L(N)$, with $N(I_{rep})$ controlled via the repumping intensity. The resulting curve is shown in Fig. 9. Here again the repumper has been switched off after the MOT laser so that all atoms are pumped into the $F = 3$ hyperfine level before probing with a detuned laser (see Appendix8.1). One can clearly identify two regimes, separated by a threshold $N_{th} \approx 1.5 \times 10^9$. For $N < N_{th}$ we observe a scaling law close to that predicted by the Wieman model, while for $N > N_{th}$ the scaling law is nearly $L(N) \propto N^{1/2}$ which is also reminiscent of what has been observed previously [4]. However, these similarities are coincidental. First, the procedures to vary N are different : in [4] N is tuned by acting on the loading of the trap without modifying the MOT control parameters, while in this part of our study we do vary one of the control parameters, namely the repumper intensity. Thus, it is the results obtained with our first procedure in the previous section 3.2.2 which should be compared to those of [4], and there we observe a single $N^{1/3}$ scaling law. Second, the measurement procedures are also different : our careful imaging procedure assures that we measure the actual atomic density profile, while the faster procedure of [4] (imaging of the MOT fluorescence) does not offer this guarantee. A better understanding of the MOT behavior might be obtained when looking differently at the same data, by extracting as in section 3.2.2 the on-resonance optical thickness b_{res} (Fig. 10) and the peak density n_0 (Fig. 11). These different ways of illustrating our experimental results reveal different phenomena. Fig. 10, for instance, clearly shows that for $N > N_{\rm th}$ the optical thickness b_{res} becomes roughly constant, which seems consistent with a scaling law of $L(N) \propto \sqrt{N}$. We also see that below the threshold value, the peak density of our cloud is not constant (Fig. 11), in contrast to what one might

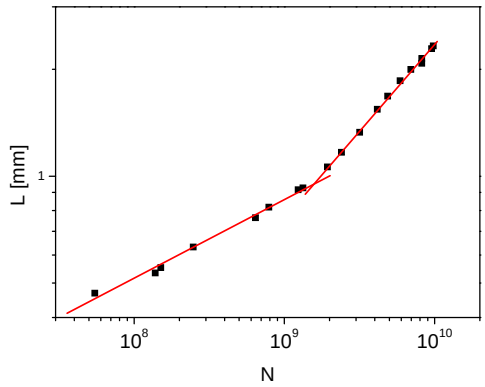

Fig. 9. MOT size vs number of trapped atoms. The atoms number is changed via the intensity of the repumper laser. The solid lines (red online) indicate the results of a fit, illustrating the different power laws below and above the threshold value ($N_{th} \approx 1.5 \times 10^9$).

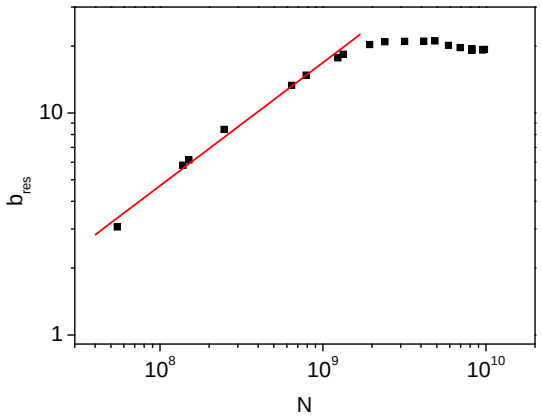

Fig. 10. Optical thickness of the MOT vs number of trapped atoms. The atoms number is changed via the intensity of the repumper laser. The solid line (red online) give a power law with an exponent of 0.55 in the low atom number regime.

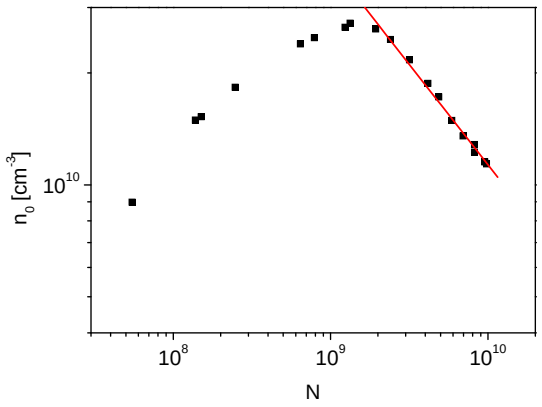

Fig. 11. MOT peak density n_0 vs number of trapped atoms. The atoms number is changed via the intensity of the repumper laser. The solid line (red online) is a power law fit corresponding to $n_0 \propto N^{-0.54}$.

expect from the Wieman model. In this regime, $L(N)$ thus behaves differently from the scaling law $L(N) \propto N^{1/3}$. In the density plot, this difference shows up more pronounced than in the size plot.

In order to quantify these two regimes, we have performed a systematic study of the scaling laws above and below the threshold value, extracting the power law exponent $\alpha_{1/3}$ below the threshold and the exponent $\alpha_{1/2}$ above the threshold. The value of atom number $N_{\rm th}$ at the threshold, and the size at threshold $L_{\rm th}$ are also given. All these results are summarized in table 2. The size scaling law for atom numbers below the threshold is different from the Wieman prediction ($\alpha_{1/3} = 1/3$) and has an exponent closer to ≈ 0.22. For the scaling law above the threshold, we find values close to $\alpha_{1/2} = 0.5$. As we will see below, we do not have a complete explanation for the observed scaling law in all regimes. The data shown in this table might become useful once such a complete model will have been developed.

One can note that the scaling law in the regime above the threshold value seems to be consistent with the observation of [6] and with the conjecture $b(\delta) \approx 1$, arguing that the MOT will self-adjust to this value, beyond which

multiple scattering becomes important [6]. As we will see in section 4.2, we derive this $\sqrt{N}$ scaling law from completely different physical arguments, which are based on the details of the trap loading as the repumping intensity is changed, and on the repartition of atoms among both hyperfine ground states. Also, as we have seen in section 3.2.2, when the atom number is controlled using a different method, this $\sqrt{N}$ scaling disappears, showing that the $\sqrt{N}$ law is not a general feature for large traps.

In summary, the experimental results described in this section show that:

i) we observe a scaling law $L(N) \propto \sqrt{N}$ above a threshold value $N_{\rm th}$, when the atom number is changed via the intensity of the repumper;

ii) below this threshold value, the density is not constant, in contrast to the Wieman model.

The different behavior observed with the two different methods used to control the number of atoms, indicates the importance of the repumper laser. A model trying to explain the scaling law of the MOT size in these regimes thus requires to go beyond a two level model for the atoms, including for instance the internal degrees of freedom of the atoms.

4.2 Wieman-Pritchard model

The aforementioned Wieman model is based on a two level model for the atom and, hence, neglects any effect of the repumper laser, which we expect to be important in the present case. Such multi-level effects have been previously considered, to reduce MOT laser re-scattering and optimize atomic densities. Based on this concepts Ketterle et al. [12] have introduced the so-called dark SPOT. In such a trap, only atoms in the upper ('bright') hyperfine level are interacting with the cooling and trapping lasers thereby reducing the light-induced atom-atom interactions. According to the model of [12] the balance between trapping, eq.(11), and repulsion forces, eq.(12) can be rewritten as:

$$F_{\rm tr} = -\kappa\, p\, r \tag{21}$$

$$F_{\rm ms} = G_3 p^2 n\, r\ . \tag{22}$$

Here $p = N_3/(N_3 + N_2)$ is the fraction of atoms in the bright hyperfine level. As only this part of the atoms interacts with the cooling and trapping lasers, the trapping

δ_{MOT} [Γ]	I_{MOT} [mW/cm^2]	∇B [G/cm]	$\alpha_{1/3}$	$\alpha_{1/2}$	N_{th}	N_{max}	L_{th} [mm]
−2.5	7	10	0.22	0.49	1.6 10^9	9.8 10^9	0.96
−2	7	10	0.21	0.48	1.0 10^9	7.4 10^9	0.87
−3	7	10	0.24	0.45	1.6 10^9	9.0 10^9	1.01
−2.5	**3.5**	10	0.21	0.45	0.6 10^9	3.8 10^9	0.86
−2.5	**1.75**	10	0.23	0.41	0.16 10^9	0.38 10^9	1.15
−2.5	7	**16**	0.25	0.44	0.9 10^9	7.1 10^9	0.81
−2.5	7	**5**	0.20	0.43	0.47 10^9	1.9 10^9	0.96

Table 2. Systematic study of scaling law exponents and threshold value. We denote $\alpha_{1/3}$ the exponent below and $\alpha_{1/2}$ the one above the threshold $N_{\rm th}$. The values indicated in this table have been extracted from a power law fit. The standard parameters are given in the first line. The parameters, that are changed are indicated in boldface. The repumper detuning is $\delta_{rep} = 0$ for all these experiments and the number of atoms has been changed via the intensity of the repumper.

force has to be multiplied by p. The repulsive interaction between atoms requires a pair of atoms in the bright state and one thus has to include a factor p^2 in $F_{\rm ms}$. Consequently, the stationary atom density resulting from eqs.(21) and (22) has an additional p-dependence according to:

$$n_{WP} = \frac{\kappa}{p\,G_3} = \frac{n_W}{p}\ . \tag{23}$$

As this model is an extension of the one discussed in section 3.1, we call this the Wieman-Pritchard model.

In our experiments when we control the number of atoms by changing the intensity of the repumping laser, we clearly expect that the fraction p of atoms in the bright state is altered. Even though we do not use a dark region in our MOT, one can apply the Wieman-Pritchard model and investigate which scaling law would be predicted with the simplest ingredients. In Fig. 12 we plot the density at the MOT center vs the parameter p, obtained by detecting either only atoms in the $F = 3$ state (N_3) or all atoms ($N_2 + N_3$). The solid line is a power law fit and gives an exponent of -1.05, in agreement with the $1/p$ prediction of the Wieman-Pritchard model.

The Wieman-Pritchard model thus appears to explain our experimental results for large MOTs as the $L(N) \propto \sqrt{N}$ scaling law can be derived from this model. Indeed, as discussed in 4.1.1, one expects both the atom number N and p to decrease as the intensity of the repumper is reduced. The bright state fraction p approaches a constant value p_∞ for large atom numbers but varies $\propto \sqrt{N}$ as the number of atoms is reduced (see eq. 20). Within the Wieman-Pritchard model, such a scaling law for $p \propto \sqrt{N}$ predicts a density $n_{\rm WP} \propto N^{-1/2}$ and thus a MOT size which scales as $L \propto N^{1/2}$. The Wieman-Pritchard model can thus explain our experimental observation in the large atom number regime. In contrast to [6], where the $L(N) \propto \sqrt{N}$ scaling law has been reported and attributed to higher-order MOT photon rescattering, the $L(N) \propto \sqrt{N}$ scaling law presented in this paper can be explained without invoking higher scattering order, and depends on the method employed to change the number of atoms. Also we recall that this power-law disappears when the atom number is changed by varying the size of the repumping laser, keeping all other parameters constant (see in Fig. 5), and this up to very large atom numbers ($N \approx 10^{10}$). However we observe a clear deviation from this scaling law for an atom number below $N \approx 10^9$ and we will argue in the next section that the missing key point is the interaction force resulting from rescattering of repumper photons.

5 Beyond the standard models for MOT scaling laws

Despite the good agreement between the Wieman model and our experimental results of section 3 on one side, the Wieman-Pritchard model and our results of section 4 for the large atom limit on the other side, there are a some results which can not be explained by the standard models used up to now for the MOT description. Indeed, one can see in Fig. 9, that for an atom number below $N = 10^9$, the density of atoms in the trap is neither constant (as

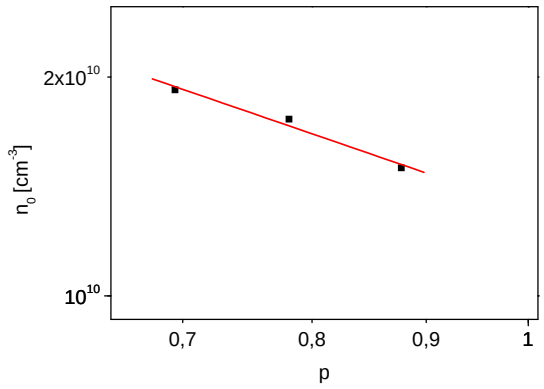

Fig. 12. MOT peak density n_0 vs p. The solid line (red online) is a power law fit gives an exponent of -1.05, in agreement with the $1/p$ prediction of the Wieman-Pritchard model. The experimental data points correspond to the largest atom number obtained for $I_{rep} = I_{rep}^{max}/2$, $I_{rep}^{max}/4$, and $I_{rep}^{max}/10$ (corresponding to total atom number $N = 9.9\,10^9$, $7.8\,10^9$, $4.7\,10^9$ and sizes $L = 2.1mm$, $1.8mm$, $1.5mm$ resp.)

predicted by a simple Wieman model) nor following the law deduced from the Wieman-Pritchard model (with $L \propto \sqrt{N}$). We thus speculate that a new physical effect has to be added to explain the MOT behavior in this regime.

5.1 Optical thickness of repumper

A further observation shows another important aspect to be considered. As described in the section 2, we use a repumper only along one axis (which is not along any axis of the MOT laser). It is thus possible to record the transmission of the repumping laser (even though without retroreflection for this measurement). A screen placed on the repumper after it has passed the MOT allowed us to observe that the intensity of the repumper is considerably reduced by the MOT. This is a direct proof that the optical thickness for the repumper light is not small! Fig. 13 shows an image of the repumper beam transmitted through the MOT. The dark region in the center indicates that many photons of the repumper are scattered by the atoms of the MOT.

This qualitative observation has an important impact on the model we will use to describe the scaling law of the MOT size. In that case, scattered repumping photons can be reabsorbed in the MOT which will yield a repulsive force, in the same way as the rescattered photons of the trapping light produces a repulsive force. Furthermore, the repulsive forces arising from rescattered repumping photons are not balanced by any trapping or cooling force. In general one has to analyze the subtle compensation between the repulsive forces due to rescattering and a shadow effect (resulting in a net compression along the axes of the laser) in order to know whether absorption and rescattering results in compression or repulsion. In our configuration, where the repumping laser is only present along one axis, the situation is somewhat different as there is no compression along the directions transverse to the repumper propagation axis.

We note that when we control the atom number via the size of the repumper laser, we can not exclude the possibility that the average intensity of the trapping and/or repumping lasers are affected when the number of atoms is changed. Indeed, a modification in the optical thickness of the cloud may change the attenuation of the different incident laser beams as well as the importance of spontaneous Raman photons (resulting in a change of the

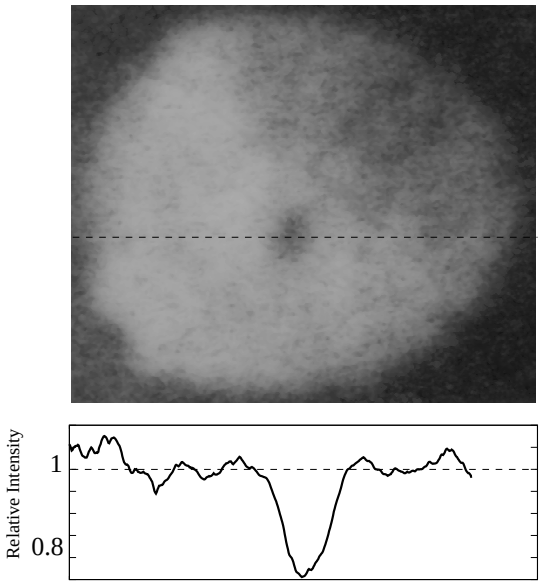

Fig. 13. Image of transmitted repumper laser: the dark region in the center corresponds to the absorption of the repumper by the MOT atoms in the dark state.

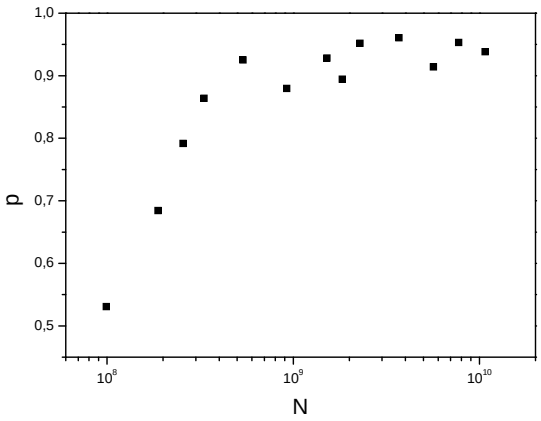

Fig. 14. Proportion $p = N_3/(N_2 + N_3)$ of atoms in the bright ($F = 3$) state as a function of the total number $N = N_2 + N_3$. N is varied by changing the repumper size.

hyperfine level), and thus affect the fraction of atoms in the bright state. To illustrate such effects, we have measured the number of atoms N_3 in the bright state $F = 3$ (no delay at repumper switch-off) and the total number of atoms $N_2 + N_3$ ($100\mu s$ delay for repumper switch-off), in an experiment where the number of atoms has again been changed by varying the size of the repumping laser. In Fig. 14 we plot the proportion of atoms in the bright state $p = N_3/(N_2 + N_3)$ as a function of the total number of atoms $N = N_2 + N_3$. As one can see, this proportion is roughly constant, except for low atom numbers where it drops. This decrease of p is not understood and the situation is far from trivial. Indeed this decrease of p depends in a complex way on the relative attenuations of the MOT, repumper lasers and on the presence of spontaneous Raman photons. A model to explain this decrease goes beyond a simple description using low saturation and/or homogeneous laser intensities. From our experimental observation, we obtain a decrease of p for smaller atom number, whereas the density is roughly constant or slightly decreasing in this regime (see Fig. 7).

We have performed further experiments in order to investigate the role of the various parameters of the repumping laser. Changing the detuning of the repumper or its intensity did not dramatically alter the maximum density obtained in our trap. Even though we pass from a regime where the saturation of the repumping transition is larger than 1 to a regime where we do not saturate this optical transition, the relevant effective saturation to be considered being the efficiency of a repumping cycle versus the optical pumping into the $F = 2$ hyperfine level. Thus, one typically only needs 1 repumper photon for every 1000 photons exchanged on the main cooling and trapping tran-

sition. We thus estimate that the optical repumping cycle saturates 1000 times faster than the optical transition. We have also verified that the size of the trap is the same if we detect atoms in both hyperfine levels or only in the bright state. This can be understood by the fact that atoms with a typically velocity of $v \approx 0.1 m/s$ would have to spend a time of about $t \approx L/v \approx 10 ms$ in the dark state, in order to undergo a larger spread than in the bright state [13]. This is not the case for our parameters.

5.2 Generalized Wieman-Pritchard model

In this section we will propose a new model which generalizes the existing theory by including the role of repumper photons. We note that this model is not valid for all MOT regimes. Indeed there are well known regimes, which are not covered by the following discussion. The first one to mention is the temperature limited regime, where the MOT size is limited by the thermal atom motion and can be estimated from the equipartition theorem for kinetic and potential energy of the atoms in a damped harmonic trap. This regime is usually realized for very low atom numbers or when multiple scattering forces can be neglected, as e.g. in the case of narrow line cooling and trapping [21]. Other regimes at low or moderate atom number include the situations where the MOT size is so small that sub-Doppler cooling features have to be taken into account [22]. Further factors, such as free travel during a period in a dark state [13] or dynamical effects [18] (clearly becoming dominant when self-sustained oscillations set in [14]) can also affect the scaling law and the shape of MOTs with large number of atoms.

Despite the agreement between the Wieman-Pritchard model and our experiments for the largest atom numbers, the density dependence observed in Fig. 11 for the lower atom numbers cannot be explained by the Wieman-Pritchard model. Indeed, trying to fit the behavior of Fig. 11 by an unknown dependence of $p(N)$ would require extremely low bright state fraction (of the order of 1%) which we find difficult to realize even in a standard dark SPOT configuration [12] with Rubidium. We thus think that a new effect, not previously reported in the literature, needs to be included.

The results of section 5.1 suggest that many repumper photons are absorbed by the atomic cloud, which may have a dramatic effect on the MOT density. Similar to scattered MOT photons, scattered repumper light can be reabsorbed, which leads to an additional repulsive force between the atoms. On the other hand, as we do not use six counter propagating lasers beams for the repumper, the corresponding shadow effect for the repumper is negligible such that the net repulsion is important even for low values of the saturation parameter. As a rough estimate we consider an optical thickness of $b_{res} = 40$ for the resonant $F = 3 \rightarrow F' = 4$ transition, with the repumping lasers being at resonance. The resulting repumper-optical thickness of the cloud for that frequency is of order $b_{res}(1-p)/p$. This means, that even a 2% fraction of atoms in the 'dark' state yields an optically thick cloud for the repumping laser: $b_{res}(1-p)/p \approx 1$. Taking into

account an interaction between atoms in the dark ground state ($F = 2$) will thus lead to add a term $\propto (1-p)^2$ in the repulsive forces.

Furthermore photons scattered on the $F' = 3 \rightarrow F = 3$ transition during a repumping process will be efficiently reabsorbed for a large optical thickness. Indeed, these photons, which are spontaneous Raman photons, are resonant with the $F = 3 \rightarrow F' = 3$ transition and the reabsorption of these photons corresponds to adding a further interaction term $\propto p(1-p)$ depending now on the product of the dark $(1-p)$ and the bright (p) state populations. One could consider spontaneous Raman photons responsible for the optical pumping from the $F = 3$ into the $F = 2$ hyperfine level can become important. They will ad to an interaction term $\propto p(1-p)$. However these photons do not affect much atoms in the dark hyperfine level $F = 2$, as they are detuned by $\approx 20\Gamma$ from the $F = 2 \rightarrow F' = 3$ transition.

Accounting for these additional interactions, we thus propose the following generalization of the Wieman-Pritchard model by modifying the multiple scattering force as follows:

$$F_{\rm ms} = G_3 n\, p^2 r + G_2 n\, (1-p)^2 r \, + G_{2,3} n\, p(1-p) r \ , \quad (24)$$

where the parameter G_2 describes the repumper induced by rescattered repumper photons (in analogy to G_3 for the rescattered MOT photons), and $G_{2,3}$ takes into account the repulsion effect of Raman scattered photons. As for the Wieman-Pritchard model, the stationary density is obtained from total force balance, which yields :

$$\begin{aligned} n_{WP+} &= \frac{\kappa\, p}{G_3 p^2 + G_2 (1-p)^2 + G_{2,3} p(1-p)} \\ &= \frac{n_{\rm W}}{p + \alpha \frac{(1-p)^2}{p} + \beta(1-p)} \end{aligned} \quad (25)$$

where $\alpha = G_2/G_3$ describes the ratio between the interaction of atoms in the bright and the dark hyperfine level and $\beta = G_{2,3}/G_3$ describes the strength of the interaction of the Raman scattered photons. This equation predicts new scaling laws and new limits for the density of cold atomic clouds.

Although this expression looks very appealing to predict the density limit of MOTs, it is not straightforward to compare this model in a quantitative way to the experiments for several reasons. First of all, in order to use this new model and compare it to our experiment where we modify the number of atoms via the intensity of the repumper, one would need to take into account how the new interaction terms depend on the intensity of the repumper (which is coupled to the bright state fraction p). Second, for large optical thickness of the repumper and MOT lasers, the total number of atoms N and p become coupled parameters. Also the effective local intensity to be considered for the interaction by the repumper laser depends on the optical thickness of the cloud. A direct and clean experimental study of these additional interaction effects would thus require a large detuning for the repumper (probably best done on the D1 line of Rb), so that the optical thickness of the repumper can be neglected and the new force can be eliminated. Such experiments go beyond the data we have gathered for this paper. However

the new model will predict a limitation and a possible decrease of the atom density for smaller values of p and correspondingly for smaller values of the repumper intensities. But a quantitative description of our observations over the full range of experimentally realized atom numbers thus requires precise knowledge of the local repumper intensity and its effect on the bright state population. As outlined above, a corresponding theoretical description turns out to be prohibitively complex, as attenuation and reabsorption leads to an intimate coupling between p and I_{rep} governed by the incident as well as the diffusive background of repumper photons, which all contribute to the repulsion forces and determine the value of p. Clearly, further experiments are required to uncover this complex interplay between the various atom-light and atom-atom interaction effects. Note that the attenuation of the repumper by the cold atoms is not affecting the dependence of $N(I_{rep})$ as the attenuation by the cold atomic cloud is only present at a small part of the capture volume for the MOT.

6 Conclusion

In summary we have presented a systematic study of the various scaling laws appearing in large MOTs. In one type of experiments, where the atom number was changed by varying the diameter of the repumper laser, we recover the prediction of the Wieman model $L \propto N^{1/3}$, and thus a constant density, up to large atom numbers of $N \sim 10^{10}$, which provides strong evidence that a $N^{1/2}$ scaling law does *not solely* arise from multiple photon scattering as previously suggested in the literature. In another series of experiments, where we change the atom number via the intensity of the repumper laser, we found a cross-over in atom number dependence of the MOT size changing from $L \propto N^{1/3}$ to $L \propto N^{1/2}$ with increasing N. We can explain the $L \propto N^{1/2}$ behavior using the Wieman-Pritchard model developed to describe a dark SPOT. We also point out unexplained behaviors which are observed in our experiment and suggest that the mechanical interaction effect induced by repumper photons can become important in large MOTs. Indeed, in certain regimes, in particular when more atoms are in the dark hyperfine state, repumper-induced interactions may impose an additional – previously overlooked – density limitation, and we speculate that a considerable density increase is possible when these effects are correctly understood and controlled. Further experiments are required to unambiguously prove the role played by the repumper photons on the MOT density. A quantitative comparison between our experimental result and the model including the mechanical effects of the repumper photons goes beyond the scope of this paper, but would be interesting to be developed in order to overcome present limitations in MOT densities. Indeed, one promising possibility, suggested by the experiments and by the model presented in this paper, is to use six independent repumper laser beams. The resulting shadow effect is expected to greatly compensate the repumper-induced repulsion between the atoms and consequently lead to significantly denser atomic samples. Increasing rapidly the atomic densities could be very useful for fast Bose-Einstein condensation of cold atoms and

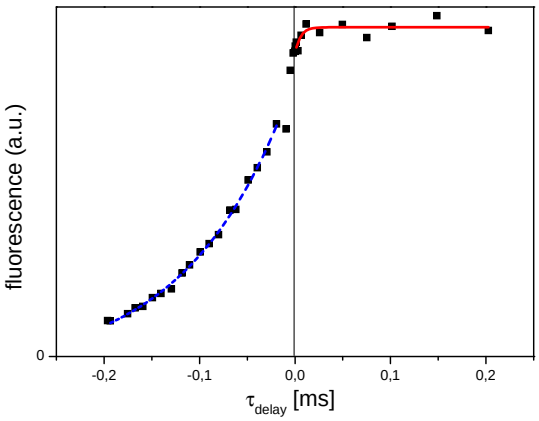

Fig. 16. Number of atoms in the bright state a function of delayed repumper turn off: τ_{delay}. The fit for $\tau_{delay} < 0$ (dashed line, blue online) gives a time scale of $110\mu s$, whereas the fit for $\tau_{delay} > 0$ (solid line, red online) gives a time scale of $5.7\mu s$.

the MOT laser and magnetic field gradient off. Obviously, turning off the repumper much earlier than the MOT laser will empty the 'bright' ($F = 3$) state and put all atoms into the 'dark'state ($F = 2$). On the other hand, leaving on the repumper after turning off the MOT laser will repump all atoms into the $F = 3$ state. Probing the fluorescence with only the MOT laser turned on gives us a signal proportional to the number of atoms in $F = 3$. As shown in Fig 16, the time scales for repumping from $F = 2$ into $F = 3$ ($\tau_{delay} > 0$) is different from the time scale to pump the atoms into the 'dark' state $F = 2$ ($\tau_{delay} < 0$). The ratio N_2/N_3 of the number of atoms N_2 in the dark state and the number of atoms N_3 in the bright state can be extracted from the ratio of the pumping (Γ'_{pump}) and repumping rates (Γ'_{rep}):

$$\frac{N_2}{N_3} = \frac{\Gamma'_{pump}}{\Gamma'_{rep}}. \tag{26}$$

From the fit of the experimental data we extract a time scale for repumping of: $\tau_{rep} = 1/\Gamma'_{rep} = 5.7\mu s$ and time scale for pumping into the dark state of: $\tau_{pump} = 1/\Gamma'_{pump} = 110\mu s$, predicting a ratio $N_2/N_3 \approx 0.052$. This is in rough agreement with the value obtained at zero delay ($\tau_{delay} = 0$): $N_2/(N_3 + N_2) \approx 0.076$. As expected this shows that the repumping of atoms from $F = 2 \rightarrow F = 3$ is much faster than the optical hyperfine pumping from $F = 3 \rightarrow F = 2$.

References

1. J. Dalibard, C.Cohen-Tannoudji, J.O.S.A. **B 6**, 2023 (1989).
2. A.Aspect, E. Arimondo, R. Kaiser, N. Vansteenkiste, C. Cohen-Tannoudji,Phys.Rev.Lett. **61**, 826-829 (1988).
3. T.Walker, D. Sesko, and C. Wieman, Phys.Rev.Lett. **64**, 408 (1990).
4. D. Sesko , T. Walker and C. Wieman, J. Opt. Soc. Am. **B8**, 946 (1991).
5. C. Monroe, W. Swann, H. Robinson, and C. Wieman, Phys. Rev. Lett. **65**, 1571 (1990).
6. K. Lindquist, M. Stephens, and C. Wieman, Phys. Rev. **A 46**, 4082 (1992).
7. A.M. Steane, M.Chowdhury and C. Foot, J. Opt. Soc. Am. **B9** 2142 (1992).
8. K.E. Gibble, S. Kasapi and Steven Chu, Opt. Lett. **17** 526 (1992).
9. W. Petrich, M. H. Anderson, J. R. Ensher, E.A. Cornell, J. Opt. Soc. Am. **B11** 1332 (1994).

10. C.G. Townsend, N.H. Edwards, C.J. Cooper, K.P. Zetie, C.J. Foot, A.M. Steane, P. Szriftgiser, H. Perrin and J. Dalibard, Phys. Rev. **A52**, 1423, (1995).
11. C. Gabbanini, A. Evangelista, S. Gozzini, A. Lucchesini, A. Fioretti, J. H. Muller, M. Colla and E. Arimondo, Europhys. Lett., **37**, 251, (1997).
12. W. Ketterle, K. Davis, M. Joffe, A. Martin, D. Pritchard, Phys. Rev. Lett. **70**, 2253 (1993).
13. C. G. Townsend, N. H. Edwards, K. P. Zetie, C. J. Cooper, J. Rink, and C. J. Foot, Phys. Rev. **A 53**, 1702 (1996).
14. G. Labeyrie, F. Michaud, R. Kaiser, Phys. Rev. Lett. **96**, 023003 (2006).
15. G. Labeyrie, F. de Tomasi, J.-C. Bernard, C.A. Müller, Ch. Miniatura and R. Kaiser, Phys. Rev. Lett. **83**, 5266 (1999).
16. G. Reinaudi, T. Lahaye, Z. Wang,and D. Guery-Odelin, http://arxiv.org/abs/0707.2930v1.
17. J. Dalibard, Opt.Comm. **68**, 203 (1988).
18. T. Pohl, G. Labeyrie, R. Kaiser, Phys. Rev. **A 74**, 023409 (2006).
19. G.L. Gattobigio, F. Michaud, G. Labeyrie, T. Pohl, R. Kaiser, AIP Conference Proceedings, **862**, 211, (2006).
20. K. Overstreet, P. Zabawa, J. Tallant, A. Schwettmann, and J. Shaffer, Opt.Express **13**, 9672 (2005).
21. T. Chanelière, L. He, R. Kaiser, D. Wilkowski, Eur. Phys. J. D **46** , 507 (2008).
22. K. Kim, H.R. Noh, H.J. Ha, W. Jhe, Phys. Rev. **A 69**, 033406 (2004).

Chapter 3

MOT Compression

In the previous section we presented our experimental results obtained in the compression stage. Here we want to overview the "standard techniques" used for MOT compression. We want to stress that this is a very critical and important stage towards high density regime, not only in our case to obtain a dense medium, but also for the cold collision field and the Bose-Einstein-Condensate (BEC). For the latter the most important parameter to be optimized is the phase-space density $n_0 \cdot \lambda_{DB}^3(v_{rms}) = 2.6$ (the combination of atomic density (n_0) and mean sample velocity).
In general, the degenerate regime described above is reached with evaporative cooling techniques, which produce lower atomic temperature in about $2\,sec$. The only side-effect is a considerable loss of atoms during the process, with only a few atoms in the condensate ($10^3 - 10^6$).

The inevitable choice of evaporative cooling relies on the fact that, up to now, the physics behind density limitation are not well understood. Many experimental efforts were carried out to compress standard MOTs but with only limited success. The density limitation explanation is still an open question in atomic physics. An experimental answer to such a question could provide the possibility of obtaining, for example, a degenerate regime such as BEC in less than $1\,sec$ with a relative rise in the experimental duty-cycle.

The steady-state of the density, as we saw, is determined by the balance between the spring constant of the trap and the repulse force of the atom-atom interactions. Thus the evident solution for increasing atomic density is to either increase the spring constant or suppress the rescattering light within the atomic cloud.

The spring constant can easily be increased by, for example, applying a strong magnetic field gradient at the end of MOT-loading, in order to leave the loading conditions unchanged.

The suppression of atom-atom interaction can be achieved by two methods. The first is the realization of a 'Dark Spot' technique, which consists of confining the atoms in the lower hyperfine ground state. As this state does not interact with the trapping light, the atoms cannot repel each other and thus the density is increased. The 'Dark-Spot' can be realized either by making a black spot on the intensity of the repumper, or dynamically, where the intensity is lowered by, typically, a factor of 100 after the loading.
The second method is based on reducing trapping light combined with increasing its detuning. Both are useful for decreasing the scattering rate of photons and consequently

the multiple scattering in the MOT.

These techniques were both experimentally demonstrated with different atomic species. We report, in Tab. (3.1), the most important results published in literature, without considering either the highest density, as much as $10^{14}\, atom \cdot cm^{-3}$ [31], obtainable by using crossed dipole traps generated by focusing high-powered ($12\, W$) infrared ($\lambda = 10.6 \mu m$) beams, or the Far-OFF-Resonant Light trap (FORL) [32], where spontaneous emission is also negligible and spatial densities of about $10^{13}\, atoms/cm^3$ are reached as well.
These particular traps require very powerful and expensive lasers, and in our case, the implementation required a complete restyling of the experimental set-up.

Observed Density (cm^{-3})	Atom	Techniques	Reference
$2.5 \cdot 10^{11}$	Cs	Static Parameters: $\Omega^2 = 0.8\Gamma^2$, $\frac{dB}{dz} = 60\, G/cm$ $N_{at} = 5 \cdot 10^5$	[33]
$\sim 10^{12}$	Cs	Temporal dark-spot ($20\, msec$) ($I_{rep}/100$,$\frac{dB}{dz} = 20 G/cm$)	[34]
$\sim 10^{12}$	Na	Spatial Dark Spot	[29]
$3 \cdot 10^{11}$	Cs	Temporal Dark Spot	[35]
$\sim 5{\cdot}10^{11}$	^{85}Rb	Changing the detuning and the gradient	[36]
$1.6 \cdot 10^{11}$	^{85}Rb	On-resonance compression beams	[37]
$\mathbf{\sim 10^{12}}$	$\mathbf{^{85}Rb}$	**Dark-Spot combined with a Dipole Trap**	**This work**

Table 3.1: *Table resuming the main published experimental results dealing with the compression of atomic clouds. We report the maximum of the density obtained, the atomic species used and the relative techniques employed.*

In accordance with the conclusions of the previous chapter, and the studies published and reported in TAB. (3.1), the highest densities are achieved for low values of p. We were able to obtain such a condition by implementing a spatial 'Dark-MOT' (Dark-spot) as well as a temporal 'Dark-MOT'. Therefore, we cannot set p as low as we want, because of spatial confinement. In fact, as the spring constant proves to be proportional to p, it became weak as well. Thus we came up with the idea of adding an external force, which provided a spatial potential to keep the atoms in the trap even for small values of p. This was achieved by using a dipole trap, combined with the 'Dark-MOT'. In our case, the dipole trap was obtained from a simple amplified and red-detuned diode-laser. More details are given in the following sections.

3.1 Experimental Setup

In this section we will describe the experimental set-up used to achieve our 'Dark-MOT' (3.1.1) , followed by the description and implementation of a Dipole Trap obtained from a laser diode $\lambda = 780\,nm$ amplified by MOPA (3.1.2). Finally, we will analyze the performance of the combined 'Dark' and Dipole trap in Sec. (3.2), and conclude by reporting the maximum density obtained.

3.1.1 The 'Dark-MOT' (DMOT)

In the following section, the details of our 'Dark-MOT' are given. We will describe the realization of our 'dark spot' in the repumper and the time sequence used. Also, during the compression experiments, we used the absorption technique to probe the atomic sample, and we will detail this new procedure. We will conclude these sections with general considerations on performance and optimization of a 'Dark-MOT' like this.

Dark line in the repumper

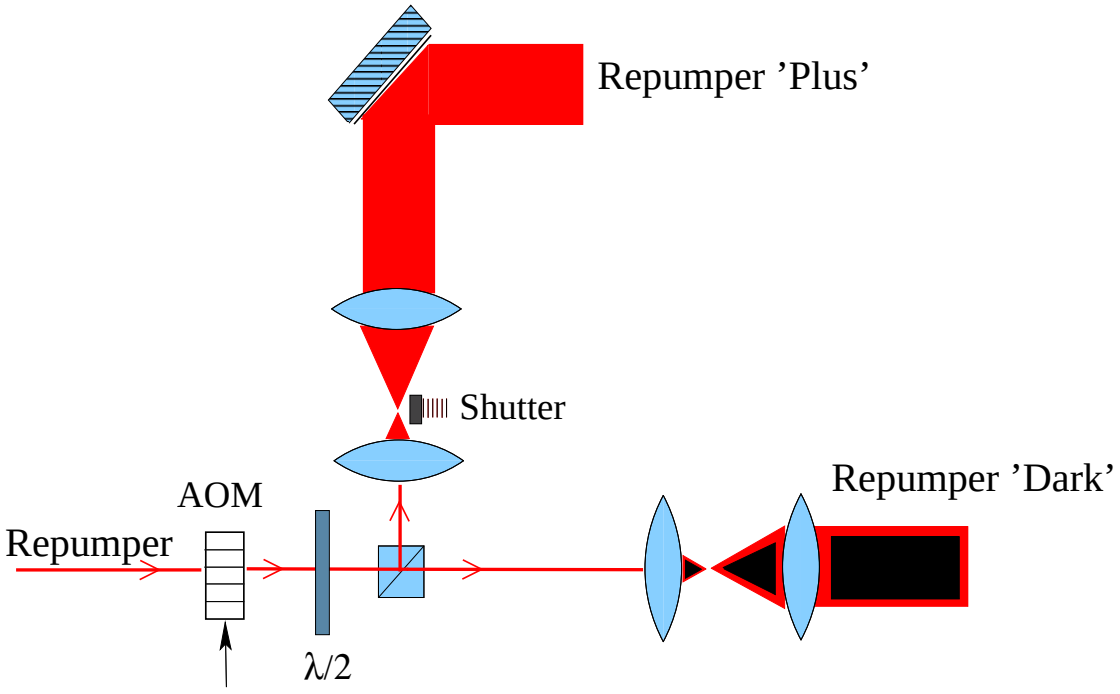

Figure 3.1: *The illustration shows the method used to realize the dark spot. The repumper intensity is separated by the $\lambda/2$-cube system in two directions. One direction, called 'Repumper Dark', involved putting a thin wire line providing a dark line in the repumper intensity at the level of the vacuum cell. The 'Repumper Plus' direction is used to pump the atoms back into the bright level before probing the cloud. In the 'Repumper Plus' direction the shutter is used to switch this additional beam on and off .*

The repumper intensity, usually of about $16\,mW$, is split in two directions by a $\lambda/2$-cube system which provides us, FIG. (3.1), with a 'repumper dark' and a 'repumper plus' with controllable intensities. The 'dark repumper' is obtained by placing a thin wire in the path of the repumper. In this way we obtain a black line in the repumper intensity profile, which gives rise to a dark plane at the atomic level, where the atoms are confined in the $F = 2$ hyperfine-ground state.
The 'repumper plus',FIG. (3.1) which is controlled in time by a mechanical shutter, is used to repump all atoms in the $F = 3$ state before shining the probe beam. The shutter is characterized by four time constants. The first is the delay time, which is the delay between the TTL command and the shutter opening (ON). The second is the rising time of the shutter opening (ON). The third is the shutter closing time (OFF). The fourth is the relative falling time (OFF). These times can be measured by looking at the intensity of the 'repumper plus', and for the 'delay on' we found: $5.5\,msec$ with a rising time of $0.6\,msec$, and for 'delay off': $16\,msec$ with a falling time of $1.25\,msec$. Throughout the whole loading time the two 'repumpers' were both present, while in the 'dark' phase only the 'dark' one was kept on.

As we wanted to obtain a low value of p, particular attention had to be paid to the geometrical alignment of the black line in the atomic cloud. The reflection on the surface of the vacuum cell has to be controlled and any extra repumper photons have to be blocked. The 'Dark-MOT' is usually realized by using a dark-spot in the repumper laser [29], and the problem lies in the geometry; we cannot control the reflections well as they cannot be superimposed due to the cylindrical symmetry of the problem. This is why we used the line.

Temporal 'Dark-MOT'

As already mentioned, the 'Dark-Spot' can also be realized dynamically, which means that the intensity of the repumper laser is lowered, typically by a factor of 100 at the end of the loading time [34], which produces high spatial density ($\sim 10^{12}\,cm^{-3}$) during a transient time of about $20\,msec$.
In our case this technique was tested to increase the density as well. Indeed, we removed the black line in the 'repumper dark' Fig. (3.1), and we altered only the respective intensities of the two 'repumpers'. By doing this, the best condition was found for a measured 'repumper plus' power of $P_{plus} \sim 13\,mW$ and 'repumper dark' power of $P_{dark} = 3\,mW$. This arrangement produces a $p = 25\%$, and consequently an increase of central density of only a factor of 4. Hence, after these considerations, we decided to choose the pure 'Dark-spot' technique as the first stage for the MOT compression.

Time Sequence

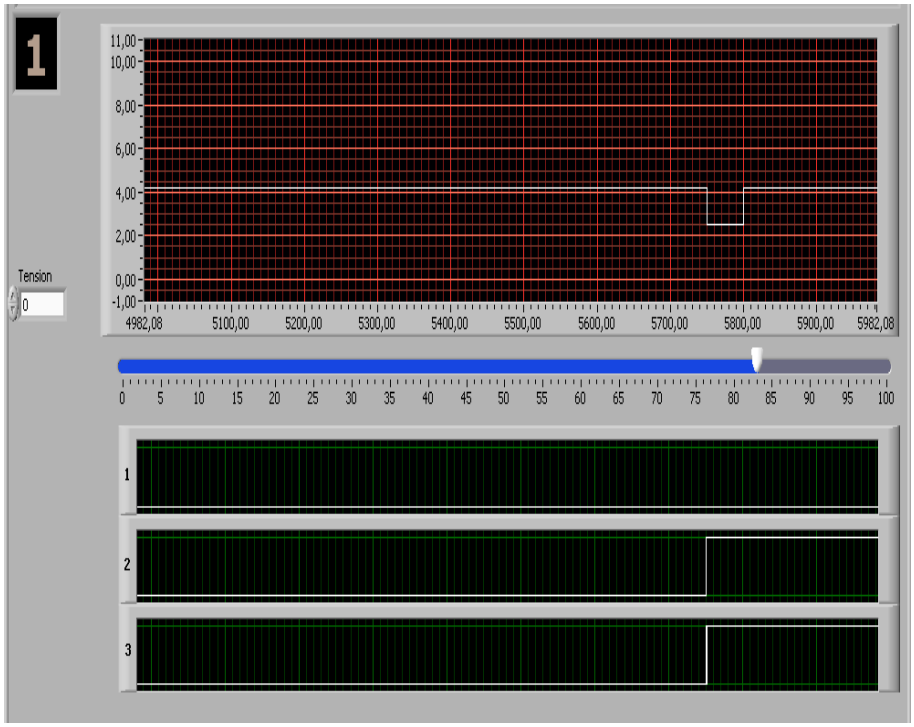

(a)

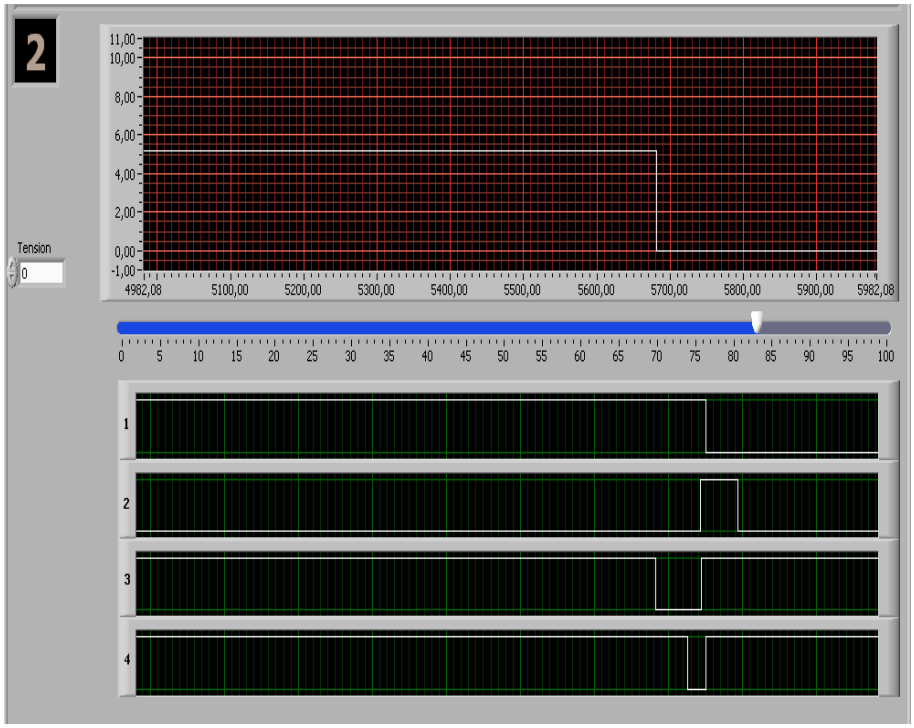

(b)

Figure 3.2: *In the illustration we report the time sequence used to realize the 'Dark-MOT'. The full description is given in the text.*

The time sequence was realized with a home-made card which gave us the possibility of performing a sequence of up to several seconds, while for the shorter time we still used a 'delay box'.

The typical time sequence is reported in the Fig. (3.2), where we are loading the MOT during the first 5700 $msec$ followed by 25 $msec$ of 'Dark-MOT' and 25 $msec$ of 'Ultra Dark-MOT'. In this latter phase we tested the controller parameters, in order to obtain the lowest possible p-values. The time sequence was realized with two home-made electronic cards. With reference to Fig. (3.2), we call card number 1 (a) and card number 2 (b). In total we used the two analog outputs and seven digital (TTLs-signal) outputs available. These outputs are described as following:

For card 1 (a):

- 1.A-(a): the analog output which controls the MOT detuning δ_{MOT}. This is set equal to -3Γ during the loading time, and suddenly changed during the 'Dark-MOT' ranging between -10Γ and resonance;
- 1.2-(a): controls the AOM on/off MOT intensity and the AOM on/off of the repumper laser when we want to probe only the N_3 atomic population, where a repumper pulse is not present;
- 1.3-(a): controls the AOM on/off repumper when we want to probe the whole atomic population N_{at}, where a repumper pulse is present, before probing the cloud.

For card 2 (b):

- 2.A-(b): the analog output that controls the repumper intensity (I_{rep});
- 2.1-(b): controls the magnetic field gradient ($\vec{\nabla}B$);
- 2.2-(b): is used as a trigger for the 'delay box'. Such a box is used to generate shorter signals (less than $1\mu sec$) which we cannot make with the cards. Particularly, by using this box, we can control:
  - the duration of the probe beam, used for the absorption images;
  - the probe detuning (δ_{probe});
  - the trigger of the CCD camera to record the absorption images;
  - the AOM on/off of the 'dipole' trap (Fig. (3.11)) when it is present;
- 2.3-(b): switches on/off the shutter in the 'repumper plus'(Fig. (3.1)) in which we also added the relative delay times. As already mentioned, the shutter is characterized by four time periods: the 'delay on' (the amount of time of delay from when the TTL command is given) of about 5.5 $msec$ with a rising time of 0.6 $msec$; the 'delay off' of about 16.6 $msec$ with a falling time of 1.25 $msec$.
- 2.4-(b): controls the AOM on/off if we want to use a 'depumper' laser which also influences p.

Absorption Imaging

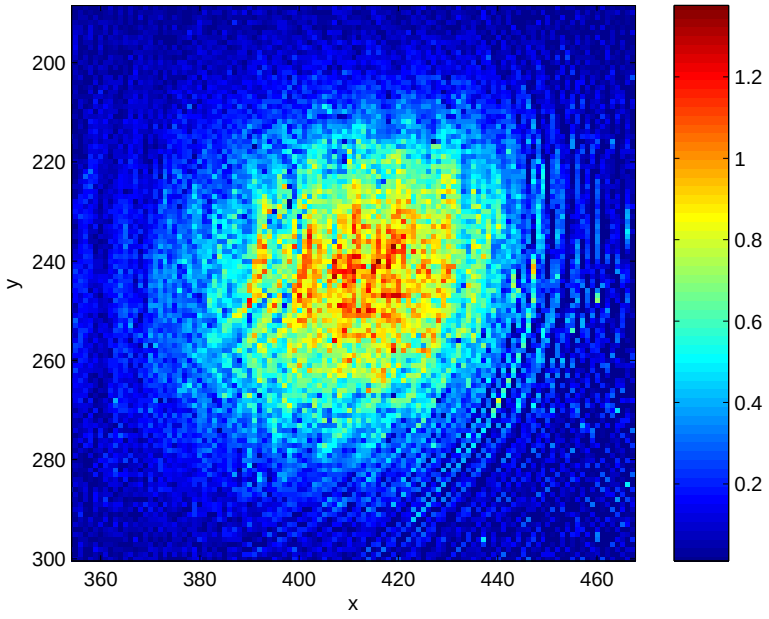

(a)

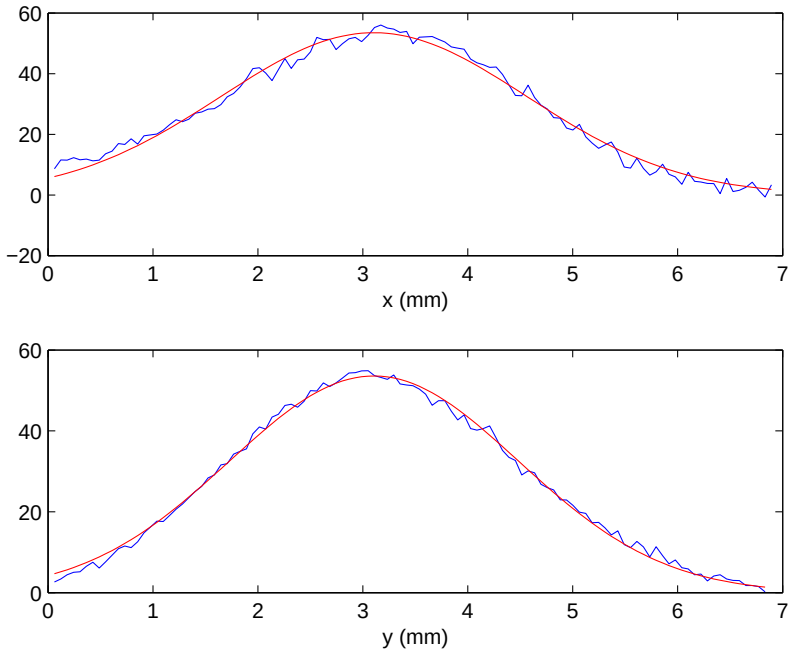

(b)

Figure 3.3: *The typical absorption image (a), obtained by the method described in the text, is shown, and the projections with the relative Gaussian fit are reported (b). The typical size is found to be* $\sigma_r \sim 1.5\,mm$*, with the assumption of an isotropic density distribution. The on-resonance optical thickness in the 'Dark-MOT' is* $b_0 \sim 100$ *with* $N_{at} \sim 10^9$ *and density of* $10^{11}\,cm^{-3}$*. The experimental image is taken with* $\delta_{probe} = -4\Gamma$*.*

We already saw in the Sec.(2.1.2) dealing with shadow effects that when the light passes through a cloud of atoms with density distribution $n(x, y, z)$, the intensity is reduced according to Beer's law:

$$I(x, y, z) = I_\infty e^{-\sigma_L \int_{-\infty}^{z} n(x,y,z')\, dz'} \quad , \qquad \sigma_L(\delta) \;=\; g_F \frac{\sigma_0}{1 + 4(\delta/\Gamma)^2} \tag{3.1}$$

where g_F accounts for the degeneracy of the atomic levels, and as usual is equal to 3/7. It is clear from the Eq. (3.1) that the intensity profile of the laser beam, after having passed through the cloud, contains information about the integrated density distribution $n(x, y)$. For the 'dark' image obtained without the atoms, $I_d(x, y)$, and the image with the cloud $I_s(x, y)$, the density profile is given by the following equation:

$$n(x, y) \;=\; -\frac{1}{\sigma_L} \ln\left(\frac{I_s(x, y)}{I_d(x, y)}\right) \tag{3.2}$$

Also, the integration of Equation (3.2) gives the total number of atoms present in the MOT. As we recorded the images into a CCD camera with discrete pixels, the integration is turned into a summation made over all the pixels:

$$N_{at} \;=\; -\frac{D}{\sigma_L} \sum_{ij} \ln\left[\frac{(I_s)_{ij}}{(I_d)_{ij}}\right] \tag{3.3}$$

where D is the area of the pixel in the object-space.
In contrast to fluorescence imaging, no camera or transmission calibration is necessary to determine the number of atoms from an absorption image. We only need to calibrate the magnification which can be done by taking an image of a ruler. By doing this we found, for the square-pixels, a calibration of $61\,\mu m/pixel$.

As well as the transverse mode quality of the absorption beam, which has been checked, the spectral properties are important. The spectral width of the imaging light needs to be much smaller than the atomic linewidth of the atomic transition so that the light scattering cross-section σ_L is the same for all frequency components of the light. This criteria is also fulfilled as we use a DBR of $2\,MHz$ width $(FWHM)$.

The duration of the absorption imaging light pulse has to be short enough for the atoms to maintain their original density distribution. In fact, the diffusion induced by photons within the cloud leads to an increase in the size of the cloud as we have already discussed.

To obtain the absorption images we used a non-saturating probe $(I_{sat}/10)$ with a diameter of $4\,cm$, which is much larger than the atomic cloud.
The typical absorption images Fig. (3.3) are taken in only one shot without a time averaging, and with a CCD camera exposition time of $0.55\,msec$.

In order to extract some physical information we assume a Gaussian density distribution for the MOT. Fitting the image obtained according to Eq. (3.2) with a Gaussian function, we directly extract the standard deviations σ_y, σ_z for the two spatial directions, as shown in Fig.(3.3).

All the relevant information we are interested in, N_{at}, n_0 and the b_0 were gathered from the image by using a Matlab routine, which could also provide us with a real time analysis of the images.

Performance and Optimization of the 'Dark-MOT'

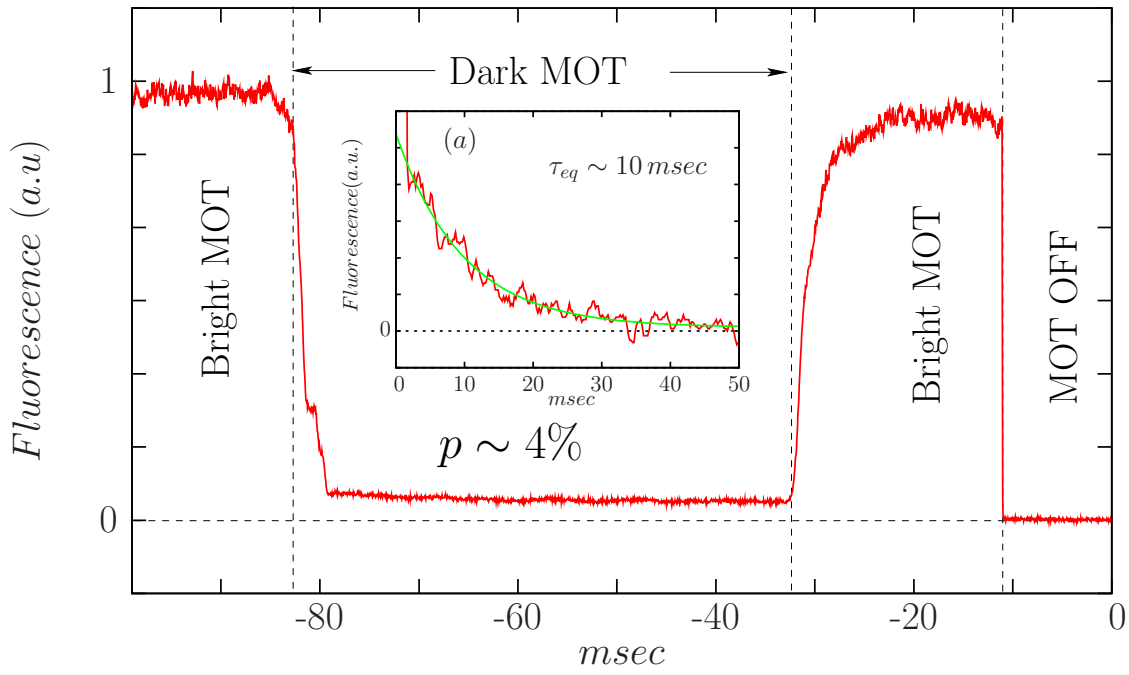

Figure 3.4: *The figure shows fluorescence as a function of time. The signal was directly recorded from the experiment: it proves that the suppression of fluorescence (proportional to p) during the 'Dark-phase' is due to a change in hyperfine ground state. In fact, the atoms are not lost and can be repumped back into the 'bright' state even after* $50\,msec$*. From such a curve, we can deduce a* $p \sim 4\%$ *in an equilibrium situation reached after about* $\tau_{eq} \sim 10\,msec$*, as shown in inset (a). The measured p is in complete agreement with the results extracted from the image technique.*

Our 'Dark-MOT' phase is obtained by switching off the 'repumper plus' laser ,Fig. (3.1), hence leaving the atoms to go into the lower Hyperfine ground state $F = 2$. By doing this we arrive at an equilibrium situation after $10\,msec$, as shown in Fig. (3.4)-(a), with a $p = \dfrac{N_3}{N_3 + N_2} \sim 3\%$. As described in the sequence shown in Fig. (3.2), we measured the p value by taking the difference between the two images with and without a repumper pulse before probing the atoms. This value could also be checked by looking at the fluorescence signal measured by a photo-diode Fig. (3.4). After the loading time we realized the 'Dark-MOT' phase during $50\,msec$ by switching off the 'rempumper plus' which was then switched on again to repumper the atom back into the 'bright' transition. If we say that the fluorescence is proportional to the number of atoms in the bright state (p), comparing the bright and dark fluorescence in Fig. (3.4), we extract a value of $p \sim 4\%$ in complete agreement with that obtained from the images. Also, the curve in Fig. (3.4) tells us that the atoms are still in the trap after $50\,msec$ of Dark MOT, and that they have not fallen out of the center of the trap.

As we have already demonstrated that the 'fluorescence' is a suitable signal, we looked

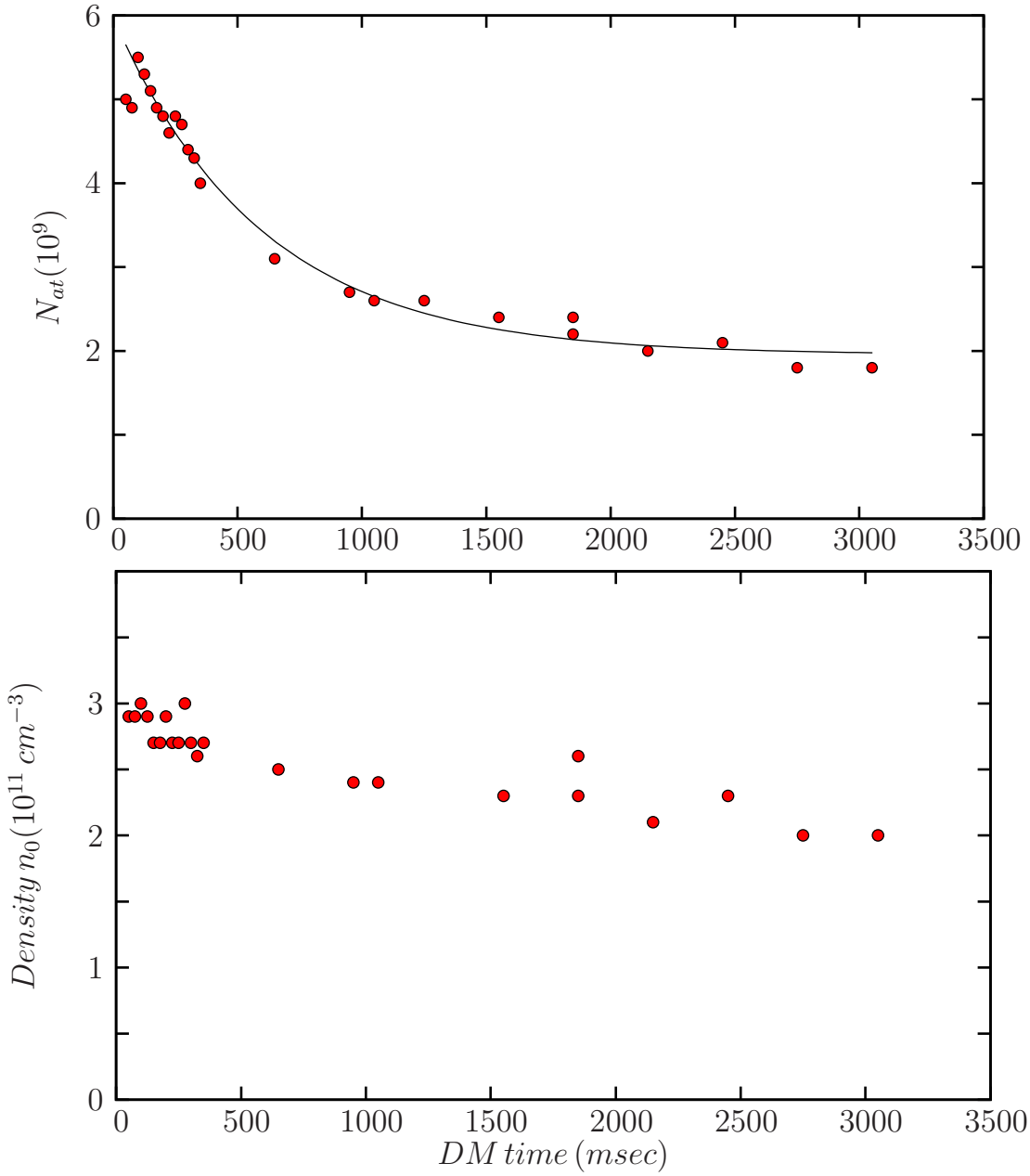

Figure 3.5: *Lifetime (τ_{life}) of the atoms in the 'Dark-MOT'. From the exponential fit we extracted ($\tau_{life} \sim 600\, msec$). We also noticed that our density was not limited by cold collision, as we observed a purely exponential decay.*

at it to optimize the repartition intensity of the repumper laser in order to have the lowest p value to increase the density in accordance with the Wieman-Pritchard model. Indeed, we wanted to have the lowest fluorescence signal during the 'Dark-Phase' without losing atoms while we were loading.

The isolation of the AOM on/off of the repumper laser was measured as $5 \cdot 10^{-3}$. This means that if we want to have an acceptable value of p we need to be aware of such light.

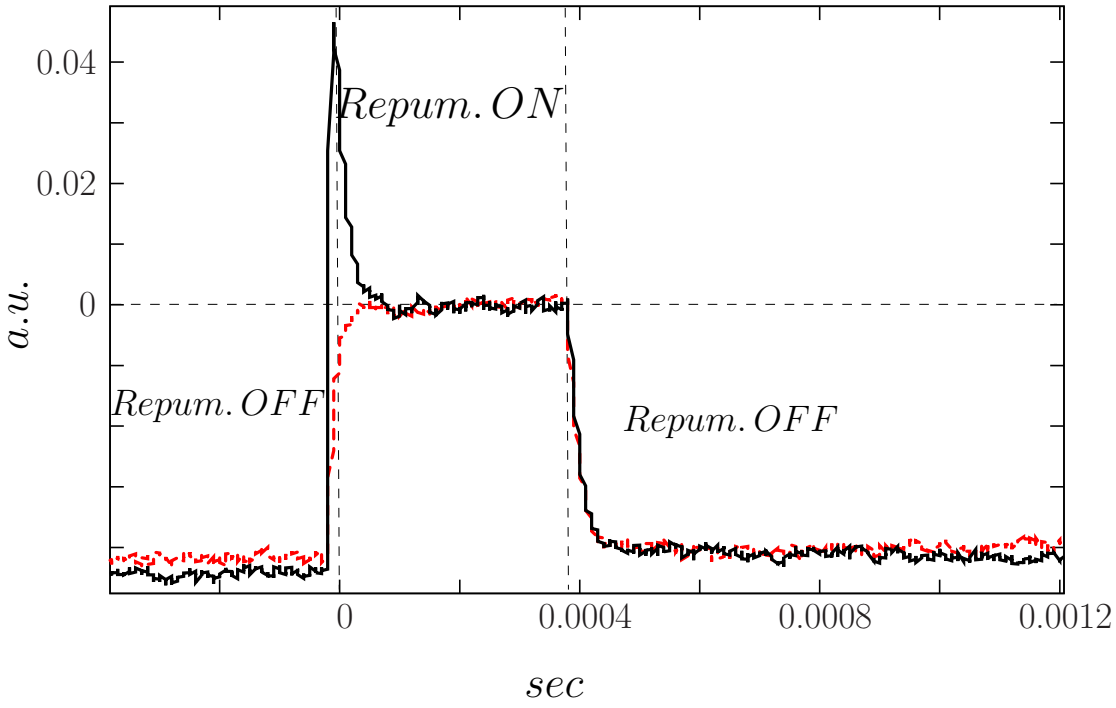

Figure 3.6: *The repumper pulse applied to the atomic cloud before probing is strong enough to rempump atoms in the bright state. The fluorescence spike is due to the photons emitted by the atoms in the $F = 2$.*

Particularly, we closed the mechanical shutter of the 'repumper plus' laser (Fig. (3.1)), during all N_3 measurements. After a careful shielding of the rempuper light a $p \sim 3\%$ was demonstrated. Such a value gives rise to an increase in the peak density by a factor of 10, and a factor of 4 for the on-resonance optical thickness (b_0).
In fact, the new density is $n_0^{'} = n_0 \cdot 10$; this means that as we keep the total number of atoms N_{at} trapped constant, the size is reduced by $L^{'} = L/(10^{1/3})$. Thus, the new on-resonance optical thickness, defined as $b_0^{'} = n_0^{'}\sigma_0\, L^{'}$, increases by a factor of about 4: $b_0^{'} = \dfrac{N_{at}}{(L')^2}\,\sigma_0$ and consequently, $b_0^{'} \sim b_0 \cdot 4$. As we have, for the non-compressed MOT, a $b_0 = 30$ after compression, we expect to have $b_0^{'} \sim 120$; these results are in complete agreement with the quantities measured. In fact, after the 'Dark-Phase', without too much effort, we ended up with a MOT with $5 \cdot 10^9$ atoms, $\sigma_r = 1\,mm$, $b_0 = 100$ and with a peak density $n_0 = 3 \cdot 10^{11}\, atoms/cm^{-3}$, as shown in the image of Fig. (3.3).

After the acceptable results obtained with the 'Dark-MOT' stage for increasing the density, we decided to investigate the influence of the MOT controller parameters. Indeed, we changed such parameters only in the last $25\,msec$ of our sequence, in the phase which we have called 'Ultra Dark-MOT'.

In the following we will report the main results obtained from such an experimental study:

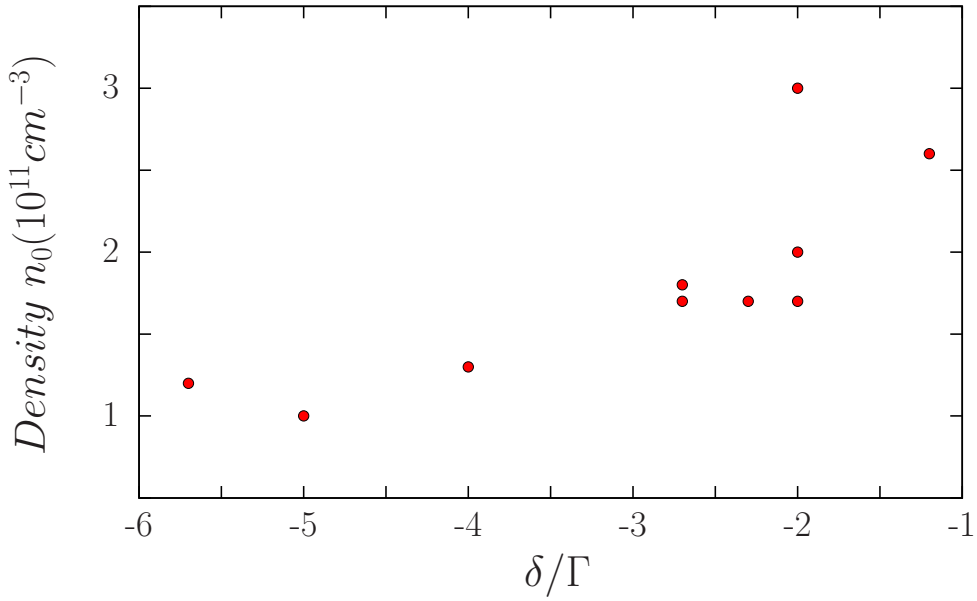

Figure 3.7: *The atomic density as a function of δ_{MOT} is shown. The detuning is only changed during the 'ultra dark phase' without affecting the loading characteristics of the trap. A maximum was found for a $\delta = -2\,\Gamma$.*

- The investigation of MOT detuning δ_{MOT} is reported in Fig. (3.7). The idea was to set the detuning near resonance to compress the MOT (i.e. minimize the G_3 interactions). We did not succeed because the cloud at resonance became unstable [38]. The density decreases when δ_{MOT} is far from resonance because we reduced the spatial confinement.
  However, a local maximum was found for $\delta_{MOT} = -\,2\,\Gamma$, and density as $n_0 = 3\,10^{11}\,cm^{-3}$ was obtained.

- We also tested the intensity of the MOT, during the 'Ultra-Dark' phase, without any noticeable effects.

- We also investigated the influence of the repumper by altering the intensity repartition (Fig. 3.1) between the 'repumper dark' and the 'repumper plus'. From this study we can conclude that such repartition is not so important as it doesn't influence the final density obtained.

- The density dependence on a delta repumper was explored and the results are reported in Fig. (3.8). As the repumper detuning can only be changed statically because of its construction, the number of atoms trapped are dependent on the repumper detuning. Thus the linear variation of density with the number of atoms strictly correlates with the MOT-trapping efficiency. We also verified that the repumper pulse before shining the probe is strong enough to put all atoms in the bright state Fig. (3.6). However, if we plot the ratio n_0 as a function of N_{at}, we find that the density is not limited and increases linearly with the number of atoms, Fig. (3.9). Moreover, if we look for blue detuning in detail, inset of Fig. (3.9), we

have a slight decrease in the MOT's volume, meaning a compression of the MOT, due to a reduction of repumper induced interactions.

- As a final test, we also tried to add a 'depumper' laser, in order to lower the p value, but we gained only an insignificant factor of two in N_{at}, without any effect on the final density value.

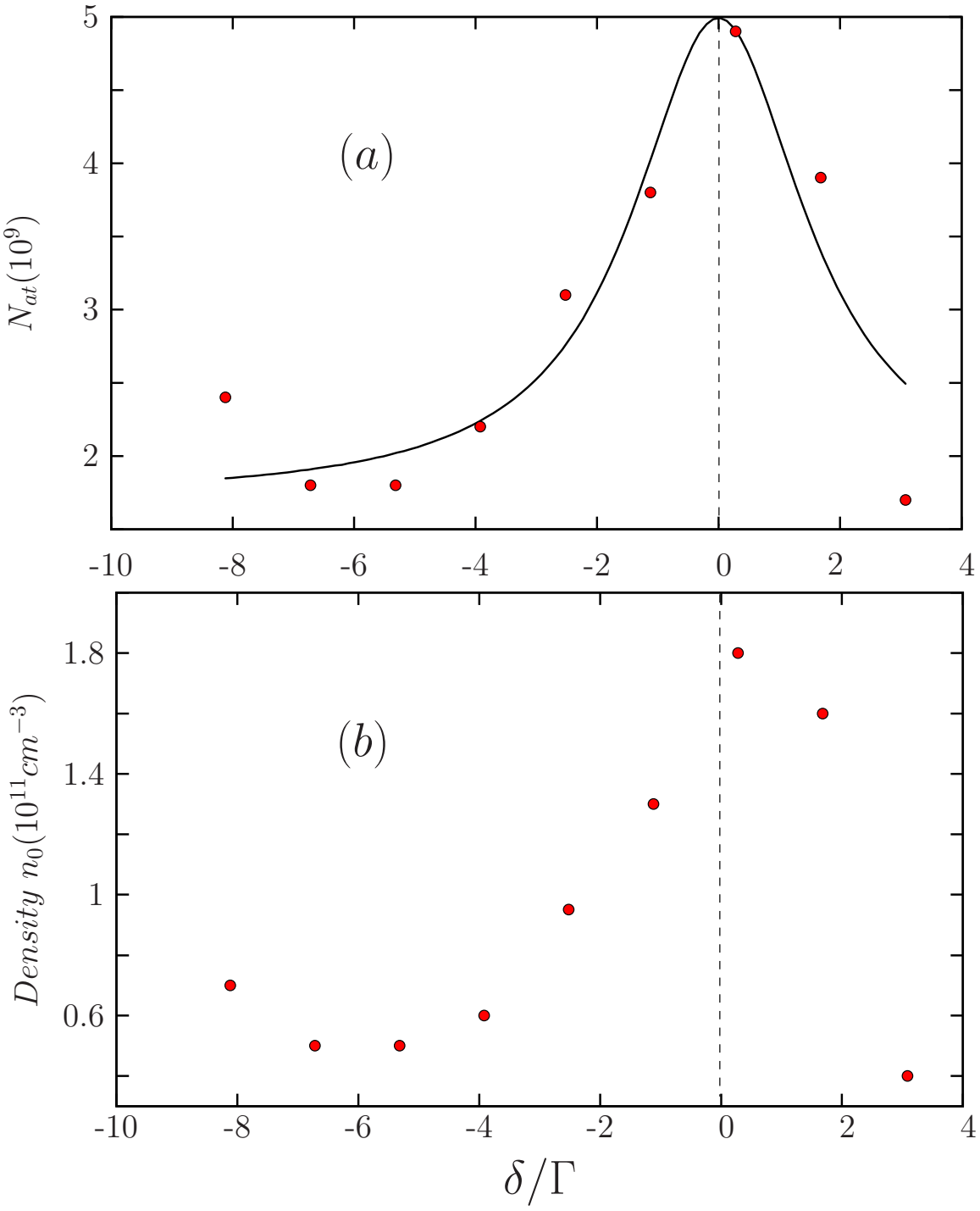

Figure 3.8: *The influence of the repumping detuning δ_{rep} on the density is reported. Fig.(a) shows the behavior of the total number of atoms N_{at} in the trap, while in Fig.(b) the relative atomic density is reported. The detuning could only be changed statically and not dynamically, influencing the trap efficiencies. This is demonstrated by the Lorentzian shaped behavior as a function of detuning, both for density and number of atoms.*

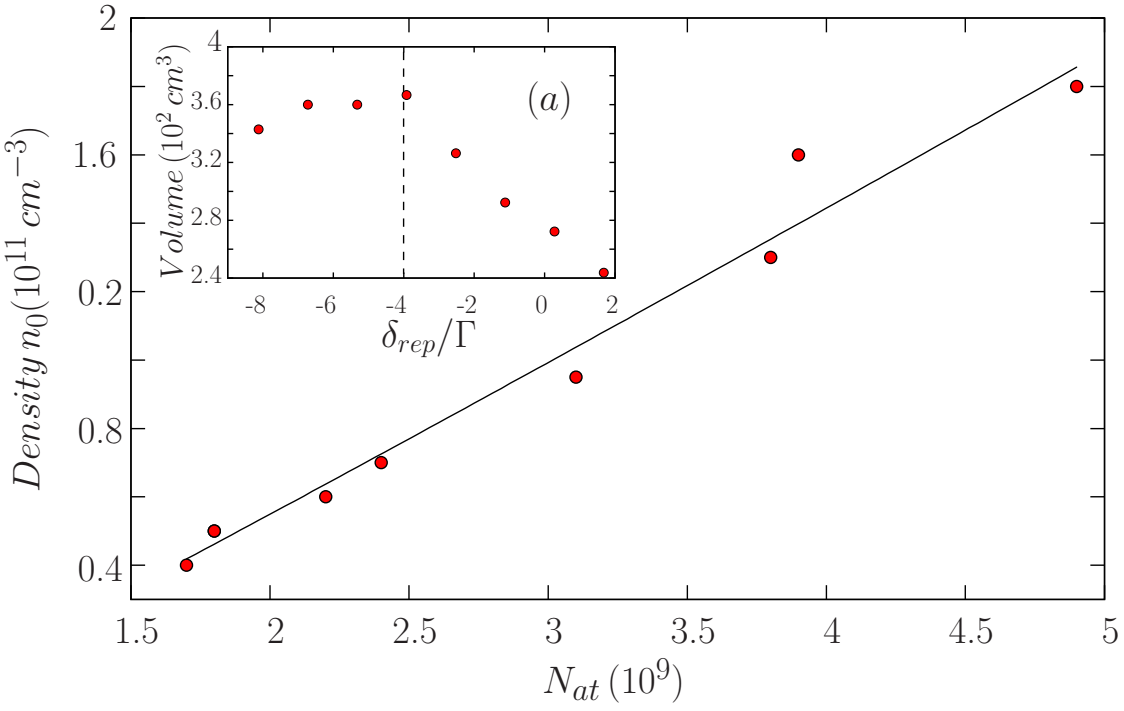

Figure 3.9: *The density (n_0) as a function of N_{at} in the 'Dark-MOT' is reported. As specified in the text, the repumper detuning could only be changed statically, influencing the trap efficiencies. However, as shown by the linear fit, the density is increasing linearly with N_{at}. Therefore, for detuning above -4Γ we observe a compression of the MOT's volume, as underlined by the inset (a). The compression of the MOT could be due to a minimization of the repumper induced interactions.*

Conclusion

We can conclude that for a $p \sim 3\%$ we obtained the maximum density and that the results were compatible with a Wieman-Pritchard model $n_0 \propto 1/p$ as reported in Fig. (3.10). However, we saw a slight decreasing of the density for p as low as 3%. In such a regime, the density scales are as follows: $n_0 \propto p^{0.3}$ as results from the fit. This power law is not compatible with a density limited by the temperature (temperature-limited regime), because in the temperature-limited regime the density scales as follows $p^{3/2}$ [29].
In general, it is well known that in the standard MOT, the effect of scattering radiation generated by a gas of cold atoms increases the temperature as predicted in [39]. In particular, it has been verified that the extra heating is proportional to the optical thickness of the cloud [40]. If we generalize and say that extra heating is only generated by atoms present in the bright state (proportional to $f(p)$), we can arrive at the following expression for the temperature in the MOT:

$$\begin{cases} T &= T_0 + \xi\, b(p) \\ b(p) &= n\,\sigma_L\, L \cdot f(p) \end{cases} \tag{3.4}$$

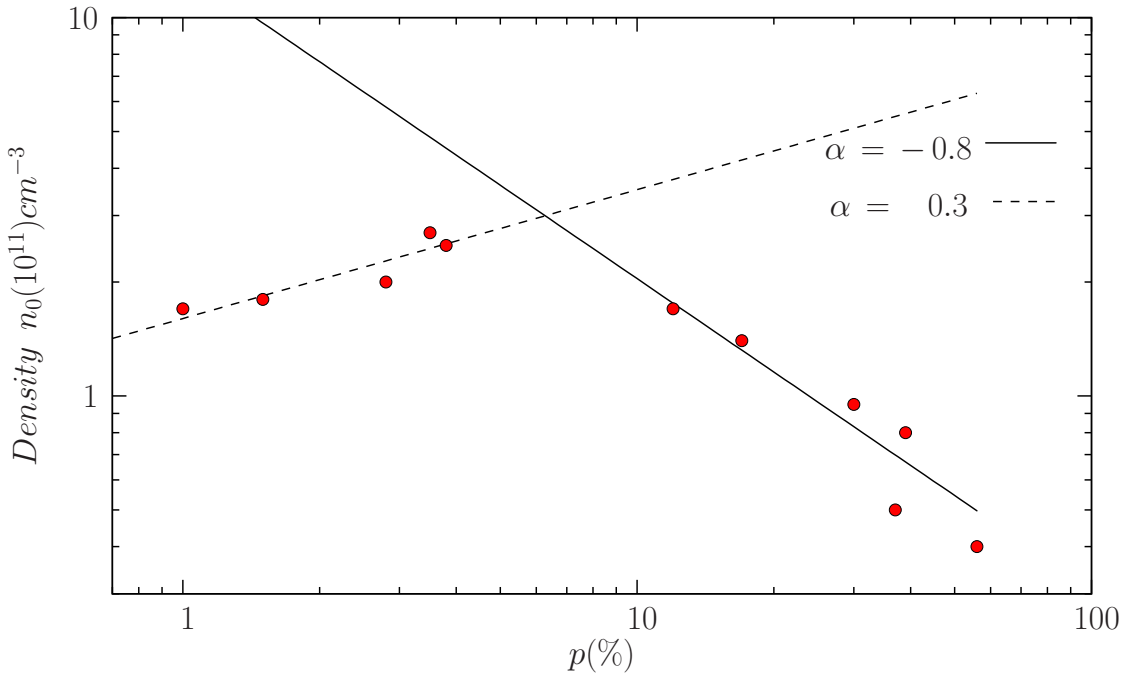

Figure 3.10: *The graph shows the density as a function of p. For the p greater than 3% we found a growth of the density as predicted by the Wieman-Pritchard model. However, below $p = 3\%$, we found that density tended to decrease slightly, which is not well understood.*

where $f(p)$ is *a priori* an unknown function, T_0 is the temperature in the MOT, L is the size of the cloud and ξ is a proportional coefficient depending on the control parameters. In the case where $\xi\, b \gg T_0$, the temperature expressed by Eq. (3.4) results $T \propto \xi\, b(p)$. As we lower p we approach the Temperature-Limited regime where $T \propto L^2\, p$ as predicted by the Wieman-Pritchard model [29] and consequently the density can by rewritten as $n \propto (N/T^{3/2})p^{3/2}$. In the case of constant temperature ($T \sim T_0$) we found the 3/2 power-law as predicted by the Wieman-Pritchard model and experimentally verified with Cs atoms in [35] .

In the case where the temperature is not constant, and considering that the optical thickness can be written as $b = n^{2/3}\sigma_L N^{1/3} \cdot f(p)$, we found the following expression for the density as a function of p :

$$n(p) = \left(\frac{N^{1/4}}{\xi^{3/4}\sigma_L^{1/2}}\right) \cdot \frac{p^{3/4}}{[f(p)]^{3/4}} \tag{3.5}$$

The Eq. (3.5) could explain our observed density measurement, in the case where $f(p) = p^{\beta}$, with a $\beta \sim 1/2$.
However, we are not sure if the approximation made for the temperature is valid or not in our experiments, as ξ is not a trivial function of the control parameters, its estimation could be difficult to calculate and we did not measure it directly.

3.1.2 The Dipole Trap

A focused Gaussian laser ($I(r,z)$) beam tuned far below the atomic resonance frequency represents the simplest way to create a dipole trap providing three dimensional confinement, particularly a potential $U(r,z) \propto I(r,z)$.
In the following section we will describe how we realized and characterized our dipole trap
.

Realization and Characterization

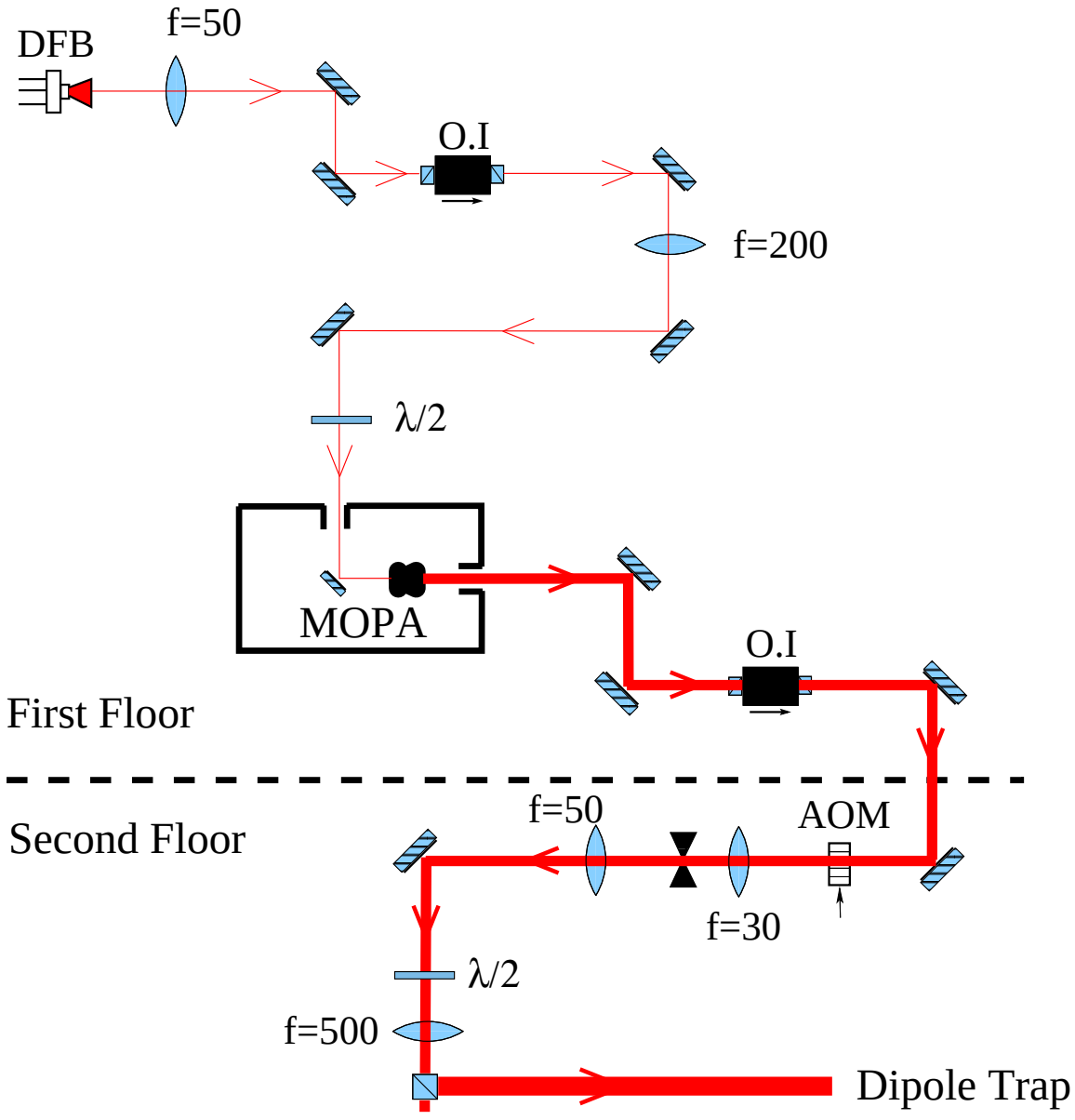

Figure 3.11: *Experimental set up used for the realization of the dipole trap. We used a DFB diode laser, amplified by a MOPA providing an output power of about* $1\,W$.

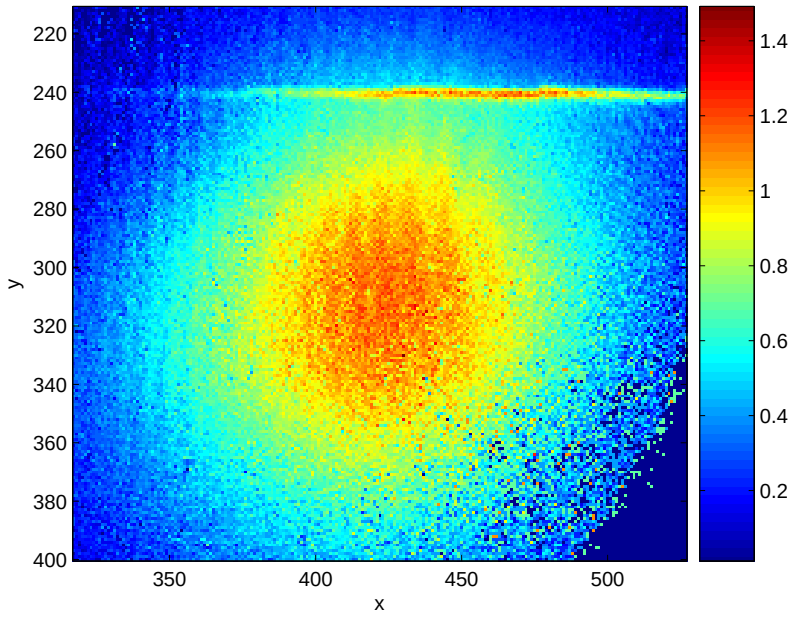

(a)

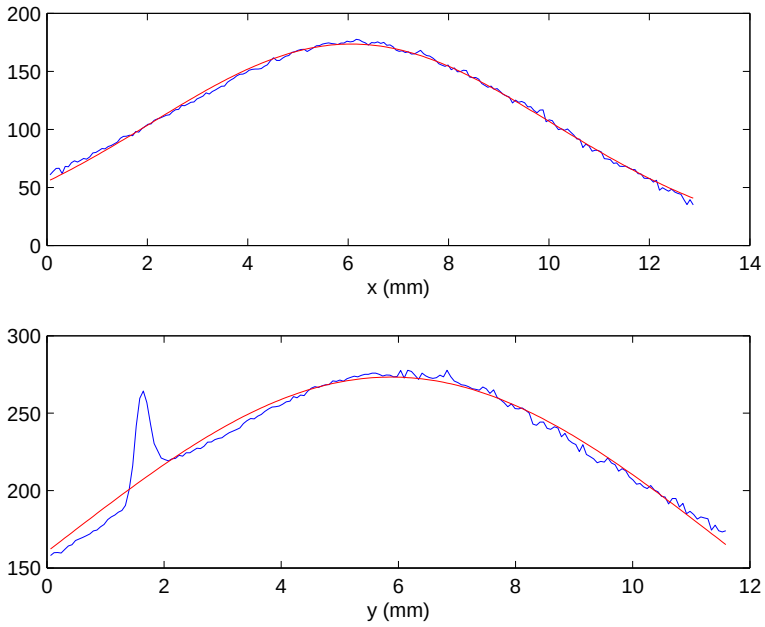

(b)

Figure 3.12: *Figure (a) shows the image of the MOT after* 30 *msec of Time Of Flight (TOF). We clearly see the atoms trapped in the dipole potential, while the rest of the atoms are falling due to gravity. The Gaussian function fits the relative projections on the x and y directions as shown in Figure (b). The typical parameters of the dipole trap are given in the text.*

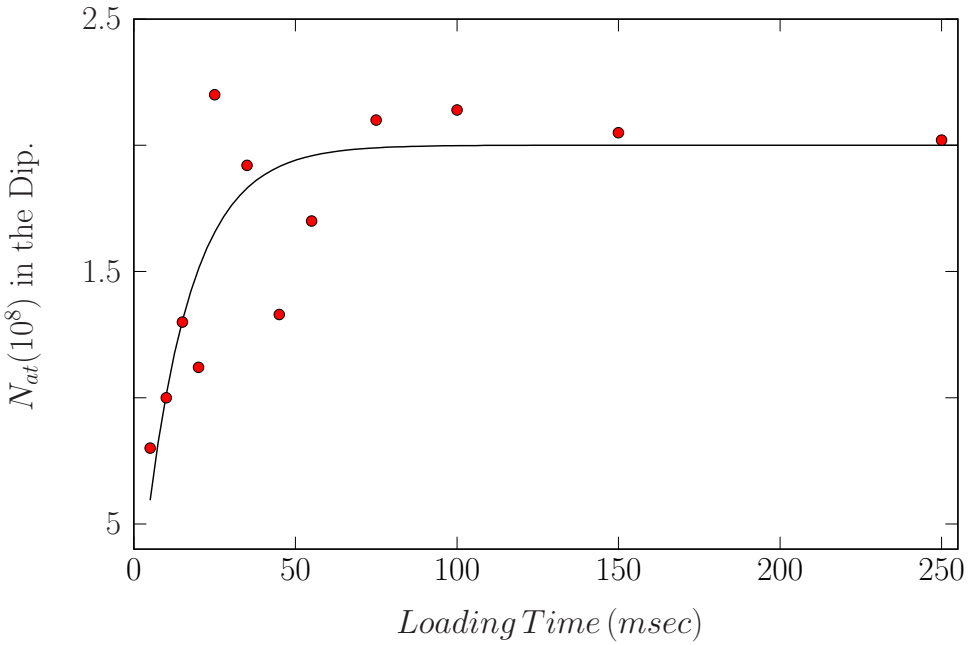

Figure 3.13: *The graph shows the loading of the atoms in the dipole trap with a* $\delta_{dip} = 20\,GHz$. *After* $50\,msec$ *we reached a steady state.*

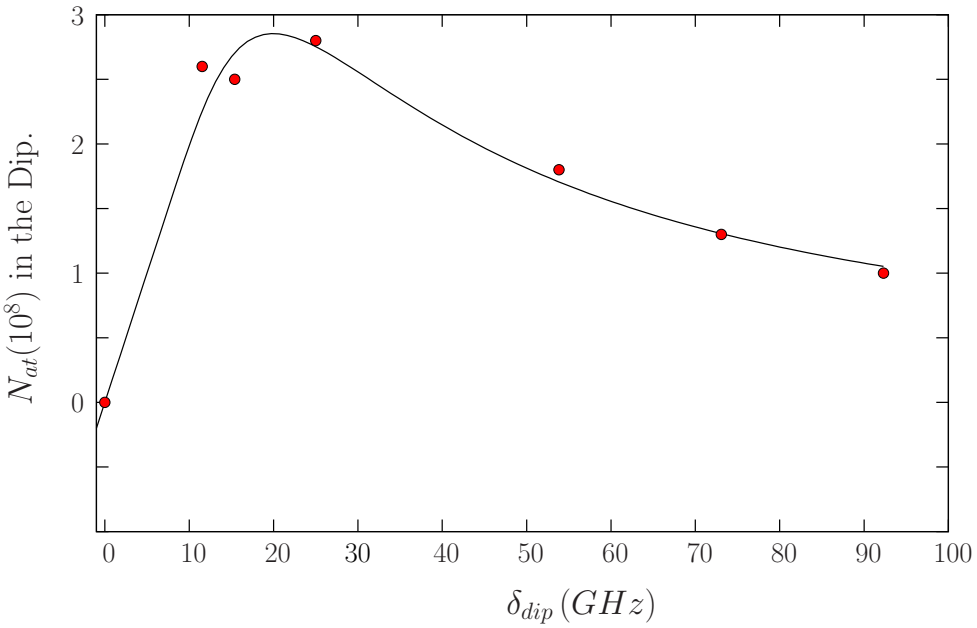

Figure 3.14: *Number of atoms in the dipole trap as a function of the detuning; a maximum is found around* $\delta_{dip} = 20\,GHz$, *which gives* $3\,10^8$ *atoms trapped with a loading-time of* $50\,msec$.

The dipole trap is realized with the set up shown in Fig. (3.11): a free-running laser DFB (with a nominal power of $80\,mW$) is injected into a MOPA laser which provides the DFB with a power amplification of $1\,Watt$.

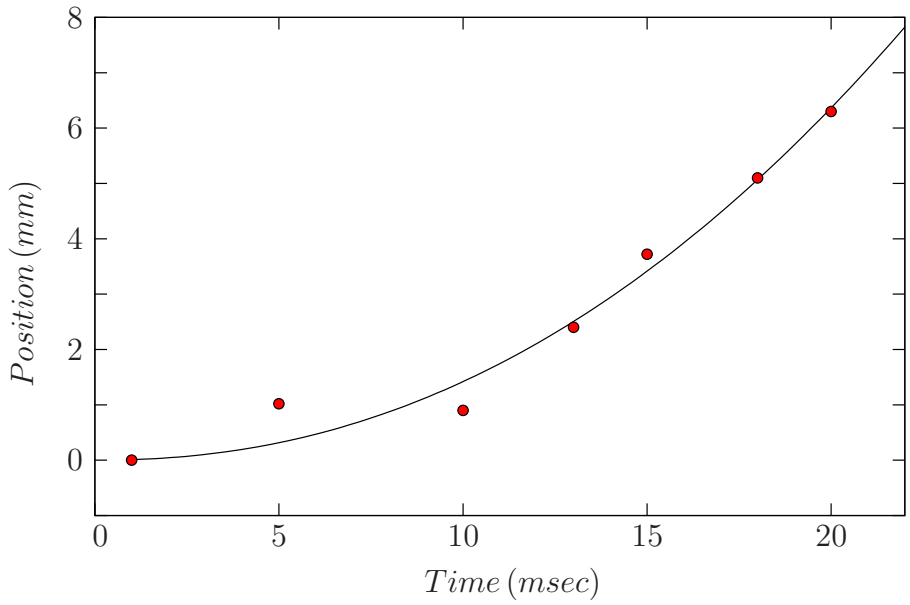

Figure 3.15: *Residual "pushing".*

After a single pass in the AOM on/off and with spatial filtering we ended up with a power of about $240\,mW$ suitable for the dipole trap (with $2\,A$ current in the MOPA power supply).

We controlled the detuning of the DFB by altering its current ($0.52\,mA/GHz$). We can easily red-detune our laser (by increasing the current) by about $100\,GHz$ without any mode-hop. We focused the laser beam, after the power amplification, with a lens of $500\,mm$. We measured a waist $w_0 = 350\,\mu m$, with a beam-profile meter. The maximum trap depth, for a pure Gaussian beam, is given by:

$$U(r=0) = \frac{2P_{dip}}{\pi w_0^2}\frac{3\,\pi\,c^2}{2\omega_0^3}\frac{\Gamma}{|\delta_{dip}|} \tag{3.6}$$

where P_{dip} and δ_{dip} are, respectively, the total power and detuning of the dipole laser. The oscillation frequencies of trapped atoms are given by [41]:

$$\omega_r = \sqrt{\frac{4\,U(r=0)}{m_{Rb}\,w_0^2}} \tag{3.7}$$

in the radial direction, while in the axial direction

$$\omega_z = \sqrt{\frac{2\,U(r=0)}{m_{Rb}\,z_R^2}} \tag{3.8}$$

where $z_R = \dfrac{\pi\,w_0^2}{\lambda}$ denotes the Rayleigh length, in our case $z_R = 50\,cm$, and m_{Rb} the Rubidium mass. To conclude, as the absorption can be interpreted in terms of photon

scattering cycles of absorption and subsequent spontaneous re-emission processes, we can define a scattering rate as:

$$\Gamma_{sp} = \frac{2\,P_{dip}}{\pi w_0^2}\frac{3\pi c^2}{2\hbar\omega_0^3}(\frac{\Gamma}{\delta_{dip}})^2 \tag{3.9}$$

Using the Eq. (3.6) Eq. (3.7), Eq. (3.8) we found, for our dipole trap, the following quantities: $U(r=0,z=0)/k_B = 2\,mK$ ($\sim 1.2\,\Gamma$), $\omega_r = 400\,Hz$ and $\omega_z = 0.2\,Hz$.

After these brief technical details of the set-up, we will discuss the experimental results obtained.

First of all, with the set-up presented in Fig. (3.11), we were able to trap atoms, as shown in Fig.(3.12). We managed to trap $N_{at} \sim 10^8$ with a typical detuning of $\delta_{dip} = 20\,GHz$.

The loading process in the dipole trap is not well understood but we will try to give one possible model.
We followed the same procedure as outlined in the previous section, dealing with the loading of a standard MOT, but instead of considering a 'Hot' vapor for the background, we considered the 'Cold' atoms present in the MOT, and as main loss-processes we considered the scattering rate Γ_{sp} given by the Eq. (3.9). By doing this the atomic time evolution on the dipole trap can be expressed with the following equation:

$$\frac{\partial}{\partial t}\,N_{dip}(t,I,\delta_{dip}) = L(\delta,I)\;-\;\Gamma_{sp}(\delta,I)\cdot N_{dip}\;. \tag{3.10}$$

Eq. (3.10) depends on 3 parameters, but we wanted to work with the maximum intensity, in order to minimize the scattering rate while maintaining a constant dipole trap depth in accordance with Eqs.(3.6)(3.9). As we had limited power (P_{max}) available for the trap in the theoretical model, we eliminated the intensity as an independent variable.
The stationary solution of Eq. (3.10), as we already know, is as follows:

$$N_{dip}(t,\delta_{dip}) = N^{\infty}_{dip}(\delta_{dip})(1-e^{-\Gamma_{sp}(\delta_{dip})\cdot t})\;, \qquad N^{\infty}_{dip} = L_{dip}/\Gamma_{sp}. \tag{3.11}$$

As we have temporal control on the dipole trap, we investigated the loading time of the atom in the dipole trap after the 'Dark-MOT' phase. The results are reported in Fig. (3.13), which fit Eq. (3.11), for a fixed trap detuning $\delta_{dip} = 20\,GHz$ which provides us with the maximum number of atoms trapped, as shown in Fig. (3.14). From the fit we can extract $1/\Gamma_{sp} = 14\,msec$, and $N^{\infty}_{dip} = 2\cdot 10^8$. However, after $50\,msec$ we loaded the maximum number of atoms into the dipole trap, and then we studied its behavior as a function of the δ_{dip}. The loading can be written as $L = \beta/\delta_{dip}$, while the 'loss' term can be written as $\Gamma_{sp} = \alpha/\delta^2_{dip}$. After the above considerations, the Eq. (3.11) for a fixed time $\tau_L = 50\,msec$ could be written as :

$$\begin{cases} N_{dip}(\delta_{dip},\tau_L) & = (\dfrac{\beta}{\alpha})|\delta|_{dip}(1-e^{-\frac{\alpha\cdot\tau_L}{\delta^2}}) \\ U_0(\delta_{dip}) & \gtrsim U_{min} \end{cases} \tag{3.12}$$

where U_{min} is the minimum potential to trap the atoms. From the fit of the data shown in Fig. (3.14) with Eq.(3.12), we can extract $\beta/\alpha = 2 \cdot 10^7 \ (GHz)^{-1}$, and $\alpha = 9361 \ (GHz)^2 \cdot sec^{-1}$, and we find the maximum number of atoms trapped for a $\delta_{dip} = 20\, GHz$.

Using the model given by Eq. (3.12), if we wait for an infinite time τ_L, we only need to raise the detuning δ_{dip} to increase the atoms trapped in the dipole trap. However, we need to account for the residual 'heating' effect which causes a pushing effect,Fig. (3.15). This limits the lifetime of the atoms in the dipole trap. Such an effect was investigated by leaving the dipole laser on for different periods of time while the background MOT expanded freely . From the fit of Fig. (3.15), obtained for a $\delta_{dip} = 20\, GHz$, we measured a residual acceleration of $a = 30\, m/s^2$, so that in $25\, msec$ the atoms in the dipole trap are pushed away by about $1\, cm$. From the measured residual acceleration, we can extract an effective saturation parameter s_{eff} :

$$a = \frac{\hbar\, k\, \Gamma}{2\, m_{Rb}}\, s_{eff} \ , \tag{3.13}$$

which yields a $s_{eff} = 0.2 \cdot 10^{-3}$.

In order to reduce the pushing effects, we have to increase the detuning of the dipole trap, while maintaining the same height of the trapping potential.

3.2 Combined Dark and Dipole Trap: Conclusion

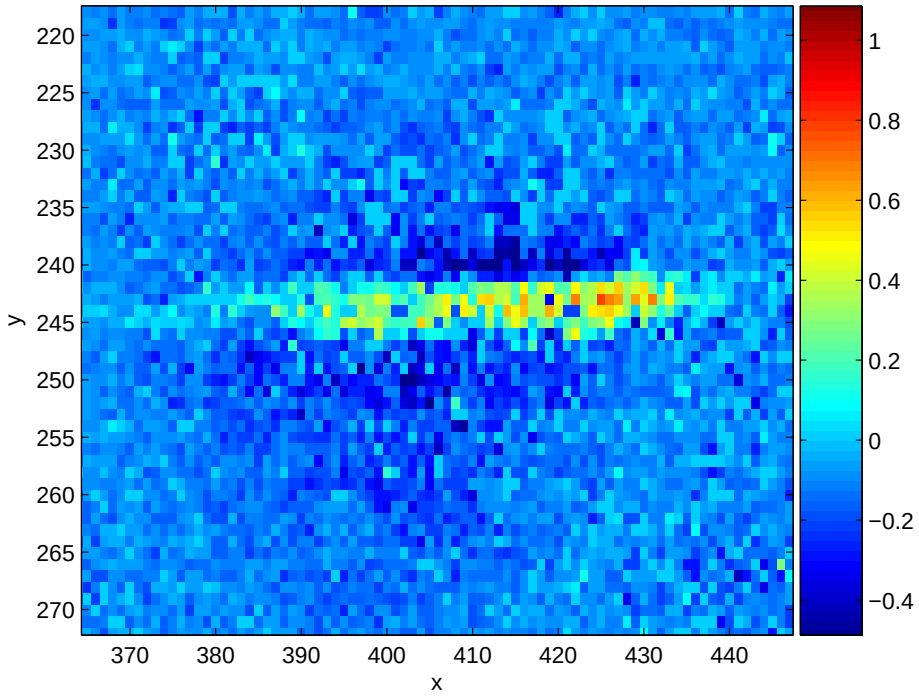

(a)

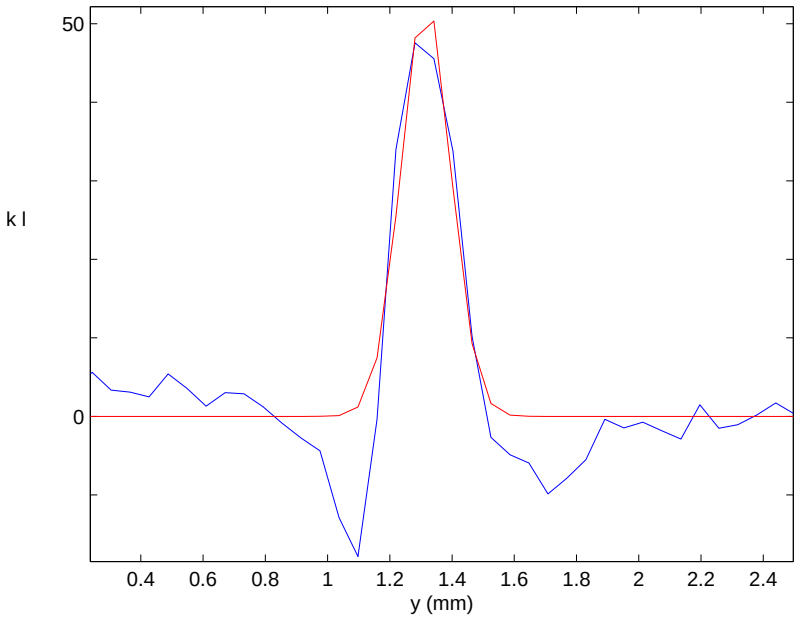

(b)

Figure 3.16: *The dipole trap loaded from a 'Dark-Mot'. We found a peak-density equal to* $n_0 = 10^{12}\, at/cm^3$*, with* $N_{at} = 2\,10^8$ *atoms, and* $\sigma_y = 80\,\mu m$ *and* $\sigma_x 1.2\, mm$*.*

After these optimizations, the maximum density obtained in the combined 'Dark-

MOT' and dipole trap, shown in Fig. (3.16), corresponds to a peak density of $n_0 = 10^{12}\, at/cm^3$ with $N_{at} = 2\,10^8$ atoms and a $\kappa \cdot \ell \sim 50$, one order of magnitude below the localization threshold.
Our dipole trap gives us the possibility of obtaining a very dense atomic sample, but some problems are still evident. For the moment, the density is limited by the maximum number of atoms which can be loaded into the trap. The steady state is reached when an equilibrium between atom loading and atom loss is established. In order to increase the trapping volume, and thus the number of atoms trapped, we need to implement a crossed-dipole trap.

Chapter 4

DFWM

In this chapter after a brief introduction given in Sec. (4.1) we will analyze the Degenerate Four Wave Mixing (DFWM) phenomena in Sec. (4.2), a particular nonlinear process of wave mixing which is made by using the cold atom as a nonlinear medium. In a first model we considered our nonlinear medium to be made of a diluted ensemble of two level atoms characterized by an atomic polarization, Sec. (4.3), which accurately describes the observed signal in the scalar situation. Therefore, if we want a full description of such phenomena, we need to account for the multi-level atomic structure which is introduced in Sec. (4.5).

The set-up used for the experimental observation will be described in Sec .(4.3.1) together with the main results obtained for both the symmetry and resonance shape of the DFWM signal. These latter aspects are the subject of two publications which are also attached.

4.1 Introduction

Nonlinear optics have been investigated for a very long time but the systematic study of these phenomena started to become quantitative after the discovery of the first laser in 1960. Thanks to this increase in research the second-harmonic generation was demonstrated in quartz with the use of a ruby laser [42].

The particular areas of nonlinear optics which will be explored in this section are the phenomena arising from the interaction of four coherent optical fields through third order nonlinear susceptibility. Particularly, this field of physics includes many diverse processes such as, for example, degenerate four-wave mixing (DFWM) non-degenerate four-wave mixing (NDFWM), stimulated Raman scattering etc.

These processes have proved to be of use in a great number of applications including optical processing, phase conjugate optics, the measurement of atomic energy structures and decay rates. In the case of NDFWM, where the two strong pumps have the same frequency while the frequency of the probe is varied, the observed spectral profiles are narrower than the natural linewidth of excited state [43]. This particular pump-probe spectroscopy can also be used as a highly sensitive diagnostic tool for atoms in a working MOT [44]. Particularly, the transient FWM signal can be used for temperature diagnostics for cold atoms [45] where a population grating in the ground state of the hyperfine atomic level is induced by the two strong pumps. Thus, the decay time of this grating is directly

related to the temperature of the cold atoms. Also, light storage processes in an ensemble of cold atoms using FWM are possible [46]. Indeed, a polarization grating is written into the atomic system as a spatially dependent Zeeman coherence, and after a dark time of about $4\,\mu sec$ can be read. This observation is proof that we can store information locally in the cold atoms. Such studies can be important for the realization of quantum memories, and are generally important in the quantum information field.

In our case we concentrated on Degenerate-Four Wave Mixing (DFWM), where the two strong pumps and weak probe have the same frequency (ω_L).

In general, two phase matching geometry is used in order to obtain the signal of the DFWM [47]. The first is the backward four-wave mixing configuration, as shown in Fig. (4.1), in which two pumps are counter propagating and a probe signal is coming at an angle of θ with respect to the pump axis Fig. (4.1). The second is the forward four-wave mixing configuration, where all beams (pumps and probe) are co-propagating.

For practical reasons, we used backward phase matching geometry in our experiments.

4.2 Theory of DFWM

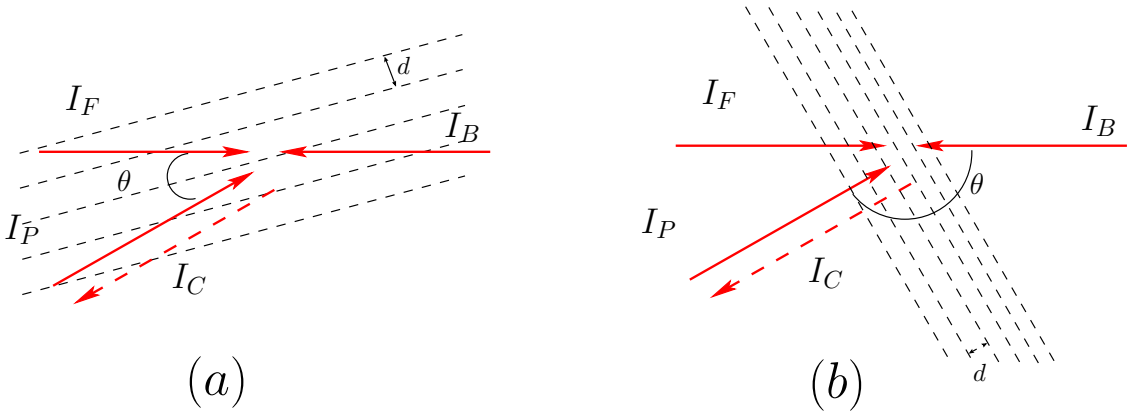

Figure 4.1: *Illustration shows the conventional geometry of phase conjugation through DFWM where we have two strong pumps (I_F and I_B) and a weak probe I_P. In Fig-(a) a grating between I_F and I_P is made in which the I_B is Bragg-diffracted. In Fig-(b) the grating where the I_B is diffracted is created by I_B and I_P. The two processes interfere with each other generating the phase-conjugate beam I_C.*

In the following section, we will focus on the basic theory of coherent third order nonlinearity that gives rise to the DFWM phenomena. The four-wave mixing is called degenerated because all the frequencies, two strong pumps and the weak probe, are the same.

In general, the concept of three electromagnetic fields interacting to produce a fourth field is central to the description of all four-wave mixing processes. In order to understand this process we need to consider the individual interactions of the fields within a dielectric medium. The first input field causes an oscillating polarization in the dielectric with the same frequency as the driven field; this is just the Rayleigh scattering as described by linear optics. The application of a second field will also drive the polarization of the dielectric, and the interference of the two waves will cause harmonics in the polarization at the sum and difference of the frequencies. Finally, the application of the third field will also drive the polarization and this will beat with both the other input fields as well as with the sum and difference frequencies. This beating with the sum and difference frequencies is what gives rise to the fourth field in four-wave mixing. The DFWM process could be interpreted in terms of the intensity dependent refractive index. Two input beams interfere, generating a grating, which is characterized by a distance $d = \dfrac{\lambda}{2sin(\theta/2)}$. From this grating the third beam is Bragg-diffracted, and generates the phase-conjugate wave. This is because the interferences result in a spatially periodic light intensity or distribution of polarization, that induces a spatial modulation in the medium. In our case the different situations are illustrated in Fig. (4.1), which gives an intuitive picture of the generated backward field.

In the case where the probe beam has a polarization that is orthogonal to the polarization of the pump beams, the intensity grating formed in the medium is a polarization

grating. That is, the interference results in a spatially uniform intensity, but a periodic variation of the polarization is realized in the direction of the optical electric field.

The traditional method of modeling the nonlinear response of an optical material is to expand the induced polarization as a power series in the electric field strength [47] :

$$\vec{P} = \chi^{(1)} \cdot \vec{E} + \chi^{(2)} \cdot \vec{E}\vec{E} + \chi^{(3)} \cdot \vec{E}\vec{E}\vec{E} + ... \tag{4.1}$$

This method assumes that the higher order susceptibilities grow progressively smaller so that the power series expansion converges to a finite polarization, which means that the $\chi^{(3)}E^2 \ll \chi^{(1)}$ and so on.

In the Eq. (4.1) the obtained third order nonlinear susceptibility $\chi^{(3)}$ is responsible for the four-wave mixing processes [47].

In general, $\chi^{(3)}$ is a fourth rank tensor with 81 elements [47] and each of these elements consists of a sum of 48 terms. This number of terms is drastically reduced through material symmetries and resonance. Explicit expression for the terms have been published, and each term has a typical form with three resonant factors in the denominator. Also, we highlight that the tensor properties of the susceptibility are derived from the vector properties of the dipole matrix elements. Indeed, by knowing the symmetry properties of such a tensor we can further simplify the general expression of $\chi^{(3)}$.

In the following, we will introduce the input scalar fields defined in accordance with the equations:

$$E_l(\vec{r}, t) = \frac{A_l(\vec{r})}{2} e^{i(\vec{k}_i \cdot \vec{r} - \omega_i \cdot t)} + c.c \qquad l = 1, 2, 3 \tag{4.2}$$

specialized in the degenerate case, which means $\omega_1 = \omega_2 = \omega_3 = \omega$. The nonlinear third order polarization produced by the interaction of the three beams oscillates at the same frequency as the input field:

$$\begin{aligned} P_l(\omega) &\propto \chi^{(3)}_{ljkm} E_j E_k E^*_m \\ &\propto \chi^{(3)}_{ljkm} A_j(\vec{r}) A_k(\vec{r}) A^*_m(\vec{r}) e^{[i(\vec{k_1} + \vec{k_2} - \vec{k_3}) - i\omega t)]} \end{aligned} \tag{4.3}$$

Since the physical quantity that is measured in the experiment is the conjugate field intensity, the observed signal will be proportional to $|\chi^{(3)}|^2$ multiplied by the three field intensities and by a "phase matching factor". As the intensity of the phase-conjugate signal is assumed to be I_C, in the case where the pump intensities are the same $I_B = I_F = I_0$, and with a probe intensity I_P, the conjugate signal should be proportional to :

$$\begin{aligned} I_C &= \eta I_B I_F I_P \\ &= \eta I_0^2 I_P \end{aligned} \tag{4.4}$$

but as the intensity of the probe can be expressed $I_P = \alpha I_0$ the Eq. (4.4) becomes:

$$I_C = \beta I_0^3 , \qquad \beta = \eta \cdot \alpha \tag{4.5}$$

The functional dependence on intensity of Eq. (4.5) could be checked in an experiment to test whether the signal measured is due to third order mixing effects. Indeed, such nonlinear susceptibility could be measured because it is proportional to the β value. We also measured the reflection coefficient, defined as $R_{DFWM} = \frac{I_C}{I_P}$. The functional dependence of the reflection coefficient in this case became:

$$R_{DFWM} = \frac{I_C}{I_P} = \beta\, I_0^2 \ , \tag{4.6}$$

and it scaled quadratically on the laser intensity.

In the following we recall some basic relations for the wave on a polarizable media.

Wave Propagation

We started from a definition of Maxwell's equations, as is normal in cases where there is no free charge and no free currents are present and the material is nonmagnetic; in such a case it can be shown that Maxwell's equations are expressed by the following equations [48]:

$$\begin{aligned} \vec{\nabla}\cdot\vec{D} &= 0 & \vec{\nabla}\times\vec{E} &= -\frac{\partial\vec{B}}{\partial t} \\ \vec{\nabla}\cdot\vec{B} &= 0 & \vec{\nabla}\times\vec{B} &= \mu_0\frac{\partial\vec{D}}{\partial t} \end{aligned} \tag{4.7}$$

with the definition of vector $\vec{D} = \varepsilon_0\vec{E} + \vec{P}$.

In a homogeneous and isotropic medium the polarization is parallel to the electric field, and the relation between the two fields can be written as $\vec{P} = \varepsilon_0\chi(E)\vec{E}$, where $\chi(E)$ is a scalar quantity which gives rise to the total nonlinear susceptibility.

As we have already shown, $\chi(E)$ can be decomposed in two terms, the linear (χ_0) and nonlinear (χ_{NL}). In the same way, the polarizability vector can be decomposed as well.

After these considerations, we can solve the system of Eqs.(4.7) by following the standard procedures [48], and we end up with a general form for wave equations in nonlinear optics:

$$\vec{\nabla}\times\vec{\nabla}\times\vec{E} = \vec{\nabla}(\vec{\nabla}\cdot\vec{E}) - \nabla^2\vec{E} = -\mu_0\frac{\partial^2\vec{D}}{\partial^2 t} \ . \tag{4.8}$$

As in the afore-mentioned geometry the electric field of the pumps and the probe lies on the plane defined by $\vec{E}\cdot\vec{k}$, the quantity $\vec{\nabla}\chi$ is always perpendicular to $\vec{E}$ without any restriction on the $\chi(z)$. Consequently, from the relation $\vec{\nabla}\cdot\vec{D} = 0$, we obtain $\varepsilon_0(1+\chi)\vec{\nabla}\cdot\vec{E} + \varepsilon_0(\vec{E}\cdot\vec{\nabla}\chi) = 0$ and in this case we can conclude that $\vec{\nabla}\cdot\vec{E} = 0$ when $\vec{E}\cdot\vec{\nabla}\chi = 0$.

By using such an assumption, the wave equation reads:

$$\nabla^2\vec{E} - \varepsilon_0\mu_0\frac{\partial^2\vec{E}}{\partial t^2} = \mu_0\frac{\partial^2(\vec{P}_L + \vec{P}_{NL})}{\partial t^2} \tag{4.9}$$

where $\vec{E}$ is the total field.

As the definition of the fields is given by Eq.(4.2) we can separately calculate the left-hand term of Eq.(4.9):

$$\nabla^2\vec{E}_l \cong -2ik_l e^{ik_l z}\frac{\partial A_l}{\partial z} - k_l^2 A_l(z)e^{ik_l z} + c.c. \qquad l = 1,2,3,4 \tag{4.10}$$

where we have used the slowly varying envelope approximation (S.V.E.A) which consists of:

$$\left|\frac{\partial^2 E_l}{\partial z^2}\right| \ll \left|k_l\frac{\partial E_l}{\partial z}\right| \qquad l = 1,2,3,4 \tag{4.11}$$

We specialized in degenerate four wave mixing (DFWM) ($\omega_1 = \omega_2 = \omega_3 = \omega$) and considered the following phase-matching condition expressed by:

$$\vec{k}_1 + \vec{k}_2 + \vec{k}_3 + \vec{k}_4 = 0 \tag{4.12}$$

which, in the case of our backward geometry, $\vec{k}_1 + \vec{k}_2 = 0$, becomes:

$$\begin{cases} \vec{k}_1 + \vec{k}_2 = 0 \\ \\ \vec{k}_3 + \vec{k}_4 = 0 \end{cases} \tag{4.13}$$

After taking the phase-match condition into consideration, the wave propagation of the conjugate field $\vec{E}_4$ is given by :

$$2\,i\,k\frac{\partial A_4}{\partial z} = -\mu_0\omega^2 P_4(\omega_4, k_4) \tag{4.14}$$

where the notation $P_4(\omega_4)$ indicates the Fourier polarization component which is oscillating at the frequency ω_4 with a k_4 wave-vector.

In our case we used a cloud of cold Rb atoms as a strong non-linear medium. The main difference with respect to the non-linear crystal is that the radiation used to pump the medium, in order to obtain nonlinearities, is almost resonant and shows strong resonances and consequent dispersion.

In the simplest case of a two-level atom, with an atomic susceptibility of $\chi(\omega)$ it can be shown that the resonance is $Im(\chi(\omega)) \propto \dfrac{1}{1+\delta^2}$ in which we found the Lorentzian shape, while the absorption is given by $Re(\chi(\omega)) \propto \dfrac{-\delta}{1+\delta^2}$, which is the normal dispersion signal. Furthermore, wave propagation in the medium is characterized by a k-vector defined as $k = n\,\dfrac{\omega}{c}$ where the diffraction index is given by $n = \sqrt{(1+\chi)}$.

However, a full description of nonlinear susceptibility in our case is more involved due to the real multilevel atomic structure, as we will see in Sec. (4.5).

After this brief introduction to Four-wave mixing in general dielectric media, we will concentrate on Degenerate Four-Wave Mixing considering an ensemble of a number (N) of two-level atoms.

4.3 Two-Level Atoms

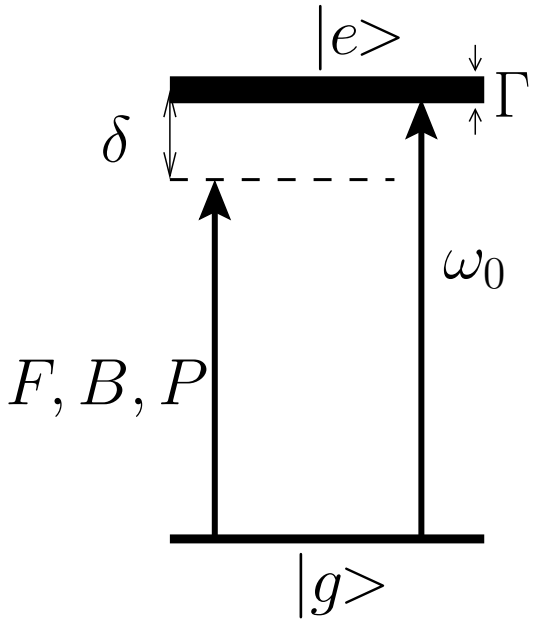

Figure 4.2: *The two level atoms scheme. In the case where all the beams have the same linear parallel polarization, the DFWM signal originates from the contribution of a two level atom with a lifetime* Γ *due to spontaneous emission.*

For a two-level atom at rest in the steady state, we can write the susceptibility as :

$$\chi(|E|) \;=\; -\sigma_0\, n_{at} \frac{(-i+\delta)}{(1+\delta^2+|(E/E_s)|^2)} \tag{4.15}$$

where $\sigma_0 = \dfrac{3\lambda^2}{2\pi}$, and with n_{at} we indicate the atomic density; $\delta = 2\,(\omega - \omega_{at})/\Gamma$ is the detuning in Γ unit (the atomic lifetime of a two level atom), and $|E_s^2|$ is proportional to the saturation intensity defined as $I_s = \dfrac{1}{2}\varepsilon_0 c|E_s|^2$.

The σ_0 is the on-resonance cross-section with k the magnitude of the wave number at the frequency ω.

Eq.(4.15) is compatible with a definition of the oscillating field $E(t) = E_0 e^{i\omega t}$; otherwise if we use a $E(t) = E_0 e^{-i\omega t}$ we have to replace i with $-i$ in Eq.(4.15).

The polarization is then expressed by the equation:

$$\vec{P} = \varepsilon_0 \chi(\vec{E}) \cdot \vec{E}\ . \tag{4.16}$$

Following the idea developed in Sec.(4.2) which gives rise to Eq. (4.1), we decided to carry out a development series, by considering two strong pumps $(\vec{E_1}, \vec{E_2})$ and a small probe $\vec{E_3} \ll \vec{E_1}, \vec{E_2}$. Consequently the conjugate generate field is $\vec{E_4} \ll \vec{E_1}, \vec{E_2}$. After such a consideration, we can define the total field as:

$$\begin{cases} \vec{E} = \vec{E_0} + \Delta\vec{E} & , \Delta\vec{E} \ll \vec{E_0} \\ \vec{E_0} = \vec{E_1} + \vec{E_2} \end{cases} \tag{4.17}$$

Now we can insert the Eq. (4.17) into the Eq. (4.16) and we expand the susceptibility to the first order in $\Delta\vec{E}$:

$$\begin{aligned} \chi(|E|)\cdot\vec{E} &= -2\frac{n_{at}\,\sigma_0}{k}\,\frac{(i+\delta)(E_0+\Delta E)}{(1+\delta^2+|(E_0+\Delta E)/E_s|)^2} \\ &= -2\frac{n_{at}\,\sigma_0}{k}\,\frac{(i+\delta)(E_0+\Delta E)}{(1+\delta^2+|(E_0/E_s)|^2|(1+\frac{\Delta E}{E_0})|^2)} \end{aligned} \tag{4.18}$$

If we make the following observation:

$$\begin{aligned} \left|1+\frac{\Delta E}{E_0}\right|^2 &= (1+\frac{\Delta E}{E_0})(1+\frac{\Delta E^*}{E_0^*}) \\ &= (1+\frac{\Delta E^*}{E_0^*}+\frac{\Delta E}{E_0}+O(|\Delta E|^2)). \end{aligned} \tag{4.19}$$

By using such an observation, we can rewrite Eq. (4.18) in the following way:

$$\chi(|E|)\cdot E = -2\frac{n_{at}\,\sigma_0}{k}\,\frac{(i+\delta)(E_0+\Delta E)}{(1+\delta^2+|(E_0/E_s)|^2)}(1-\frac{(E_0\Delta E^*+E_0^*\Delta E)}{|E_s|^2}\frac{1}{1+\delta^2+|(E_0/E_s)|^2}) \tag{4.20}$$

$$= -2\frac{n_{at}\,\sigma_0}{k}\,\frac{(i+\delta)(E_0+\Delta E)}{(1+\delta^2+|(E_0/E_s)|^2)} - 2\frac{n_{at}\,\sigma_0}{k\cdot|E_s|^2}\,\frac{(i+\delta)(E_0+\Delta E)}{(1+\delta^2+|(E_0/E_s)|^2)}(E_0^2\Delta E^*+|E_0|^2\,\Delta E)$$

If we introduce linear atomic susceptibility as:

$$\chi_0(E_0) = -\frac{2\,i\,n_{at}\,\sigma_0}{k}\,\frac{(1-i\delta)}{(1+\delta^2+|\frac{E_0}{E_s}|^2)}\,, \tag{4.21}$$

we are able to define the atomic polarization as :

$$\vec{P}(E) = \varepsilon_0\chi_0(\vec{E_0}+\Delta\vec{E}) - \underbrace{\frac{\varepsilon_0\chi_0}{|E_s|^2}\frac{(E_0^2\Delta E^*+|E_0|^2\Delta E)}{(1+\delta^2+|(E_0/E_s)|^2)}}_{\|\;P_{NL}(E)} \tag{4.22}$$

The second term of the right-hand part of Eq.(4.22), is the nonlinear polarization which we call $P_{NL}(E)$. Such an expression contains all the high order susceptibilities because of the presence of the saturation intensity.

The expression of the polarization given by Eq. (4.22) is the same found in the reference [49].

Finally, if the nonlinear polarization is substituted into Maxwell's equations, a set of four coupled wave equations may be found for the fields. If we focus on the wave propagation of the phase generated conjugate beam, after some calculation we can demonstrate that the Fourier component of the polarization oscillating at the frequency ω_4, is expressed by:

$$\begin{cases} P_4 = \varepsilon_0\chi_0 A_4 - \dfrac{\varepsilon_0\chi_0}{I_s(1+\frac{|E_0(z)|^2}{I_s})}(I_1 e^{-2ikz} + I_2 e^{2ikz} + 2\sqrt{I_1 I_2})A_3^* \\ \\ I_s \propto (1+\delta^2)|E_s|^2 \end{cases} \tag{4.23}$$

which can be inserted into Eq.(4.14), to obtain the following wave propagation equation for the conjugate field:

$$\frac{\partial A_4}{\partial z} = \alpha(z)A_4 + i\kappa(z)A_3^* \ . \tag{4.24}$$

The spatial dependent coefficients are given by the following expression:

$$\begin{cases} \alpha(z) = \sigma_0\, n_{at}\, \dfrac{(1-i\delta)}{(1+\delta^2)}\dfrac{1}{(1+\frac{|E_0|^2}{I_s})^2} \\ \\ \kappa(z) = i\sigma_0\, n_{at}\, \dfrac{(1-i\delta)}{I_s(1+\delta^2)}\dfrac{(I_1 e^{-2ikz} + I_2 e^{2ikz} + 2\sqrt{I_1 I_2})}{(1+\frac{|E_0|^2}{I_s})^2} \end{cases} \tag{4.25}$$

where, as usual, σ_0, n_{at}, and δ are respectively the on resonance cross-section, the atomic density and the laser detuning.

Following the same procedure described above, we can obtain a similar wave propagation equation for the probe A_3.

The intensity of the phase conjugate beams is then determined by the power reflection coefficients, for a nonlinear medium L long, expressed by [49] :

$$R \ = \ \frac{|\kappa \ \sin(w\, L)|^2}{|w \ \cos(w\, L) + \ \alpha_R \ \sin(w\, L)|^2} \tag{4.26}$$

where $w \ = \ \sqrt{|\kappa|^2 - \alpha_R^2}$ is a measure by which the strength of the nonlinearity exceeds the absorption in the medium, and $|E_0(z)|^2 \ \propto \ 4\, I\, cos^2(kz)$ is our definition of standing waves.

In the case of a small amount of absorption, i.e small optical thickness ($b_0 = n_{at}\sigma_0 L \ll 1$), we can consider the limit $w\, L \ll 1$ of the reflection coefficient expressed by Eq.(4.26). In such a regime we observed that a more suitable parameter to describe the phase conjugate beam is the on-resonance optical thickness (b_0), in fact:

$$R \ \propto \ n_{at}^2 \cdot \ L^2 = const \cdot \ b_0^2 \ . \tag{4.27}$$

Such a relationship has been demonstrated experimentally for moderate optical thicknesses ranging from 0 to 5 [50].

In the case where we have the same pump intensities ($I_1 = I_2 = I$), and performing a spatial average of the intensity by setting $cos^2(kz) = 1/2$, the expression of the coefficients given in Eq. (4.25), became:

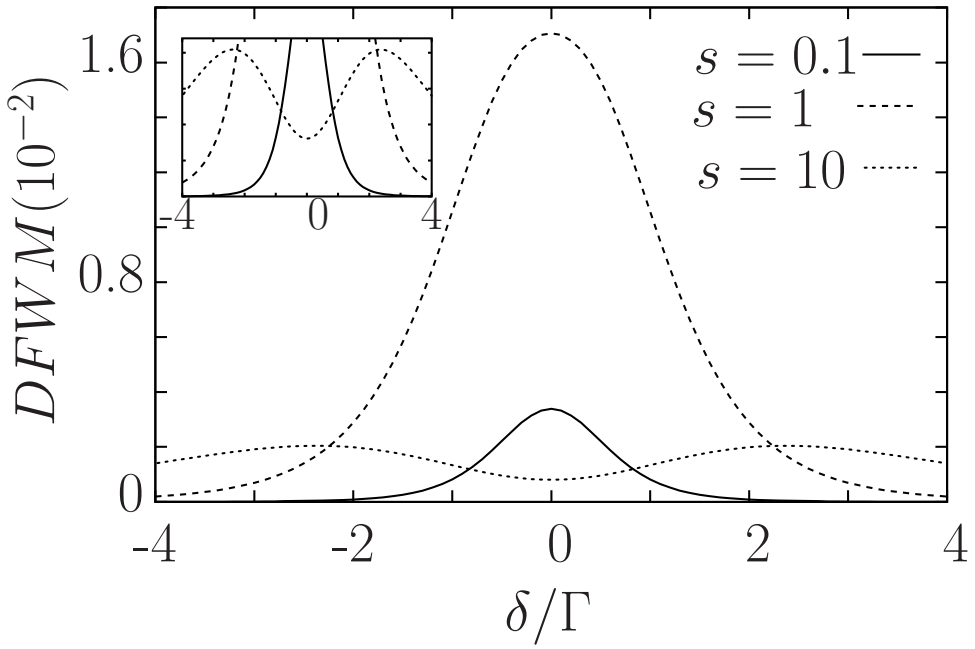

Figure 4.3: *Degenerate Four Wave Mixing theoretical signal when all fields have the same polarization by considering an averaged intensity by setting* $cos^2(kz) = 1/2$. *We observe a clear splitting, as underlined by the inset, for high pump intensities (*$s = 10$*). The on-resonance optical thickness for such curves was* $b_0 = 0.6$.

$$\begin{cases} \alpha(z) = \sigma_0\, n_{at}\, \dfrac{(1 - i\delta)}{(1 + \delta^2)}\, \dfrac{1}{(1 + 2\frac{s}{(1+\delta^2)})^2} \\ \\ \kappa(z) = i\sigma_0\, n_{at}\, \dfrac{(1 - i\delta)}{(1 + \delta^2)}\, \dfrac{2 \cdot s}{(1 + 2\,\frac{s}{(1+\delta^2)})^2} \end{cases} \tag{4.28}$$

where we introduced the saturation parameter $s = I/I_s$. By using such coefficients, we can compute the reflection coefficient for the conjugate beams for any optical thickness and saturation parameter. As shown in Fig.(4.3), the conjugate signal (R) shows one interesting feature; a clear splitting in the limit of high pump intensity ($s = 10$) even considering a small optical thickness ($b_0 = 0.6$).

Spatial Average

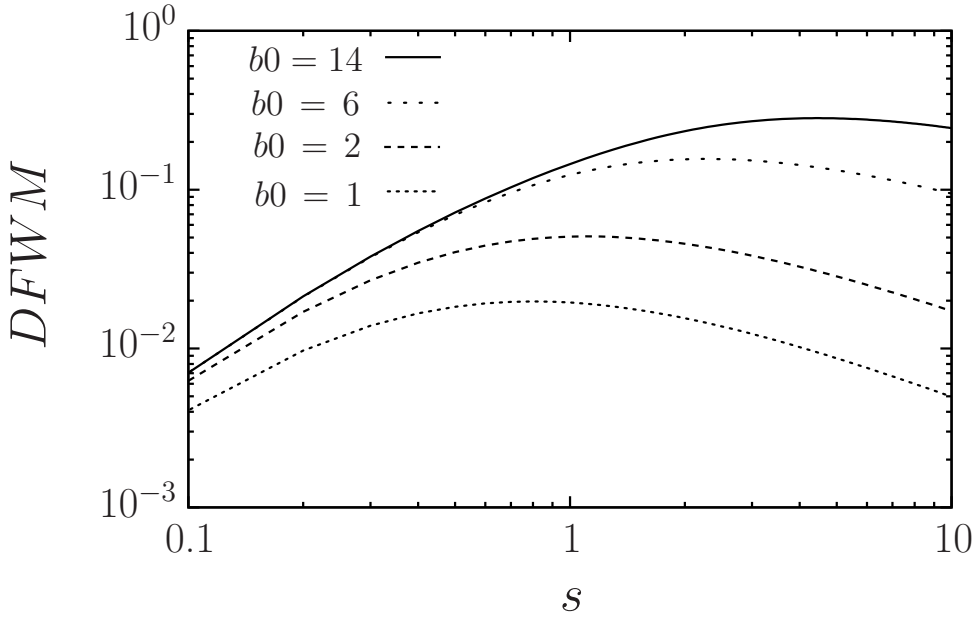

Figure 4.4: *DFWM signal obtained by considering the average coefficients given by Eqs.(4.29) versus the pump saturation parameters at resonance $\delta = 0$, and considering different optical thicknesses b_0.*

In the above considerations, the expression for the conjugate beam was obtained by taking the average value of the total intensity. In fact, the coefficients presented in Eq.(4.24) have spatial dependence, and as our atomic sample extended more than one wave-length, a spatial average had to be considered by averaging the polarizability and not the intensity in accordance with the reference [51]. We achieved this by integrating these coefficients over a $\lambda/2$ by computing the following integrals:

$$\langle \alpha(z) \rangle \;=\; \int_0^{\lambda/2} \alpha(z)\, dz \;, \qquad\qquad \langle \kappa(z) \rangle = \int_0^{\lambda/2} \kappa(z)\, dz \;. \tag{4.29}$$

The expressions of Eqs.(4.29) can be found analytically, considering a constant atomic density ($n_{at}(z) = const$), and setting the pump values as the same ($I_1 = I_2 = I_0$). After some calculation, the averaged coefficients can be written as:

$$\begin{cases} \langle \alpha(z) \rangle \;=\; n_{at}\, \sigma_0 \dfrac{(1 - i\delta)}{(1 + \delta^2)} \dfrac{(1 + 2I/I_s)}{[1 + 4(I/I_s)]^{3/2}} \\ \\ \langle \kappa(z) \rangle \;=\; -\, n_{at}\, \sigma_0 \dfrac{(1 - i\delta)}{(1 + \delta^2)} \dfrac{(2I/I_s)}{[1 + 4(I/I_s)]^{3/2}} \end{cases} \tag{4.30}$$

The Eqs. (4.30) are the same as that found in reference [51].

In the limit of small absorption ($w\, L \ll 1$), as before we can arrive at an analytical expression of the reflected coefficient (or DFWM signal). In such a limit, as we had

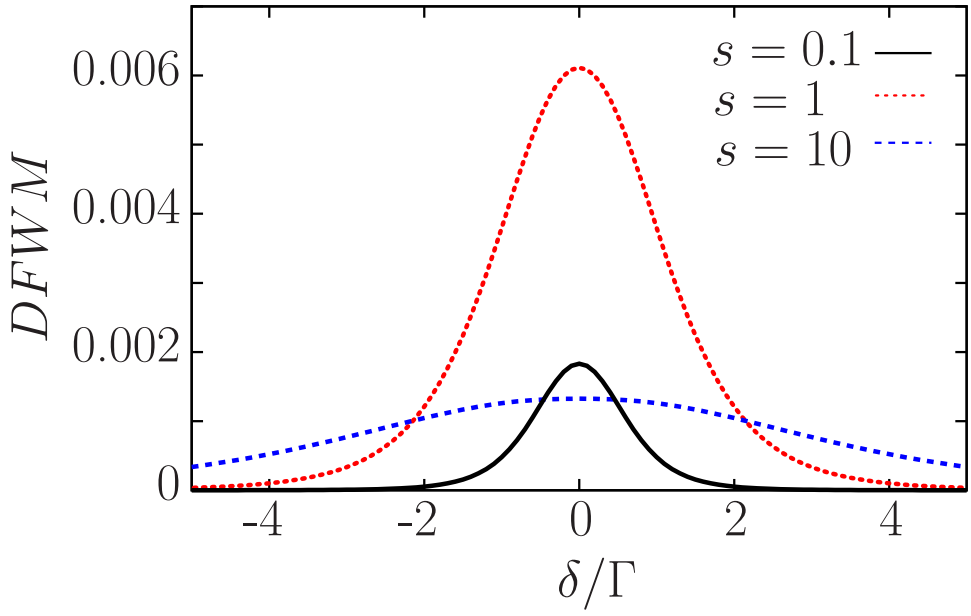

Figure 4.5: *DFWM signal obtained in the limit of small optical thickness ($b_0 = 0.6$) and for different saturation parameters. The double peak structure is no longer observed.*

already noticed, the reflection coefficient is proportional to the $R \cong |\langle\kappa\rangle|^2 L^2$, and precisely expressed by the following equation:

$$R \cong \frac{n_{at}^2\,\sigma_0^2\,L^2}{(1+\delta^2)}\,\frac{4\,(I/I_s)^2}{(1+4I/I_s)^3}\ . \tag{4.31}$$

From Eq. (4.31) we observe that the signal has a Lorentzian-like shape symmetrical in δ, and proportional to the square of the optical thickness. Moreover, in the limit of high-pump intensity ($I/I_s \gg 1$) the signal R goes to zero as shown in Fig. (4.4).

To conclude, the main difference with respect to the reflected signal obtained without the spatial average, is that there is no longer a double peak structure for larger intensity as reported in Fig.(4.5). In fact, this feature has been eliminated by considering the spatial averaging of the polarizability as discussed in references [49] [51]. But even in this case, a more trivial center line splitting could be observed in the high optical thickness limit ($b_0 \gg 1$) as shown in Fig. (4.6).

However, as we will see later on in the case where the polarization of the probe is perpendicular to that of the pumps and in the limit of small absorption, we can experimentally observe a splitting, but this time, if we want to understand its nature, we need to use a more complicated model in which the multi-level atomic structure has to be included, as discussed in Sec.(4.5).

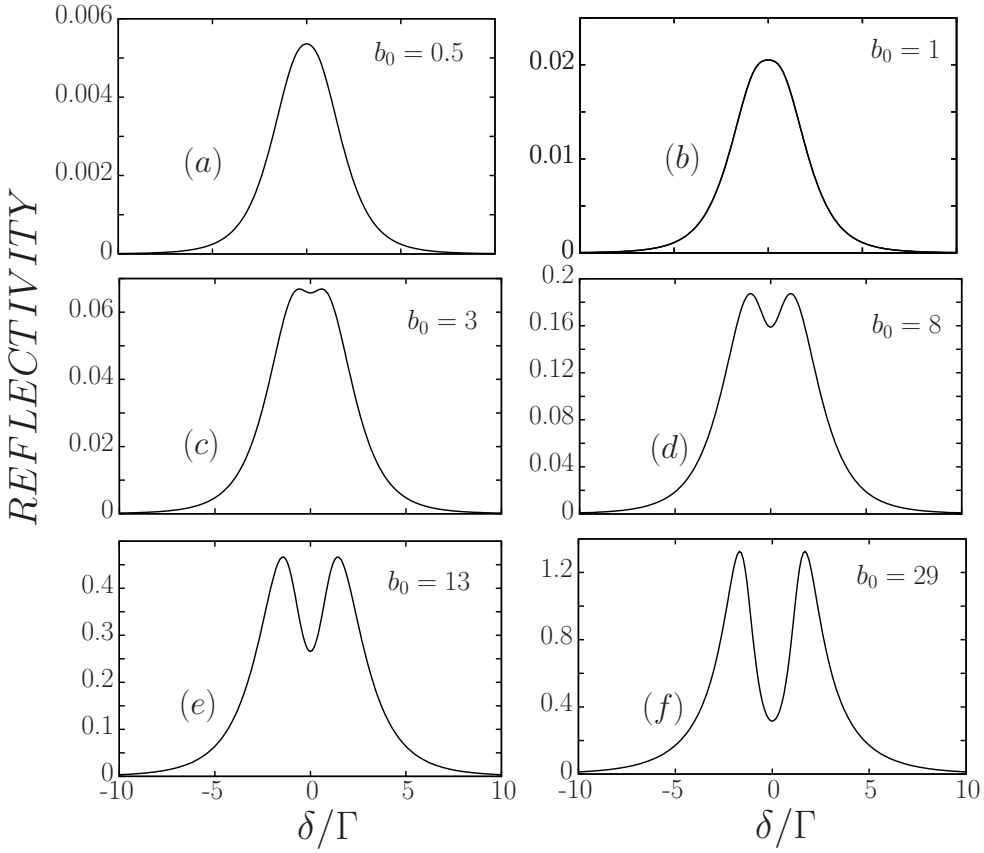

Figure 4.6: *DFWM signal for a fixed saturation parameter* ($s = 3$) *and different optical thicknesses. A clear splitting of the signal due to the central line absorption is obtained for a large optical thickness* ($b_0 = 29$).

Non-Homogeneous atomic distribution

However, as shown in the attached paper, we observed a red-blue asymmetry of our DFWM signal, in the rubidium-atomic sample, in the high pump intensity limits even with a moderate optical thickness.

We explained this asymmetry by introducing a spatial bunching of the atoms in the nodes or anti-nodes of the strong standing wave created by the pump beams, which created a spatial dependence on the atomic density distribution at half of the wave-length ($n_{at}(z)$). In this particular case, we needed to introduce the bunching parameter ($\mathbb{B}$) expressed by the following quantity:

$$\mathbb{B} = \frac{k}{2\,\pi} \int_0^{2\,\pi/k} n_{at}(z)\, e^{2\,i\,k\,z}\, dz \ . \tag{4.32}$$

This phenomena of atomic bunching has been presented and analyzed in the article attached in Sec. (4.4), and titled: **"Bunching-induced asymmetry in Degenerate Four-Wave Mixing with cold atoms."** As reported in the paper, the observed asymmetry on the DFWM signal, is also is also confirmed by computer simulations, also presented in the paper.

4.3.1 Experiments

In the following section we will describe, in the first part, the experimental set-up used for the observation of the DFWM signal, while in the second part the main results concerning the linear shape of the DFWM signal are presented.

Setup

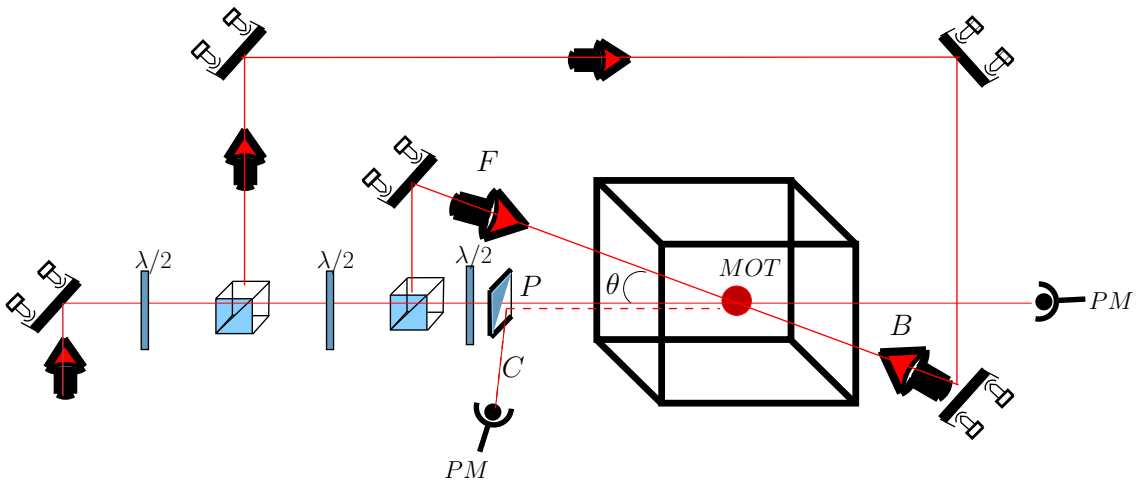

Figure 4.7: *The illustration shows the backward geometry realized in our set-up to obtain degenerate four wave mixing with cold ^{85}Rb atoms. With the capital letters F and B, we indicate the two strong pumps (not retro-reflected), and with P and C, respectively, the probe and conjugate beam. The polarizations of these beams are adjusted by using polarized-cubes and wave-plates.*

The experiment was performed in a sample of cold rubidium atoms obtained by a MOT as described in Chapter. 1. As we have already seen, the atom number can be adjusted in the experiment by varying the intensity of the repumper laser.

The DFWM beams are provided by the same laser at frequency ω_L, and can be time controlled to adjust the pulse duration. In all the experiments carried out for this thesis we employed the backward DFWM configuration with two independent and not retro-reflected beams as shown in Fig. (4.7). We usually use the names F and B for, respectively, the forward beam and backward pump. The angle between the probe P and the forward beam, is maintained as a constant during all experiments at $\theta = 0.2$rad. The waist of the laser beams is $w \cong 6\,mm$ which is larger than the atomic size of our cloud ($\sigma_r = 1\,mm$). The polarization on the DFWM beams can be adjusted by appropriate wave plates and polarizing cubes placed along the beam path, as shown in Fig. (4.7). The conjugate beam, propagating in the opposite direction of the probe, is recuperated by using a beam-splitter, and recorded into a Photo-Multiplier (PM).

The time sequence was as follows. The atoms were collected and cooled from the background vapor for about $20\,ms$. Then, the trapping beams as well as the quadrupole magnetic field were switched off for about $1\,msec$. During this "dark time", the DFWM beams were switched on to generate the phase conjugated beam.

The pulse duration of the DFWM beams, had been set as small as $20\mu sec$ in order to avoid mechanical effects of the pumps on the atomic cloud.
However, the repumping laser was kept on all the time to avoid atomic losses of interacting atoms by hyperfine optical pumping.

The final DFWM spectra was obtained by looking at the time resolved conjugate beam analyzed in a fixed time window. However, it was also possible to perform continuous frequency scans, but in such a case, we lost important atomic effects. Particularly, the bunching-induced asymmetry on the frequency spectrum was washed out, and consequently, a symmetric spectrum was expected. Such a prediction was experimentally observed in the recorded signal, as shown Fig. (4.11)-(b) Sec.(4.5).

Experimental Results

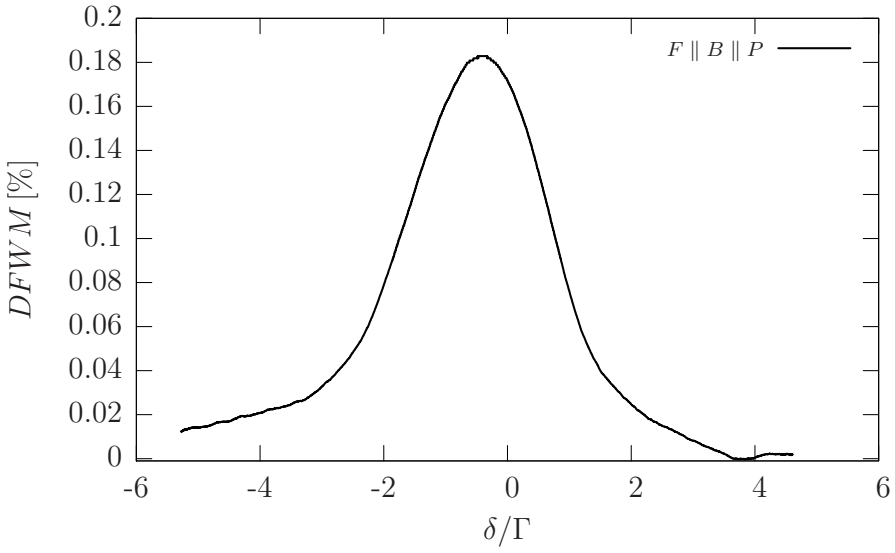

(a)

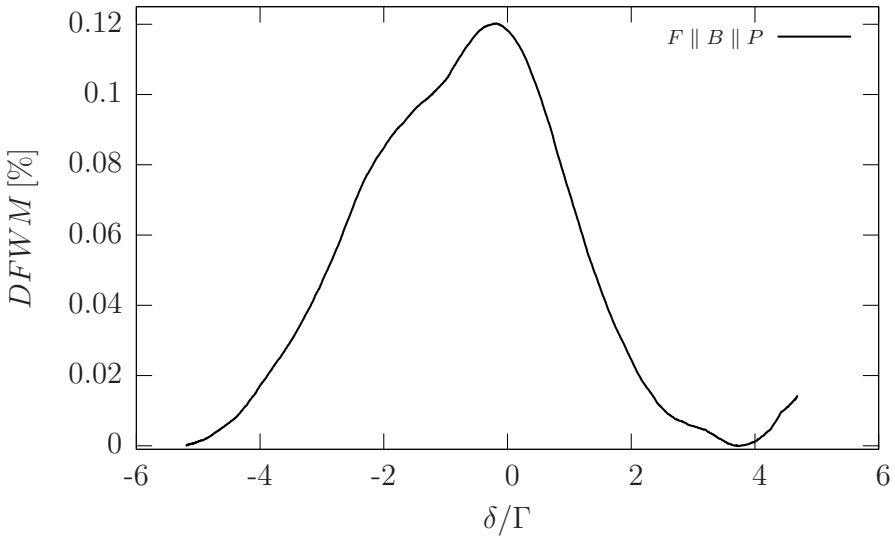

(b)

Figure 4.8: *Experimental results obtained on DFWM. In graph (a) the pump intensity parameters were set equal to $s = 2$, while in graph (b) they were $s = 4$. Both curves were obtained within the limit of small optical thickness ($b_0 \ll 1$) in order to avoid center line absorption. No splitting, but only a broadening of the central power peak was observed by increasing the pump intensities by a factor of two .*

Fig. (4.8), shows the typical experimental results on DFWM obtained, in the parallel case ($F \| B \| P$), with the set-up already described in the first part of this section.

The pulse duration of FWM beams was chosen to be approximately equal to $20 \mu sec$ during which a "fast" frequency scan of the DFWM was performed. In such a situation, the bunching has no time to appear, and thus the signal was symmetric with respect to

the resonance $\delta = 0$.

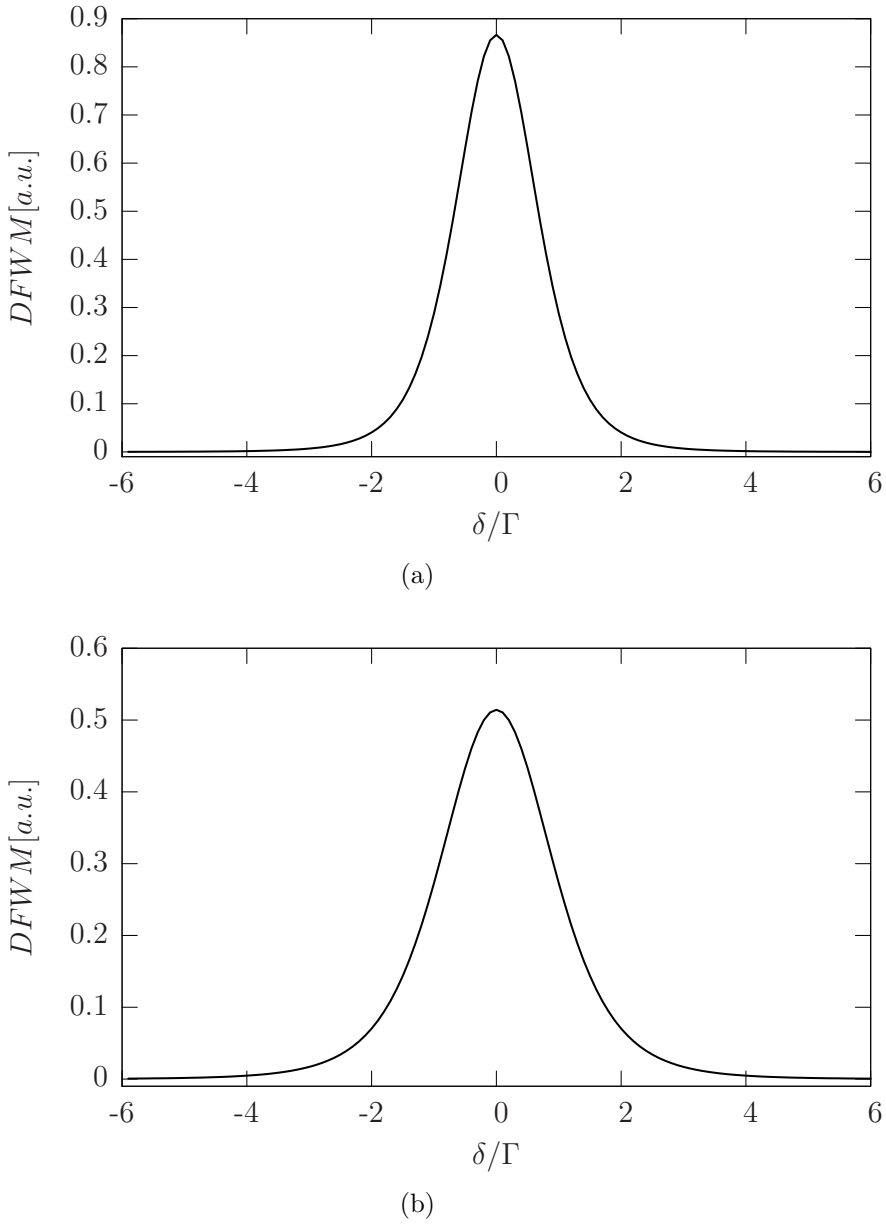

Figure 4.9: *Theoretical prediction for DFWM using the Abrams and Lind theory in the parallel case. The spectra shown were obtained by using Eq. (4.31) given in the text. In order to reproduce the experimental condition, in graph (a) the saturation parameter for the pumps was set to $s = 2$, while in graph (b) the saturation parameter was set equal to $s = 4$.*

The DFWM signal shown in Fig.(4.11)-(a) was obtained with a saturation parameter, averaged on the Clebsch-Gordon coefficients, and was set equal to $s = 2$ for the pumps, and $s = 0.03$ for the probe.

In Fig.(4.11)-(b), the saturation parameter was equal to $s = 4$ for the pumps, while the probe intensity was kept constant ($s = 0.03$). The spectra were recorded as a function of the common frequency detuning δ with respect to the atomic transition. For both values of pump saturation parameters ($s = 2$,and $s = 4$), the DFWM spectrum consisted

of a single symmetrical peak centered around the $\delta = 0$.

In parallel polarization ($F \| B \| P$), the rising by a factor of two of the pump intensity had the single effect of broadening the resonance.

The line shape behavior is completely in agreement with the simple theory of DFWM proposed by Abrams and Lind in [51] [49] and expressed by Eq.(4.31) in the limit of small absorption. In such a limit, by using this equation, we can plot the theoretical curves, corresponding to the two experimental situations observed: Fig. (4.9)-(a) shows the DFWM signal for pump saturation parameter $s = 2$, while Fig. (4.9)-(b) shows the situation where the saturation parameter was set to be $s = 4$.

The spectra reported in Fig. (4.9) were obtained by considering the spatial average of the nonlinear susceptibility over half a wave-length, and they are completely in agreement with the experimental observations.

4.4 Bunching-induced asymmetry in degenerate four-wave mixing with cold atoms

4.4. BUNCHING-INDUCED ASYMMETRY IN DEGENERATE FOUR-WAVE MIXING WITH COLD ATOMS

PHYSICAL REVIEW A **74**, 043407 (2006)

Bunching-induced asymmetry in degenerate four-wave mixing with cold atoms

G. L. Gattobigio,[1,2] F. Michaud,[1] J. Javaloyes,[3] J. W. R. Tabosa,[4] and R. Kaiser[1]
[1]*Institut Non Linéaire de Nice, UMR 6618 CNRS, 1361 route des Lucioles, F-06560 Valbonne, France*
[2]*Dipartimento di Fisica dell'Universita' di Ferrara and INFN-Sezione di Ferrara, 44100 Ferrara, Italy*
[3]*Department de Fisica Interdisciplinar, IMEDEA (CSIC-UIB), C/Miquel Marques, 21, E-07190 Esporles, Spain*
[4]*Departamento de Fisica, Universidade Federal de Pernambuco, Av. Professor Luiz Freire, s/n Cidade Universitaria, 50670-901, Recife-PE, Brasil*
(Received 1 June 2006; published 12 October 2006)

We have investigated degenerate four-wave mixing in a sample of cold rubidium atoms. A red-blue asymmetry is observed for high intensities of the pumping beams. This asymmetry is explained by the spatial bunching of the atoms in the nodes or antinodes of the strong standing wave of the pump beams. This explanation is confirmed by different experimental configurations and by numerical simulations.

DOI: 10.1103/PhysRevA.74.043407 PACS number(s): 32.80.Pj, 42.50.Gy, 03.67.−a

Four-wave mixing (FWM) has been extensively studied in the past three decades and constitutes a very powerful spectroscopic technique both in frequency and time domain [1]. From a practical perspective, the possibility of performing wave-front reconstruction is one of the most fascinating applications of this nonlinear optical process. The use of cold atoms to obtain FWM optical phase conjugation benefits from the reduced atomic motion where broadening mechanisms such as transit time broadening and second-order Doppler effect can be completely eliminated. This allows us to obtain wave-front reconstruction over a large angular aperture between the pump and the probe beams [2,3]. In this regime one can also directly compare theoretical predictions with experiments without the need to perform any velocity averaging. For instance, the polarization dependence of the nondegenerate FWM spectrum has been measured in cold cesium atoms which is in complete agreement with the theoretical predictions [4]. Another interesting application associated with the FWM process is the possibility to investigate the atomic dynamics either in room temperature vapors [5] or in the domain of ultracold temperatures associated with laser cooled atoms. In particular, degenerate and nondegenerate FWM were employed to probe the quantized atomic motion of atoms in optical lattice [6,7]. The total FWM signal arises from the coherent superposition of the fields generated at different position along the nonlinear medium. Actually, for a spatially uniform atomic medium, this leads to the well-known phase matching condition which determines the propagation direction of the generated field in terms of the wave vectors of the incident waves. However, this situation is rather changed when the medium presents some spatial modulation where the generated field can pick up a wave-vector component associated with the Fourier decomposition of the spatial modulation of the medium, therefore affecting the overall efficiency of the nonlinear process and changing the propagation direction of the generated wave [8]. In this work we experimentally investigate the degenerate four-wave mixing (DFWM) process [9] in a sample of cold rubidium atoms both in the time and in the frequency domain using different polarization configurations for the DFWM beams. Note that we study DFWM where the frequency of both pump beams and the probe beam are identical, in contrast to many pump-probe spectroscopy experiments where the probe frequency has been scanned around the pump frequency. In most of the experiments using cold atoms, the pump beams have a fixed (red) detuning and the observed subnatural linewidths in nearly degenerate FWM have been explained by the dynamics of atoms in dissipative optical lattices [10]. We have registered the DFWM spectra for positive (blue) and negative (red) detuning of the pump and probe beams and observed an unexpected red-blue asymmetry for high intensity of the pumping beams. This asymmetry in the FWM spectrum can be explained by the presence of different spatial atomic distributions on the red and on the blue side of the atomic resonance. We associate this atom bunching to the dipole forces in strong fields with modulated intensity.

The experiment was performed in a sample of cold rubidium atoms obtained from magneto-optical trap (MOT). Our MOT scheme has been described elsewhere [11] and allows a time controlled switching of the trapping and repumping beams as well as the magnetic quadrupole field. The atom number can be adjusted in this experiment by a variable intensity of the repumping laser. Unless otherwise specified, the results shown in this paper have been obtained with a moderate number of atoms ($\sim 10^9$) as more complex collective effects appear for the maximum number of atoms, of the order of 10^{10}, we are able to trap. The DFWM beams are provided by the same laser (frequency ω_L) and can be controlled in time to adjust the pulse duration. We employ the conventional backward DFWM configuration with two independent (not retroreflected) counterpropagating pumping beams (forward F and backward B). Figure 1(a) shows a simplified scheme of the experimental configuration. The angle between the probe (P) and forward beam (F) has been maintained constant at around 0.2 rad. The waist of the laser beams (w=6 mm) is slightly larger than the size of our cloud. The polarization of the DFWM beams can be adjusted by appropriate wave plates and polarizing cubes placed along the beam paths. Table I summarizes the different combinations of polarization we have used for this work. In Fig. 1(b) we show the timing sequence of the experiment. First the atoms are collected and cooled for about 20 ms, then the MOT trapping beams and the quadrupole magnetic field are switched off for about 1 ms. During this time window, the

 ©2006 The American Physical Society

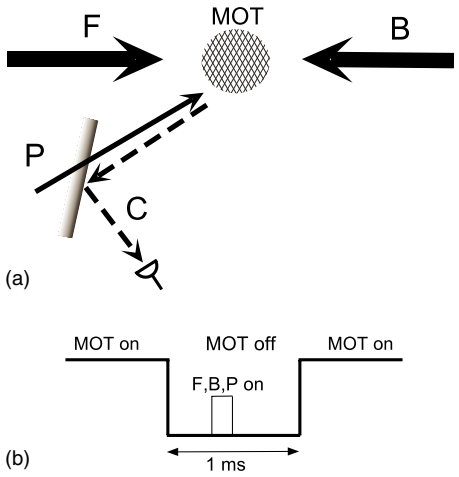

FIG. 1. (Color online) (a) Schematic setup of the experiment: two strong counterpropagating pump beams (F and B) and one weak probe beam (P) yield the conjugate four-wave mixing signal (C); (b) timing of the experiment, the MOT beams and magnetic fields are switched off during the short DFWM pulse.

DFWM beams are switched on and the generated phase conjugated beam, after being reflected off a beam splitter, is detected by a fast photomultiplier. The duration ΔT of the DFWM beam (in the range of 20 to 40 μs) has been adjusted to be short enough so that the strong pump beams do not influence the atom number at the turn off of each MOT sequence. The repumping laser of the MOT has been kept on during the DFWM sequence, in order to avoid losses of interacting atoms by optical hyperfine pumping. The DFWM spectra shown in this paper correspond to an integration over interaction times of several μs typically after 20 μs of interaction. The precise value of the DFWM depends on the choice of these values, but the qualitative features discussed in this work are robust against a decent variation of these parameters.

We have first analyzed the case where the pump and probe beams have orthogonal linear polarizations $F\|B\perp P$, as this choice of polarization is known to yield large DFWM signals [4]. For this configuration, the signal originates from a coherence grating induced in the Zeeman sublevels by the orthogonal polarization components of the probe and pump fields. We record the DFWM spectrum as a function of the common frequency detuning $\delta=\omega_L-\omega_{at}$ of DFWM beams in relation to the resonance frequency $5S_{1/2}$, $F_g=3-5P_{3/2}$, $F_e=4$ of the D_2 transition of rubidium ^{85}Rb (wavelength $\lambda=\frac{2\pi}{k}=\frac{2\pi c}{\omega_{at}}=780$ nm, width of the resonance line

TABLE I. Various polarization configurations used in this paper.

	F	B	P
$F\|B\|P$	↕	↕	↕
$F\|B\perp P$	↕	↕	↔
σ^+-σ^+	↻	↻	↕
σ^+-σ^-	↻	↺	↕

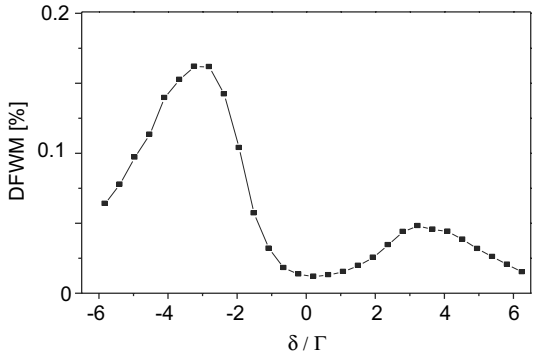

FIG. 2. DFWM spectrum for orthogonal polarizations ($F\|B\perp P$) and strong saturation of the pump beams, $s=5$.

$\Gamma=5.89$ MHz, saturation intensity $I_{\rm sat}=1.6$ mW/cm^2). Assuming a uniform distribution of the atoms among the various Zeeman sublevels, we define the on-resonance saturation parameter $s=\frac{3}{7}\frac{I}{I_{\rm sat}}$ by including an average over the Clebsch-Gordan coefficients.

The spectrum obtained for pump intensities corresponding to a saturating parameter of about $s=5$ for the F and B pump beams and $s_P=0.5$ for the probe beam, is shown in Fig. 2 and consists of a double peak centered around the detuning $\delta=0$. Note that the precise values (including the shape) of these DFWM spectra depend on the precise time window used for the evaluation, as illustrated by time resolved results shown below. The physical origin of this double peak structure for the $F\|B\perp P$ and σ^+-σ^- configurations lies in a combination of the saturation induced by the strong pump field and line center absorption due to the larger optical thickness around the resonance [12,13]. We have verified that with a reduced atoms number ($\sim 10^8$) the line center absorption vanishes and there is no double peak structure for the $F\|B\|P$ and the σ^+-σ^+ configuration for saturation values up to $s=30$. As expected a double peak structure however remains for the σ^+-σ^- configuration [14]. Another possibility of double peak structure can be obtained for large probe beam intensities [15], but can be excluded with our choice of probe beam intensities. Note also that for DFWM in Doppler broadened hot atomic vapors, the average over the various velocity classes leads to a splitting even in the $F\|B\|P$ configuration. This can be understood by the fact that in the rest frame for each velocity class, the laser frequency of the pump beams are shifted by the Doppler effect and one has a situation which is no longer DFWM but nondegenerate FWM [14].

A more surprising feature however is the clear red-blue asymmetry: the DFWM signal is clearly larger for negative (red) detuning than for positive (blue) detuning. A model based on only the internal degrees of freedom of the individual atoms, taking into account all Zeeman sublevels of the relevant ground $(5S_{1/2},F_g=3)$ and excited $(5P_{3/2},F_e=4)$ states cannot predict such a red-blue asymmetry [9,14,16]. We neglect the influence of other hyperfine states in the excited level, separated by more than 20 linewidths, and the ground state, even further detuned, even though subtle polarization effects due to the neighboring excited state levels

have been reported [17]. As our red-blue asymmetry has been robust against slight changes in alignment, intensity imbalance and atom number, we do not think that a change in the index of refraction of the effective medium [12] nor self-focusing [13] plays an important role in our experimental observation. We have however observed that for longer interaction times (up to 800 μs) the number of atoms after each MOT period of 20 ms (as monitored by the fluorescence signal at the end of the MOT period) is reduced for blue detuning of the pump beams. This loss of atoms is attributed to classical Doppler heating of atoms. For long enough interaction times (typically for DFWM pulses exceeding 100 μs), atoms can be accelerated beyond the velocity capture range of the MOT and cannot be recaptured by the next MOT period. This effect can also give rise to a more trivial red-blue asymmetry and must be ruled out when studying the bunching induced asymmetry.

As discussed below we attribute the asymmetry observed for short interaction times to the bunching of atoms along the standing wave pattern associated with the counterpropagating pumping beams. Dipole forces acting on atoms are known to change sign with the atom-laser detuning as the light shift induced by the laser depends on its detuning [18]. For large Rabi frequencies atoms are high field seekers at red detuning and low field seekers at blue detunings (as used, e.g., in atom mirrors [19]). The red-blue asymmetry in the DFWM signal presented in this paper appears when atoms are moving in a intense modulated standing wave with a light shift comparable to the kinetic energy of the atoms [20].

In order to investigate the origin of this asymmetry experimentally and theoretically, we have performed a number of control experiments which allow for clearer signatures corresponding to this interpretation and an easier comparison to theory. We have thus performed experiments with circular polarized pump beams. The pump beams F and B have either the same circular polarization (σ^+-σ^+) or opposite circular polarizations (σ^+-σ^-). As the probe beam for the (σ^+-σ^-) configuration has been kept linear (see Table I), the signal originates from a coherence grating induced in the Zeeman sublevels by the orthogonal polarization components of the probe and pump fields. Note that a minimal description for the (σ^+-σ^-) and the $F \perp B \| P$ configurations require a three-level system, whereas the $F \| B \perp P$ is better described by a four-level system. On the other side, the (σ^+-σ^+) and the $F \| B \| P$ configuration are well described by two-level systems. A quantitative comparison between the various polarization configurations is hence not possible. The important point however is the change in the intensity modulation for these two configurations. In the σ^+-σ^+ configuration, the polarization of the field is σ^+ and constant in space but the amplitude of the local electric field is strongly modulated, and corresponding strong dipole forces will act onto the atoms. In the σ^+-σ^- configuration however, for identical intensities for the F and B beams, the local polarization is linear (with a spatially rotating axis) but the amplitude of this field is constant in space (neglecting at first order the influence of the probe beam). In this σ^+-σ^- situation the light shift of the atoms is not modulated in space and no dipole force is expected to occur. We thus predict a red-blue asymmetry for the σ^+-σ^+ configuration but we do not expect any asymmetry for the σ^+-σ^- configuration.

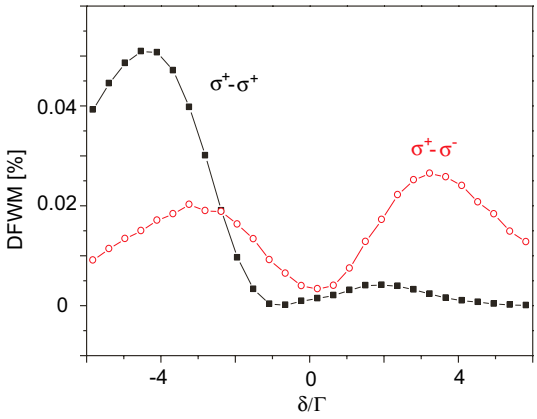

FIG. 3. (Color online) DFWM spectrum for circular polarizations of the pump beams, σ^+-σ^+ (full squares) and σ^+-σ^- (open circles); pump beam saturation, s=3.3.

This is what we have observed in the experiment as shown in Fig. 3. We have recorded the DFWM spectrum for the two circular polarization configuration of the pumping beams in the regime of strong pump saturation (s=3.3). As can be seen in Fig. 3, the red-blue asymmetry is strongly reduced for the case where the pump beams have opposite circular polarization and where no modulation of the light shift due to the pump beams is expected. This result strongly supports our explanation that mechanical effects based on dipole forces, absent in the σ^+-σ^- configuration, are at the origin of the observed red-blue asymmetry.

One should however bear in mind the mechanism for DFWM is different for these two polarization configurations. Indeed, in the σ^+-σ^- case, the strong pump beams F and B directly induce a coupling between different Zeeman sublevels, which are then probed by the weaker beam P. Comparing our σ^+-σ^- case, with linear probe polarization with a configuration using $F \perp B \| P$ would involve more closely related four-wave mixing mechanisms, as both configuration should be well described with a four-level model. One can thus compare the results of the σ^+-σ^- shown in Fig. 3 to those of Fig. 2. The important point is the change in the intensity modulation for these two configurations. In the $F \| B \perp P$ configuration, the polarization of the strong pump field is linear and constant in space but the amplitude of the local electric field is strongly modulated, with corresponding strong dipole forces acting on the atoms. However even such experiments would only allow for qualitative comparison, as optical pumping and the relative polarization of the probe-pump beams would not be the same. We have therefore chosen to use a comparison using a minimal change in the experiment (switching polarization of the B beam from σ^+ to σ^-). The main result is that we have systematically observed a strong red-blue asymmetry for strong enough pump beam for all polarization configurations, except for our σ^+-σ^- configuration, where we expect no spatial modulation of the light shift induced by the pump beams.

In order to further investigate the consequence of such mechanical effects on the DFWM signal, we have performed experiments, specifically designed for an easier comparison with theoretical simulations. Indeed, when the spatial distri-

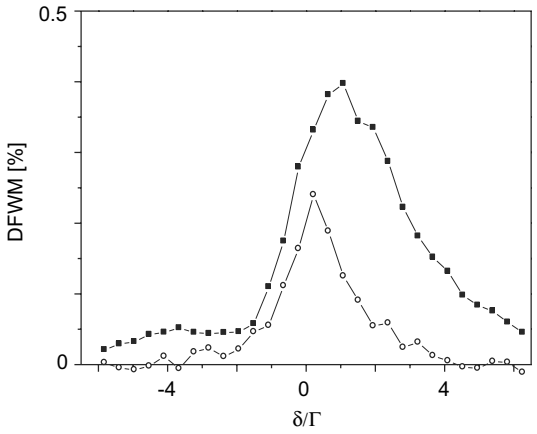

FIG. 4. DFWM spectrum for parallel polarizations of the pump and probe beams, $F\|B\|P$. Weak pump intensity $s=0.4$ (rescaled $\times 100$) (open circles) and strong pump intensity $s=4$ (full squares).

bution of the atoms is no longer uniform, one must take into consideration not only the coherences (Zeeman or optical coherences) but also the density modulation of the atoms. Let us, e.g., consider the situation with a strong spatial intensity modulation (e.g., $F\|B\perp P$, $F\|B\|P$ or σ^+-σ^+). As the intensity of the pump beam is increased up to the point when the induced light shifts are larger than the kinetic energy of the atoms, dipole forces are important enough to induce a bunching of the atoms. One now must evaluate whether bunching at the antinodes of the standing wave (for red detuning) will increase or decrease the DFWM signal in comparison with bunching at the nodes of the standing wave (for blue detuning). The theoretical description of DFWM including these effects of the external degrees of freedom of the atoms is somehow less complex if one considers all polarizations for both pump and probe field parallel, $F\|B\|P$. In contrast to the previous configurations, the signal now originates from an optical coherence grating of two-level atoms and Zeeman coherences in the ground state can be neglected. This allows for an easier numerical simulation of the experimental situation. In the low saturation limit, one thus expects an increased DFWM when atoms are bunched around the antinodes of the standing wave, increasing the average local intensity the atoms experience. This argument is supported by numerical simulations presented below. The experimental result are shown in Fig. 4.

In contrast to the orthogonal and circular configurations, where Zeeman coherences are responsible for the DFWM signal, no splitting is observed for the parallel configuration, as expected for two-level atoms at rest [9]. For low saturation of the pump beams, the DFWM is symmetrically centered around $\delta=0$ (Fig. 4, open circles). For larger saturation however, the maximum of the DFWM signal is shifted towards the blue ($\delta>0$) side of the spectrum (Fig. 4, full squares). However this blueshift does not correspond to the asymmetry predicted above. By changing the saturation parameter of the probe beam and by carefully balancing the intensities of the forward and backward pump beams, we have verified in a series of experiments, that this blueshift is not caused by a residual light pressure of the pump and probe beam [21]. In fact, this blueshift for larger saturation parameter is due to the bleaching (saturation) of the nonlinearity of the atoms [8]. Indeed, for a two level atom, a perturbative description of the nonlinearity is only valid at low saturation of the atomic transition. For too large saturation, the nonlinearity will decrease again with a total bleaching of the transition for infinite saturation. When the saturation parameter of the pump beam exceeds a certain threshold, an increase of the intensity of the pump beams will lead to a decrease of the nonlinear DFWM signal. Correspondingly a bunching of atoms at the antinodes of the standing wave (high field seekers for red detuning) will not increase but decrease the DFWM in this regime. On the other hand, bunching of the atoms (by dipole forces) at the nodes of the standing wave (low field seekers for blue detuning) will lead to an increase of the DFWM. This is what we observe in our experiment. Note that for the experiments where a center line dip is present, the asymmetry is more striking at larger values of detuning, where this bleaching of the atomic response does not occur. This is how we explain the larger DFWM for red detuning in Figs. 2 and 3. A redshift of the DFWM around resonance would be expected for lower saturation parameters. However, the bunching of atoms due to the dipole forces of the pump field also depends on the saturation parameter and we cannot produce significant bunching in the low intensity limit where a redshift is expected. As detailed below we have confirmed these effects by numerical simulations using a two-level model for the atoms.

Before turning to the description of our numerical simulations, let us present further experimental results for the $F\|B\|P$ configuration. As we can register not only the DFWM signal at the end of the short pulse (all results presented above) but also the time resolved DFWM, the dynamics of DFWM can be probed. This is illustrated in Fig. 5.

As one can see in these figures, the DFWM is almost independent of time for low saturation. This is consistent with the explanation that for these values of the saturation parameter no bunching is obtained. Also the values for red and blue detuning are similar, as already shown in Fig. 4. For larger pump intensities however, one can see the red-blue asymmetry already shown in Fig. 4, but one can also clearly distinguish a strong time dependence (with initial oscillations) of the DFWM. This time dependence is another confirmation of the bunching induced DFWM as it is consistent with the time scales of the spatial motion of the atoms experiencing strong dipole forces in the modulated light field. This time-dependent DFWM could be exploited to measure the time-dependent bunching as explained below. Note that due to this strong time dependence for large saturation values, a more precise comparison between the various polarization configurations would require a time resolved comparison. This complexity will be illustrated in Fig. 6 for the results of our numerical simulations. Furthermore for large values of the saturation parameter there is not always a steady state, as one can lose atoms by Doppler heating. This makes a complete quantitative analysis almost impossible and we have thus extracted the results shown in Figs. 2–4 from a time window ranging from 10 to 40 μs. In order to further support our analysis of a bunching induced red-blue asymmetry, we have performed numerical simulations to es-

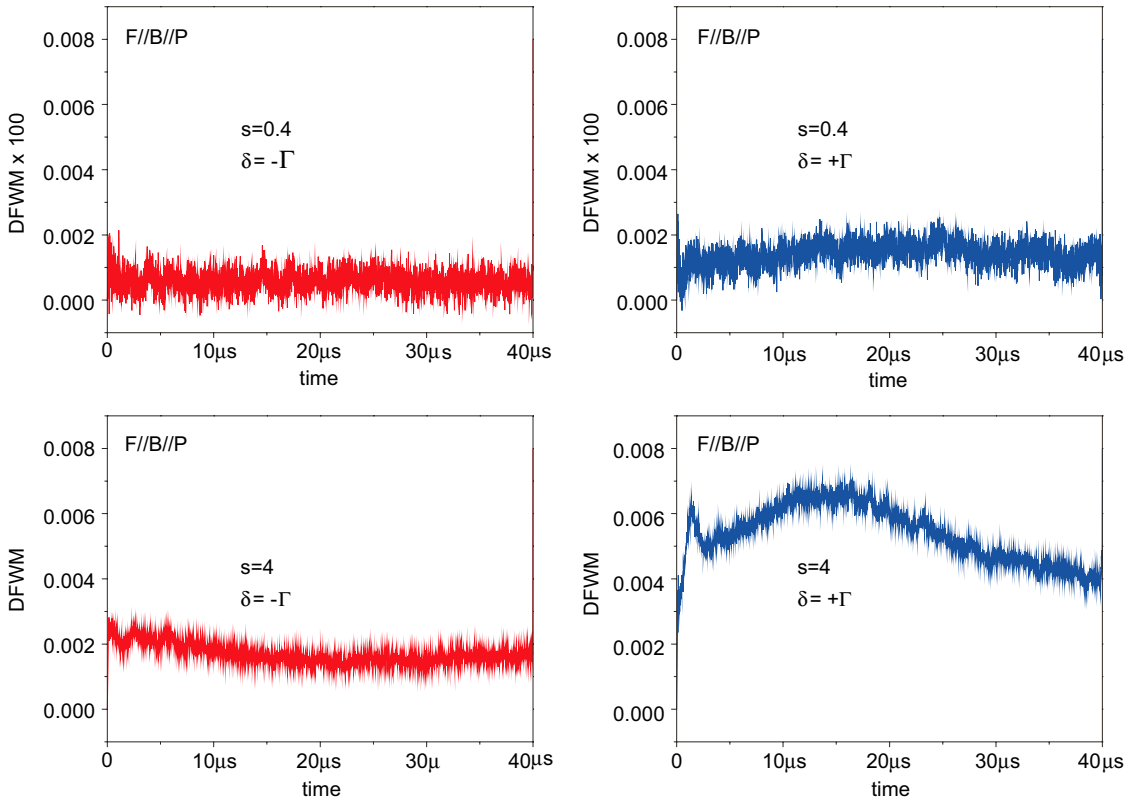

FIG. 5. (Color online) Time resolved DFWM signal for linear polarizations of the pump and probe beams, $F\|B\|P$. Upper curves, low saturation $s=0.4$ for red ($\delta=-\Gamma$, left curve) and blue ($\delta=\Gamma$, left curve) detuning. Lower curves, high saturation $s=4$ for red ($\delta=-\Gamma$, left curve) and blue ($\delta=\Gamma$, left curve) detuning. Note the change of the vertical scale due to increased DFWM for larger saturation.

timate the spatial ordering induced by the strong standing light wave. Following the method described in Ref. [22], we used the dressed state basis and solved the coupled Heisenberg equations for the position, momentum, optical coherence, and populations for each atom. The reversible dynamics for each particle is interrupted by stochastic events, corresponding to stimulated emissions between dressed states and thus to a reset of the atomic internal degree of freedoms. In our numerical simulation, we have neglected the retroactions of the atoms onto the pump fields which could occur due to the stimulated or spontaneous radiation of the atoms. Such interaction can give rise to interesting collective features [23] which are however not in the scope of this paper. Moreover, this approximation is justified by the relatively modest number of atoms used in the experiment. We expect the transition toward a collective regime to appear only above a critical value of atom number. Indeed, in the experiments we encountered more complex collective behavior for larger atomic clouds, when $N_{at}>10^{10}$.

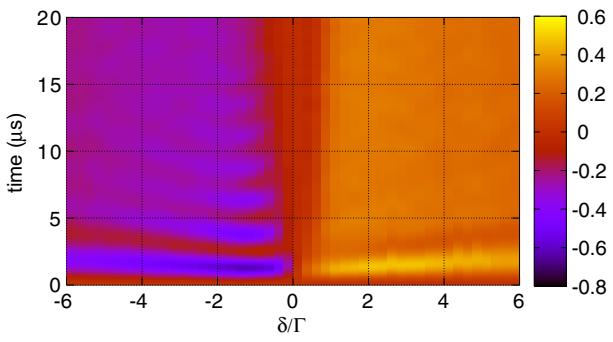

FIG. 6. (Color online) Numerical simulation of the bunching for a two level atom with a pump beam saturation of $s=4$.

In order to characterize the atomic ensemble, we defined the bunching parameter within the cloud b as the harmonic modulation of the atomic density distribution $\rho(z)$ at half the wavelength,

$$b=\frac{k}{2\pi}\int_0^{2\pi/k}\rho(z)e^{2ikz}dz. \quad (1)$$

As expected, the bunching parameter b is an increasing function of the pump intensities. By an appropriate choice of the origin $z=0$ and of the relative phase between the two pump beams F and B, we impose the standing wave to be proportional to $\sin(kz)$. Accordingly, due to the mirror symmetry $(z,F,B)\rightarrow(-z,B,F)$ of the problem, the bunching b can be considered as a real valued quantity, up to finite size scaling fluctuations. The expected behavior consisting of bunching at the nodes (field minima) for blue detuning ($\delta>0$) correspond to $b>0$, while bunching at the antinodes (field maxima) for red detuning ($\delta<0$) correspond to $b<0$. In Fig. 6 we show the resulting time evolution of b as a function of

detuning for an initial temperature of the cloud of $T=100\ \mu$K, a saturation parameter $s=4$ and an atom number $N=4096$. One can see that the bunching takes a non-negligible value in a broad range of detuning values. However, it is vanishing in the vicinity of $\delta=0$ since in this case the dipole forces are too weak to sustain the periodic modulation against spontaneous emission recoils. Generalizing the calculations by Ref. [9], by explicitly including the density profile, the conjugate DFWM field is given in the limit of small optical thickness by the following expression:

$$\kappa = 4s(1-2i\delta)\int_0^{2\pi/k} \frac{\rho(z)\sin^2 kz}{(1+4\delta^2+4s\sin^2 kz)^2}dz. \qquad (2)$$

The DFWM signal we measure is then given by $|\kappa|^2$. Assuming a harmonic ansatz for the spatial modulation of the atomic density $\rho(z)=(1+2b)-4b\sin^2 kz$, we can write the conjugate field κ as

$$\kappa = \kappa_0[\mathcal{I}_1(1+2b)-4b\mathcal{I}_2] \qquad (3)$$

with $\kappa_0=4s(1-2i\delta)/(1+4\delta^2)$ and

$$\mathcal{I}_j = \int_0^{2\pi/k} \frac{\sin^{2j} kz}{(1+a^2\sin^2 kz)^2}dz. \qquad (4)$$

The two integrals $\mathcal{I}_1,\mathcal{I}_2$ can be evaluated numerically and only depend on the pump beam detuning δ and saturation s through $a^2=4s/(1+\delta^2)$. Assuming that the modulation amplitude is small, we can express the relative modification r of the DFWM signal as

$$r = \left|\frac{\kappa(b)}{\kappa(0)}\right|^2 - 1 \approx 4\alpha b + O(b^2) \qquad (5)$$

with $\alpha=(1-2\mathcal{I}_2/\mathcal{I}_1)$. At this point, one can notice that $|\kappa|^2$ and α depends on δ only through δ^2. Thus the absolute DFWM signal $|\kappa|^2$ and its bunching induced modification r would be symmetric. It can be seen from the expression of r that this symmetry is broken only by the bunching since it is an antisymmetric function of the detuning, i.e., $b<0$ (respectively, >0) if $\delta<0$ (respectively, >0). It is possible to invert this problem and to evaluate the spatial modulation from the modified FWM signal r. Using this approach one could estimate the bunching from experimental time resolved data. However one must consider that α is negative for $a\lesssim 2.2$ and positive above this value. This means that either for very small saturation or very large detuning, the DFWM signal is *enhanced* on the red side and *diminished* on the blue side. This is not however the case that we considered here and we are in a regime where the Rabi frequency in the high intensity region of the standing wave is sufficiently large not only to saturate the nonlinearity but also to practically cancel its magnitude.

We can now compare the numerical results to our experimental data. First we confirm that for the parallel polarization $F\|B\|P$, there is no splitting in the DFWM spectrum. Also we find that for the larger saturation parameters $s=4$ of our experiment, the DFWM is larger for positive (blue) detuning. Figure 7 illustrates this asymmetry for detuning of $\delta=\pm 0.5\Gamma$. Transient bunching of several percent are predicted and the time dependence of the bunching resembles the DFWM of Fig. 5. For saturation parameter of $s=0.4$ we do not obtain noticeable bunching, and the corresponding DFWM signal is again symmetric around $\delta=0$. We note that the region of the inverted red-blue asymmetry DFWM is larger in the experiment than in the simulation. Several effects might explain this difference, such as an oversimplified two-level system or an inhomogeneous intensity distribution of the DFWM beams. The purpose of this paper is to demonstrate the importance of the spatial rearrangement of the atoms for a DFWM signal, but we did not aim at a quantitative description of our signals.

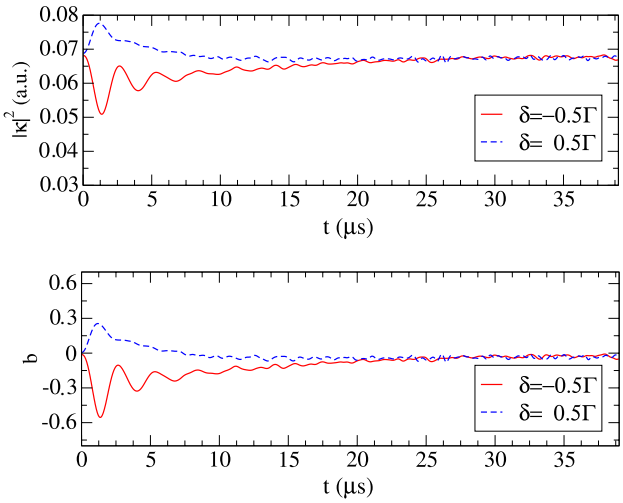

FIG. 7. (Color online) Numerical simulation for the time resolved DFWM signal (upper curve) and bunching (lower curve) for $\delta=\pm 0.5\Gamma$ and $s=4$.

In conclusion, we reported observation of DFWM with cold atoms, both for red and blue detuned light. We observe a red-blue asymmetry when atoms are exposed to dipole forces in the standing wave of the strong pump beams. The origin for an asymmetry of FWM spectra have not been reported so far and must be considered in particular when cold atoms are used as the nonlinear medium. We expect that it will be possible to increase by a considerable amount the efficiency of FWM in our cloud of cold atoms and it might then be interesting to study nonclassical features (squeezing) of the FWM signal and also add a cavity around the atomic cloud to yield self-oscillation [13,24]. Other possibilities with our pump-probe geometry include the combination of gain provided by the pump beams and multiple scattering if the optical thickness of the cloud is large. This could lead to the realization of a random laser [25] using cold atoms as a scattering and gain medium.

The authors thank G. Labeyrie for valuable help on the experimental setup. The authors acknowledge the financial support of CNRS and of the PACA Region. One of the authors (J.W.R.T.) would like to thank CNRS, CAPES-COFECUB, and CNPq for travel support. One of the authors (J.J.) acknowledges support from the program Juan de la Cierva through Grant No. TIC2002-04255-C04-03.

[1] M. D. Lukin, P. R. Hemmer, and M. O. Scully, Adv. At., Mol., Opt. Phys. **42B**, 347 (2000).
[2] L. Hilico, P. Verkerk, and G. Grynberg, C. R. Acad. Sci. III **315**, 285 (1992).
[3] J. W. R. Tabosa, S. S. Vianna, and F. A. M. de Oliveira, Phys. Rev. A **55**, 2968 (1997).
[4] A. Lezama, G. C. Cardoso, and J. W. R. Tabosa, Phys. Rev. A **63**, 013805 (2001).
[5] D. S. Glassner and R. J. Knize, Phys. Rev. Lett. **74**, 2212 (1995).
[6] B. Lounis, P. Verkerk, J. Y. Courtois, C. Salomon, and G. Grynberg, Europhys. Lett. **21**, 13 (1993).
[7] A. Hemmerich, M. Weidermuller, and T. Hänsch, Europhys. Lett. **27**, 247 (1994).
[8] M. Yocota and P. Yeh, J. Opt. Soc. Am. A **15**, 2678 (1998).
[9] R. L. Abrams and R. C. Lind, Opt. Lett. **2**, 94 (1978); **3**, 205 (1978).
[10] G. Grynberg and C. Robillard, Phys. Rep. **355**, 335 (2001).
[11] G. Labeyrie, F. de Tomasi, J. C. Bernard, C. A. Müller, C. Miniatura, and R. Kaiser, Phys. Rev. Lett. **83**, 5266 (1999).
[12] G. Birkl, M. Gatzke, I. H. Deutsch, S. L. Rolston, and W. D. Phillips, Phys. Rev. Lett. **75**, 2823 (1995).
[13] M. Oria *et al.*, Opt. Lett. **14**, 1082 (1989).
[14] M. Pinard, P. Verkerk, and G. Grynberg, Phys. Rev. A **35**, 4679 (1987).
[15] R. T. Bratfalean, G. M. Lloyd, and P. Ewart, J. Opt. Soc. Am. B **16**, 952 (1999).
[16] R. W. Boyd, M. G. Raymer, P. Narum, and D. J. Harter, Phys. Rev. A **24**, 411 (1981).
[17] S. Balik, R. Olave, C. I. Sukenik, M. D. Havey, V. B. Datsyuk, I. M. Sokolov, and D. V. Kupriyanov, Phys. Rev. A **72**, 051402(R) (2005).
[18] C. Salomon, J. Dalibard, A. Aspect, H. Metcalf, and C. Cohen-Tannoudji, Phys. Rev. Lett. **59**, 1659 (1987).
[19] V. I. Balykin, V. S. Letokhov, Yu. B. Ovchinnikov, and A. I. Sidorov, Phys. Rev. Lett. **60**, 2137 (1988).
[20] M. Schiffer, E. Cruse, and W. Lange, Opt. Commun. **116**, 143 (1995).
[21] S. Guibal, C. Mennerat-Robilliard, D. Larousserie, C. Triche, J.-Y. Courtois, and G. Grynberg, Phys. Rev. Lett. **78**, 4709 (1997).
[22] J. Chen, J. G. Story, and R. G. Hulet, Phys. Rev. A **47**, 2128 (1993).
[23] C. von Cube, S. Slama, D. Kruse, C. Zimmermann, P. W. Courteille, G. R. M. Robb, N. Piovella, and R. Bonifacio, Phys. Rev. Lett. **93**, 083601 (2004); J. Javaloyes, M. Perrin, G. L. Lippi, and A. Politi, Phys. Rev. A **70**, 023405 (2004).
[24] L. Hilico, C. Fabre, and E. Giacobino, Europhys. Lett. **18**, 685 (1992).
[25] N. M. Lawandy, R. M. Balachandran, A. S. L. Gomes, and E. Sauvain, Nature (London) **369**, 436 (1994).

4.5 Multi-Levels Atoms

In order to model the case of DFWM for orthogonal linear polarization between the pumps and probe beams ($F \| B \perp P$) we need to introduce a four level scheme, as shown in Fig. (4.10).

This model, and the relative results predicted from it, are presented in the following sections.

4.5.1 Theory

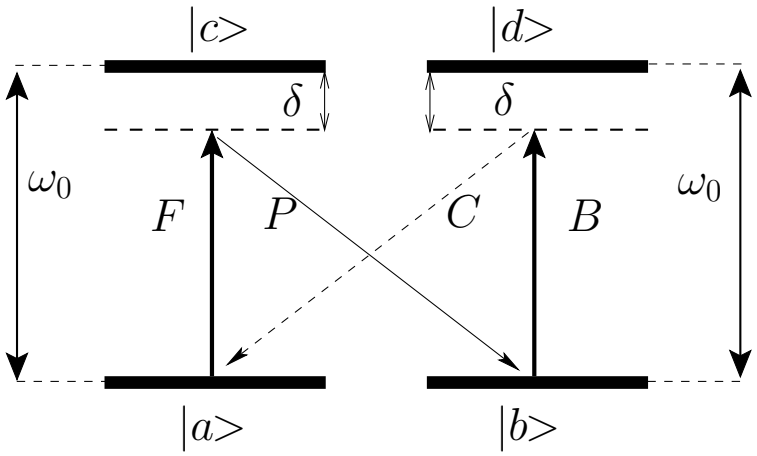

Figure 4.10: *The atomic four level scheme used to model the case of DFWM for orthogonal linear polarization, where the arrows represent the coupling between the fields and the different atomic transitions.*

This four level model for the atomic medium can be used to explain the characteristics of the observed DFWM spectra.

Let us introduce the main ingredients of this four level model. Referring to Fig. (4.10), we can consider two ground states $|a\rangle$ and $|b\rangle$ with zero energy and two excited states $|c\rangle$, and $|d\rangle$ with energy of $\hbar\omega_0$, and spontaneous relaxation rate Γ. Indeed, the forward F and the backward B pumping fields are coupled, respectively, to transition $|a\rangle \rightarrow |c\rangle$ and transition $|b\rangle \rightarrow |d\rangle$ while the probe P couples $|b\rangle \rightarrow |c\rangle$.

To account for a finite interaction time of the atoms with the light, we assume an escaping rate $\gamma \ll \Gamma$ from the interaction region. Under these assumptions, the temporal evolution for the density matrix ρ could be written as [52]:

$$\frac{\partial \rho}{\partial t} = -\frac{i}{\hbar}[H, \rho] - \frac{\Gamma}{2}\{\mathbb{P}_e, \rho\} + \Gamma\, \Xi - \gamma(\rho - \rho_0) \tag{4.33}$$

where the Hamiltonian, $H = H_0 + H_{Int}$ is, as usual, given, in the rotating-wave approximation (RWA), by:

$$\begin{cases} H_0 = \hbar\omega_0 \mathbb{P}_e \\ \\ H_{Int} = A\hbar\Omega_F(z)e^{i\omega t}|a\rangle\langle c| + D\hbar\Omega_B(z)e^{i\omega t}|b\rangle\langle d| + \\ \quad + \quad B\hbar\Omega_P(z)e^{i\omega t}|b\rangle\langle c| \end{cases} \tag{4.34}$$

and $\mathbb{P}_e = |c\rangle\langle c| + |d\rangle\langle d|$ is the projector onto the excited states, and $\Omega_F(z)$,$\Omega_B(z)$,and $\Omega_P(z)$ are the Raby frequency associated, respectively, with the two pumps (F,B) and probe (P).

Finally, the last operators introduced in Eq.(4.33) are defined as following:

$$\begin{cases} \Xi = \sum_{q=1,2} Q^q_{ge} \rho\, Q^q_{eg} \\ \\ Q^1_{ge} = A|a\rangle\langle c| + B|b\rangle\langle c| \\ \\ Q^2_{ge} = C|a\rangle\langle d| + D|b\rangle\langle d| \end{cases} \tag{4.35}$$

in which the coefficients A,B,C,D govern the relative transition amplitudes and satisfy the relation:

$$\begin{cases} A^2 + B^2 = 1 \\ C^2 + D^2 = 1 \end{cases} \tag{4.36}$$

In order to obtain the atomic response we can solve the density matrix equation by looking for the steady state of Eq. (4.33), and finding the optical coherence responsible for the NDFWM. This is the approach used for solving the four level model that, as we will see later on, reproduces the measured spectra reported on Sec. (4.5.2). More details on this particular model and its theoretical results are provided in the draft of the paper attached in Sec. (4.7), which forms the subject of the future publication titled: "Line-shape in Degenerate Four-Wave Mixing in cold atoms".

4.5.2 Experimental Results

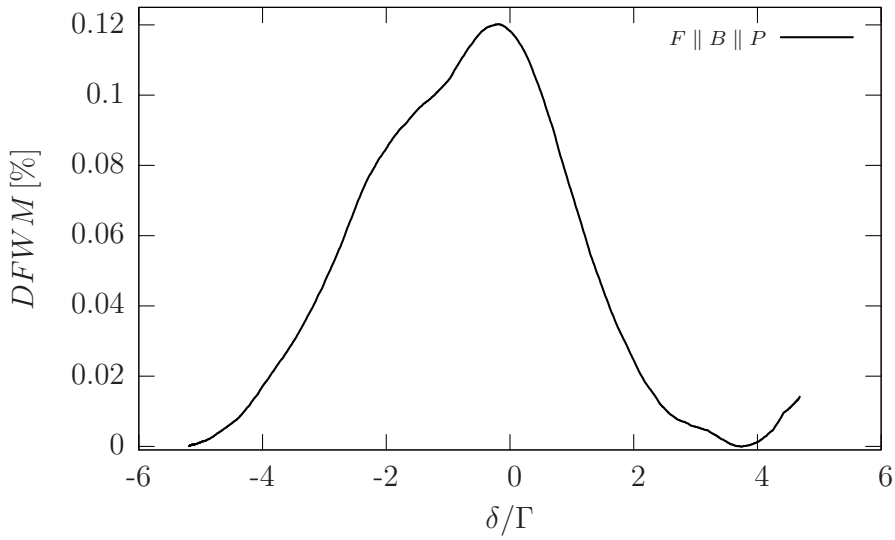

(a)

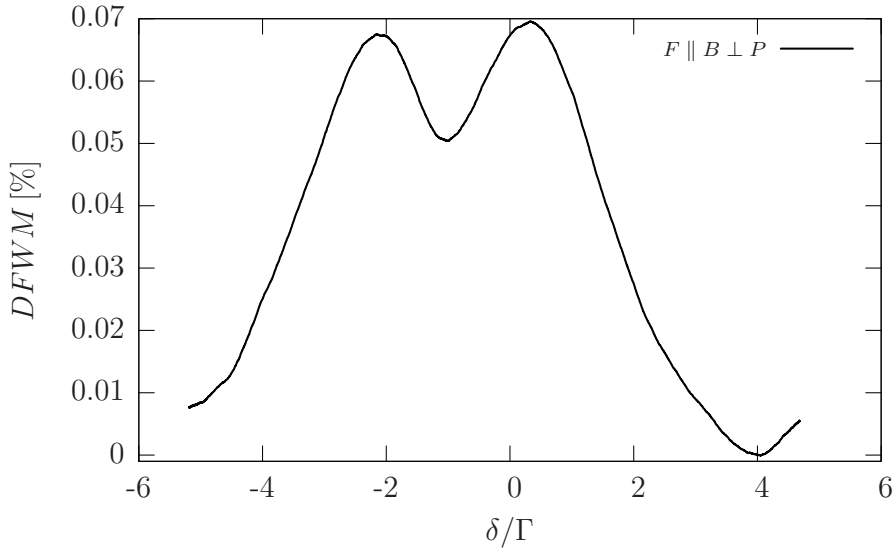

(b)

Figure 4.11: *Experimental results on DFWM. A clear splitting of the central peak is observed in the $F\|B \perp P$ configuration at small optical thickness (b_0) as shown in (a). This feature can be explained by using a four level atomic system as reported in the text.*

As described in the theory section and further detailed in the draft paper in Sec. (4.7), we can obtain the DFWM signal for four level atoms. The theory describes the $F\|B \perp P$ configuration, and such a theory can predict, for high pump intensity limits, a clear splitting of the central peak (around $\delta = 0$).

This prediction was in accordance with the results obtained in the experiment as reported in Fig.(4.11).

Fig. (4.11)-(a) shows the experimental DFWM signal in the parallel configuration ($F \| B \| P$); as we have already pointed out in Sec. (4.3), we did not observe any splitting. However, under the same experimental conditions, in the perpendicular configuration ($F \| B \perp P$), we clearly observed a splitting in the high intensity limit.

Throughout the whole experiment we used a moderate number of atoms in order to avoid central absorption of the pump intensity due to optical thickness. Such absorption also gives rise to a more trivial splitting, as reported in Fig. (4.6).

The theoretical results presented in this section, which were in agreement with the experimental observations, were obtained without realizing any spatial integration of the coefficient responsible for the DFWM in the perpendicular case ($F \| B \perp P$).

This peculiar aspect is still under investigation, and will be clarified in the future publication attached in Sec. (4.7).

4.6 Conclusions

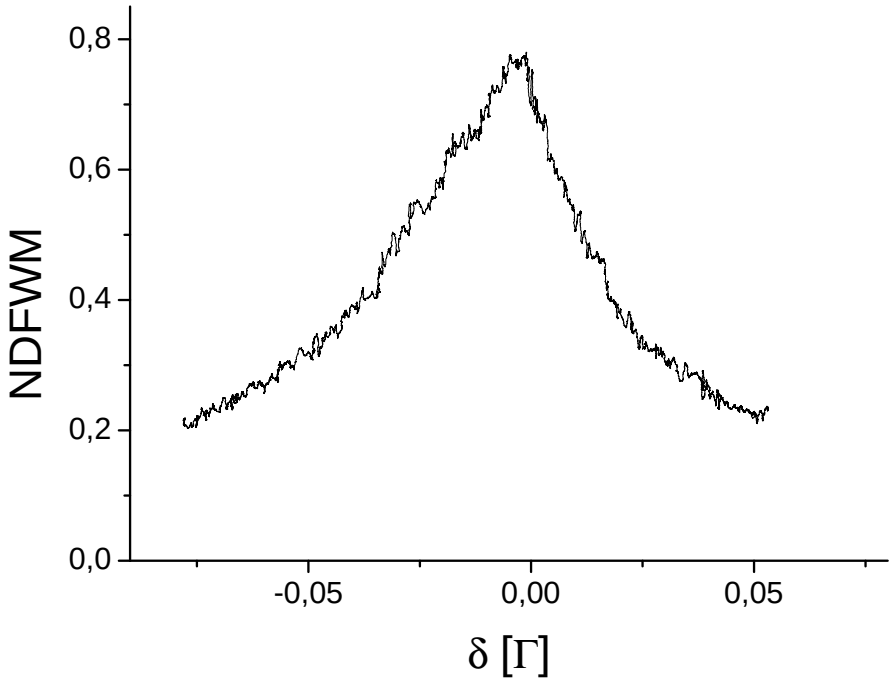

Figure 4.12: *Non-Degenerate Four-Wave Mixing (NDFWM) recorded as a function of* $\delta = \omega_{P'} - \omega_{F,B}$*, the relative detuning between the probe and pump frequencies. The figure was taken from reference [14]. A width of about* $100\,kHz$ *was observed and was consistent with the Doppler width of our atomic sample.*

By using the experimental set-up presented in Sec.(4.3.1), it is also possible to add an independent probe $P^{'}$ with a different frequency with respect to the frequency of the pumps. The recoded signal, obtained as a function of the relative detuning between the new probe and the pumps ($\delta = \omega_{P'} - \omega_{F,B}$), is called Non-Degenerate Four Wave Mixing ($NDFWM$). For a fixed $\Delta = \omega_{F,B} - \omega_0$, we scanned the δ frequency during $100\mu sec$, and we observed a width of the NDFWM of about $100\,kHz$, consistent with the Doppler width of our atomic sample.

The set-up described in Sec.(4.3.1), can be used to pump energy into the atomic sample by using a pump probe technique to produce a sample with gain [53]. As the atoms are sensitive to radiation pressure forces, we used counter-propagating pump beams to balance such radiation forces.

Various gain mechanisms can be used with cold atoms; Mollow gain [54], Raman gain [55] [56] [57] [44] or recoil-induced resonances [58] [59].

In the past, only moderate single-pass gain has been observed with cold atoms, mainly limited by the reduced optical thickness obtainable in the sample.

In our case, using clouds with a large optical thickness and number of atoms, we observed a large gain even without high-finesse cavity. In particular, a double-pass gain

of 1800% was obtained due to interference between Raman gain and Four-wave mixing [14].

The multiple scattering combined with gain can make the study of new interesting interference effects in multiple scattering possible, even when the threshold for strong localization in the passive system cannot be achieved.

4.7 Lineshapes in degenerated four-wave mixing in cold atoms

Lineshapes in degenerated four-wave mixing in cold atoms

G.L. Gattobigio[1,2], F. Michaud[1], and R. Kaiser[1]
(1) Institut Non Linéaire de Nice, UMR 6618 CNRS,
1361 route des Lucioles, F-06560 Valbonne, France and
(2)Dipartimento di Fisica dell'Universita' di Ferrara and INFN-Sezione di Ferrara, 44100 Ferrara, Italy

S. Barreiro[2] and J.W.R. Tabosa[1]
(1) Departamento de Fsica, Universidade Federal de Pernambuco,
Av. Professor Luiz Freire, s/n Cidade Universitria, 50670-901, Recife-PE and
(2) Instituto de Fsica, Facultad de Ingeniera, Montevideo, Uruguay

We observe degenerate four-wave mixing in a sample of cold rubidium atoms for different polarizations configuration of the pump and probe beams, which correspond to different atomic levels schemes. Contrary to the single peaked spectral lineshape predicted and observed for a simple two-level system, a doubled peaked lineshape is observed for strong saturation of the incident pump beams when a more complex level scheme is involved. A density matrix calculations reproduces reasonably well the measured spectra.

PACS numbers: 32.80.Pj, 42.50.Gy, 03.67.-a

1- Introduction

Spectral lineshapes in degenerate and nearly-degenerate four-wave mixing (DFWM and NDFWM) in different saturation regimes have been extensively studied in the past several years both theoretical and experimentally [1–4, 6–10]. However, most of the these investigation were experimentally realized employing samples of Doppler broadened atomic or molecular gas where the observed spectral line shape results from the contribution of different classes of atomic velocity [4–7, 9]. The facility provided by magneto-optical traps (MOT) for producing dense cloud of cold atoms renewed the interest to investigate FWM in a domain where atomic motion has a reduced role, practically eliminating broadening mechanisms such as transit time and first and second order Doppler effect and allowing us to obtain optical phase conjugation, or wave-front reconstruction, for large angular aperture between the pump and the probe beams [11]. In this regime one can also directly compare calculated FWM spectra with experiments without the need of performing any velocity averaging. For instance, the NDFWM spectra using degenerate two- and three- level schemes of cold cesium atoms have been measured which are in reasonable agreement with the theoretical predictions [12, 13]. NDFWM has also been employed to probe very narrow resonances in an operating MOT [14, 15]. In addition, some of the DFWM and NDFWM schemes can be associated with the creation of coherence between metastable ground levels and have gained much recent interest owing to possibility of the storage and processing of quantum information as well as to the production of correlated photons pairs [16].

In a recent experiment [17] we have used DFWM in a sample of cold atoms to demonstrate the bunching of atoms at the nodes and antinodes of a standing wave created by the strong couterpropagating pump beams. In this paper we investigate both theoretical and experimentally the line shape of the DFWM process in a sample of cold rubidium atoms for different polarization configuration of the FWM beams. Opposite to the well known single peaked spectrum observed for DFWM in a two-level atomic system [3, 10], we predict and experimentally observe that for strong saturation of the pump beams the DFWM spectrum presents a double peak structure which is not evident from a simple dressed state model [12].

2- The experimental set-up and results

The experiment was performed in a sample of cold rubidium atoms obtained from magneto-optical trap (MOT). Our MOT scheme has been described elsewhere [18] and allows a rapid and time controlled switching of the trapping and repumping beams as well as the magnetic quadrupole field. The FWM beams are provided by the same laser and also can be time controlled both in relative delay and duration. We employ the conventional backward FWM configuration with two independent counterpropagating pumping beams, i.e. the forward (F) and the backward (B) indicated in the Fig. 1-(a) which shows a simplified experimental configuration scheme. In Fig. 1-(b) we show the timing sequence of the experiment. First the atoms are collected and cooled for about 20 ms, then the MOT beams and the quadrupole magnetic field are switched off for about 1 ms. During this time window, the FWM beams are switched on and the generated phase conjugated beam after being reflected off a 50/50 beam splitter is detected by a fast photomultiplier. The polarization and intensities of the FWM beams can be controlled by appropriate wave plates and polarizing cubes placed along the beams path. We have essentially analyzed two different polarization configuration for the pumps and probe beams: The case where all the beams have the same linear parallel polar-

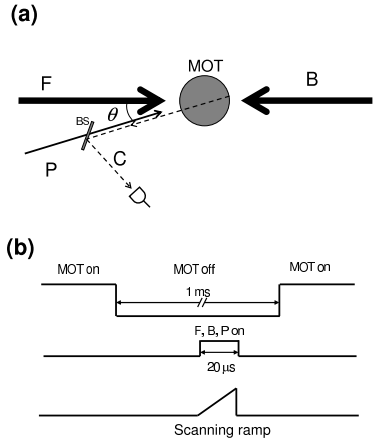

FIG. 1: (a) simplified experiment setup: two strong counterpropagating pump beams (F and B with parallel linear polarization) and one weak probe beam (P, which linear polarization can be made either parallel or orthogonal to that of F and B) are applied. The generated phase conjugate beam (C) is reflected off the 50-50 beamsplit BS. b) the timing sequence of the experiment : the MOT beams and magnetic fields are switched off during the short pump/probe pulse. The frequency of all the beams are continuously scanned by a voltage ramp

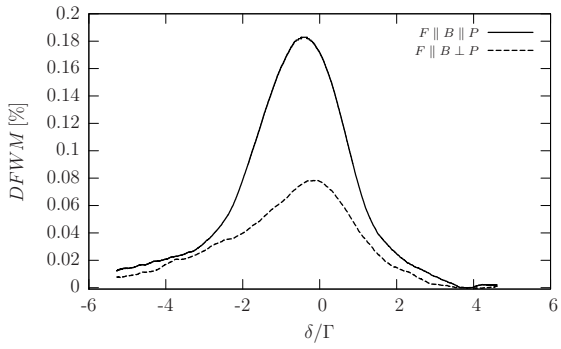

FIG. 2: solid curve: DFWM spectrum observed when all the beams have the same linear polarization (configuration ∥) ; Dashed curve: DFWM spectrum for pumps and probe with orthogonal linear polarization (configuration ⊥) . In both case the pump saturation parameter is approximately s=2.

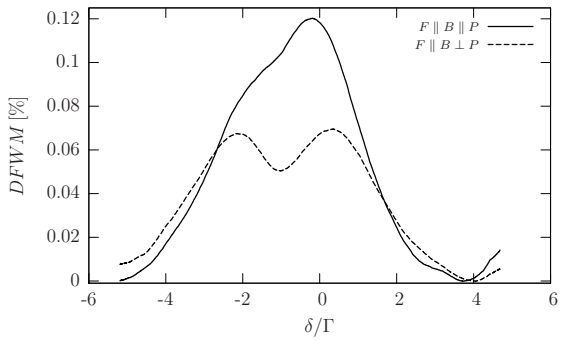

FIG. 3: DFWM spectrum observed for a pump saturation parameter of approximately s=4. solid curve: configuration ∥; Dashed curve:configuration ⊥

ization (∥) and the case where the forward and backward pump beams have linear parallel polarization orthogonal to the linear polarization of the probe beam (⊥). Although our MOT can trap very large number of atoms, up to 10^{10}, we have choose to use a moderate number of atoms in order to avoid propagation effects.

In Fig. 2 we show the DFWM spectra corresponding to the polarization configuration ∥ and ⊥ respectively. The FWM beams pulse duration is approximately equal to 20 μs. For these spectra the saturating parameter (averaged on the Clebsch-Gordan coefficients) is about $s = 2$ for the F and B pump beams and $s = 0.03$ for the probe beam P. The FWM spectra are recorded as a function of the common frequency detuning δ of the FWM beams in relation to the atomic resonance frequency of the rubidium $5S_{1/2}, F_g = 2 - 5P_{3/2}, F_e = 3$ D_2 transition . For this range of intensity, the spectrum corresponding to the polarization configuration ∥ consists essentially of a single symmetric peak centered around the detuning $\delta = 0$. On the other hand, for the polarization configuration ⊥ the spectrum presents an clear asymmetry evidencing a more complex structure. This structure becomes more evident as we increase the saturating parameter as shown in Fig. 3, where we recorded the spectra corresponding to the polarization configuration ∥ and ⊥ for a saturation parameter of $s = 4$. A clear splitting is now observed in the spectrum for the configuration ⊥. The reflectivity of each four-wave mixing process, as measured in relation to the probe beam intensity, are indicated in the vertical axis of the Fig. 2 and Fig. 3.

We should note that the physical mechanism responsible to the generation of the conjugated signal C is quite different in these two polarization configuration. Although in both cases the signal can be interpreted as being originated from Bragg diffraction into an induced grating, in the first case a population grating is induced in the medium while in the second case the signal originates from a Zeeman coherence grating.

As observed, although the spectra associated with parallel polarization essentially show no splitting for these values of saturation parameter, the spectrum for orthogonal polarization of the pump and probe beams, which should involve necessarily a more complex atomic level scheme, clearly shows a intensity dependent splitting. It is worth to mention that the double peak spectrum shown in Fig. 3 for the configuration ⊥ is approximately symmetric in contrast with the red-blue asymmetry we have previously observed which is associated with the bunching of atoms along the standing wave induced by the strong pumps beam [17]. In the

atomic level scheme, clearly shows a intensity dependent splitting. It is worth to mention that the double peak spectrum shown in Fig. 3 for the configuration $\perp$ is approximately symmetric in contrast with the red-blue asymmetry we have previously observed which is associated with the bunching of atoms along the standing wave induced by the strong pumps beam [17]. In the presented spectra the scanning time was made faster than the time required to form any bunching. In the next section we consider a simple theoretical model which predicts the observed line shape splitting.

3-Theoretical model and discussions

a) Two-level model

For the particular transition used in the experiment, the DFWM signal originates from the contributions of several different Zeeman sublevels and a complete description of the process would need to consider the degeneracy of both ground and excite levels. For the case where all the beams have the same linear parallel polarization they will couple only with transitions between Zemman sublevels with $\Delta m = 0$. In this case, the generated signal originates from the contribution of several pairs of open tow-level systems which are coupled by spontaneous emission. Therefore, the simplest theory to model this situation is the well established two-level theory of DFWM of Abrams and Lind [3, 10]. In Fig. 4 we have plotted the predicted DFWM spectra for different values of the saturation parameter as defined by $s = \frac{I}{I_{sat}} = \frac{\Omega^2}{\Gamma^2}$, where I is the individual pump intensity, Ω is the corresponding Rabi frequency, Γ is the common longitudinal and transversal relaxation rate, and I_{sat} is the transition saturation intensity.

As can be seen, according to this simple theory the DFWM spectrum just presents a broadening for increasing pump beam intensities, which accounts reasonably well for the observed results. Although the Abrams and Lind theory consider a spatial averaging of the nonlinear susceptibility over a wavelength due to the spatial variation of the pump intensity, we have verified that a local theory for a two-level system, also do not shows any line splitting .

b) Four-level model

For modelling the case of DFWM for orthogonal linear polarization between the pumps and probe beams, it is clear that a more complex level scheme is needed. As we will see, modelling the atomic medium as a simple four-level system can reveal the main characteristics of the observed spectra. Therefore, we consider a homogeneously broadened four-level atomic system, labelled by $|i\rangle$, $i = a, b, c, d$, coupled to the FWM laser fields as shown in Fig.1. The states $|a\rangle$ and $|b\rangle$ belong to the non-

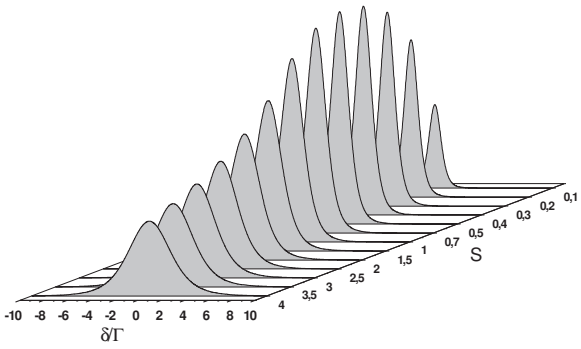

FIG. 4: Calculated DFWM spectra for different saturation parameter using the Abrams and Lind Theory.

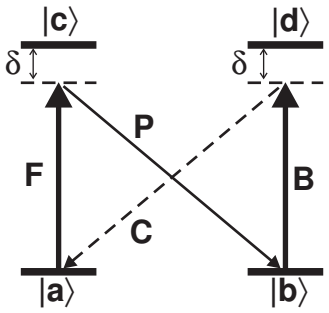

FIG. 5: Atomic four-level scheme. The arrows represent the coupling between the corresponding field with the atomic transition.

relaxing ground level with zero energy. The states $|c\rangle$ and $|d\rangle$ form the excited level with energy $\hbar\omega_0$ and spontaneous relaxation rate Γ. We therefore consider that the forward F and backward B pumping fields couples to the transitions $|a\rangle - |c\rangle$ and $|b\rangle - |d\rangle$ respectively while the probe P field couple to the transition $|b\rangle - |c\rangle$.

To account for the finite interaction time of the atoms with the light we assume an escaping rate γ ($\gamma \ll \Gamma$) from the interaction region. Under these assumptions, the temporal evolution for the density matrix ρ is determined by [19]:

$$\frac{\partial \rho}{\partial t} = -\frac{i}{\hbar}[H, \rho] - \frac{\Gamma}{2}\{P_e, \rho\} + \Gamma \sum_{q=1,2} Q^q_{ge}\rho Q^q_{eg} - \gamma(\rho - \rho_0) \tag{1}$$

where, $H = H_0 + H_{AF}$, with $H_0 = \hbar\omega_0 P_e$ and,

$$\begin{aligned} H_{AF} = {} & A\hbar\Omega_F|a\rangle\langle c|e^{i\omega t} + D\hbar\Omega_B|b\rangle\langle d|e^{i\omega t} \\ & + B\hbar\Omega_P|b\rangle\langle c|e^{i\omega t} \end{aligned} \tag{2}$$

In the equation 2, the rotating wave approximation was used. The operator P_e is the projector onto the excited states and Ω_F, Ω_B and Ω_P are the reduced Rabi frequencies for the FWM beams respectively and the numbers A^2, B^2, C^2, D^2 govern the relative transition amplitudes (analog to the Clebsh-Gordan coefficients) and satisfy:

$$A^2 + B^2 = 1 \quad (3)$$
$$C^2 + D^2 = 1 \quad (4)$$

The operators Q^q_{ge} are given by:

$$Q^1_{ge} = A|a\rangle\langle c| + B|b\rangle\langle c| \quad (5)$$
$$Q^2_{ge} = C|a\rangle\langle d| + D|b\rangle\langle d| \quad (6)$$

The first term on the right-hand side of Eq. 1 represents the free atomic evolution in the presence of the three optical fields. The remaining terms correspond to atomic relaxation. The second term on the right-hand side accounts for the radiative relaxation of the excited level. The third term describes the feeding of the ground level by atoms decaying from the excited level. The last term phenomenologically accounts for the finite interaction time and ensures the relaxation of the system, in the absence of the optical fields, to the thermal equilibrium state assumed to be described by the density matrix $\rho_0 = \frac{1}{2}[|a\rangle\langle a| + |b\rangle\langle b|]$ corresponding to an isotropic distribution of the population in the ground level. The rate γ ($\gamma \ll \Gamma$) effectively plays the role of the ground-level relaxation coefficient.

To obtain the response of the atomic system to the incident fields, it is convenient to introduce the slowly varying variables:

$$\rho_{ac} = \sigma_{ac}\exp[i\omega t] \quad (7a)$$
$$\rho_{bd} = \sigma_{bd}\exp[i\omega t] \quad (7b)$$
$$\rho_{ab} = \sigma_{ab}\exp[i\delta t] \quad (7c)$$
$$\rho_{bc} = \sigma_{bc}\exp[i\omega t] \quad (7d)$$
$$\rho_{ad} = \sigma_{ad}\exp[i\omega t] \quad (7e)$$
$$\rho_{cd} = \sigma_{cd} \quad (7f)$$
$$\rho_{ii} = \sigma_{ii} \quad i = 1,2,3,4 \quad (7g)$$

Substituting Eq. 7 into Eq. 1, we obtain the following set of equations for the slowly varying variables:

$$\frac{\partial\sigma_{ab}}{\partial t} = -\gamma\sigma_{ab} - i\Omega_F A\sigma_{cb} + i\Omega_B^* D\sigma_{ad} + i\Omega_P^* B\sigma_{aa} \quad (8a)$$
$$+ \Gamma AD\sigma_{cd}$$
$$\frac{\partial\sigma_{ac}}{\partial t} = \left[i\Delta - \frac{\Gamma}{2} - \gamma\right]\sigma_{ac} + i\Omega_F A(\sigma_{aa} - \sigma_{cc}) \quad (8b)$$
$$+ i\Omega_P B\sigma_{ab}$$
$$\frac{\partial\sigma_{ad}}{\partial t} = \left[i\Delta - \frac{\Gamma}{2} - \gamma\right]\sigma_{ad} - i\Omega_F A\sigma_{cd} \quad (8c)$$
$$+ i\Omega_B D\sigma_{ab}$$
$$\frac{\partial\sigma_{bc}}{\partial t} = \left[i\Delta - \frac{\Gamma}{2} - \gamma\right]\sigma_{bc} - i\Omega_B D\sigma_{dc} \quad (8d)$$
$$+ i\Omega_F A\sigma_{ba} + i\Omega_P B(\sigma_{bb} - \sigma_{cc}$$
$$\frac{\partial\sigma_{bd}}{\partial t} = \left[i\Delta - \frac{\Gamma}{2} - \gamma\right]\sigma_{bd} + i\Omega_B D(\sigma_{bb} - \sigma_{dd}) \quad (8e)$$
$$- i\Omega_P B\sigma_{cd}$$
$$\frac{\partial\sigma_{cd}}{\partial t} = -[\Gamma + \gamma]\sigma_{cd} - i\Omega_F^* A\sigma_{ad} - i\Omega_P^* B\sigma_{bd} \quad (8f)$$
$$+ i\Omega_B D\sigma_{cb}$$
$$\frac{\partial\sigma_{aa}}{\partial t} = -\gamma\sigma_{aa} - i\Omega_F A\sigma_{ca} + i\Omega_F^* A\sigma_{ac} \quad (8g)$$
$$+ \Gamma(C^2\sigma_{dd} + A^2\sigma_{cc}) + \frac{\gamma}{2}$$
$$\frac{\partial\sigma_{bb}}{\partial t} = -\gamma\sigma_{bb} - i\Omega_B D\sigma_{db} + i\Omega_B^* D\sigma_{bd} \quad (8h)$$
$$- i\Omega_P B\sigma_{cb} + i\Omega_P^* B\sigma_{bc}$$
$$+ \Gamma(D^2\sigma_{dd} + B^2\sigma_{cc}) + \frac{\gamma}{2}$$
$$\frac{\partial\sigma_{cc}}{\partial t} = -(\Gamma + \gamma)\sigma_{cc} - i\Omega_F^* A\sigma_{ac} + i\Omega_F A\sigma_{ca} \quad (8i)$$
$$- i\Omega_P^* B\sigma_{bc} + i\Omega_P B\sigma_{cb}$$
$$\frac{\partial\sigma_{dd}}{\partial t} = -(\Gamma + \gamma)\sigma_{dd} - i\Omega_B^* D\sigma_{bd} + i\Omega_B D\sigma_{db} \quad (8j)$$

with $\Delta = \omega_0 - \omega$

The term responsible for the generation of the DFWM signal is the matrix element σ_{ad}. We have solved through perturbation theory and on steady state regime the complete set of density matrix equations 8, to obtain $\sigma^{(1)}_{ad}$ in first order in Ω_P and in all orders in Ω_F and Ω_B. The DFWM signal is then proportional to $|\sigma^{(1)}_{ad}|^2$. In Fig. 6 we plot the calculated DFWM spectrum for different values of the saturation parameter for equal pump Rabi frequency, i.e., $s = \frac{\Omega_F^2}{\Gamma^2} = \frac{\Omega_B^2}{\Gamma^2}$. As can be seen, for small Rabi frequency the spectrum presents just a single peak which evolves to a double peak structure for higher values of the Rabi frequency. This is in qualitative agreement with the observed spectra shown in Fig. 2.

4-Summary

We have observed DFWM mixing in a degenerate two-level system of cold rubidium atoms. Two different po-

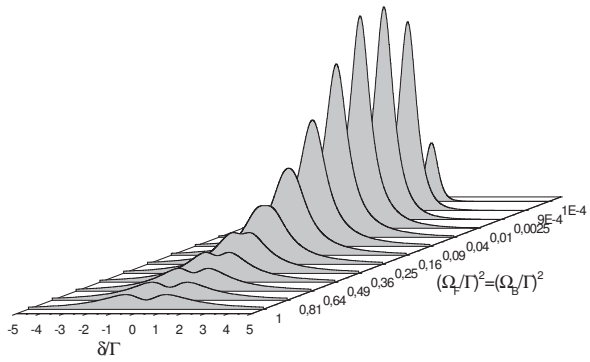

FIG. 6: Calculated DFWM spectrum for different values of the pump saturation parameter $s = \frac{\Omega_F^2}{\Gamma^2} = \frac{\Omega_B^2}{\Gamma^2}$

.

larization configuration of the incident beams were analyzed. For the case of parallel linear polarization the observed spectrum is well described by the theory of Abrams and Lind. However, when the pump and probe have orthogonal linear polarization a spectrum shown an intensity dependent splitting is observed. We have developed a simple theoretical model based on four-level scheme which accounts reasonably well for the measured spectrum.

[1] Robert A. Fisher, *Optical Phase Conjugation* (Academic Press, 1983),

[2] Robert W. Boyd, Michael G. Raymer, Paul Narum,and Donald J. Harter, Phys. Rev. A **24**, 411 (1981).

[3] R. L. Abrams,and R. C. Lind, Opt. Lett. **2**, 2678 (1978).

[4] Martial Ducloy, Fernando A. M. de Oliveira, Daniel Bloch, Phys. Rev. A **32**, 1614 (1985);

[5] J. W. R. Tabosa, S. Le Boiteux, P. Simoneau, D. Bloch, M. Ducloy Europhys. Lett. **4**, 433 (1986);

[6] Sylvie Le Boiteux, Pierre Simoneau, Daniel Bloch, Fernando A. M. de Oliveira, Martial Ducloy, IEEE J. Quantum Electron. **22**, 1229 (1986);

[7] P. Verkerk, M. Pinard, G. Grynberg Phys. Rev. A **638**, 4008 (1986).

[8] H. Friedmann, A. D. Wilson-Gordon Phys. Rev. A **57**, 4854 (1998);

[9] J. W. R. Tabosa, C. L. Cesar, M. Ducloy, J. R. Rios Leite, Opt. Commun. **67**, 240 (1988);

[10] Binh. Do, Jongwhan Cha, D. S. Elliot S. J. Smith Phys. Rev A **58**, 3089 (1998);

[11] J. W. R. Tabosa, S. S. Vianna F. A. M. de Oliveira Phys. Rev. A **755**, 2968 (1997)

[12] A. Lezama, G. C. Cardoso J. W. R. Tabosa Phys. Rev. A **63**, 013805 (2001);

[13] S. Barreiro, J. W. R. Tabosa Opt. Commun. **233**, 383 (2004);

[14] G. C. Cardoso, J. W. R. Tabosa Opt. Commun. **185**, 353 (2000);

[15] Thomaz M. Brzozowska, Maria Brzozowska, Jerzy Zachorowski, Michal Zawada, and Wojciech Gawlik Phys. Rev A **71**, 013401 (2005);

[16] M. D. Lukin, P. R. Hemmer, and M. O. Scully, Adv. Atom Mol Opt. Phys **42**, 347 (2000).

[17] G. L. Gattobigio, F. Michaud, J. Javaloyes, J. W. R. Tabosa, R. Kaiser, Phys. Rev. A **74**, 043407 (2006).

[18] G. Labeyrie, F. de Tomasi, J.-C. Bernard, C. A. Muller, C. Miniatura,and R. Kaiser, Phys. Rev. Lett. **83**, 5266 (1999).

[19] A. Lezama, S. Barreiro, A. M. Akulshin Phys. Rev. A **59**, 4732 (1999);

Conclusion

In this thesis we presented a study of a Magneto-Optical Trap (MOT) of ^{85}Rb in the limit of a very large number of atoms (N=10^{10}). We reported a detailed experimental investigation of size and density scaling laws, and we introduced a new mechanism which can limit the density of atoms in such a system.

In one type of experiment, where the atom number was changed by varying the intensity of the repumper laser, our observations confirmed several previous measurements, which had found a cross-over in atom number dependence on MOT size (L) changing from $L \propto N^{1/3}$ to $L \propto N^{1/2}$ with an increasing N. However, this cross-over disappears when we control the atom number by varying the diameter of the repumper laser. This latter procedure gives rise to a scaling law $L \propto N^{1/3}$, and thus a constant density up to a large atom number (N=10^{10}), which provides experimental evidence that the $N^{1/2}$ does not arise from multiple photon scattering beyond double scattering, as previously suggested in the literature[22] [60]. In order to have a better understanding of the MOT scaling laws, we proposed a qualitative model for the density (and thus for the size) which introduces, for the first time, the mechanical interactions induced by the repumper photons scattered in the MOT. This effect becomes more and more evident as more atoms are added in the dark hyperfine ground state, giving rise to a new limit for the density. We speculate that a considerable increase of spatial density should be possible if we are able to control the repumper effects. For example, we predict that spatial atomic density could be increased by using six independent repumper beams instead of only one retro-reflected beam, as realized in the experiment. In fact, the resulting shadow effect of the repumper should compensate the repulsive interaction of light scattered by the repumper and lead to a denser atomic medium.

But this is not the only way to increase the density by 3 orders of magnitude, as required to reach the densities needed in order to observe strong localization of light. More precisely, we need to eliminate the laser-induced interactions produced by the multiple scattering, for both the MOT and for the repumper photons, in the atomic cloud. This is why we realized a 'Dark MOT', obtained by using the lower hyperfine ground state, in which the preloaded atoms in the standard MOT were optically 'depumped'. Indeed, the atoms in this state do not interact with the trapping light (i.e. they are dark for such a light), thus the repulsions were considerably lowered and an increase of the density was observed. On the other hand, the less confining characteristics of the 'Dark MOT' required an additional external potential to confine the atoms. An optical potential was obtained from a free-running DFB laser at $780\,nm$ amplified by a Tapered Amplifier. After amplification, the laser beam was focused to a waist of about $350\,\mu m$, and superimposed onto the 'Dark MOT'. By following this protocol, we observed the highest density ever obtained in our set-up ($\sim 10^{12}\,atms/cm^3$).

A medium with high spatial density like this, even if it is one order of magnitude below the localization threshold, could be used as a random medium to observe the effects of light trapping due to interferences in multiple scattering. As we sometimes like to think of localization as closed loops made by light in the medium, the introduction of gain in such a medium could be used to amplify these closed loops. This analogy has motivated us to start new research in an attempt to combine gain and multiple scattering, which - if successful - will allow us to produce a random laser with cold atoms.

As a first step, we decided to set up the pump-probe technique which is suitable for the production of gain in the atomic sample. A typical pump technique with cold atoms makes use of two counterpropagating pump fields, in order to minimalize the mechanical effects due to radiation pressure. The pump-probe set-up naturally lead to a well known configuration: the four-wave mixing process. Indeed, we investigated the properties and the characteristics of the Degenerate Four-Wave Mixing (DFWM) signal, where the two pumps and the probe have the same frequencies. We measured the DFWM for different configurations of polarizations of the pumps and probe beams which corresponded to different atomic level schemes. In the case in which the pumps have the same polarization as the probe (parallel configuration), we can consider our atomic medium as being composed of an ensemble of two-level atoms. In such a situation we observed a single peaked spectral lineshape even within the limits of high pump intensity in accordance with the theory of Abrams and Lind [49][51]. However, if we consider the situation where the probe polarization is perpendicular to that of the pumps, a double peak structure was observed even when the center line absorption, generated by large optical thickness of the atomic cloud, was avoided. The physical origin of such a splitting of the center line has been explained by taking into account a more complex atomic level scheme.

In addition to the effects predicted by standard atomic physics, we also observed a new surprising feature: a clear red-blue asymmetry of the DFWM signal for high intensities of the pumping beams. We explained this asymmetry as the spatial bunching of the atoms in the nodes or antinodes of the strong standing wave of the pump beams. This characteristic should always be considered, particularly when cold atoms are used as the nonlinear medium. Mechanical effects related to this bunching might become important when we want to approach the "random laser" regime with cold atoms, where strong pumping will be necessary.

The same set-up used for the DFWM was employed to create gain in the atomic cloud. Indeed, large gain in single and double pass was observed in our set-up [14]. The surprising large double pass gain was explained via DFWM mechanisms. This large gain allowed us to build up a Fabry-Perot type laser with cold atoms as the gain medium. At present, and for the future, the properties of such an intriguing laser can be used to investigate the effect of coherent multiple scattering in the presence of gain while approaching the threshold of Anderson's localization.

In conclusion, the work presented in this manuscript has contributed to the possibility of approaching Anderson's localization threshold via a better understanding of the limitations of the spatial densities in a MOT and by first pump-probe experiments opening the way for a "random laser" with cold atoms.

Appendix A

Re-scattering cross section

In this appendix, we'll present the details of the calculation of absorption cross section σ_L, the re-absorption cross section $\langle\sigma_R\rangle$ for a two-level atom illuminated by laser light using the dressed atom approach. In general scattered light from a single atoms at rest has two distinct contribution: a coherent part I_{coh}, arising form the mean dipole oscillating in phase with the driving field, and an incoherent part I_{coh} originating from fluctuations of the atomic dipole [23].

The re-absorption cross section is obtained by the evaluation of absorption of the emitted light by the neighboring atoms. If we define $S(\omega)$ the emission spectral density and $\sigma_A(\omega)$ the absorption spectra of the atom illuminated by the laser light, then the re-absorption cross section is equal to:

$$\langle\sigma_R\rangle \;=\; \frac{\int \sigma_A(\omega')S(\omega')\,d\omega'}{\int\, S(\omega')\,d\omega'} \tag{A.1}$$

As we can found in many references, the expression of absorption and the fluorescence spectra can be done with the dressed atom approach, like in reference [18].

As done in reference [61], we indicate with $\Omega = \Gamma\sqrt{I/2I_{sat}}$ the Rabi frequency, with $\Omega_G = \sqrt{\Omega^2+\delta^2}$ the generalized Rabi frequency, and $c^2 = \cos^2(\theta)$, $s^2 = \sin^2(\theta)$ and again $c^4 = \cos^4(\theta)$, $s^4 = \sin^4(\theta)$, with the angle defined by $\tan(\theta) = \Omega/\delta$. Thus we indicated as $\mathcal{L}(\omega-\omega',\Gamma)$ the normalized Lorentzian function centered in $\omega = \omega'$ of width equal to 2Γ, and with $\mathcal{L}(\omega-\omega',0)$ the limit of the Lorentzian when its width goes to zero; the definition of delta function. Also we define $\Gamma_p = \Gamma(c^4+s^4)$ and $\Gamma_c = \frac{\Gamma}{2}(1+2c^2s^2)$. By using such a definition, it is possible to demonstrate that the relative expressions for the normalized emission and absorption spectra, in the limit of $\Omega_G \gg \Gamma$ are given by :

$$S(\omega) \;=\; \frac{(c^2-s^2)}{(c^4+s^4)}\mathcal{L}(\omega-\delta,0)+\frac{4c^4s^4}{c^4+s^4}\mathcal{L}(\omega-\delta,\Gamma_p)\cdot[c^2s^2\{\mathcal{L}(\omega-\delta-\Omega_G,\Gamma_c)+\mathcal{L}(\omega-\delta+\Omega_G,\Gamma_c)\}] \tag{A.2}$$

and

$$\sigma_A(\omega) = \qquad \sigma_0\pi\frac{\Gamma}{2}\frac{c^2-s^2}{c^4+s^4}\cdot\{c^4\mathcal{L}(\omega-\delta-\Omega_G,\Gamma_c)-s^4\mathcal{L}(\omega-\delta+\Omega_G,\Gamma_c)\} \tag{A.3}$$

Is important to remind, the all those formula are valid in the limit of large generalized Rabi frequency with respect to natural line width Γ, i.e $\Omega_G = \sqrt{\Omega^2 + \delta^2} \gg \Gamma$. This condition can be fulfilled in the regime of high intensities and large detuning. After these approximations, we are now able to evaluate the integral(A.1) and write the expression for the re-absorption cross section [25]:

$$\begin{aligned} \langle \sigma_R \rangle \;=\; & \sigma_0 \;\; \frac{\Gamma}{2} \frac{(c^2 - s^2)^2}{c^4 + s^4} \Big\{ \frac{(c^2 - s^2)^2}{c^4 + s^4} \frac{\Gamma_c}{\Omega^2 + \delta^2 + \Gamma_c^2} \\ & + \;\; \frac{4\, c^4 s^4}{c^4 + s^4} \frac{(\Gamma_c + \Gamma_p)}{\Omega^2 + \delta^2 + (\Gamma_c + \Gamma_p)^2} \\ & + \;\; \frac{c^2 s^2}{2} \Big(\frac{1}{\Gamma_c} + \frac{\Gamma_c}{\Omega^2 + \delta^2 + \Gamma_c^2} \Big) \Big\} \,. \end{aligned} \tag{A.4}$$

We can give for the Eq. (A.4) asymptotic expression. In our case, we are interested at expression in the limit of large laser detuning $|\delta| \gg \Omega \gg \Gamma$. In that limit we have also, $\theta \cong \Omega/\delta$ and the approximated expressions for the cross sections are :

$$\sigma_L \cong \frac{\sigma_0 \Gamma^2}{4\delta^2} \;, \qquad \langle \sigma_R \rangle - \sigma_L \;\cong\; \sigma_0 \frac{\Omega^2}{8\delta^2} \tag{A.5}$$

Bibliography

[1] Freeman, *Stellar Atmospheres*, San Francisco, 1978.

[2] J. Sajeev, *Scattering and Localization of Classical Waves in Random Media*, World Scientific (1990), 1990.

[3] P. W. Anderson, Phys. Rev. **109**, 1492 (1958).

[4] N. Mott, *Metal-Insulator Transitions*, London, 1974.

[5] D. S. Wiersma, P. Bartolini, A. L. A., and R. Righini, Nature **390**, 671 (1997).

[6] F. Scheffold, R. Lenke, R. Tweer, and G. Maret, Nature **398**, 206 (1999).

[7] C. M. Aegerter, M. Störzer, and G. Maret, Europhys. Lett. **75**, 562 (2006).

[8] M. Storzer, P. Gross, C. M. Aegerter, and G. Maret, Phys. Rev. Lett. **96**, 063904 (2006).

[9] G. Labeyrie et al., Phys. Rev. Lett. **83**, 5266 (1999).

[10] S. Chu, Rev. Mod. Phys. **70**, 685 (1998).

[11] M. H. Anderson, J. R. Ensher, M. R. Matthews, C. E. Wieman, and E. A. Cornell, science **269**, 198 (1995).

[12] K. B. Davis et al., Phys. Rev. Lett. **75**, 3969 (1995).

[13] T. Walker, D. Sesko, and C. Wieman, Phys. Rev. Lett. **64**, 408 (1990).

[14] F. Michaud, G. L. Gattobigio, J. W. R. Tabosa, and R. Kaiser, J. Opt. Soc. Am. B **24**, A40 (2007).

[15] http://www.hellma-worldwide.de/, Technical report.

[16] J. Dalibard, J. M. Raimond, and J. Zinn-Justin, *Atomic Motion in laser light, C.COHEN-TANNOUDJI*, eds. Proceeding of the Summer School in Les Houches 1990, 1990.

[17] H. J. Metcalf and P. van der Straten, *Laser Cooling and Trapping*, Springer, 1999.

[18] G. G. C.Cohen-Tannoudji J. Dupont-Roc, *Preocessus d'interaction entre photons et atomes*, Editions du CNRS, 1988.

[19] T. W. Hansch and A. L. Schawlow, Opt. Commun. **13**, 68 (1975).

[20] A. M. Steane and C. J. Foot, Europhys. Lett. **14**, 231 (1991).

[21] J.Dalibard, Opt. Comm. **68**, 203 (1988).

[22] D. Sesko, T.G.Walker, and C. Wieman, J. Opt. Soc. Am. B **8**, 946 (1991).

[23] B. R. Mollow, Phys. Rev. Lett. **188** (1969).

[24] D. Hoffmann, P. Feng, and T. Walker, Phys. Rev. Lett. **69**, 753 (1992).

[25] D.Grison, *Atomes piégés et refroidis par laser à quelques microKelvins: Un piège magnéto-optique dans une cellule de césium et quelque applications.*, PhD thesis, Paris VI, 1992.

[26] C. Wallace, T. Dinneen, K. Tan, T. Grove, and P. Gould, Phys. Rev. Lett. **69**, 897 (1992).

[27] D. Sesko, T. Walker, C. Monroe, A. Gallagher, and C. Wieman, Phys. Rev. Lett. **63**, 961 (1989).

[28] S. D. Gensemer, V. Sanchez-Villicana, K. Y. N. Tan, T. T. Grove, and P. L. Gould, Phys. Rev. A **56**, 4055 (1997).

[29] W. Ketterle, K. B. Davis, M. A. Joffe, A. Martin, and D. E. Pritchard, Phys. Rev. Lett. **70**, 2253 (1993).

[30] G. L. Gattobigio, Coherent-backscattering e atomi freddi di stronzio, Master's thesis, Universita di Pisa, 2003.

[31] M. D. Barrett, J. A. Sauer, and M. S. Chapman, Phys. Rev. Lett. **87**, 010404 (2001).

[32] D. J. Han, M. T. DePue, and D. S. Weiss, Phys. Rev. A **63**, 023405 (2001).

[33] C. G. Townsend et al., Phys. Rev. A **52**, 1423 (1995).

[34] M. DePue, W. S. Lukman, D. J. Han, and D. S. Weiss, Opt. Comm. **180**, 73 (2000).

[35] C. G. Townsend, N. H. Edwards, and C. J. Foot, Phys. Rev. A **53**, 1702 (1996).

[36] W. Petrich, M. H. Anderson, J. R. Ensher, and E. A. Cornell, J. Opt. Soc. Am. B **11**, 1332 (1994).

[37] L. Khaykovich and N. Davidson, J. Opt. Soc. Am. B **16**, 702 (1999).

[38] G.Labeyrie, F. Michaud, and R.Kaiser, Phys. Rev. Lett. **96**, 023003 (2007).

[39] G. Hillenbrand, K. Burnett, and C. J. Foot, Phys. Rev. A **52**, 4763 (1995).

[40] C. D. Wallace, T. P. Dinneen, and J. Javanainen, J. Opt. Soc. Am. B **11**, 703 (1994).

[41] R. Grimm, M. Weidemuller, and Y. B. Ovchinnikov, Adv. At. Mol. Opt. Phys. **42**, 95 (2000).

[42] A. Savage and R. C. Miller, Appl. Opt. **1**, 661 (1962).

[43] Y.-C. Chen, Y.-W. Chen, J.-J. Su, J.-Y. Huang, and I. A. Yu, Phys. Rev. A **63**, 043808 (2001).

[44] T. M. Brzozowski, M. Brzozowska, and W. Gawlik, Phys. Rev. A **71**, 013401 (2005).

[45] M. Masaharu, Y. Makoto, K. Masato, and I. Nobuyuki, Opt. Lett. **23**, 840 (1998).

[46] J. Tabosa and A. Lezama, J.Phys.B:At.Mol. Opt. Phys. **40**, 2809 (2007).

[47] R. W.Boyd, *Nonlinear Optics*, Academic Press Inc., 1992.

[48] J. D. Jackson, *Classical Electrodynamics Third Edition*, Wiley and Sons, 2001.

[49] R. L. Abrams and R. C. Lind, Opt. Lett. **2**, 94 (1978).

[50] D. A. Braje, V. Balic, S. Goda, G. Y. Yin, and S. E. Harris, Phys. Rev. Lett. **93**, 183601 (2004).

[51] R. L. Abrams and R. C. Lind, Opt. Lett. **3**, 205 (1978).

[52] S. B. A. Lezama and A. M. Akulshin, Phys. Rev. A **59**, 4732 (1999).

[53] G.Grynberg and C. Robillard, Phys. Rep. **355**, 335 (2001).

[54] F. Y. Wu, S. Ezekiel, M. Ducloy, and B. R. Mollow, Phys. Rev. Lett. **38**, 1077 (1977).

[55] C. Mennerat-Robilliard and L. Guidoni, Eur. Phys. J. D **1**, 33 (1998).

[56] J. Tabosa, G. Chen, Z. Hu, R. Lee, and H. Kimble, Phys. Rev. Lett. **66**, 3245 (1991).

[57] D. Grison, B. Lounis, and G. Grynberg, Europhys. Lett. (1991).

[58] J.-Y. Courtois, G. Grynberg, B. Lounis, and P. Verkerk, Phys. Rev. Lett. **72**, 3017 (1994).

[59] J. Guo, P. Berman, B. Dubetsky, and G. Grynberg, Phys. Rev. A **46**, 1426 (1992).

[60] C. Monroe, W. Swann, H. Robinson, and C. Wieman, Phys. Rev. Lett. **65**, 1571 (1990).

[61] L.Pruvost, I.Serre, H. Duong, and J. Jortner, Phys. Rev. A **61**, 053408 (2000).

Ringraziamenti

I ringraziamenti sono sempre un po' difficili da fare: ma è vero che sono anche doverosi. Anche perchè in una tesi ci sono molte persone che s'incontrano e molte vite che s'intrecciano. Scopri amicizie che mai avresti pensato prima, scopri posti e sentimenti mai visti e provati prima. Scopri come sei fatto tu per quel che sei e che ognuno è fatto com'è fatto. Scopri come comportarti con le persone; scopri come loro possano darti qualche cosa e come tu possa dare qualche cosa a loro. Scopri quanto sia dura la lontananza dalla famiglia: babbo e mamma grazie; dalla ragazza, superfluo dire che se non c'era Silvia io non sarei mai arrivato fino a questo punto: Grazie Silvia. Scopri come i posti che ti hanno visto crescere diventino importanti. Scopri che la famiglia numerosa che lasci in Italia la ritrovi in Francia, dando una certa continuità con i luoghi dove hai vissuto quest'esperienza: Grazie Mario, Patty, Futura, Ezra e Galassia. Scopri che il mare è diventato importante per te. Scopri che, fare colazione tutti i giorni davanti una terrazza con il sole caldo ti riempe di gioia. Scopri che hai un'altra famiglia che ti vuole bene e che ti ha dato la possibilità di compiere questa esperienza in una casa importante che mai dimenticherò: Grazie Suzanne, Michel e Thierry. E così scopri che i colleghi diventano amici veri, nei quali puoi contare, e che sei felice di averli: Grazie ancora a Thierry e grazie anche a Nadine. Scopri che, gli amici lontani, non sono poi così lontani: grazie per tutto, e loro lo sanno, a Francesco e Barbara ed a Gianni, Stefano. Grazie anche agli amici di sempre che quando hanno potuto mi hanno sempre aiutato: Stefano, Carmelo, Rosario, grazie; senza, chiaramente dimenticare, Davide e Fabiola.
Grazie anche a tutti gli amici del paesello, Riccardo, Andrea grazie; a Paddy per aver corretto con attenzione la tesi, senza dimenticare Susy; e a tutti quelli di Fano, mia seconda patria: grazie a tutti. Un grazie particolare va anche a Marisa che mi ha ospitato, con pazienza, durante i lunghi soggiorni a Fano. Grazie anche a Michela, Diego, Sara e Lucia. Grazie ancora.

Scopri che il laboratorio dove lavori, con tutti i suo abitanti, diventi casa tua. Grazie, quindi, a tutti gli abitanti del laboratorio: dalla segreteria, all'ufficio d'informatica passando da quello dell'elettronica fino all'atelier di meccanica. Grazie a tutti. Scopri che il tuo ufficio si transforma anche nella tua camera da letto, spogliatoglio e garage per la tua bicicletta. Tutto questo reso possibile dalla pazienza di Stéphane: grazie per tutto. Scopri, che il tuo direttore di tesi, diventi una guida ed uno psicologo alla stesso tempo: grazie Robin. Scopri che puoi imparare "il mestiere" anche divertendoti: un grazie particolare va a Guillaume. Grazie a lui ho imparto a gestire un'esperienza, invece di essere gestito dalla stessa: grazie veramente per tutto . E un grazie particolare va anche a tutti gli altri componeni dell'equipe "atomes froid" di Nizza: David, Christian ed anche agli ultimi arrivati Franck e William. Ma anche all'altra equipe di atomi freddi, quella di Ferrara. Grazie a Roberto per avermi concesso la possibilità di aver realizzato questa tesi in cotutela.

Ma puoi scoprire che tutto questo può essere un "gioco", come la vita del laboratorio, a cui tutti partecipiamo senza rendercene conto: Grazie Lorenzo, Marco e Fiorenza per i bei momenti e le ottime cene.

Ed infine i ringraziementi per chi, economicamente parlando, mi ha supportato. Grazie all'università italo-francese per avermi concesso il contributo di mobilità internazionale; all'ANR, progetto CAROL, per aver finanziato il mio ultimo anno di dottorato.

E per concludere, anche se durante questa tesi di ricerca non ho “trovato” rivoluzionari risultati, posso dire di aver SCOPERTO un sacco di cose. Grazie ancora a Tutti!!

Abstract

In this thesis we present a detailed experimental investigation of size- and density-scaling laws for large Magneto-Optical Traps (MOT) with up to 10^{10} atoms. It is well known that laser-induced interactions, produced by multiple scattering, is the main limitation to spatial densities in a MOT. We therefore realized a 'Dark MOT' combined with a Dipole-Trap. Thus, the repulsions were considerably lower and an increase by two factor of magnitude (up to $10^{12}\,atm/cm^3$) has been observed. We also propose a qualitative model for the density (and thus for the size), which introduces the mechanical interactions induced by the repumper photons when its optical thickness becomes important. This work is part of the research project to observe Anderson localization of light in cold atoms, where densities of the order of $(10^{13} - 10^{14}\,atm/cm^3)$ are required. For densities lower than this critical value gain mechanisms could be useful to amplify prelocalized modes. We thus implemented a pump-probe technique suitable for gain production in the atomic sample. In our case, we have been naturally lead to a Four-Wave Mixing (FWM) configuration. A detailed analysis of the properties and characteristics of FWM-signal has been presented, with, in particularly, a clear red-blue asymmetry of FWM-spectrum for high intensities of the pump beams. We explained this asymmetry by the spatial bunching of the atoms in the nodes or antinodes of the strong standing wave of the pump beams.

Résumé

Dans cette thèse, nous présentons une recherche expérimentale détaillée des lois caractérisant la taille et la densité atomique de grands pièges magnéto-optiques contenant typiquement 10^{10} atomes. Il est bien connu que les interactions induites par laser, produites par la diffusion multiple, y constituent la limitation principale à l'obtention de densités atomiques élevées. Pour contourner cette limite, nous avons réalisé un piège magnéto-optique "noir" combiné un piège dipolaire. Les forces de répulsion assistées par la lumière ont ainsi pu être considérablement réduites et une augmentation de près de deux ordres des grandeur sur le densité (jusqu'à $10^{12}\,atm/cm^{-3}$) a été corrélativement observée. Nous avons proposé également un modèle qualitatif pour rendre compte de la densité atomique (et également pour la taille) où nous avons introduit les interactions mécaniques induites par les photons du laser repompeur quand son épaisseur optique devient importante. Ce travail fait partie d'un projet de recherche qui vise à terme à observer la localisation d'Anderson de la lumière dans des nuages d'atomes froids, mais pour laquelle des densités de l'ordre $(10^{13} - 10^{14}\,atm/cm^3)$ sont requises. Pour des densités inférieures, des mécanismes de gain peuvent toutefois être mis à profit pour amplifier des modes pre-localisés. Nous avons, ainsi, mis en place une technique pompe-sonde pour la création d'un gain dans l'échantillon atomique. La configuration des pompes a autorisé l'observation du signal de mélange a quatre ondes. Une analyse détaillée de ses propriétés et de ses caractéristiques a été présentée. En particulier, une asymétrie rouge-bleu dans le spectre, pour des intensités élevées des faisceaux pompes, a été mise en évidence. Cette asymétrie a pu tre expliquée en tenant compte du regroupement des atomes dans les noeuds ou dans les ventres de l'onde stationnaire des faisceaux de pompe.

Keywords : Rubidium, Magneto-Optical Trap, Multiple Scattering, Mechanical Effects, Compression Techniques, Four-Wave Mixing, Dipole Forces.